UNIVERSITA' degli STUDI di MILANO-BICOCCA
Dottorato di Ricerca XXIII ciclo
in
Scienze della Terra

Quantitative provenance analysis of modern sands:
bulk petrography, heavy minerals,
apatite fission tracks

Tutor: Eduardo Garzanti
Co-tutors: Marco G. Malusà, Giovanni Vezzoli

Laboratory for Provenance Studies
Department of Geology and Geotechnology
University Milano-Bicocca, Italy

Alberto Resentini
matr. 044978

Abstract

Sediment petrography and heavy mineral analysis represent two key techniques to decipher the pieces of information stored in the sedimentary record, shedding light on source rocks compositon, weathering conditions and paleodrainages. Traditionally, even though orogenic detritus has always received large attention, orogenic provenance has been recognized as “composite”, thus preventing clear classification. Notwithstanding the composite nature of collision orogens, the detrital fingerprints of neometamorphic axial belts, largely experiencing strong exhumation and erosion, can be regarded as the diagnostic signature of orogenic detritus. We thus decided to focus our attention on the analysis of modern river sands from the Alpine belt, getting full quantitative information both on bulk compositions and heavy mineral assemblages.

Within the Austroalpine Cretaceous and Penninic Eocene axial belts of the Alps, we ideally distinguish three structural levels, each characterized by diagnostic detrital fingerprints. The shallow level chiefly consists of offscraped remnant-ocean turbidites and unmetamorphosed continental-margin sediments, and mostly produces lithic to quartzolithic sedimentaclastic sands yielding very-poor heavy-mineral suites including ultrastable minerals. The intermediate level includes low-grade metasediments and polymetamorphic basements, and sheds quartzolithic to feldspatholithoquartzose metamorphiclastic sands yielding moderately-rich epidote-amphibole suites with chloritoid or garnet. The deep level contains eclogitic remnants of continent-ocean transitions, and supplies feldspatholithoquartzose/feldspathoquartzose high-rank metamorphiclastic to lithic ultramaficlastic sands yielding rich to extremely-rich suites dominated by garnet, hornblende, or epidote depending on protoliths (continental vs. oceanic) and pressure/temperature paths during exhumation. Although widely overprinted under greenschist-facies or amphibolite-facies conditions, occurrence of ultradense eclogite in source areas is readily revealed by the Heavy Mineral Concentration (HMC) index, which mirrors the average density of source rocks in the absence of hydraulic-sorting effects. Rather than the pressure peak reached at depth, the Metamorphic Index (MI) and Hornblende Colour Index (HCI) reflect peak temperatures reached at later stages, when subduction is throttled by arrival of thicker continental crust and geothermal gradients increase, as documented in detritus derived from the Tauern window and Lepontine dome. Experience gained from modern sediments, and appropriate statistical techniques provides fundamental help to decrypt the information stored in the sedimentary record, and thus to identify and reconstruct subduction events of the past.

Besides the fundamental contribution that modern sediment analysis can bring in understanding ancient sandstone successions, it can also give insights on short-term erosion distribution over wide areas and readily detect potential area of focused erosion.

We tested a new quantitative approach based on the integration of compositional data and detrital apatite fission-tracks in two valleys of the western Alps (Arc and Dora Baltea basins).

Samples for bulk-petrography and fission-track analysis were collected at different closure sections along the trunk, in order to investigate how the detrital signal evolves when detritus from different sub-basins is progressively added to the system. Fission-track analysis is a powerful integration tool to quantify sediments mixing if source areas experienced contrasting exhumation paths. Fission-track grain-age distributions provide not only information on long-term exhumation patterns, based on the age of the peaks, but also provide first-order constraints on short-term erosion rates by comparison between the size of the peaks and the size of potential source areas. In the Dora Baltea catchment, the apatite load derives from two major fault-bounded blocks, the Western one yielding 43% of the total amount of apatite, and the Eastern one yielding the remaining 57%. In the Arc catchment, contribution is 29% from the Eastern Block, 14% from the Houiller-Subbriançonnais units and 57% from the Belledonne-Dauphinois units. We assessed apatite fertility in source-rocks by measuring apatite content in processed sediments, after checking for anomalous hydraulic concentrations by geochemical analyses. The lack of compositional anomalies for elements between Y and Cr, largely hosted in ultradense minerals, grants that source-rocks distribution in the basin is faithfully reflected by detrital assemblages.

Results demonstrate that erosional processes were focused in different areas of the Western Alps at long-term and short-term timescales, and are now concentrated in the External Massifs. No clear relationship between erosion and climate or relief is observed in this sector of the belt, where endogenic forces may represent the main controlling factor on both long-term and short-term erosion rates.

INDEX

PART 1 BULK PETROGRAPHY AND HEAVY MINERAL ANALYSIS IN MODERN RIVER SANDS: Axial Belt Provenance

PART 2 DETRITAL FISSION-TRACK ANALYSIS IN PROVENANCE STUDIES: determining long- and short term erosion rates

References cited

Appendices

> *"It is now more than 100 years since the study of sediment composition was established. The methods employed are well-proven and always evolving, and have thus stood the test of time"*
>
> *M .Mange*

1 INTRODUCTION

1.1 General remarks

Clastic sediments can be considered as geological archives recording and preserving the signatures of ancient geological events in source areas, along transport pathways and in the deposition basin.

Sediment particles cover a spectrum of more than 5 orders of magnitude in diameter, deriving from the physical and chemical weathering of parent rocks exposed at the Earth surface. The size and composition of detrital grains largely depends on their genetic processes (mainly linked to climate and relief) and can dramatically change in time and space during transportation due to mechanical crushing, chemical alteration, and formation of oxide coatings. Among sediment particles, sand is the best suited for analysis as it is quite common in many tectonic and climatic settings (unlike coarser sediments, which require extreme high-energy conditions to be produced and transported) and its analysis can be performed under a polarizing microscope.

Finer sediments, silt and clay, which are hard to recognize under a standard polarizing microscope, represent the largest amount of sediment on Earth and are considered the future evolution of provenance analyses, thanks to the development and refinement of new techniques (e.g. X-Ray diffraction, Raman spectroscopy: Heberer et al., 2010; Morton and Chenery, 2009; Andò et al., 2009). The development of major, minor and trace element geochemistry and single-crystal geochronometers (e.g. Bernet et al., 2004a) has given a further impulse over sediment analysis, allowing a better discrimination of sediment provenance.

The idea that sand particles can be considered a microscopic representation of the geological setting of the source area is very old, as all arenites classification proposed so far (Krynine, 1948; Pettijohn, 1949, 1954; Folk, 1954; Packham, 1954; Gilbert, 1954) are devoted to unravel rock genesis.

Unravelling the provenance of a sedimentary basin fill has always been interpreted as a fundamental tool to reconstruct and eventually interpret the evolution of sediments, from their initial erosion to their final lithification, through transport, reworking and deposition.

As tectonics and climate are the main controlling factors on source rocks composition and sediments modifications through time and space (Dickinson, 1970), the correct identification of sediment sources can provide insights both on paleogeography (paleocurrents orientation, paleodrainage patterns, localization of uplifting and subsiding areas…) and paleoclimatology (mainly due to chemical weathering effects observation).

Sedimentary rocks are thus the complex product of the interactions of source rocks composition, erosion, transport, deposition, weathering and lithification. For this reason, progressively greater importance has been attributed to the study of modern sediments, allowing reconstructing the effects tectonics or climate on modern sediments from settings of well-constrained climate or geological setting, respectively. If the present can be the key to understand the past, this actualistic approach allows to create refined models for sediment provenance, individually investigating the effects of climate and/or tectonics, which can eventually be combined to unravel clastic rock provenance, shedding new light on long-term evolution of the Earth surface.

1.2 Aims and outline of the thesis

The present thesis is devoted to the analysis of modern sand-sized sediments to refine classical provenance models and integrate bulk petrographic data with detrital geochronology to enhance its fields of application in unraveling sediment sources and quantify sediment budgets in modern settings.

The first part of the thesis is devoted to the analysis of modern sediments shed by collision orogens. Orogenic belts produced by continental collision are the most prominent product of plate tectonics. Orogenic detritus is stored not only in foreland basin fills but also in submarine fans accumulating in remnant ocean basins (Ingersoll et al. 2003), and can thus be subsequently offscraped at trenches, tectonically stacked in subduction complexes, and recycled (Velbel 1985; Allen et al. 2008). The recognition of diagnostic detrital signatures sourced from collision orogens such as the Himalayas or the Alps is thus a fundamental issue in sedimentary petrology and provenance analysis.

In traditional approaches of sedimentary petrology, largely based on the analysis of ancient sandstone successions, the main efforts have always been focused on a large scale analysis, loosely distinguishing three broad and partially overlapping types of orogenic provenances, corresponding to sub-types of "Recycled Orogen Provenances" ("Subduction complex", "Collision orogen"/"Suture belt", and "Foreland fold-thrust belt") (Dickinson and Suczek 1979; Dickinson 1985).

Subsequent studies on modern sands (e.g., DeCelles and Hertel 1989; Critelli et al. 2003; Garzanti et al. 2004a) led to a more accurate definition of orogenic signatures. Several orogen types exist and, within each, distinct subparallel belts of contrasting rock assemblages shed detritus with distinct petrography and mineralogy (i.e., Axial Belt, Ophiolite, Magmatic Arc, Continental Block and Clastic Wedge Provenances of Garzanti et al. 2007). Orogenic detritus can be thus regarded as a mixture, produced in various proportions from diverse sources, none of which is peculiar of collision orogens such as the Alps or the Himalayas. Nonetheless, because erosional exhumation is generally focused within the neometamorphic core of collision orogens, undergoing rapid tectonic uplift during the initial stages of continental indentation (Garzanti and Malusà 2008), axial-belt detritus overwhelms detritus from external belts.

Axial belt sub-provenance can be regarded as the typifying feature of orogenic detritus. Its recognition and definition in a modern environment, like the European Alps, where geological setting has been extensively studied, climate exerts negligible effects on rocks weathering and diagenesis doesn't alter sediment primary composition, allows to create refined provenance models, enabling the distinction in the sedimentary record of the primary key features of the different structural levels forming the axial belt.

Another key application of bulk petrography/heavy-mineral analyses is represented by the unmixing of sediment compositions in the relative contribution of their sources. The wealth of data obtained from the analysis of detritus from low-order streams draining single tectono-metamorphic units in the Alps can be proficiently applied to unravel sediment sources and create quantitative sediment budgets to infer erosion rates and their distribution in the catchments.

Part II of the thesis focuses on the quantification of sediment budgets and short-term erosion rates in two valleys of the Western Alps (Dora Baltea and Arc basins). Sedimentary petrography represents a fundamental key to unravel sediment mixing because it considers the whole detrital spectrum and readily allows identification of main detrital sources. In complex geological settings, however, where sources are mixed and end-members may not be distinct enough mineralogically to allow sufficiently accurate unmixing calculations, sources relative contributions may be hard to discriminate by a petrographical/mineralogical approach alone. Detrital geochronology coupled with geochemistry provides a powerful integration tool to check and improve robustness in quantitative sediment budgets, provided that age-signatures in the sources are spread enough to be statistically discriminated, and “fertility” and hydraulic sorting effects are properly taken into account.

Chapter 1 gives a brief introduction to sediment petrography and the processes acting on sediments composition. An outline of the Thesis is also given.

Chapter 2 briefly traces back the evolution of petrographic analysis on sand(stone). A definition of the classification scheme, ratios and parameters used in samples analysis is also reported.

Chapter 3 examines the effects of the “closure constraint” on compositional data and its implication in the statistical analysis of closed compositional data.

Chapter 4 illustrates the representation of compositional data. Classical triangular diagram representation is discussed together with the powerful and much more holistic decision tree representation.

Chapter 5 presents the results of the analysis of first cycle modern sands derived from rivers draining the European Alps and delineates the primary features of Axial Belt Provenance.

Chapter 6 presents the theoretical basis of the fission-track method with particular attention to apatite analysis.

Chapter 7 shows the integration of bulk petrography and fission track analyses on multi-sourced sediments from the Arc and Dora Baltea valleys to unravel the short-term erosion pattern.

PART 1

BULK PETROGRAPHY AND HEAVY MINERAL ANALYSIS IN MODERN RIVER SANDS:

AXIAL BELT PROVENANCE

2 Sediments analysis: history, methods and developments

2.1 Framework petrography and heavy mineral analysis of sandstones and modern sands

First pioneering studies on mineralogical composition of sandstones to deduce their genesis appeared since the nineteenth century (Sorby, 1880; Phillips, 1881; Artioli, 1891; Dick, 1887; Cayeux, 1929), primarily focusing on accessory species. Although these species usually represent only a small part of the detrital particles in sediment, they can often be related to some characteristic paragenesis, and were thought to be much better suited for provenance studies, whereas framework composition were referred to with some skepticism due to the ubiquitous distribution of major constituents such as quartz or feldspars (Solomon, 1932).

After a first phase of qualitative provenance studies, focused on the recognition of characteristic "distribution provinces" (e.g. Brammall, *in* Milner, 1922), Fleet (1926) and Edelmann (1931, 1933) first introduced a quantitative approach (grain counting) to retrieve the relative frequencies of mineral occurrences.

Interest for the bulk mineralogy of sandstones strongly increased since the 1940's after Krynine (1948) and Pettijohn (1948) introduced their classification schemes for arenites, which are still in use.

The early recognition of the linkage between framework composition and source rocks tectonic and climatic setting (Barrell, 1908; Krynine, 1935, 1936, 1941; Blatt, 1967; Suttner, 1974; Crook, 1974; Schwab, 1975), received a great impulse by the advent of the plate tectonics and the contributions of W.R. Dickinson (Dickinson, 1974; Dickinson and Suczek, 1979), who clearly demonstrated the primary influence of tectonic setting on sandstone composition.

Since sandstones are the combined product of tectonic setting – i.e. source rocks – relief, climate, and transport, it soon became clear that each of these factors should be individually investigated in modern settings to highlight their effects and produce an integrated and holistic approach over sediment provenance interpretation (e.g. Wetten and Kelley, 1969; Dickinson and Valloni, 1980; Suttner et al., 1981; Basu, 1985; Grantham and Velbel, 1988).

In the last years, framework composition studies have still been applied to ancient sandstones successions (e.g. DeCelles et al., 1998; Fuentes et al., 2009; Di Giulio et al., 1999, 2001), even though the main objective of present days studies is to revise and refine classical provenance models, integrating the effects of source rocks, climate, hydraulic sorting, weathering and lithification as result from framework, heavy mineral and geochemical studies on modern sediments (Garzanti et al., 2000; 2002; 2004; 2005; 2006a,b; 2007a; 2009a; 2010b; Le Pera et al., 2001a, b; Critelli et al., 2003; Di Giulio et al., 2003).

2.2 Data acquisition and classification schemes

Data acquisition in sedimentary petrography is usually performed via optical analyses (point counting, modal analysis) on thin sections (or grain mounts, for heavy mineral analyses). Usually analyses on 200 to 500 detrital grains are considered as a reliable statistical sample of sediment composition, although recent papers have investigated and quantified the uncertainty of modal compositions relative to the number of analyzed grains (Vermeesch, 2004).

Due to the variety of grains that can be encountered in sand(stone) and the resulting multitude of possible classification criteria, different “schools” evolved through the past decades, making data correlation quite cumbersome, especially for coarse crystalline polymineralic grains.

2.2.1 Indiana Method

The point-counting method proposed by the “Indiana school” (Suttner, 1976; Suttner and Basu, 1985) considers sand(stone) composition the result of the complex interaction of provenance, transport, and further modification during and after deposition. The progressive variations of sediment composition during transport and lithification due to mechanical and chemical grains size changes are thus considered a valuable tool to trace back climatic and sedimentological evidences on source terrains (Basu, 1976; Suttner et al., 1981; Suttner and Dutta, 1986; Dutta and Suttner, 1986). The application of such a technique results in an extreme size-dependence of sand(stone) composition. All grains consisting of two or more mineral phases with none of them representing more than 90% of the whole fragment area in thin section or with a minimum of two phases larger than 62.5 μm in size are classified as rock fragments. Results are usually presented in terms of QFR percentages, closely reflecting Folk’s classification diagrams (for a review of sandstone classification, Folk, 1974).

2.2.2 Gazzi-Dickinson method

The Gazzi-Dickinson point counting method, independently developed by Gazzi (1966) and Dickinson (1970), tries to minimize the effect of sediments grain-size on sediments composition as they are eroded and deposited (weathering and chemical dissolution) and transported (mechanical abrasion). In trying doing so, coarser crystals (>62.5 μm) occurring in polycrystalline fragments are classified in the corresponding monomineralic grain category when hit by the crosshair. Although this method is largely unaffected by the breakage of polycrystalline fragments into sand-sized monocrystalline fragments, detrital modes calculated with this method are still largely affected by the biasing effects of particles size-density sorting during both transport and deposition (Garzanti et al., 2009).

Results are reported in terms of QFL percentages.

2.2.3 Classification schemes

Beside different data acquisition techniques, sediment petrography is usually hampered by a general lack of clear-cut classification schemes, especially for rock fragments. This is due to the great number of possible grains that can be encountered during point-counting. The wealth of information that detrital modes carry, concerns source rocks tectonic setting, climate, transport and deposition conditions, which individually represent the main goals of any provenance study. Such a wide spectrum of subjects forced to adopt a large number of classifications, ever evolving through time. Although data acquisition should be performed classifying grains in many restricted classes (Gazzi, 1966), data interpretation and confrontation usually require a further step of simplification of the classification schemes to produce a synthetic representation of samples detrital modes. This is generally accomplished by grouping the different classes used during data acquisition into few classes of homogeneous diagnostic signature, thus enhancing provenance discrimination.

Either the choice of the categories used for data acquisition either their amalgamation to interpret provenance can be performed in different ways, resulting in a variety of different classification schemes (especially for rock fragments), devoted to highlight specific features of sediment provenance (source rocks tectonic setting, climate…) that make data comparison and creation of large datasets of compositional data an haunting task (for a list of classification schemes proposed to describe sand(stone) composition and unravel their provenance see, among others, Gazzi, 1966; Dickinson, 1970; Basu, 1985; Dickinson, 1985; Zuffa, 1987; Dorsey, 1988; Garzanti, 1991, Garzanti and Vezzoli, 2003, encompassing the full spectrum of monocrystalline grains, polycrystalline rock fragments, intrababasinal/extrabasinal carbonate/non carbonate grains).

Table 2.1. *Classification schemes proposed by different authors through the years. For the classification scheme used in the present work, see table 5.1.*

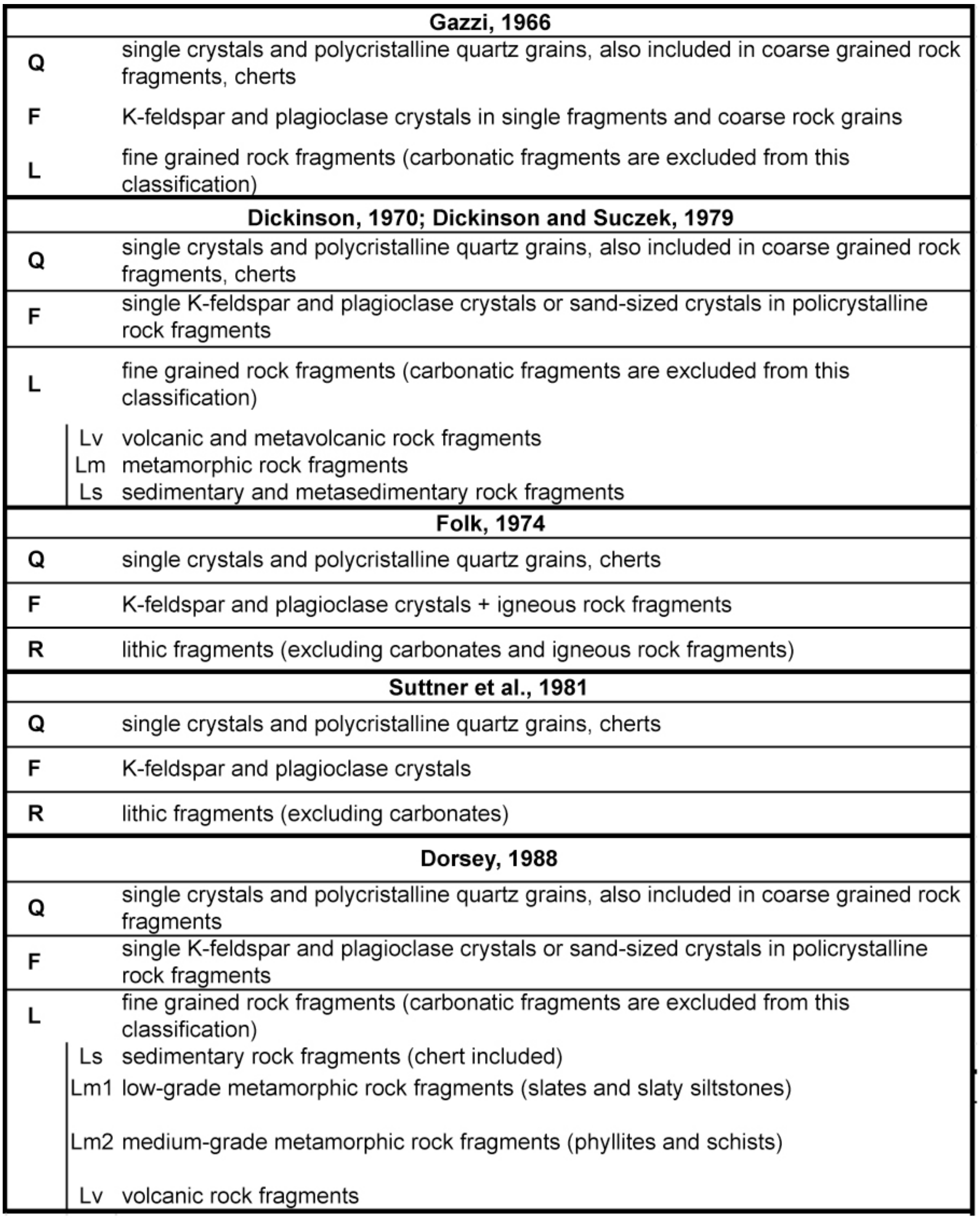

		Gazzi, 1966
Q		single crystals and polycristalline quartz grains, also included in coarse grained rock fragments, cherts
F		K-feldspar and plagioclase crystals in single fragments and coarse rock grains
L		fine grained rock fragments (carbonatic fragments are excluded from this classification)
		Dickinson, 1970; Dickinson and Suczek, 1979
Q		single crystals and polycristalline quartz grains, also included in coarse grained rock fragments, cherts
F		single K-feldspar and plagioclase crystals or sand-sized crystals in policrystalline rock fragments
L		fine grained rock fragments (carbonatic fragments are excluded from this classification)
	Lv	volcanic and metavolcanic rock fragments
	Lm	metamorphic rock fragments
	Ls	sedimentary and metasedimentary rock fragments
		Folk, 1974
Q		single crystals and polycristalline quartz grains, cherts
F		K-feldspar and plagioclase crystals + igneous rock fragments
R		lithic fragments (excluding carbonates and igneous rock fragments)
		Suttner et al., 1981
Q		single crystals and polycristalline quartz grains, cherts
F		K-feldspar and plagioclase crystals
R		lithic fragments (excluding carbonates)
		Dorsey, 1988
Q		single crystals and polycristalline quartz grains, also included in coarse grained rock fragments
F		single K-feldspar and plagioclase crystals or sand-sized crystals in policrystalline rock fragments
L		fine grained rock fragments (carbonatic fragments are excluded from this classification)
	Ls	sedimentary rock fragments (chert included)
	Lm1	low-grade metamorphic rock fragments (slates and slaty siltstones)
	Lm2	medium-grade metamorphic rock fragments (phyllites and schists)
	Lv	volcanic rock fragments

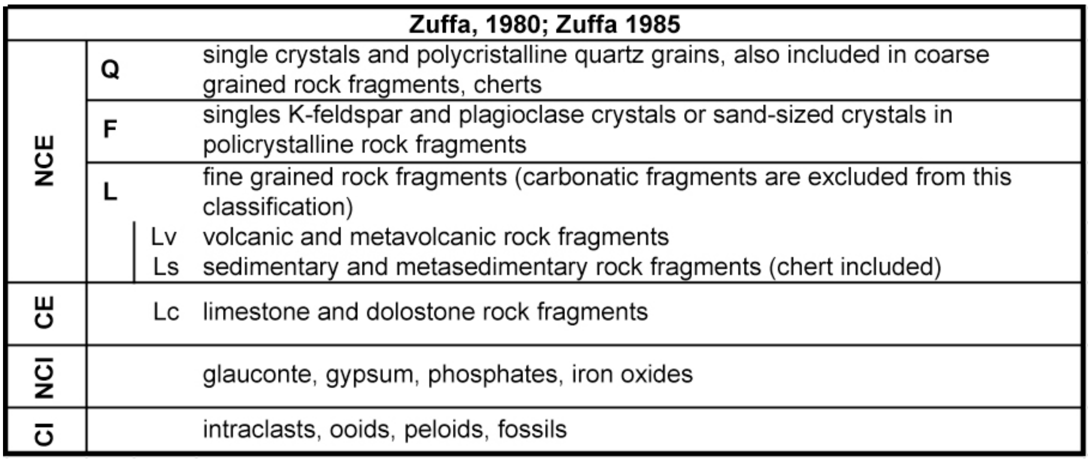

Zuffa, 1980; Zuffa 1985			
NCE	Q		single crystals and polycristalline quartz grains, also included in coarse grained rock fragments, cherts
	F		singles K-feldspar and plagioclase crystals or sand-sized crystals in policrystalline rock fragments
	L		fine grained rock fragments (carbonatic fragments are excluded from this classification)
		Lv	volcanic and metavolcanic rock fragments
		Ls	sedimentary and metasedimentary rock fragments (chert included)
CE		Lc	limestone and dolostone rock fragments
NCI			glauconte, gypsum, phosphates, iron oxides
CI			intraclasts, ooids, peloids, fossils

2.3 Heavy-mineral analysis

Analysis of heavy minerals retrieved from sand(stones) probably dates back to the golden age of economic minerals prospection (Dick, 1887), and even before in Italy, with Artini (1891). Heavy minerals ($\rho > 2.90$ g/cm^3, Mange and Maurer, 1992), representing usually ~ 0.1-10% of siliciclastic deposits (although heavy mineral concentrations may strongly depend on source rocks composition and hydraulic sorting processes) consist of both essential rock-forming minerals (garnet, amphiboles, pyroxenes, micas) and accessories (zircon, tourmaline, rutile, apatite).

The pieces of information that can be retrieved from each mineral faithfully reflects its history which begins during the petrogenesis of its parent rock, determining its crystal structure, morphology, colour, chemical and optical zoning, inclusions and twinning, and continues through transport, alluvial storage and ends in deposition, burial and diagenesis.

Heavy mineral are highly diagnostic species that convey crucial information on source area, transport pathways and deposition areas. Since heavy minerals usually represent 1% to 10% of the entire detrital population that can be found in siliciclastic deposits, heavy mineral analysis allows to retrieve such a wealth of information that otherwise could be easily lost, being strongly diluted in framework assemblages.

The use of single-mineral geochronological techniques usually relies on heavy mineralogical species (i.e. mica, amphibole, apatite, zircon, titanite, monazite, xenotime) and heavy mineral analyses can greatly improved our knowledge on the detrital assemblages from which such minerals have been extracted, adding crucial information on the depositional setting of the analyzed deposits and allowing to better interpreting significance of geochronological data.

Because of their high specific density, heavy minerals are particularly prone to the sorting effects of hydraulic settling equivalence (Rubey, 1933) as their occurrence in sediments in often controlled by their shape and density, and can also be determined by selective dissolution. These effects can severely alter original mineralogical assemblages during transport and deposition and have long been recognized as a major obstacle in correctly interpreting heavy mineral suites in terms of source areas, transport pathways, climate and deposition areas (e.g. Briggs, 1965; van Andel, 1950).

Since heavy minerals represent only a small part of the entire detrital suite forming sedimentary deposits, they need to be concentrated and extracted from the bulk of sediment before they can be efficiently analyzed. Standard preparation techniques provide:

- sampling of sand(stone) of interest;
- crushing and disaggregation of coherent sediments to liberate individual grains;
- sieving to remove silt-clay particles. This phase is crucial as it usually requires the selection of a size-window from which to extract heavy minerals;
- separation of heavy and light minerals with dense liquids: samples are poured in a test-tube with sodium-metatungstate ($3Na_2WO_4 \cdot 9WO_3 \cdot xH_2O$), a non-toxic dense liquid which allows to separate grains with cut-off density values that ranges from 1 to 3 g/cm^3 according to liquid dilution. Arbitrary, standard cut-off density for heavy minerals analysis is $\rho = 2.90$ g/cm^3. Denser grains will sink to the bottom of the test-tube, whereas lighter grains will float. A centrifuge can be used to speed up separation of the light and dense fractions. Partial freezing with liquid nitrogen of the bottom of the test-tube allows to separately retrieve heavy and light mineral fractions;
- A quartered fraction of the retrieved heavy mineral fraction is mounted in Canada balsam ($n = 1.54$) to obtain a permanent grain mount slide.

To determine the relative abundance of heavy minerals in sediments, grain mounts are usually analyzed by point-counting. Different methods have been developed:

- *Fleet method* (Fleet, 1926): requires all grains in the mount to be counted. It is time consuming and the precision of the analysis does not significatively improve once 200-300 grains have been analyzed (Dryden, 1931; van Andel, 1950).

- *line counting*: the slide is moved along a line and all the grains intersected by the crosshair are identified and counted. As larger grains have larger chances to be hit by the crosshair, this method can lead to frequency distortion in favor of larger grains.

- *area (or ribbon) method* (Galehouse, 1969): all grains contained in randomly selected areas (ribbons) of the slide are analyzed and counted. Such approach ensures independence of results from minerals grain size (provided that analyzed ribbons width are larger than the maximum size of crystals) and mineral number frequencies can be converted into number percentages. This method appears to be the most widely accepted in heavy mineral amalysis.

- *point counting:* a slide of heavy minerals is prepared using a larger amount of grains to facilitate and speed up analyses. The mount is progressively moved, with the aid of a stage, by a fixed distance and grains hit by the microscope crosshair are identified and counted. This method is appropriate when sediments are poorly sorted and big grains (e.g. tourmaline) are mixed with very small grains (e.g. zircon) in the same suite.

2.4 Further developments in sediment petrography and heavy mineral analysis

2.4.1 Metamorphic Index (MI)

The classical classification of metamorphic grains in a single category (Lm) both in sands and sandstones carries very little information on sediment provenance, as a generic “metamorphic grain” can derive from a very low-rank anchimetamorphic terrain as well as from a deeply subducted eclogitic source unit. The adoption of a single Lm class also prevents from distinguishing (when primary textures are preserved) to recognize source protoliths. Much vast knowledge on metamorphic rock fragments origin could be retrieved if only they were classified both according their protolith and metamorphic grade.

First attempts to classify metamorphic lithic fragments according to their grade were made by Dorsey (1988), although limited to very-low to medium grade metasedimentary grains.

A more extensive classification of metamorphic grains that can be encountered in analyzing sediments derived from collision orogens was proposed by Garzanti and Vezzoli (2003). It recognizes four main groups of metamorphic rock fragments (metapelite, metapsammite/metafelsite, metacarbonate, metabasite) according to protolith composition. For each group, five classes of increasing metamorphic rank are defined according to the degree of recrystalization and the progressive formation of cleavage and schistosity.

The relative abundance of rock fragments classified in the 5 metamorphic rank classes can be used to calculate an average Metamorphic Index (Garzanti and Vezzoli, 2003) of each sample, calculated as:

$$MI = \frac{Rm1}{Rm} \bullet 100 + \frac{Rm2}{Rm} \bullet 200 + \frac{Rm3}{Rm} \bullet 300 + \frac{Rm4}{Rm} \bullet 400 + \frac{Rm5}{Rm} \bullet 500$$

where Rm represents all metamorphic grains and $Rm_{1,2,3,4,5}$ the relative abundances of metamorphic grains (independently from their protolith) of rank 1,2,3,4,5.

2.4.2 Heavy mineral metasedimentary minerals index (MMI) and hornblende color index (HCI)

Source rock average metamorphic grade can be estimated also by looking at heavy mineral assemblages.

Average metamorphic grade of metasedimentary source rocks can be estimated by the MMI index (metasedimentary minerals index, Garzanti et al., 2006a; Garzanti and Andò, 2007b), defined as:

$$MMI = \frac{\left(\frac{1}{3}\, staurolite + \frac{2}{3}\, kyanite + sillimanite\right)}{chloritoid + staurolite + kyanite + sillimanite} \bullet 100$$

For medium- to high–grade metaigneous source rocks, hornblende color represents a useful indicator of average source rock grade. Analysis of modern river sediments drained from the Central European Alps (Garzanti et al., 2004) showed that blue-green hornblende are dominant in heavy mineral suites from staurolite-grade rocks below 600°C, and are progressively replaced by green, green-brown, and brown grains as metamorphic grade of source rocks increases towards sillimanite-grade parageneses.

The HCI index (Hornblende color index) is defined as:

$$HCI = \frac{\left(\frac{1}{3}\ green\ hbl + \frac{2}{3} green\text{ - }brown\ hbl + brown\ hbl\right)}{hbl} \bullet 100$$

MMI and HCI range from 0 in detritus from greenschist facies to lowermost amphibolite facies rocks yielding chloritoid and blue/green amphibole to 100 in detritus from granulite facies rocks yielding sillimanite and brown hornblende.

2.4.3 Heavy mineral concentration index (HMC) and source rock density (SRD)

Extensive studies on heavy mineral assemblages from modern sediments in a variety of geodynamical settings (Garzanti et al., 2000; 2002; 2006a), has lead to the recognition that beside the spectrum of heavy mineral found in sedimentary deposits, also their overall abundance can be proficiently used to unravel composition of parent rocks and their tectono-stratigraphic level. Denser rocks, equilibrated at depth, contain and consequently shed more heavy minerals than less denser, shallower rocks as well as basement rocks usually shed more abundant suites than sedimentary cover rocks.

Heavy mineral abundance in sediments can be calculated as the Heavy Mineral Concentration index (HMC, Garzanti and Andò, 2007), defined as:

$$HMC = \frac{\left(\frac{W_D}{W_T}\right)\left(\frac{D_T}{D_D}\right)\left(1 - \frac{s}{h}\right)}{1 - \frac{d}{t}} \bullet 100$$

where W_D/W_T indicates the ratio between the weight of the mineral fraction denser than 2.90 g/cm^3 and the weight of the sediment fraction considered, D_T/D_D the ratio between the weighted average densities of total framework grains and total dense grains, s/h the relative abundance of spurious grains in the dense fraction (carbonates, phyllosilicates, dense inclusion-filled light minerals…), and d/t the relative abundance of allochemical and orthochemical components.

Since most heavy mineral studies focus on transparent grains (which can be identified under a polarizing microscope), HMC can be converted into tHMC (transparent Heavy Mineral Concentration Index) according to the following simple formula:

$$tHMC = HMC\ (1 - \%\ opaque - \%\ turbid)$$

Another parameter that can help in determining source rocks crustal level (but also to highlight hydraulic effects on sediments composition) is the Source Rock Density (SRD) index (Garzanti et al., 2006a; Garzanti and Andò, 2007), calculated as:

$$SRD = \frac{\left[D_{tHM}\left(\left(1 - \%\ opaque\right) + 5.00 \bullet \%opaque\right)HMC + 2.65\left(100 - HMC\right)\right]}{100}$$

where D_{tHM} is the weighted average density of transparent dense mineral, 5 is the average density (g/cm^3) for opaque grains (intermediate between that of magnetite and ilmenite), HMC is the heavy mineral concentration index and 2.65 is the average density (g/cm^3) of “light” grains.

3 Statistical analysis of compositional data

3.1 Compositional data

All care and attention paid in sediment sampling, preparation and analysis can result in almost useless time-consuming procedures unless frequency distribution data are properly analyzed in terms of multivariate statistical methods. Quantitative detrital modes obtained from point-counting are usually referred to as compositional data (or compositions).

Like geochemical compositional data, detrital modes are usually expressed in closed form (Chayes, 1971), i.e. summing to a constant (usually 1 or 100) like data in table 3.1.

Table 3.1. *Compositional dataset of modern sands shed by oceanic basement units in the Alps. Q: quartz, F: feldspars, L: lithic fragments.*
Data from Garzanti et al., 2010 (see chapter 5 and appendix A.2)

sample ID	***River***	***Site***	***Q***	***F***	***L***
S4027	*Gimont*	*Rif. Gimont*	*2*	*2*	*97*
S3731	*Totalp*	*Wolfgang*	*0*	*0*	*100*
S3430	*Mallero Ventina*	*Rif. Porro*	*0*	*0*	*99*
S148	*Arrestra*	*Cogoleto*	*16*	*7*	*76*
S2829	*Stura Turchino*	*Ovada*	*24*	*12*	*64*
S175	*Orba*	*Capriata*	*19*	*7*	*74*
S142	*Varenna*	*Pegli*	*11*	*4*	*85*
S3745	*Casternone*	*Val Torre*	*16*	*15*	*69*
S2178	*Stura di Ala*	*Ceres*	*13*	*28*	*59*
S2193	*Chalamy*	*Champdepraz*	*17*	*11*	*73*

Table 3.1 reports the composition of 10 modern sand samples (observations) described in terms of 3 parts (Q, F, L) assuming different values (components) for each observation. Parts are thus labels describing or identifying the constituents into which the whole has been divided, whereas components are the numerical proportions into which individual parts occur.

Compositional data are usually in a(n) array-matricial form so that each row corresponds to a single specimen or more generally to a single replicate (the basic experimental or observational unit, i.e. a single sand sample) whereas each column corresponds to a specific ingredient or part of each composition (i.e. quartz, feldspars, lithic fragments…).

Each D-part closed compositional data x = (x_1, x_2, x_3, …, x_D) must fulfill the following requirements:

- closure (*K*): $\sum_{i=1}^{D} x_i = k$,

with *k*, constraining constant (i.e. 1 or 100)

- non-negativity: $x_i \geq 0$, with *i*=1, …, D

The non-negativity constraint is often substituted by the much more restrictive positivity constraint:

- $x_i > 0$, with *i*=1, …, D

avoiding the occurrence of parts with zero components, which require special attention during statistical analysis (see paragraph 3.7).

3.2 Subcompositions and data amalgamation

As compositional data usually consist of a M x N matrix with N parts and M observations, visual representation of compositional data is often tricky. Visualization is possible only for two- (represented with a line), three- (triangle) and four-parts (tetrahedron).

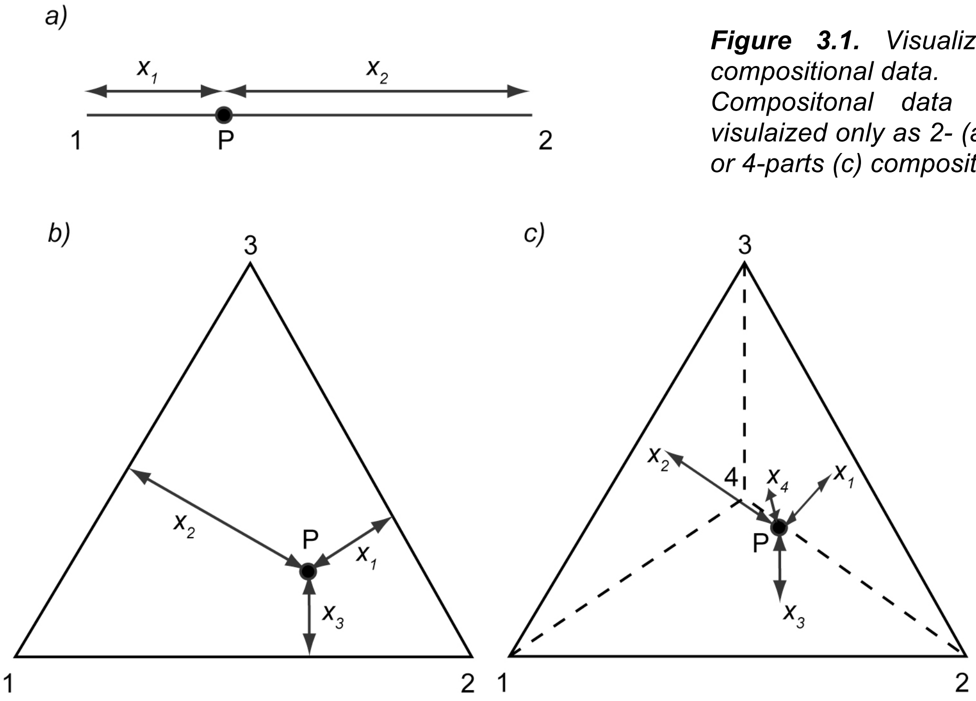

Figure 3.1. *Visualization of compositional data. Compositonal data can be visulaized only as 2- (a), 3- (b), or 4-parts (c) compositions*

Such a visualization limit, together with the fact that interest may lay only in a sub-set of the whole dataset, forces many analysts to work with subcompositions (i.e. only with a limited number of parts – generally two or three).

A 3-part subcomposition **y** of a 5-part composition **x** is a closed subset of the original dataset can be represented as:

y = [y1, y2, y3] = K[x1, x3, x5]

with K representing the closure operation. An important propriety is that the ratio of any two components of a subcompositon is the same as the ratio of the two corresponding components in the full composition.

Another common practice in compositional data analysis to reduce the order of the dataset matrix is to amalgamate, or group parts that carry similar information into new ones.

3.3 Interdependency of compositional data and covariance structure

Compositional data closure constrain implies that parts are not independent from each other, as in a D-part composition, the magnitude of the d-th component is fully determined by the sum of all other components and the closure constant. Compositional data are thus constrained data as they are not free to take on any value or to vary independently, as very often the forced adjustment in all components in response to a change in a single component does not necessarily reflect any physical process:

" if one analyzes the content of a jar half-filled with sand and finds, by a random sample, that it contained (by volume) about 20% quartz, 30% feldspar, 40% rock fragments, and 10% miscellaneous constituents, then if the volume of the jar were doubled by addiction of grains of pure quartz, a second random sample would reveal that the jar contains 60% of quartz, 15% of feldspar, 20% of rock fragments, and 5% of miscellaneous constituents. Feldspar, rock fragments, and miscellaneous constituents appear pairwise positively correlated and all three appear negatively correlated with the quartz abundance. Also, all four components have shifted mean values despite the fact that only the quartz content of the jar changed…" (*Woronov, 1991*).

Another major problem affecting compositional data, due to their closure constrain, is that their covariance structure is forced to have at least a negative covariance value, and a negative correlation coefficient, as well (this can be exemplified by the trivial case of a two-parts composition summing to a constant: the correlation between the two elements must necessarily be -1).

Such a feature implies that, if one of the coefficients has to be negative, than none of the correlation coefficients is free to range between -1 and +1, unlike unconstrained data (Aitchison, 1986).

Consequently compositional data do not fit in common statistical techniques, which are expressly devoted to analysis of unconstrained data (i.e. Rencher, 2002).

Although the interdependency of compositional data has been recognized for over a century (Pearson, 1897; Sarmanov and Vistelius, 1959; Chayes, 1960; Krumbein, 1962; Butler, 1979; Aitchinson, 1986; Davis, 1986; Rock, 1988; Rollinson, 1995), appropriate statistical methods for analyzing such data have been extremely low to emerge and find extensive application in geological sciences (von Eynatten et al., 2003; von Eynatten, 2004; Weltje, 1995; Weltje, 1998; Thomas and Aitchison, 2006; Garzanti and Vezzoli, 2009).

3.4 The simplex as the sample space for compositional data

Since compositional data consist of vectors of positive components subject to a constant-sum constraint, their sample space (i.e. the set of all possible outcomes of the observational or experimental process) is a restricted part of the real space R termed simplex (S):

$$S^D = \{(x_1, x_2, x_3,\ldots, x_D): x_1\geq 0, \quad , x_D\geq 0; x_1+ \quad +x_D=k\}$$

The D-part simplex, S^D, is a subset of D dimensional real space. For D=2 it can be represented with a line segment; for D=3 as a triangle (ternary diagram) and for D=4 as a tetrahedron. No graphical representations are possible for D>4, although number of parts can exceed 4.

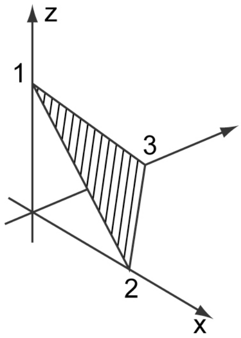

Figure 3.2. *Simplex Three-part simplex embedded in* R^3

The simplex, unlike the real space, is not a linear vector space in which we can add vectors, multiply them by a constant or scalar value, look for properties like orthogonality, or calculate the distance between two points as in Euclidean geometry.

If we consider the two groups of compositions:

A	*B*	*C*
5	*65*	*30*
10	*60*	*30*

A	*B*	*C*
50	*20*	*30*
55	*15*	*30*

we can say that the Euclidean distance between the points in both groups is the same (5 units for both the first and second component), but we'll certainly miss the fact that the first component is doubled in the first group, whereas relative increase in the second group is only 10%.

Another problem arising from the application of Euclidean geometry to the simplex is that results may fall outside the simplex (which is only a part of the real space), as in traditional hexagonal confidence regions (see paragraph 4.3).

3.5 Aitchison geometry in the simplex

In order to operate as in the real space, a vector space structure has to be defined for the simplex.

The two basic operations required for defining a vector space structure in the simplex are the *perturbation* and *power transformation* operations (Aitchison, 1986).

For a given composition $x \in S^D$,

perturbation by a composition $y \in S^D$ is defined as:

$$x \oplus y = K[x_1 y_1, x_2 y_2, \ldots, x_D y_D]$$

and power transformation by a constant $a \in R$ is defined as:

$$a \otimes x = K[x_1^a, x_2^a, \ldots, x_D^a]$$

with *K* representing the closure operation:

$$K(x) = \left[\frac{k\, x_1}{\sum_{i=1}^{D} x_i}, \frac{k\, x_2}{\sum_{i=1}^{D} x_i}, \ldots, \frac{k\, x_D}{\sum_{i=1}^{D} x_i} \right]$$

Perturbation has analogous properties (commutative, associative and distributive) of translation (i.e. sum of vectors) and scalar multiplication in the real space, whereas power transformation satisfies the properties of an external

product (associative and distributive properties).

Other crucial elements in defining a linear vector space are distances, moduli and norms.

The Aitchison inner product of x, y$\in$S^D is defined as:

$$\langle x,y\rangle_a = \frac{1}{2D}\sum_{i=1}^{D}\sum_{j=1}^{D} ln\frac{x_i}{x_j}\, ln\frac{y_i}{y_j}$$

From the inner product it is possible to define a norm (the distance of a composition from the origin of the liner space)

$$||x||_a = \sqrt{\frac{1}{2D}\sum_{i=1}^{D}\sum_{j=1}^{D}\left(ln\frac{x_i}{x_j}\right)^2}$$

and the (Aitchison) distance between x and y$\in$S^D,

$$d_a(x,y) = \sqrt{\frac{1}{2D}\sum_{i=1}^{D}\sum_{j=1}^{D}\left(ln\frac{x_i}{x_j} - ln\frac{y_i}{y_j}\right)^2}$$

Within this framework of Euclidean vector space structure (Billheimer et al., 2001; Pawlowsky-Glahn and Egozcue, 2001; Martin-Fernandez et al., 1998, 1999; Aitchison et al., 2000; Martin-Fernandez, 2001), any multivariate statistical analysis on compositional data can be performed.

Any statistical method is applied to compositional data should satisfy the conditions of scale invariance, permutation invariance and subcompositional coherence.

Permutation invariance: a function is permutation-invariant if it yields equivalent results when the order of the parts of the composition has been changed.

Subcompositional coherence: the distance measured between two full compositions must be greater (or at least equal) then the distance between them when considering any subcomposition. In simple words, subcompositions should behave as orthogonal projections do in conventional real analysis. The size of a projected segment is less or equal than the size of the segment itself.

Scale invariance: closed compositional data carry only relative information. They report values following a closure operation. Closure is a projection of any point in the positive orthant of D-dimensional real space onto the simplex. All points on a ray starting from the origin are thus projected onto the same point in S^D.

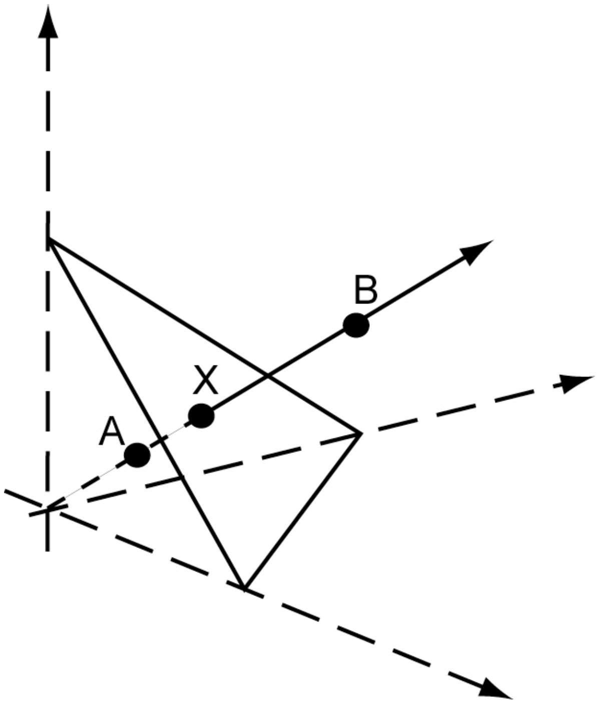

Figure 3.3. Compositional equivalence relationship.
In real space, points A and B derive from a change in the closure constant (e.g. from % to ppm). Closure operation, force them lying on a ray starting from the origin. Their projections on the simplex, however, coincide (point X).

A function f() is defined as scale-invariant if for any positive real value $a \in R$ and for any composition $x \in S^D$, the function satisfies $f(ax) = f(x)$.

3.6 Log-ratios of compositional data

Although mathematically straightforward, the operations required to work within Aitchison geometry are unusual and not necessarily easy to follow. For these reasons, alternative approaches, based on appropriate log-ratio representations, have been developed.

Such approaches are based on the observation that compositional data convey only relative information (i.e. interest lies in relative proportions rather than in absolute size), as exemplified by the fact that, if a is a real number, $[x_1, x_2, \ldots, x_D]$ and $[ax_1, ax_2, \ldots, ax_D]$ carry the same information and are indistinguishable in terms of compositions (scale invariance, chapter 3.5).

John Aitchison (1982, 1986) realized that statements concerning compositions could be expressed in terms of ratios of components, and that log-ratios could be much more easily handled mathematically than ratios.

Log-ratio transformation also provides a one-to-one correspondence between compositional vectors and associated log-ratios, allowing reformulating any statement on compositions in terms of log-ratios, and vice-versa. Moreover, an advantage of such transformation is that they remove the limitation of a constrained sample space to an unconstrained space into which standard multivariate techniques can be applied.

Among all possible log-bases, natural logarithms are routinely used in compositional data and represent a standard approach in statistical analysis (Pawlowsky-Glahn and Egozcue, 2006).

In order to map log-ratio classes onto a classical coordinate-based sample space, Aitchison introduced two log-ratio transformations, the *additive* and *centered* log-ratios, which allow to represent compositions as real vectors:

alr (additive log-ratio) *transformation*: coordinates of a D-parts composition are calculated dividing D-1 of the components by the remaining one and calculating their logarithms.

$$alr(x) = \left[ln\frac{x_1}{x_D}, ln\frac{x_2}{x_D}, ..., ln\frac{x_{D-1}}{x_D} \right] = y$$

The resulting log-ratios are real variables that can be analyzed by standard statistical techniques. However, alr transformation results in coordinates that cannot be projected onto orthogonal axes, as they actually are at 60°. A limiting factor of alr transformation is thus that it doesn’t preserve distances.

clr (centered log-ratio) *transformation*: coefficients of a D-parts composition are calculated dividing the D components by the geometric mean of the parts, and then taking logarithms:

$$clr(x) = \left[ln\frac{x_1}{g}, ln\frac{x_2}{g}, ..., ln\frac{x_D}{g} \right] = y$$

clr transformation preserves distances and reduces calculation of Aitchison distances to ordinary distances. The only major drawback of clr transformation is that it introduces a new constrain as the coefficients must sum to zero. Since clr coordinates are very useful in the construction of biplots (see paragraph 4.3), they are the most common in compositional data analysis.

3.7 Dealing with zero in compositional data analysis

When dealing with compositional data, two kinds of null values in compositions can be frequently found:

essential (or structural) *zeros* are null components that are informative by themselves, as they indicate the absolute absence of a part in an observation;

rounded zeros indicate the presence of a part in the observation, but below the its detection limit.

Since compositional data need to be converted in log-ratios to facilitate their statistical handling, null components must be eliminated from the dataset before attempting any analysis.

Essential zeros can either indicate that the part has no significance for the purpose of the study (and that it can be ignored or amalgamated with other parts of the compositional dataset) or that it can be used to divide the sample into two subsets, according to the presence or absence of zero value in a specific part.

As rounded zeros represent amounts too small to be detected, they can be considered as “missing values” and it is common practice to substitute them with small values. Substitution of zeros, however, is not straightforward, as it can result in serious distortion of the structure of the entire compositional dataset.

Three non-parametric methods of imputations for rounded zeros can be applied to compositional data.

Additive replacement strategy:

Every composition $x \in S^D$ containing Z rounded zeros can be replaced by a new composition $r \in S^D$ without zeros according to the following replacement rule:

$$r_j = \begin{cases} \dfrac{\delta(Z+1)(D-1)}{D^2}, & \text{if } x_j = 0 \\ x_j - \dfrac{\delta(Z+1)Z}{D^2}, & \text{if } x_j > 0 \end{cases} \qquad \text{where } \delta \text{ is a small value.}$$

The imputed values when applying such a replacement technique depend both on δ and D. for this reason, two compositions x and x* containing a different amount of zeros, but some of them in the same parts, can be replaced by r and r* having different values in this parts.

Simple replacement strategy:

Rounded zeros are simply replaced by a small quantity and to the resulting vector is then applied a closure operation:

$$r_j = \begin{cases} \dfrac{k}{k + \sum_{n \mid xn = 0} \delta n} \delta j, & \text{if } xj = 0 \\ \dfrac{k}{k + \sum_{n \mid xn = 0} \delta n} xj, & \text{if } xj > 0 \end{cases} \quad \text{where } \delta \text{ is the imputed value}$$

The resulting imputed values depends both on δ and the number of zeros in x.

Multiplicative replacement strategy:

A composition x $\in$ S^D containing Z rounded zeros can be replaced by a new composition r $\in$ S^D without zeros using the expression:

$$rj = \begin{cases} \delta j, & \text{if } xj = 0 \\ 1 - \dfrac{\sum_{n \mid xn = 0} \delta n}{k} xj, & \text{if } xj > 0 \end{cases} \quad \text{where } \delta \text{ is the imputed value.}$$

The imputed values do no depend on the amount of parts neither on the number of zeros, ratios for non-zero values are preserved ($r_j/r_k=x_j/x_k$). This technique is also coherent with basics operations in the simplex and thus represents the more suitable strategy for replacing rounded zeros in compositional data analysis.

4 Exploratory data analysis of compositional data and their visualization

4.1 General remarks

The initial steps of any statistical analysis of (compositional) data should begin checking data for errors and/or missing data. A careful observation of the dataset and the values assumed by each part, lead also by careful geological considerations, should help in discriminating “essential zeros” from “rounded zeros”. If essential zeros are persistent and widespread within some parts in the whole dataset, these parts can be amalgamated with other parts (with similar provenance significance) or simply ignored, in order to reduce the rank of the dataset matrix. Scattered zeros along the dataset are then substituted applying one of the proposed replacing strategies (Martin-Fernandez and Thio-Henestrosa, 2006; Martin-Fernandez et al., 2003). Because of its intrinsic properties (see 3.7), that make it the more suitable method when working with compositional data, the multiplicative replacement strategy usually represents the best choice.

4.2 Dataset central tendency, variation matrix

Although the most popular statistical model in sediment petrography literature (e.g. Ingersoll et al., 1993; Valloni, 1985; Ryan et al., 2007), standard descriptive statistics based on univariate Gaussian distribution of compositional data are not very informative when dealing with compositional data in representing data central tendency and dispersion.

The arithmetic mean:

$$m_x = \frac{1}{D} \sum_{i=1}^{D} x_i$$

represents an hypothetical composition obtained by mixing in equal proportions all compositions from which the arithmetic mean has been calculated. As a consequence, univariate arithmetic mean is an affordable measure of location only when dealing with physical mixing.

In the algebraic-geometric structure of the simplex, a much more affordable measure of the central tendency of a compositional dataset is provided by the column-wise closed geometric mean (Aitchison, 1989, 1997):

$$K(g_1, \quad g_D) = \frac{[g_1, \dots, g_D]}{(g_1 + \dots + g_D)},$$

$$g_i = \prod_{j=1}^{D} x_j^{1/D}$$

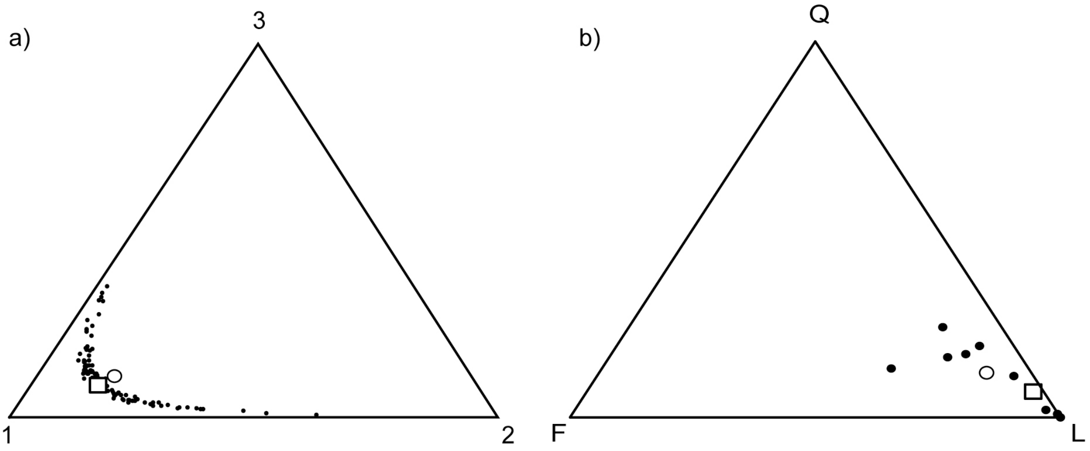

Figure 4.1. *Arithmetic vs. geometric mean with compositional data.*
When dealing with compositional data, the arithmetic mean (open dots) has no physical meaning. It usually fall away from the data as it doesn't represent a real composition but derives from the mixing in equal proportions of all the samples. The geometric mean (open squares) successfully represents dataset central tendency as it plots within the data cluster
a) figure from Vermeesch, 2005). b) data from table 3.1

Estimates of dispersion (generally referred to as "standard errors", "standard deviations", or "confidence intervals") are usually based on the assumption that the relative proportions of each component can be approximated by a normal (or Gaussian) distribution and are independent from each other. They are usually calculated from the standard deviations of each part:

$$S_x = \sqrt{\frac{\sum_{i=1}^{D} (x_i - m_x)^2}{D - 1}}$$

and multiplied by a value of Student's *t* with (D-1) degree of freedom and corresponding to the desired significance level α (usually 90, 95 and 99%) to obtain a confidence limit about the population or the mean of the dataset.

The normal-distribution approximation is unsuited for closure-constrained compositional data, as exemplified in figure 4.2 (from Weltje, 2002), which illustrates the univariate normal approximation of the confidence limits of the relative proportions (p) of two components, as a function of the number of observations (N).

It is clear from the previous example that one of the major drawbacks of the univariate normal-distribution assumption is that for relatively small samples the calculated variability can be greater than the compositional space itself.

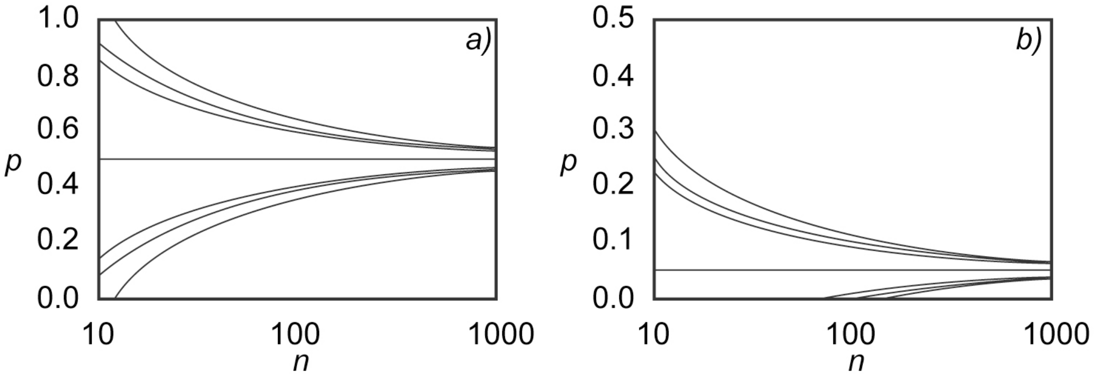

Figure 4.2. *Univariate normal approximation to binomial confidence limits of proportions (p) as a function of the observation (n).*
a) p=0.5; b) p=0.05. Confidence limits (90%, 95%, and 99%) extend into >1 and <0 proportions.

According to the log-ratio approach proposed by Aitchison (1986), a measure of the global dispersion of a D-part compositional dataset [X] is given by the total variance:

$$totvar[X] = \frac{1}{2D} \sum_{i=1}^{D} \sum_{j=1}^{D} var(ln \frac{x_i}{x_j})$$

The total variance can be split among all ratios calculating the variation matrix:

$$T = \begin{pmatrix} t11 & t12 & \dots & t1D \\ t21 & t22 & \dots & t2D \\ \vdots & \vdots & \ddots & \vdots \\ tD1 & tD2 & \dots & tDD \end{pmatrix} \quad , \quad t_{ij} = var(ln \frac{x_i}{x_j})$$

4.3 Biplot

A graphical way to display the variability of a compositional dataset is provided by biplot visualization.

Biplots (Gabriel, 1971) allow to simultaneously represent in two dimensions rows and columns of any M x N matrix by means of a rank-2 approximation. Aitchison (1997; Aitchison and Greenacre, 2002) adapted biplot for compositional data and since then, it proved to be a useful exploratory and explanatory tool (von Eynatten et al., 2003).

Compositional biplots are constructed applying principal component analysis (PCA; Pearson, 1901) to clr-transformed centered compositional matrices.

For any centered compositional dataset X, a corresponding Z matrix can be created applying a centered log-ratio (clr) transformation. The best rank-two approximation of such clr-transformed matrix is provided by its singular value decomposition (Sylvester, 1889; Eckart and Young, 1936; Krzanowski, 1988), which allows to obtain two matrices, one representing the projection of the samples on the plane defined by the first two eigenvectors, and one for the representation of the clr-parts (see Aitchison and Greenacre, 2002 and Daunis-I-Estadella et al., 2006 for further details about the calculation and construction of a compositional biplot).

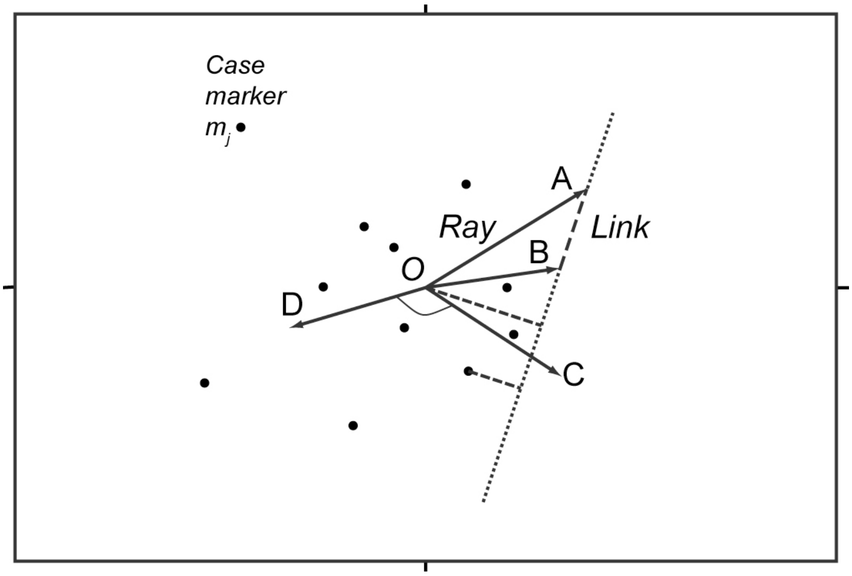

Figure 4.3. *Compositional biplot. Parts are visualized as rays; samples as case markers.*
Information on the relative variation of each part is given by rays length; angle cosine between rays provides an estimate of correlation between parts.

Any biplot consists of:

- an origin O representing the centre of the dataset;
- a vertex at position v_i for each of the D parts;
- a case marker m_j for each of the n samples of the dataset.

The joins of O to each of the vertices v_i constitute the “rays” of the biplot, whereas the join of two vertices v_i and v_j is termed “link”.

The relative position of vertices and case markers gives the following information on data variability:

- length of rays approximates relative variations of parts;
- distance between case markers approximates distance in the simplex between rows;
- cosine of angles between rays approximates correlation between parts;
- distances between column points (links and rays) provide approximations of the standard deviation of the corresponding log-ratios. Short links indicate a relatively constant component ratio, whereas large links indicate large relative variation;
- if two vertices coincide (or nearly so), variation of the corresponding log-ratio is nearly zero and the two variables can be considered as redundant;
- collinearity of vertices indicates that compositions plot along a compositional line;
- angle cosines between links approximates to correlation between log-ratios.
- since ratios are preserved under the formation of subcompositions, biplot of any subset of parts can be drawn selecting the vertices of the selected parts and taking the centre O of the new biplot as the centroid of the vertices.
- projection of the origin O onto a link corresponds to the average difference of the two variables;
- projection of a case marker onto a link approximates the difference of the two linked variables in the sample.

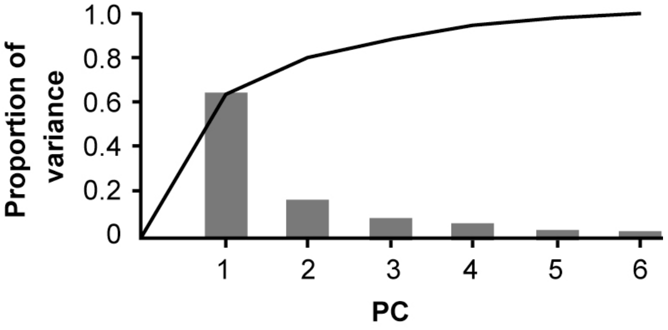

Fig. 4.4. *Scree plot of total variability explained. The variance explained by each component is expressed by the bar-plot, whereas the line visualizes the cumulative value. In this case, the first two principal components account for 80% of the entire dataset variance.*

The accuracy of any consideration about the compositional dataset variability extrapolated from a biplot is strongly influenced by the total variability retained by the two displayed principal components. The cumulative proportion of the total data variance expressed by each principal component is usually visualized in a “scree plot” diagram (fig. 4.4).

4.4 Subcomposition visualization (centering, pertubation, confidence region)

As compositional dataset usually consist of multiple parts, their representation in simple and easy-to-read form has always been a serious challenge for sediment petrographers. Compositional data representation has been traditionally performed considering 2- 3- or 4-part subcompositions of the whole dataset, represented in a “line” plot, a ternary and a tetrahedral graph, respectively (see fig 3.1). Since biplots, although they are based on log-ratios among components and their interpretation may not be straightforward, allow to visually explore the whole compositional dataset and give information on the correlation among different parts, they can be efficiently used to identify groups, homogeneities, trends and outliers among the samples.

Biplot analysis can be efficiently used for selecting the subcompositions to be used for representation in ternary diagrams to highlight trend, grouping and dispersion among samples.

Triangular compositional diagrams provide a convenient mean to plot graphically data in a quantitative format. Since their introduction in sediment petrography as a tool for classifying sedimentary rocks (Krynine, 1948), they have always found large diffusion playing a central role in classifications schemes and provenance models of sand and sandstone (Gazzi, 1966; Dickinson and Suczek, 1979; Basu, 1985; Zuffa, 1991).

The urge to visualize grouping and scattering among compositional data led many petrographers to the construction of the so-called *fields of compositional variation* (Weltje, 2002).

Such fields can be constructed according to statistical and non-statistical approaches.

Qualitative non-statistical approaches are the simplest way to visualize compositional variations in ternary diagrams and consist in hand-drawing the outline of a cluster of data (Dickinson and Rich, 1972; Fontana et al., 1989).

Quantitative approaches are based on the assumption of a univariate or multivariate distribution of the samples and fields of compositional variations are intended as the diagram regions enclosed by lines of equal-probability for any sample belonging to a specific population to fall inside the calculated field of variation for that population.

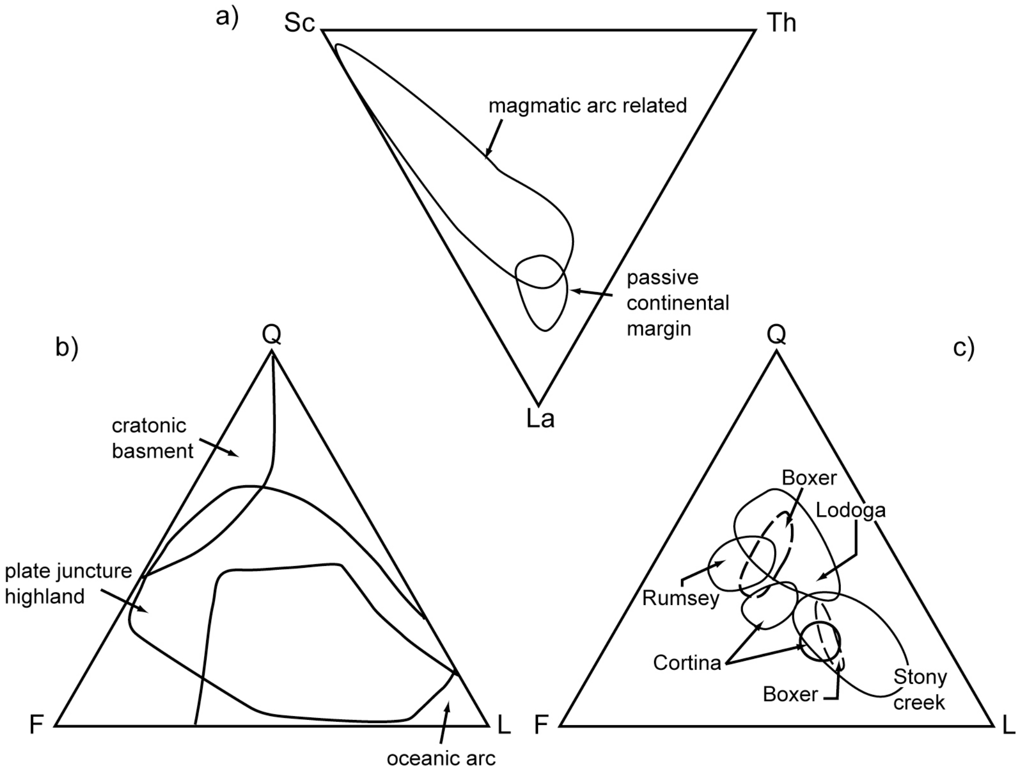

Figure 4.5. *Qualitative discrimination fields. Discrimination fields are drawn around sample clusters to qualitatively visualize data grouping, without any statistical significance. Due to the fact that compositional data can not vary independently from each others, such an approach can lead to misinterpretation. Fields from: a) Girty et al., 1993; b) Valloni, 1985; c) Dickinson and Rich, 1972.*

As mentioned above (paragraph 4.2), the assumption of a univariate normal distribution is general unsuited for describing compositional data variability. The inadequacy of such a statistical model reflects also in the calculation and representation of fields of compositional variation as hexagonal fields. Hexagonal fields of compositional variation are usually constructed plotting each measure of spread, calculated by means of normal approximation as a pair of lines around the arithmetic mean of the samples (e.g. Cavazza, 1986; Howard, 1994), oriented parallel to the side of the diagram that is opposite to the component vertex, at a distance of 1σ from the mean composition.

Since hexagonal fields enclose the intersection area of three independently calculated univariate ranges (one for each component), their outline does not represent an equal-probability contour. As a consequence of the univariate distribution assumption, another major problem of hexagonal fields is that they do not necessarily comply with the constant-sum constraint of compositional data (see figure 4.6).

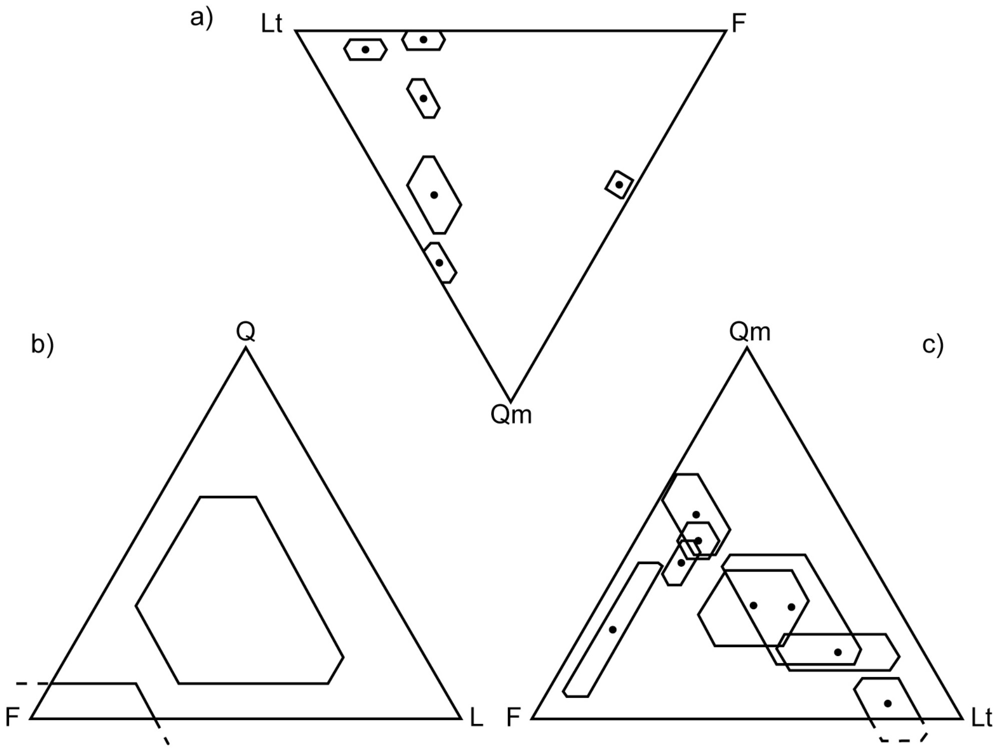

Figure 4.6. *Hexagonal fields of variations. Fields are drawn according to mean (arithmetic) composition and 1σ spreading of each part. Since standard deviations values are independently calculated for each part, hexagonal fields do not satisfy compositional data closure constrain and can not be regarded as equal probability fields. Redrawn after a) Dickinson, 1985; b) Valloni, 1985; c) Critelli et al., 1997.*

Additive logistic normal confidence regions represent the graphical visualization in ternary diagrams of compositional variability under the assumption of a multivariate statistical distribution. Multivariate distribution assumption (justified by the use of additive log-ratio transformation of compositional data, Aitchison 1986) allows to treat compositions as a whole and to take into account their covariance structure.

They are based on the application of significance tests (like the Student t-test for normal distribution) to the compositional parameters and allow to define a region in the ternary diagram representing all possible combinations of compositional parameters that are consistent with the corresponding parameter values estimated from the dataset, at a confidence level equal or greater than a specified value α. A $\alpha=0.1$ confidence region about the mean of a compositional dataset, has p=0.9 probability of containing dataset mean composition (see Weltje, 2002 for the math behind the construction of such confidence region in compositional ternary plots).

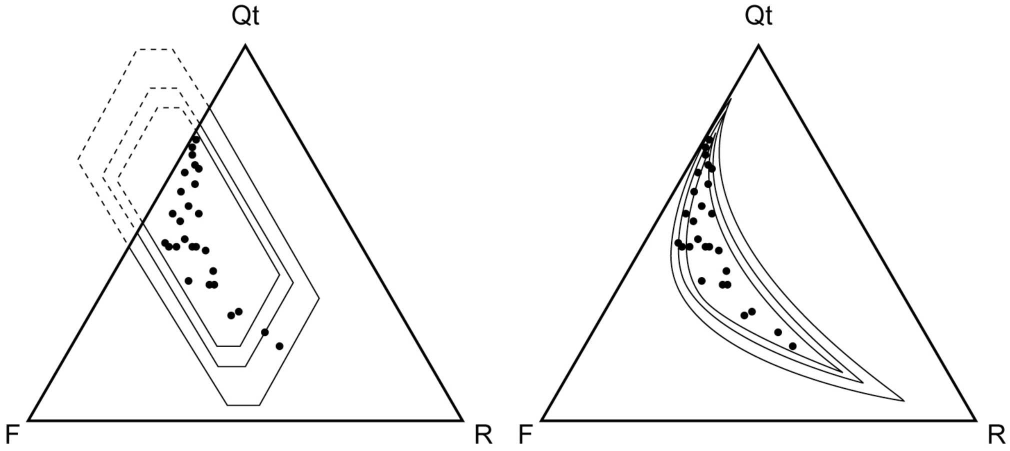

Figure 4.7. *90- 95- and 99% confidence regions calculated according to univariate (left) and multivariate (right) distributions. Redrawn after Weltje, 2002.*

A common issue for both visualization and graphical interpretation when using ternary diagram arises when compositions are close to the vertices (one dominant component) or to the boundaries (two dominant components) of the diagrams. In such situations, two workarounds are conventionally used:

- a part of the diagram is simply cut away, allowing magnification of the residual part where data cluster (e.g. DeCelles et al., 1998; Morton, 1991;Gazzi, 1966). See figure 4.8a;

- the diagram is rescaled by multiplying at least one of the components by a scalar. This is a common procedure especially in geochemistry (e.g. Bhatia and Crook, 1986; Meschede, 1986). See figure 4.8b.

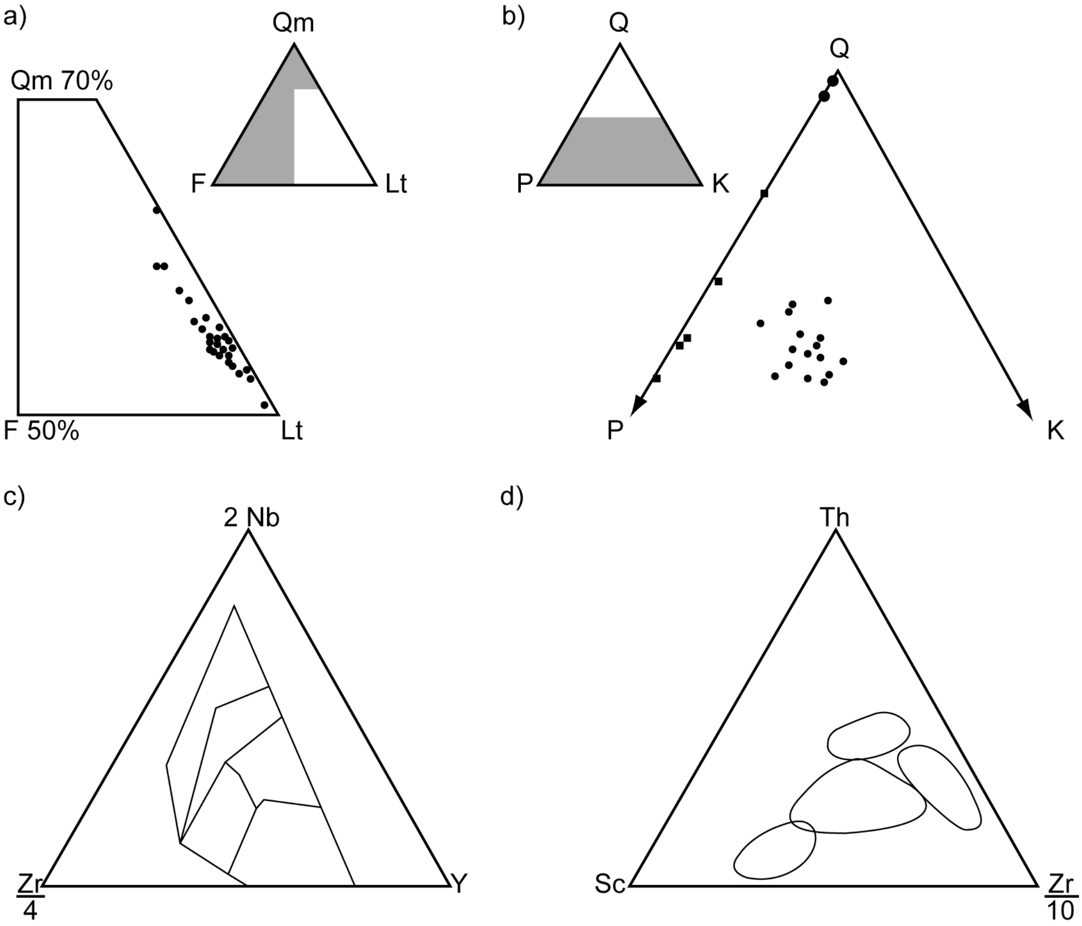

Figure 4.8. *Use of close-up and rescaling. the two most common workarounds when visualizing compositions that plot near an edge of the diagram or simply occupy only small parts of the diagram, are the magnification of the part of interest (a,b) or rescaling (c,d).*
a) after von Eynatten et al., 2003; b) after Gazzi, 1966; c) after Meschede, 1986; d) after Bhatia and Crook, 1986.

Instead of perturbing data by a randomly chosen scalar, a much more convenient and objective approach to improve data visualization is to perturb data (see chapter 3.5; Aitchison, 1986) by the inverse of their closed geometric mean (“centering” operation, Buccianti et al., 1999; Martin-Fernandez et al., 1999; Von Eynatten et al., 2002), moving data towards the baricenter of the triangular plot.

Perturbation of a single three-part vector in the simplex by its inverse results in the neutral element, which is exactly located in the baricenter of the triangular diagram.

When dealing with a dataset, centering can be proficiently performed by perturbing the dataset by the inverse of the closed geometric mean, which provides the most accurate location of the central tendency of the whole dataset (Aitchison, 1989).

Perturbation can be performed on straight lines and compositional fields, resulting in straight lines also in the transformed diagram, enabling the interpretation of the centered diagram. Vertices are invariant under perturbation as they have one component equal to 100 and the remaining ones equal to zero.

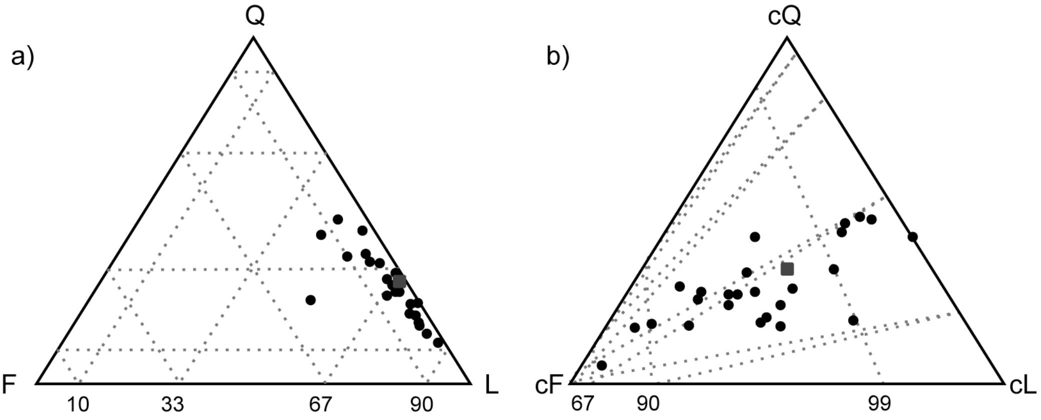

Figure 4.9. *Centering of compositions in a triangular diagram.*
a) QFL composition of modern sands derived from alpine subcreted oceanic cover units (see Appendix A2).
b) visualization of the same data after centering. Note that the geometric mean of the dataset (gray square) plot in the baricenter of the diagram.

Centering allows better understanding of the internal structure of the data, especially when they plot near a vertex or a boundary. Besides providing a better visualization of the compositions, centering allows a more accurate evaluation of the compositional distances among samples: as a common rule, the distance between two compositions cannot be expressed as the Euclidean distance but the closer two compositions are to the baricenter of a triangular diagram, the more “Euclidean” is their true Aitchison distance (see paragraphs 3.4 and 3.5).

Centering thus represents a powerful tool that enables both better visualization and interpretation of compositional data, still allowing reconstruction of the original compositions thanks to grid lines. It represents the best way to transform data as it ensures objective perturbation of the entire dataset and still provides a representation of the whole dataset.

4.5 Classification and regression trees

When dealing with the definition of a new model, (statistical) discrimination of compositional data of known origin has traditionally been performed with discrimination analysis (Filzmoser and Hron, 2009; Chayes and Velde, 1965; Pearce, 1976; Kovacs et al., 2006; Gorelikova et al., 2006). Although discriminant analysis works in any number of dimensions, visual interpretation is possible only for bi- or three-variate data (with the exception of the biplot whose interpretation however is not straightforward), thus loosing all the pieces of information contained in the components left outside of the representation. In addition most of the classification schemes adopted in sediment petrography allow the calculation of secondary parameters and ratios (i.e. Metamorphic Index –MI, Heavy Mineral Concentration index –HMC, Source Rock Density index –SRD, P/F, Lcd/Lc…) that do not fall in the constant sum constraint that characterizes the primary compositional data from which they have been calculated.

A powerful alternative and complementary approach to discrimination diagrams can be represented by classifications trees, a very popular "data mining" technique (Breiman et al., 1984; Ripley, 1996; Hastie et al., 2001).

Classification and regression trees (CART) allow to approximate the parameters space by a piecewise constant function. Among all possible partitions of the feature space, decision trees are built using a binary recursive partitioning of the data (figure 4.10), which represents a powerful tool for data mining and also allows visualization of multi-dimensional decision space in two dimension tree graph.

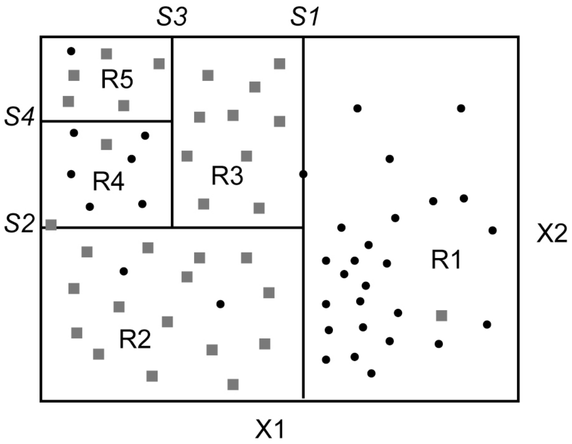

Figure 4.10. *Binary partitioning of a bivariate sample space. Recursive partitioning of the sample space ensures improving discrimination of the two groups.*

A dataset of compositional data and ratios obtained from point-counting of sediments of constrained origin, can be described as a dataset consisting of N samples, each of them characterized by J features, and belonging to one of K classes.

Each partition is defined by two quantities: the split feature j ($1 \leq j \leq J$) and the split value s ($-\infty < s < \infty$). This implies that for each split R of a tree, there are NxJ possible partitions. Among all possible choices, the best solution is the one that minimize node impurity Q:

$$Q_m = \sum_{k=1}^{K} p_k(1 - p_k),$$

where m is a node of the tree, p_k is the proportion of class k observations in the node m and Q is the “Gini index of diversity”.

Recursive binary partitioning and minimizing nodes impurity will eventually lead to a maximum sized tree, characterized only pure nodes (i.e. nodes containing only sample belonging to a single class).

Such a tree perfectly describes training data (i.e. data of known origin), but performs badly for predictive purposes, i.e. when used to define the class of an unknown origin sample. This is because the zero-impurity tree usually overfits training data causing high variance (figure 4.11).

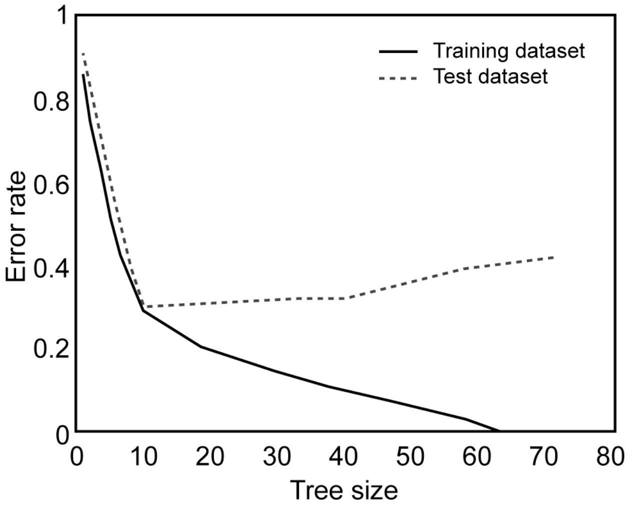

Figure 4.11. *Choosing the correct size for a classification tree. Bigger tree are able to correctly classify all samples from which they had been constructed but fail in properly classify other dataset due to overfitting of the training dataset. Data from Breiman et al., 1984.*

A smaller sized tree with the best predictive power can be found by means of "cost-complexity (cp) pruning".

The cost-complexity criterion can be defined as:

$$\text{cp} = \sum_{m=1}^{Z} NmQm + \alpha Z,$$

where Z is the terminal number of nodes in the tree, Nm is the number of observations in the m-th terminal node, Qm is the node impurity and α (≥0) is a tuning parameters.

For any given value of α, it is possible to find a sub-tree of the maximum size tree that minimizes cp, although not containing only pure nodes.

The choice of α can be performed by "V-cross validation" (e.g. Stone, 1978) which ensures the best predictive potential for the tree. The training dataset is randomly split into V subset. Then V trees are built and "pruned" using only V-1 subsets. The subset left out in the building of such new trees is used to asses tree discrimination performance.

A plot of the cross-validation (XV) prediction errors vs. the number of nodes (or cp value) can be then used to choose the best size of the tree.

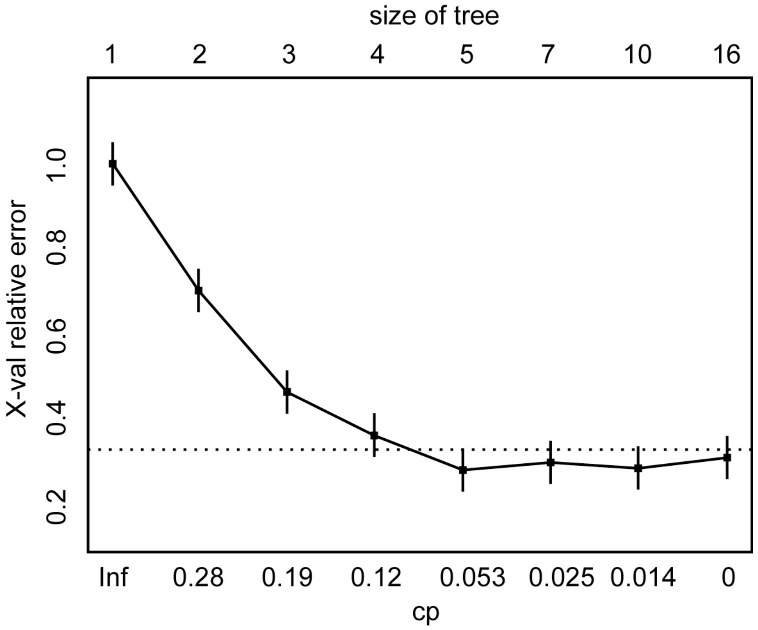

Fig. 4.12. *"Pruning the tree" and choosing its correct size. Tree size (x) vs. cross validation relative error (y). The best choice for prediction purposes is represented by a 5-branches tree (lowest cross-validation error). Larger trees better describe the training dataset but perform poorly in the classification of other datasets (higher cross-validation errors). See Appendix A2 and A3 for data.*

Since there will be several trees with XV errors close to the minimum and node number must be kept as low as possible to prevent high variance, the best solution will be represented by the smallest tree whose XV error does not exceed the XV minimum error tree plus 1σ of the error of the minimum XV error tree.

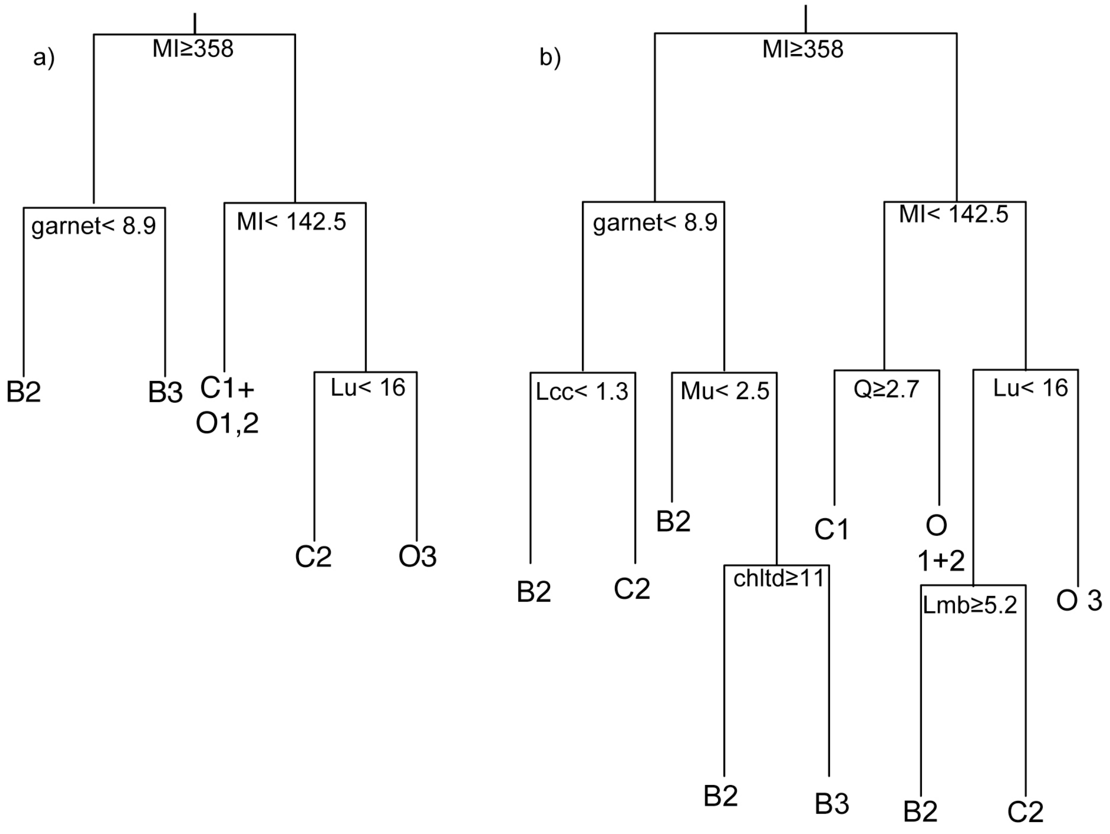

Figure 4.13. *Classification trees for detritus shed by the European Alps Axial belt. Classification trees correspond to a cp-value of 0.053 (a) and 0.014 (b) –see figure 5.3. Left branches mean "YES", right branches mean "NO".*
B: continental basement units; C: cover units; O: oceanic basement units. 1: offscraped units; 2: subcreted units; 3: deeply subducted units. MI: framework metamorphic index; Lu: ultramafic rock fragments; Lcc: calcareous rock fragments; Mu: muscovite; chltd: chloritoid; Q: quartz; Lmb: metabasite rock fragments.
See paragraph 5.6.2 and appendices A2 and A3 for details on the dataset.

Classification trees thus represent an invaluable data mining technique as they can cope with any data structure and type; they are simple, are invariant under transformations of the variables, are robust with respect to outliers and give estimates on the misclassification rate. They can also cope with missing data as in such cases a "follow the majority" rule can be used for samples that are missing one or more variables used for classification. Once classification trees have been properly constructed using a complete training dataset they can be easily, due to their nested structure, they can be easily implemented in spreadsheet, allowing a friendly and familiar interface for most of the users.

Major disadvantages of classification and regression trees are represented by the fact that tree structure may be unstable, resulting in different trees when a change in the sample occurs.

As classification trees are fundamentally a non-parametric tool, they are not affected by the closure constraints of compositional data and they don’t need the use of log-ratios (that would make treatment of missing data much more complex).

5 Detrital Fingerprints of Fossil Continental-Subduction Zones (Axial Belt Provenance, European Alps)

published in the Journal of Geology, v. 118, p. 341-362. "Detrital Fingerprints of Fossil Continental-Subduction Zones (Axial Belt Provenance, European Alps)" by Eduardo Garzanti, Alberto Resentini, Giovanni Vezzoli, Sergio Andò, Marco G. Malusà, Marta Padoan, and Paolo Paparella (with the exception of figures 5.4-.5-.10-.11-.13).

5.1 Introduction

Orogenic belts produced by continental collision are the most prominent product of plate tectonics. Metamorphic parageneses of high-pressure rocks exposed at the core of the orogen testify to multiphase deformation suffered first when pulled down the subduction zone to depths even exceeding 100 km, and next when pushed back at comparable speed toward the surface (Compagnoni et al. 1995; Ernst et al. 1997; Rubatto and Hermann 2001; Chopin 2003; Parrish et al. 2006; Beaumont et al. 2009). A doubly-vergent nappe stack, several km in height, hundreds of km in width, and thousands of km in length, is eventually produced by ongoing compressive tectonics during the subsequent paroxismal stage of continent-continent indentation (Gansser 1982; Doglioni et al. 1999).

The largest detrital factories on Earth, collision orogens produce sediment volumes so huge (up to 10^7 km^3) that they typically overspill associated foreland basins (Doglioni 1994), and reach unrelated subsident regions even several thousands of kilometers away (Einsele et al. 1996; Clift et al. 2001). Orogenic detritus is stored not only in foreland basin fills but also in submarine fans accumulating in remnant ocean basins (Ingersoll et al. 2003), and can thus be subsequently offscraped at trenches, tectonically stacked in subduction complexes, and recycled (Velbel 1985; Allen et al. 2008). The recognition of diagnostic detrital signatures sourced from collision orogens such as the Himalayas or the Alps is thus a fundamental issue in sedimentary petrology and provenance analysis.

Collision orogens are formed by a neometamorphic axial nappe pile ("axial belt"), the remnant of stretched outer-continental-margin crust and adjacent continent-ocean transition, and by mildly deformed basement and cover rocks on both sides, the remnants of the originally less-thinned parts of collided paleomargins ("external belts"). The axial backbone of the orogen represents a fossil continental-subduction zone, including oceanic and thinned-continental-margin units that underwent attempted subduction to deep subcrustal levels, were detached and subcreted at intermediate crustal levels, or were offscraped at shallow structural levels and thus escaped significant metamorphism (e.g., remnant-ocean turbidites; Graham et al. 1975). Basement and cover rocks of the axial belt, after undergoing subduction down to eclogite-facies depths, are retrogressed or re-equilibrated at variable pressure/temperature conditions (greenschist or amphibolite facies of Barrovian regional metamorphism), but mineral parageneses grown during peak high-pressure to ultra-high-pressure metamorphism are locally preserved (Spalla et al. 1996; Hacker et al. 2006).

In traditional approaches of sedimentary petrology, largely based on the study of ancient sandstones, only three broad and partly overlapping types of orogenic detrital sources were identified, corresponding to subtypes of “Recycled Orogen Provenance” (“Subduction complex”, “Collision orogen” and “Foreland fold-thrust belt” subprovenances; Dickinson and Suczek 1979; Dickinson 1985). Subsequent studies on modern sands (e.g., DeCelles and Hertel 1989; Critelli et al. 2003; Garzanti et al. 2004a) led to a more accurate definition of orogenic signatures. Several orogen types exist and, within each, distinct subparallel belts of contrasting rock assemblages shed detritus with distinct petrography and mineralogy (i.e., Axial Belt, Ophiolite, Magmatic Arc, Continental Block and Clastic Wedge Provenances of Garzanti et al. 2007). Orogenic detritus is thus a mixture, produced in various proportions from diverse sources, none of which is peculiar of collision orogens such as the Alps or the Himalayas. Nonetheless, because erosional exhumation is generally focused within the neometamorphic core of collision orogens, undergoing rapid tectonic uplift during the initial stages of continental indentation (Garzanti and Malusà 2008), axial-belt detritus overwhelms detritus from external belts. The mark of axial-belt provenance is thus imposed on sediments stored in foreland and remnant-ocean basins, typically characterized by feldspatholithoquartzose/lithofeldspathoquartzose metamorphiclastic composition and rich hornblende-epidote-garnet suites (Ingersoll and Suczek 1979; Suczek and Ingersoll 1985; Garzanti et al. 2004b; 2005).

Neometamorphic high-pressure units are thus the characterizing feature of collision orogens. Where preserved in the stratigraphic record and correctly identified, the distinctive detrital fingerprints of such rocks allow us to identify and reconstruct events of attempted continental subduction and subsequent exhumation, which have led to the growth of collision orogens in the geological past ("Axial Belt Provenance" of Garzanti et al. 2007).

The purpose of the present study is to describe in full detail the primary petrographic and mineralogical features of detritus derived from fossil continental-subduction zones representing the metamorphic core of the Alpine orogen. The Alps are an unrivalled natural laboratory for such sedimentary-petrology investigation. Completely and easily accessible, their geological framework is thoroughly known after more than a century of accurate studies. High-pressure metamorphic rocks including both felsic crustal and ultramafic mantle eclogites are widely exposed along two distinct sub-parallel axial belts, one of Late Cretaceous and one of Eocene age, which can be followed from Corsica and Piemonte to Austria and Slovenia.

In high-relief, temperate-cold mountain settings like the Alps, where chemical weathering is negligible and sediment transport rapid and short, first-cycle detritus can be considered as faithfully reflecting the mineralogy of parent rocks. The wealth of details that an actualistic approach can obtain from a modern orogenic system in which geological and geomorphological parameters are fully known and climatic or diagenetic alterations irrelevant, allow us to establish a direct, univocal relationship between eroded rocks and detritus produced, thus providing all information needed to refine sophisticated orogenic-provenance models. Detailed quantitative information obtained from actualistic studies (Ingersoll 1990) is vital to interpret the tectonic and erosional evolution of orogenic belts from sedimentary successions preserved in ancient foreland to remnant-ocean basins.

5.2 Fossil continental-subduction zones in the Alps

The Alps formed by two distinct phases of attempted continental subduction. The first one took place in the Late Cretaceous, and involved subduction of Adriatic continental crust, thinned and densified by Lower Permian and Upper Triassic delamination and mafic intrusions (Rebay and Spalla 2001; Thöni et al. 2008). The second one took place in the Eocene, and involved subduction of thinned European continental crust, largely including granitoid rocks (figure 5.1).

The relationship between these two distinct subduction events still awaits understanding. The hypothesis that postulates the fewest entities and introduces the

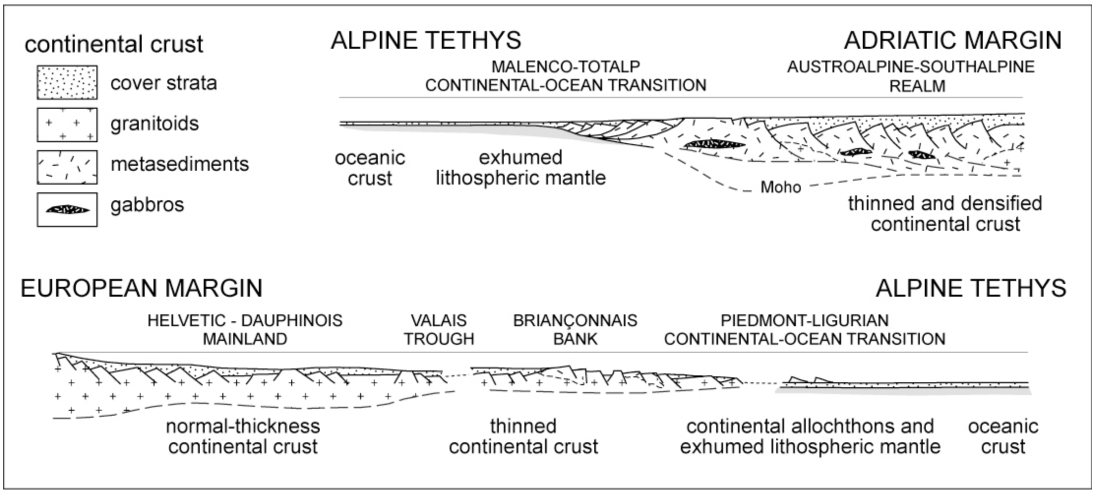

Figure 5.1. *Pre-collisional profiles of continental margins in the Central and Western Alps (mod. after Lemoine and De Graciansky 1988; Manatschal and Bernoulli 1999). The upper-plate Adriatic margin (including metasediments intruded by Permian and Triassic gabbros) and the lower-plate European margin (including abundant granitoids) underwent attempted subduction in the Late Cretaceous and Eocene, respectively.*

fewest arbitrary assumptions involves one prolonged subduction of Alpine Tethys beneath Adria, until final arrival of European crust at the trench in the Eocene.

Subduction tectonic erosion of Austroalpine crust took place in the Late Cretaceous (Polino et al. 1990; Wagreich 1993), possibly related to closure of oceanic realms in the east (Faupl and Wagreich 1999).

Rock complexes produced during such phases of attempted continental subduction are preserved into two distinct axial belts, the Austroalpine Cretaceous belt and the Penninic Eocene belt. The former was chiefly fed by upper-plate Adriatic units in Andean-style tectonics, the latter by lower-plate European units in Himalayan-style tectonics (Doglioni et al. 2007).

Within each fossil continental-subduction zone we ideally identify three distinct structural levels, characterized by increasing thermo-baric conditions (Figure 5.2). Sedimentary thrust-sheets detached from their oceanic to continental basements characterize the shallow level, subcreted blueschist-facies to greenschist-facies cover and basement nappes characterize the intermediate level, and eclogite-facies continental to oceanic basement slivers characterize the deep level.

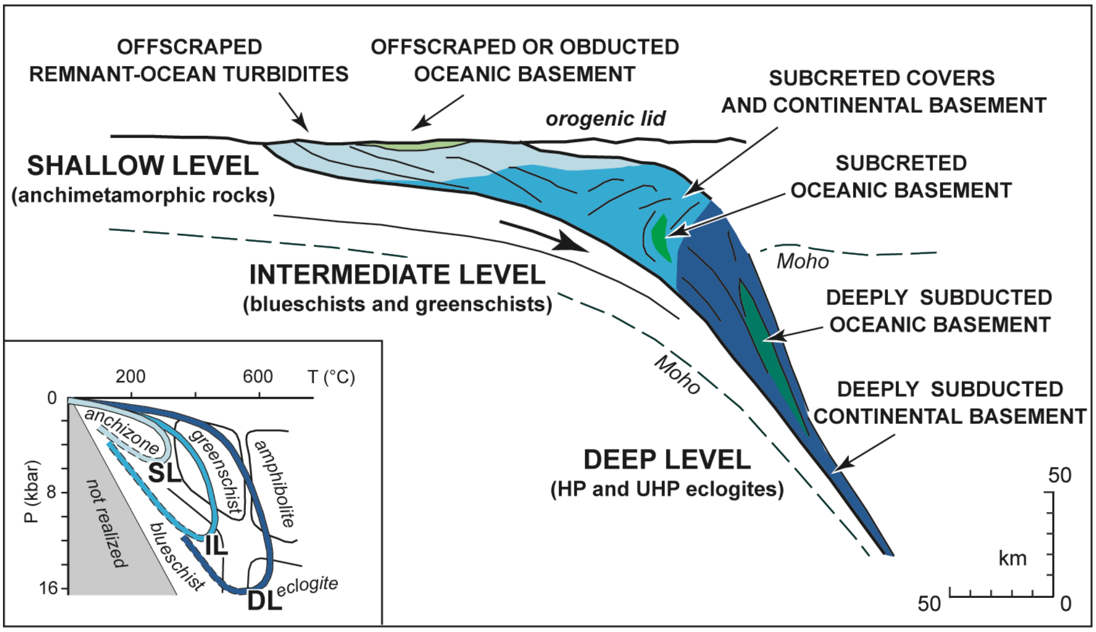

Figure 5.2. *Idealized profile of a continental-subduction zone. Tectonic units within the orogenic wedge may dominantly include rocks originally belonging to the downgoing plate, detached at various depths and accreted to the upper plate, as in the Eocene axial belt. Rocks belonging to the upper plate can behave either passively as a continental or oceanic lid (obducted ophiolite), or be tectonically eroded and dragged themselves in subduction (von Huene and Lallemand 1990), as in the Cretaceous axial belt. Inset shows typical P-T path for shallow (SL), intermediate (IL) and deep-level (DL) tectonic units.*

The Cretaceous (Eoalpine; Thöni and Jagoutz 1993) axial belt is chiefly preserved in the Eastern Alps (Saualpe-Koralpe, Pohorje), whereas only local remnants are preserved in the Central Alps (Texel unit). Its western continuation, also involved in the Eocene axial belt, is represented by the Sesia-Lanzo unit (Rubatto et al. 1999). We will consider here in full detail the deep-level continental eclogites of the Cretaceous subduction zone, but not the bulk of Austroalpine nappes including the Northern Calcareous Alps. We will also consider the continent-ocean transition of the Adriatic margin (Manatschal and Bernoulli 1999; Trommsdorff et al. 2005), as well as the Dent Blanche unit, representing an Austroalpine basement sliver involved in the Eocene subduction zone.

The Eocene Penninic axial belt is widely exposed in the Western and Central Alps (Rubatto et al. 1998), and delimited between the Insubric and Frontal Penninic Faults (Polino et al. 1990). The Briançonnais domain is seen as a distal part of the thinned European margin, originally representing a continental ribbon partially detached from mainland Europe by Mesozoic rifting of the Valais trough (Stampfli et al. 1998). In the

Eastern Alps, subcreted metamorphic units of the Eocene axial belt are exposed in tectonic windows (Engadine, Tauern, Rechnitz). We will consider in full detail subducted metamorphic units of deep and intermediate structural levels. Within the shallow level, comprising offscraped sedimentary successions and minor ophiolite slivers, we will focus on detrital signatures of remnant-ocean turbidites, including those fed by erosion of the Cretaceous axial belt and subsequently incorporated in the Eocene axial belt. Paleozoic continental basements and Permo-Mesozoic covers of the external belts (Helvetic-Dauphinois and Southalpine domains), which were not involved in Alpine subduction, will not be considered.

Discriminating structural levels within a fossil continental-subduction zone implies a certain degree of uncertainty, particularly as regards polymetamorphic units with extensive thermal overprint. We assign the whole of the Lepontine dome to the deep level, but the Tambò and Suretta units at its eastern side to the intermediate level (Nussbaum et al. 1998). Conversely, we assign the Tauern-window basements to the intermediate level, and only its Eclogite zone (Spear and Franz 1986) to the deep level.

5.3 Geological outline

5.3.1 The shallow level of the Eocene continental-subduction zone

Offscraped anchimetamorphic arenaceous to calcareous ("Helminthoid Flysch") remnant-ocean turbidites of Cretaceous to Early Eocene age are widely exposed in the Alps. These include the S.Remo Flysch in Liguria (Di Giulio 1992), the Parpaillon (Embrunais-Ubaye) Flysch between the Argentera and Pelvoux Massifs (Kerkhove 1969), the Simme and Niesen Flysches in the Préalpes Romandes (Elter et al. 1966), the Prättigau Flysch in the northern Central Alps (Lihou and Allen 1996), and the Vorarlberg and Rheno-Danubian Flysches exposed along the northern front of the Eastern Alps (Trautwein et al. 2001). Largely Mesozoic carbonate sequences of the Briançonnais domain, detached from their continental basement that reached greater depths in the subduction zone, are exposed in the Préalpes Romandes (Mosar et al. 1996).

Unmetamorphosed ophiolite slivers including serpentinite, gabbro, pillow-basalt and radiolarite are known from Corsica and the Northern Apennines to the Western Alps. Here the tabular Chenaillet ophiolite, lying atop subcreted blueschist-facies ophiolites, escaped subduction and orogenic overprint (Chalot-Prat 2005), as indicated by Mesozoic ages yielded even by low-temperature geochronometers (Schwartz et al.

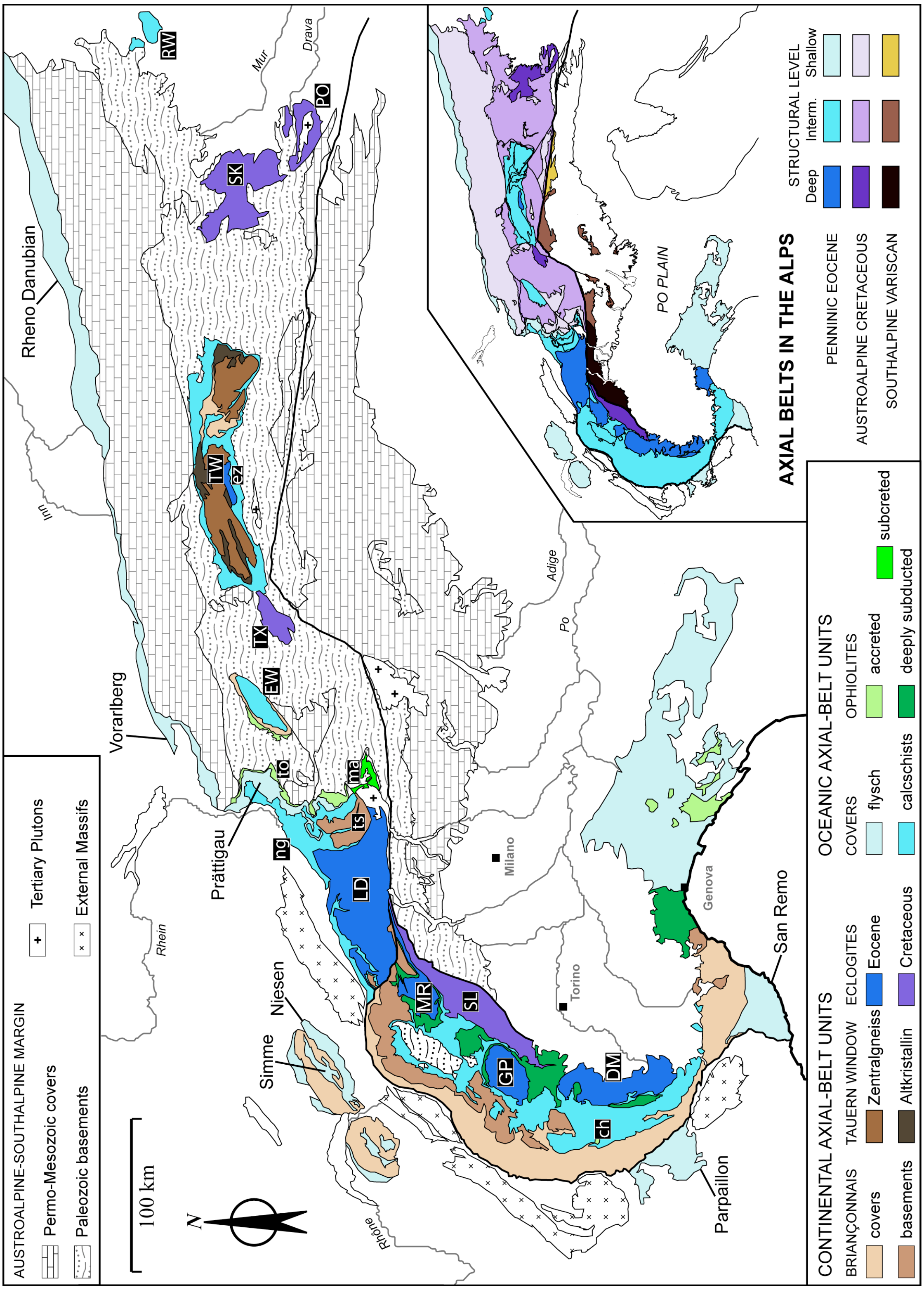

Figure 5.3. *Geology of the Alps (map after Frey et al. 1999; Schmid et al. 2004). Structural levels of Variscan, Cretaceous, and Eocene axial belts are shown in inset.* DM= *Dora Maira;* EW= *Engadine window;* GP= *Gran Paradiso;* LD= *Lepontine dome;* MR= *Monte Rosa***;** PO= *Pohorje;* RW= *Rechnitz window;* SK= *Saualpe-Packalpe-Koralpe;* SL= *Sesia-Lanzo;* TW= *Tauern window;* ch= *Chenaillet;* ez= *Tauern eclogite zone;* ma= *Malenco ;* ng= *northern Graubünden;* to= *Totalp;* ts= *Tambò-Suretta.*

2007). In the Central Alps, lizardite serpentinites and overlying oceanic sediments with very low-grade metamorphic overprint (prehnite-pumpellyite facies) represent the preserved Adriatic continent-ocean transition (Totalp unit; Bernoulli and Weissert 1985), belonging to the Austroalpine lid of the subduction zone.

5.3.2 The intermediate level of the Eocene continental-subduction zone

Basement and sedimentary rocks displaying blueschist-facies to greenschist-facies metamorphism were detached at crustal depths from the subducting European slab, exhumed tectonically, and subcreted at intermediate level beneath the accretionary prism. Calcschists and micaschists, representing Mesozoic calcareous to arenaceous turbidites with minor ophiolitic detritus and displaying blueschist-facies metamorphism, are widespread in the Piedmont zone of the Western Alps, including the Combin unit and the Schistes lustrés (Caron 1977). Associated are slices of serpentineschist, metagabbro and metabasalt with locally preserved oceanic covers (Barfety et al. 1996). Carbonate metaturbidites and continental-margin metabreccias are exposed in the hanging wall of the Frontal Penninic Fault (Sion-Courmayeur unit; Elter and Elter 1965). In the Central Alps, blueschist-facies calcschists (Bündnerschiefer) occur in northern Graubünden (Engi et al. 2004). One of the largest serpentinite masses in the Alps, associated with lower crustal metapelites intruded by Permian gabbro, is found in the Malenco unit. These rocks represent the remnants of the Adriatic continent-ocean transition, deformed under epidote-amphibolite conditions (Trommsdorff et al. 2005). Blueschist-facies metaturbidites locally associated with ophiolite bodies are also exposed beneath Lower Austroalpine basement nappes in the Engadine window (Bousquet et al. 1998), Tauern window (Kurz et al. 1998), and Rechnitz window (Hoinkes et al. 1999).

Subcreted continental basements chiefly consist of paragneisses and micaschists including pre-Alpine granitoids and associated with minor cover slices. In the Western Alps, Briançonnais basements of the Gran S.Bernardo nappe (Desmons 1992) underwent blueschist-facies to greenschist-facies metamorphism, were coupled at depth and finally subcreted along west-dipping shear zones (Malusà et al. 2002; 2005). On the western side of the Briançonnais tectonic fan, instead, low-grade Upper Paleozoic metasedimentary and metavolcanic rocks were subcreted along east-dipping shear zones (Houillère zone; Fabre 1961). Small basement units and very-low grade Permo-Triassic volcanic and sedimentary covers occur in the Ligurian Alps (Vanossi et al. 1986). In the Central Alps, largely metapelitic Paleozoic basements intruded by granitoids are exposed east of the Lepontine dome (Tambò and Suretta nappes; Nussbaum et al. 1998). The Austroalpine Dent Blanche unit includes Paleozoic metagranitoids intruded by Permian gabbros and pervasively retrogressed under greenschist-facies conditions during the Eocene subduction (Arolla Series), along with Paleozoic amphibolite-facies to granulite-facies paragneisses, metabasites, marbles and metapegmatites (Valpelline unit; Dal Piaz 1993). Basement units of the Tauern window include metavolcanic and metasedimentary rocks (Altkristallin) intruded by Upper Paleozoic granitoids (Zentralgneiss). Widespread blueschist-facies metamorphism was followed by greenschist-facies to lower-amphibolite-facies re-equilibration (Zimmermann et al. 1994).

5.3.3 The deep level of the Eocene continental-subduction zone

Eclogite-facies continental to oceanic basement slivers and minor cover sequences, representing the strongly thinned European continent-ocean transition subducted at subcrustal depth, tectonically detached, and exhumed backward along the subduction zone, are largely exposed on the retro-side of the axial belt. Exposed in the Internal Massifs (Dora Maira, Gran Paradiso, Monte Rosa) are metapelites and metabasites intruded by Upper Paleozoic granitoids (Vialon 1966; Compagnoni et al. 1974). Pressure conditions up to ~3.5 GPa are documented by coesite-bearing rocks in the Dora Maira Massif (Chopin 1984). Re-equilibration under greenschist-facies conditions is widespread (Frey et al. 1999).

Granitoid gneisses representing the deepest units of the post-collisional nappe stack are exposed within the Lepontine dome, where high-pressure relics only locally escaped re-equilibration under lower to upper amphibolite-facies conditions (Engi et al. 2004). A sliver of eclogite-facies metasediments (schist, quartzite, marble) and metabasites occurs in the southernmost part of the Tauern window (Eclogite zone; Spear and Franz 1986), where high-pressure metamorphism is dated at 31.5±0.7 Ma (Glodny et al. 2005).

Metaophiolites including mantle (antigorite serpentinite) and crustal rocks (metagabbro, metabasalt, metachert, metapelite) are exposed in the Western Alps (Zermatt-Saas and Monviso units; Bearth 1967; Lombardo et al., 1978) and Ligurian Alps (Voltri unit; Scambelluri et al. 1995). A large body of subcontinental mantle, consisting of spinel lherzolite and foliated serpentinite with minor dunite, pyroxenite and gabbro, is exposed in the Lanzo Massif (Piccardo et al. 2007).

5.3.4 The deep level of the Cretaceous continental-subduction zone

Austroalpine units that underwent eclogite-facies metamorphism in the Late Cretaceous (Thöni 2006) are discontinuously exposed north of the Insubric Fault, on the retro side of the Eocene axial belt. The Pohorje unit includes eclogite-facies metapelites, marbles, quartzites, metabasites and garnet-peridotites, occurring as lenses within amphibolite-facies gneisses (Sassi et al. 2004). The Koralpe and Saualpe units, including the eclogite type-locality, chiefly consist of garnet-kyanite metapelites, metapegmatites, marbles and metabasites, re-equilibrated under amphibolite-facies conditions (Miller et al. 2005). The Texel Unit includes eclogite-facies metapelites, orthogneisses and metabasites, partly re-equilibrated under amphibolite-facies conditions (Habler et al. 2006). The Sesia-Lanzo unit contains high-pressure metapelites, metagranitoids and minor metagabbros (Eclogitic Micaschists), pervasively retrogressed metagranitoids (Gneiss Minuti), as well as relict Paleozoic granulites (II Diorito-kinzigitic zone; Compagnoni et al. 1977). Eclogite-facies conditions, reached at 70-65 Ma and/or earlier (Rubatto et al. 1999), were followed by re-equilibration under greenschist-facies conditions in the Eocene (Inger et al. 1996).

5.4 Methods

5.4.1 Sampling

In high relief, temperate-cold mountain settings like the Alpine chain, where chemical weathering is negligible and sediment transport is rapid and short, detrital modes can be considered as faithfully representing the mineralogy of source rocks.

Between 1995 and 2009, preferentially during drought periods, 211 samples of loose bedload sand (figure 5.4) were collected from active fluvial bars in northern Italy, Switzerland, Austria, and Slovenia. Sediments were collected at major geological boundaries, upstream of major confluences and lakes, and at the mountain front before entering the sedimentary basin. Estimates on morphometric parameters of river's channel, of water discharge, banks characterization (natural vs. manmade), mean sediment size and their in-situ petrographic characterization were collected, together with a brief description of the sampling point, providing useful additional informations to unravel possible effects of hydraulic sorting and antropic contamination of the natural petrographic signals.

Sampling of small-sized catchments comprised entirely within single tectonic units ("first-order sampling scale" of Ingersoll 1990) allowed us to identify all distinctive end-member detrital signatures.

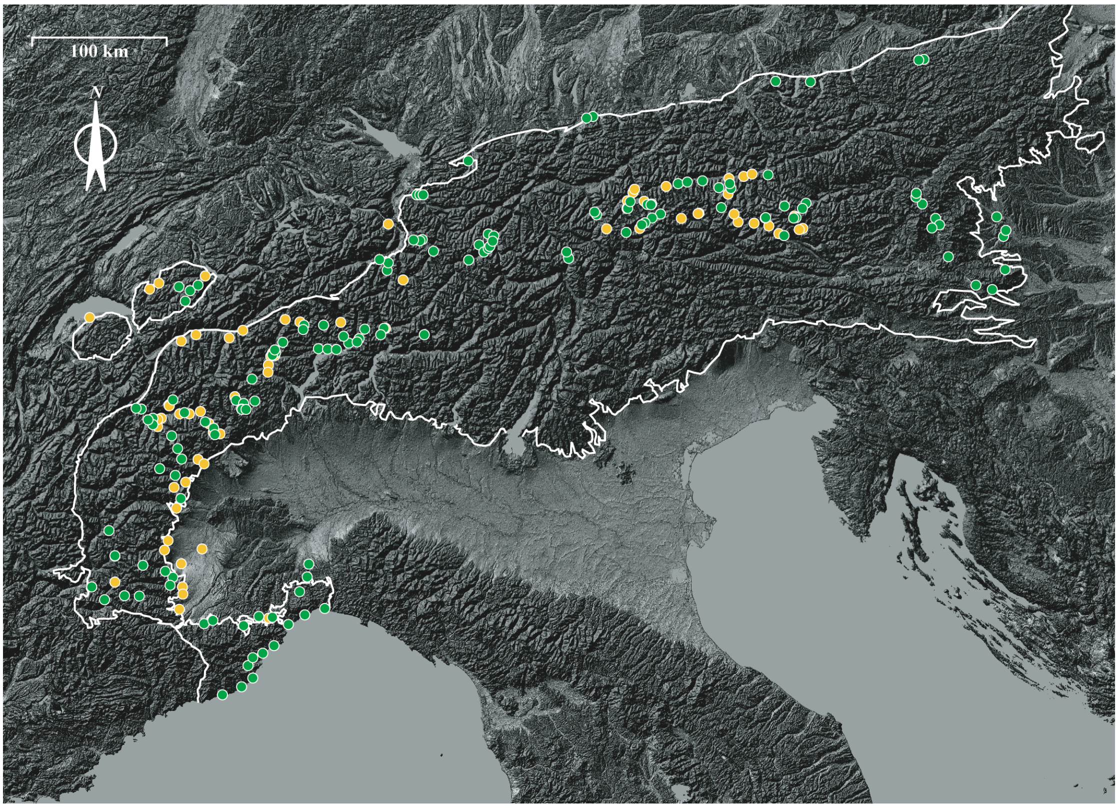

Figure 5.4. *Sampling locations. Samples exclusively derived from single tectono-metamorphic units are reported in green. Multi-sourced samples are reported in yellow.*

5.4.2 Sand petrography

In each sample, 400 points were counted by the Gazzi-Dickinson method (Ingersoll et al. 1984) on the whole sand fraction, impregnated with Araldite, cut into standard thin sections, and stained with alizarine red to distinguish dolomite and calcite. Following a simple nomenclature scheme (figure. 5.5), first introduced by Crook (1960) and endorsed by Dickinson (1970), sands are here classified according to their main components exceeding 10%QFL, (e.g., a lithofeldspathoquartzose sand has quartz > feldspar > lithics > 10%); an adjective reflecting the dominant rock-fragment type may be added (e.g., volcaniclastic, metamorphiclastic, carbonaticlastic; Ingersoll, 1983).

Full quantitative information was collected on coarse-grained rock fragments, and recalculated to an extended spectrum of primary proportional parameters (table 5.1). Metamorphic rock fragments are classified according to protolith composition and metamorphic rank.

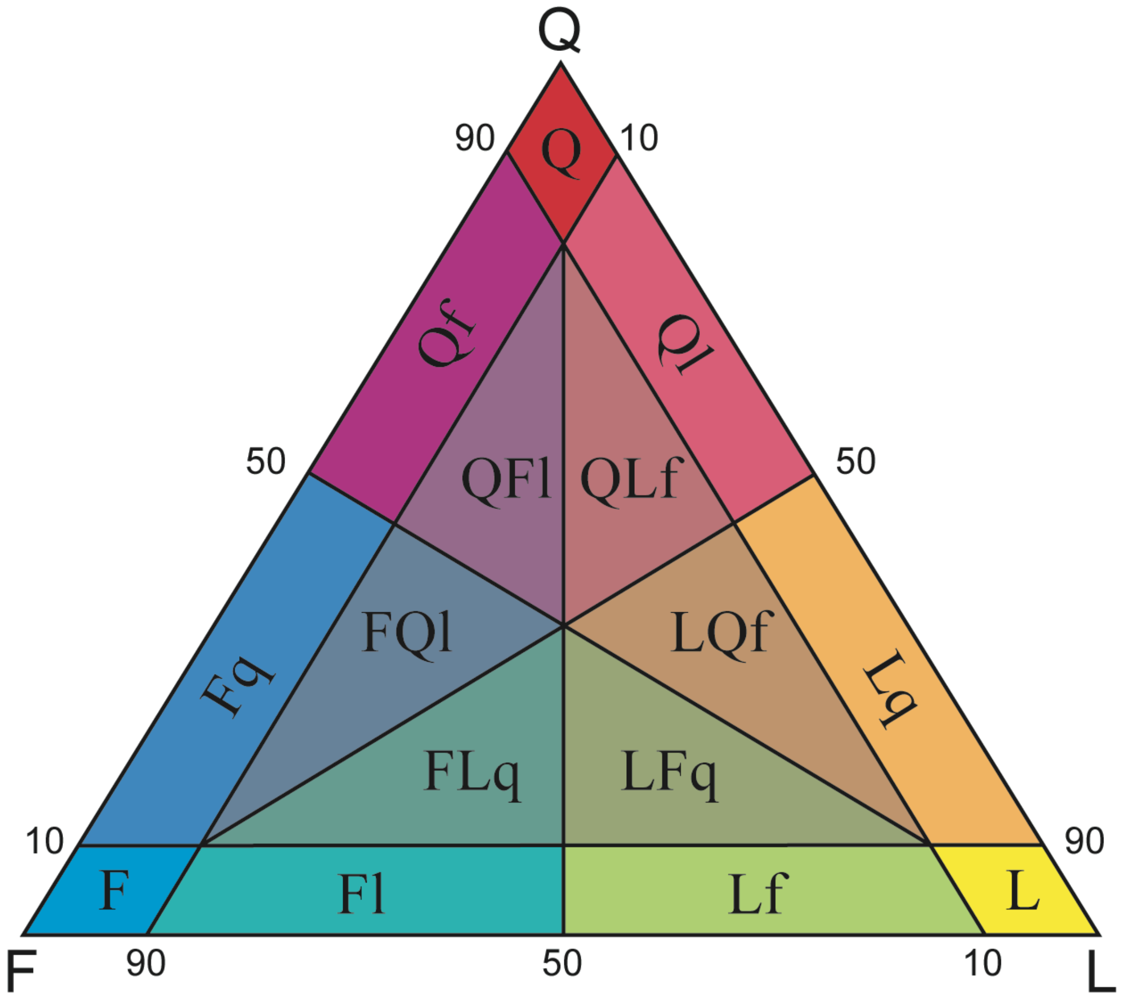

Figure 5.5. *QFL nomenclature scheme. Detrital modes are classified according the relative abundance of quartz (Q), feldspars (F), and lithic fragments (L), listed in order of abundance. Fl: feldspatholithic; Fq: feldspathoquartzose; Lf: lithosfeldspathic; Lq: lithoquartzose; Qf: quartzofeldspathic; Ql: quartzolihic; FLq: feldspatholithoquartzose; FQl: feldspathoquartzolithic; LFq: lithofeldspathoquartzose; LQf: lithoquartzofeldspathic; QFl: quartzofeldspatholithic; QLf: quartzolithofeldspathic.*

Average rank for each sample is expressed by the “Metamorphic Index” MI, which varies from 0 in detritus exclusively from sedimentary and volcanic cover rocks to 500 in detritus from exclusively high-grade basement rocks. Very low to low-rank metamorphic lithics, for which protolith can still be inferred, are subdivided into metasedimentary (Lms) and metavolcanic (Lmv) categories. Medium to high-rank metamorphic lithics are subdivided into felsic (metapelite, metapsammite, metafelsite; Lmf) and mafic (metabasite; Lmb) categories. Pure marble grains are included with carbonate grains (limestone Lcc or dolostone Lcd), whereas impure metacarbonate grains are split equally between carbonate (Lcc or Lcd) and metamorphic (Lms or Lmf) grains. Because the limit between high-rank and very-high rank metamorphic grains is set conventionally at a groundmass crystal size of 62.5 μm (Garzanti and Vezzoli 2003), the Gazzi-Dickinson point-counting method assigns only very-low-rank to high-rank rock fragments to the L pole, whereas coarser very-high-rank rock fragments are assigned to the Q pole, F pole, or accessory mineral depending on the single mineral hit by the crosshair. The 62.5 μm crystal-size limit thus marks a shift of detrital modes from feldspatholithoquartzose metamorphiclastic to feldspathoquartzose, which in river sands from the Central Alps corresponds roughly with the boundary of the high-grade Lepontine dome (Garzanti et al. 2004a). Among ultramafic grains we distinguish foliated serpentineschist, displaying non-pseudomorphic textures made of interpenetrating antigorite blades to interlocking equant serpentine crystals grown during dynamic recrystallization (Lus), from cellular serpentinite, displaying pseudomorphic mesh textures with rims of lizardite enclosing reddish-brown brucite-lizardite or locally relict olivine or orthopyroxene (Luc).

5.4.3 Heavy minerals

A quartered fraction of each sample was dry-sieved or wet-sieved at 1ϕ intervals in order to determine grain size. The very-fine to fine-sand fraction (63-250 μm) was treated with acetic acid to remove carbonates and with oxalic acid or sodium ditionite-citrate-bicarbonate to remove iron-oxide coatings. Heavy minerals were separated by centrifuging in Na-metatungstate (density 2.90 g/cm^3), and recovered by partial freezing with liquid nitrogen. From each sample, 200 to 250 transparent detrital minerals were counted in grain mounts by the area method (Galehouse 1971; Mange and Maurer 1992).

The abundance of total (transparent + opaque + turbid) and transparent heavy minerals in the sediment is expressed by the "Heavy Mineral Concentration" (HMC) and "transparent Heavy Mineral Concentration" (tHMC) indices. Heavy-mineral suites are described as "extremely poor" (HMC < 0.1), "very poor" ($0.1 \le$ HMC < 0.5), "poor" ($0.5 \le$ HMC < 1), "moderately poor" ($1 \le$ HMC < 2), "moderately rich" ($2 \le$ HMC < 5), "rich"

($5 \leq \mathrm{HMC} < 10$), “very-rich” ($10 \leq \mathrm{HMC} < 20$), or “extremely rich” ($20 \leq \mathrm{HMC} < 50$). Heavy-mineral-dominated sands ($\mathrm{HMC} > 50$) occur only in the case of either local monolithologic provenance from very dense rock (peridotite, eclogite, granulite) or strong hydraulic concentration (“placer deposits”; Garzanti et al., 2009). Significant heavy-mineral species are listed in order of abundance throughout the text.

Table 5.1. *Key parameters and indices used for analysis and classification*

Key Indices	Definition
Bulk Composition	
Q	quartz
KF	K-feldspar
P	plagioclase
Lvf	felsic volcanic and subvolcanic lithic grains
Lvm	intermediate and mafic volcanic and subvolcanic lithic grains
Lcc	limestone grains
Lcd	dolostone grains
Lp	terrigenous lithic grains (shale, siltstone)
Lch	chert lithic grains
Lms	metasedimentary lithic grains (very-low to low rank)
Lmv	metavolcanic lithic grains (very-low to low rank)
Lmf	metapelite/metapsammite and metafelsite lithic grains (medium to high rank)
Lmb	metabasite lithic grains (medium to high rank)
Lu	ultramafic lithic grains (serpentinite, foliated serpentineschist)
Metamorphic rank	
Rm0	unmetamorphosed sedimentary and volcanic to subvolcanic rock fragments
Rm1	very-low rank metamorphic rock fragments (rough cleavage, illite-chlorite)
Rm2	low-rank metamorphic rock fragments (strong cleavage, sericite)
Rm3	medium-rank metamorphic rock fragments (schistosity, tiny micas)
Rm4	high-rank metamorphic rock fragments (new crystals <62.5 microns, muscovite)
Rm5	very-high rank metamorphic rock fragments (new crystals >62.5 microns, biotite)
Rm	Rm0 + Rm1 + Rm2 + Rm3 + Rm4 + Rm5
MI Index	Rm1/Rm*100 + Rm2/Rm*200 + Rm3/Rm*300 + Rm4/Rm*400 + Rm5/Rm*500
Ratio parameters	
P/F	plagioclase vs. total feldspars
Qp/Q	polycristalline quartz vs. total quartz
Lcd/Lc	dolomitic rock fragments vs. total carbonate rock fragments
Lmb/Lm	metabasite rock fragments vs. total metamorphic rock fragments
Luc/Lu	cellular serpentinite rock fragments vs. total serpentinite rock fragments
Heavy minerals	
ZTR	ultrastable minerals (zircon, tourmaline, rutile)
LgM	low-grade metamorphic minerals (mostly epidote-group and chloritoid)
Grt	garnet
HgM	high-grade metasedimentary minerals (staurolite, andalusite, kyanite, sillimanite)
A	amphiboles
P	pyroxenes
O + S	olivine + spinel
&HM	other transparent heavy minerals (mostly titanite, apatite, anatase/brookite)
HMC Index	total (transparent + opaque + turbid) heavy minerals / total terrigenous grains * 100
tHMC Index	transparent heavy minerals / total terrigenous grains * 100
SRD Index	weighted average density of terrigenous grains (g/cm^3)
HCI Index	(1/3 green Hbl + 2/3 green/brown Hbl + brown Hbl) / total hornblende * 100
MMI Index	(1/3 St + 2/3 Ky + Sil) / (chloritoid + staurolite + kyanite + sillimanite) * 100

Key petrographic indices calculated by the Gazzi-Dickinson method. L = Lvf + Lvm + Lcc + Lcd + Lp + Lch + Lms + Lmv + Lmf + Lmb + Lu = total aphanitic lithic fragments (crystal size <62.5 microns). Q + F + L = total main extrabasinal grains (excluding micas and dense minerals). The five metamorphic ranks of lithic grains are defined operationally in Garzanti and Vezzoli (2003). MI= Metamorphic Index. P/F ratio calculated by the Gazzi-Dickinson QFL method. Other ratios calculated by the traditional QFR method. HMC and tHMC = total and transparent Heavy Mineral Concentration indices; SRD = Source Rock Density index (Garzanti and Andò, 2007a). HCI= Hornblende Color Index; MMI = Metasedimentary Minerals Index (Garzanti and Andò, 2007b).

The “Source Rock Density” (SRD) index is defined as the weighted average density of extrabasinal terrigenous grains, and used as an estimator of the average density of source rocks in the absence of hydraulic effects. Further details on the methods used to calculate HMC, tHMC, and SRD indices are given in Garzanti and Andò (2007a). The “Hornblende Colour Index” HCI and “Metasedimentary Minerals Index” MMI (Garzanti and Andò 2007b) are used to estimate the average metamorphic grade of metaigneous and metasedimentary source rocks, respectively. They vary from 0 in detritus from greenschist-facies to lowermost amphibolite-facies rocks yielding exclusively blue/green amphibole and chloritoid, to 100 in detritus from granulite-facies rocks yielding exclusively brown hornblende and sillimanite.

5.4.4 Statistics

Detrital modes obtained with petrographic and mineralogical analyses are non-negative and invariably sum up to a constant (i.e., 1 or 100%). Such constant-sum constraint implies that variables neither vary independently from each other nor follow a multivariate normal distribution, and therefore fail major prerequisites of standard statistical methods (Aitchison 1986). A family of log-ratio transformations from the simplex to the Euclidean space were thus introduced to perform statistical techniques such as principal component analysis (Buccianti et al. 2006). In order to discriminate homogeneous provenance groups within our data set, we applied centered log-ratio (clr) transformations (Aitchison and Greenacre 2002). We used the compositional biplot (Gabriel 1971) for graphical display of both multivariate observations (points) and variables (rays). The problem of zero values was solved by the “multiplicative replacement strategy” (Martin Fernandez et al. 2003). As input value for zero replacement we chose 0.001, which is less than half the value corresponding to 1 out of 400 counted grains.

Decision trees were used to rigorously determine affinities among sample groups and to objectively define their compositional boundaries. This data-mining method based on the “Classification And Regression Tree” algorithm (CART; Breiman et al. 1984; Vermeesch 2006) allows the simultaneous use of an unlimited number of parameters while still permitting visualization by a friendly two-dimensional graph. Using detrital signatures of known provenance, CART finds a set of recursive binary partitions approximating the data space by a stepwise constant function. These partitions can be visualised by a tree-like structure with branches splitting off according to a recursive sequence of yes-no questions. Missing data are classified using surrogate variables, which give approximatively the same decision as the primary variable.

5.5 Modern sands from Alpine Axial Belts

Composition of detritus carried by first-order streams draining distinct geological units of axial belts depends both on metamorphic evolution (peak temperature/pressure conditions and subsequent retrogression/re-equilibration) and protolith of source rocks (sedimentary vs. igneous, felsic vs. mafic, continental vs. oceanic; Table 5.1). In this section, we describe contrasting detrital fingerprints of shallow (offscraped anchimetamorphic sediments), intermediate (subcreted low-grade covers and basements), and deep (continental to oceanic eclogites) structural levels of Eocene and Cretaceous continental-subduction zones. Differences in detritus from deeply subducted, subcreted, and accreted/obducted lithospheric sections of continent-ocean transitions are also illustrated.

5.5.1 Offscraped sedimentary covers

Flysch" units shed mainly lithic carbonaticlastic (Parpaillon, Prättigau) to quartzolithic sedimentaclastic detritus (S.Remo, Rheno-Danubian) with microsparite/sparite, shale/slate, and siltite/metasiltite grains (figure 5.6A). Minor quartz and feldspar are recycled from arenaceous intervals. Medium to high-rank metamorphic rock fragments and micas are negligible. Heavy-mineral suites are invariably extremely-poor to poor, reflecting diagenetic depletion in arenaceous source rocks. Ultrastable minerals (zircon, tourmaline, rutile; Parpaillon), epidote, garnet (Rheno-Danubian), amphibole (Prättigau, Vorarlberg), apatite, titanite, anatase/brookite commonly occur. Pyroxene (S.Remo) or Cr-spinel (Simme) may be derived from associated ophiolitic bodies. Chloritoid, staurolite, kyanite, sillimanite are also observed. Sedimentary successions of the Préalpes Médianes shed quartzolithic carbonaticlastic detritus with sparite/microsparite, dolostone, shale/slate/metasandstone, and rare chert grains.

5.5.2 Subcreted covers and continental basements

Detrital signatures of calcschist units are mostly quartzolithic metamorphiclastic (Piedmont zone) to carbonaticlastic (N Graubünden, Engadine window), and compare with those of offscraped turbidites but reflect stronger metamorphism of source rocks.

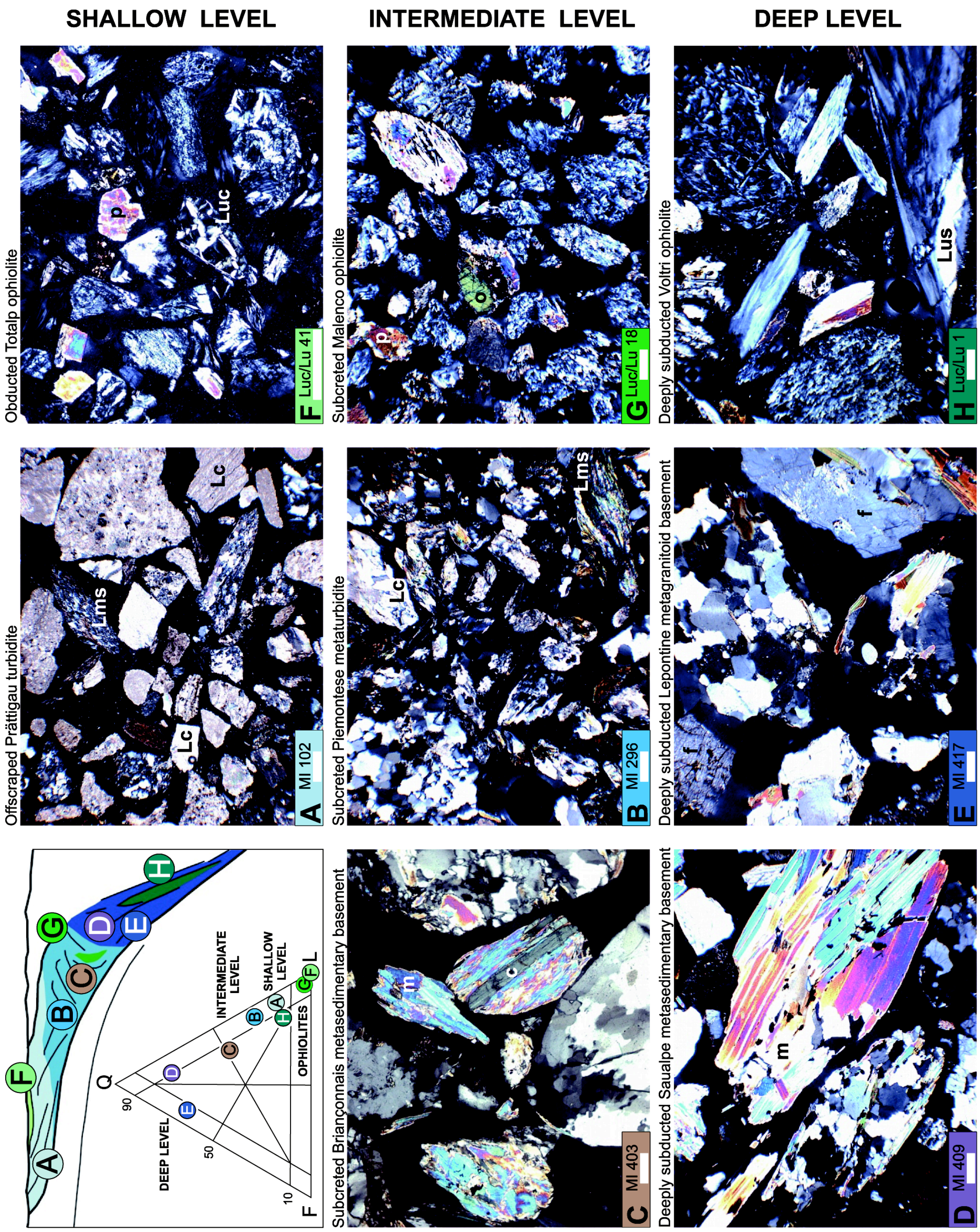

Figure 5.6 *Detrital assemblages from shallow, intermediate, and deep structural levels of Eocene and Cretaceous continental-subduction zones.* ***A****) Lithic sedimentaclastic sand from anchimetamorphic remnant-ocean covers.* ***B****) Quartzolithic metamorphiclastic sand from low-grade metasedimentary covers. Lithoquartzose metamorphiclastic sand from blueschist/greenschist (****C****) and eclogite-facies (****D****) metasedimentary basements.*

E*) Feldspathoquartzose sand from eclogite-facies metagranitoid basements. Lithic ultramaficlastic sand from prehnite-pumpellyite (****F****), epidote-amphibolite (****G****), and eclogite-facies (****H****) mantle rocks of continent-ocean transitions. MI increases and Luc/Lu decreases with deeper structural level of source rocks. Lc= carbonate grain; Lms= metasedimentary grain; Luc= cellular serpentinite grain; Lus= foliated serpentineschist grain; f= feldspar; m= mica; c= chloritoid; p= pyroxene; o= olivine. All photos with cross-polars; white scale bar 250 μm.*

Invariably dominant slate/phyllite/schist and metacarbonate grains (figure 5.6B) display low (Engadine window) to medium (Piedmont zone, N Graubünden, Tauern window) metamorphic rank. Feldspar and white mica are significant. Metabasite (Tauern window) or ultramafic grains (mostly antigorite serpentineschist; Piedmont zone, Engadine window) are locally derived from embedded metaophiolitic bodies or interlayered ophioliticlastic turbidites. Where embedded metaophiolites are rare, very-poor to moderately-poor heavy-mineral suites include epidote and chloritoid associated with ultrastable grains and garnet recycled from arenaceous layers (N Graubünden). Chloritoid is negligible only in the Engadine window. Where embedded metaophiolites are common, moderately-rich but locally up to very-rich heavy-mineral suites are dominated by either epidote-group minerals (Tauern window) or amphiboles (actinolite, barrositic hornblende, glaucophane) with minor relict magmatic clinopyroxene (Piedmont zone). Low-grade Upper Paleozoic to Mesozoic Briançonnais successions of Liguria and the Western Alps supply quartzolithic to feldspathoquartzolithic metasedimentaclastic detritus with phyllite/schist, metasandstone, metacarbonate, metarhyolite grains and negligible micas. Poor to moderately-poor heavy-mineral suites include epidote-group minerals, amphiboles (hornblende, actinolite, glaucophane), ultrastable grains and garnet. Apatite, chloritoid, or pyroxene occur locally.

Low-grade Briançonnais basements supply feldspathoquartzolithic to feldspatholithoquartzose metamorphiclastic detritus including medium- to high-rank schist, quartz-mica, gneiss and subordinate metacarbonate and metabasite grains, and mainly white micas (figure 5.6C). Moderately-rich heavy-mineral suites include epidote-group minerals, amphiboles (actinolite, hornblende, glaucophane) and garnet, with minor chloritoid, titanite, ultrastable grains, and occasionally pyroxene. In the Tauern window, Zentralgneiss units supply lithofeldspathoquartzose high-rank metamorphiclastic detritus, with biotite slightly more abundant than muscovite. Pre-Variscan basements (Altkristallin) supply feldspatholithoquartzose detritus with common metabasite grains, reflecting more mafic protoliths. Moderately-rich to rich (granitoid Zentralgneiss protoliths) and rich to very-rich (more mafic Altkristallin protoliths) epidote-amphibole suites include some garnet and minor titanite and rutile. The Dent Blanche nappe sheds feldspatholithoquartzose medium-high-rank metamorphiclastic detritus with very-rich heavy-mineral suites including garnet, sillimanite, clinopyroxene, brown hornblende and hypersthene derived from relict Permian granulites, and common epidote formed during Eocene greenschist-facies metamorphism.

5.5.3 Deeply subducted continental basements

Metapelites of the Austroalpine domain, representing the eclogite-facies backbone of the Late Cretaceous axial belt, supply feldspatholithoquartzose (Sesia-Lanzo) to lithoquartzose (Koralpe-Saualpe) or even quartzolithic (Pohorje) metamorphiclastic detritus, with abundant high-rank metapelite/paragneiss grains and mainly white micas (figure 5.6D). Dolomitic-marble grains occur locally (Koralpe-Saualpe, Pohorje). Very-rich to extremely-rich heavy-mineral suites are either garnet-dominated (Koralpe-Saualpe) or include abundant hornblende (Pohorje, Texel). Particularly extensive greenschist-facies retrogression is reflected by rich to very-rich epidote-dominated suites from the Sesia-Lanzo unit. Detrital relics of earlier high-pressure conditions include glaucophane (Sesia-Lanzo) or kyanite (Koralpe-Saualpe). Staurolite is locally significant (Texel).

The Internal Massifs, representing the eclogite-facies backbone of the Eocene axial belt, supply mostly feldspatholithoquartzose to lithofeldspathoquartzose high-rank metamorphiclastic detritus, with white mica slightly more abundant than biotite. Moderately-rich (mainly granitoid protoliths; Gran Paradiso) to very-rich (mainly sedimentary protoliths; Dora Maira) epidote-garnet suites include subordinate amphibole. Granitoid gneisses of the Lepontine dome supply feldspathoquartzose detritus with biotite slightly more abundant than muscovite (figure 5.6E). Rich hornblende-dominated suites include garnet, epidote, minor pyroxene, kyanite, staurolite, and sillimanite. Tauern-window rivers draining partly into the Eclogite zone carry feldspatholithoquartzose high-rank metamorphiclastic sands with rich to very-rich epidote-garnet-amphibole suites.

5.5.4 Oceanic basements

Accreted or obducted remnants of the Adriatic continent-ocean transition (Totalp unit; figure 5.6F) and the Chenaillet ophiolite shed lithic ultramaficlastic sands with subequal amounts of antigorite-serpentineschist and lizardite-serpentinite grains, subordinate basaltic, metabasite and carbonate grains, and very rich to extremely rich heavy-mineral suites consisting of clinopyroxene, epidote, opaques, amphiboles, and locally rare Cr-rich spinel. Subcreted remnants of the Adriatic continent-ocean transition (Malenco unit; figure 5.6G) shed lithic ultramaficlastic sand with antigorite-serpentineschist and minor lizardite-serpentinite grains.

Table 5.2. *Bulk petrography and heavy-mineral assemblages of modern sands from Alpine axial belts. N°= number of samples. Q= quartz; F= feldspar; L= aphanitic lithic grains (Lv= volcanic; Lcc= limestone; Lcd= dolostone; Lp= shale/siltstone; Lch= chert; Lms= metasedimentary; Lmv= metavolcanic; Lmf= felsic metamorphic; Lmb= metabasite; Lu= ultramafic); Ms= muscovite; Bt= biotite; HM= heavy minerals (i.e., HMC index). MI= Metamorphic Index. Zrn= zircon; Tur= tourmaline; Rt= rutile; Ttn= titanite; Ap= apatite; TiOx= anatase/brookite; Hbl= hornblende; Act= actinolite; NaA= sodic amphiboles; Cpx= clinopyroxenes; Opx= orthopyroxenes; Ep= epidote-group minerals; Cld= chloritoid; Grt= garnet; St= staurolite; Ky= kyanite; Sil= sillimanite; &tHM= other transparent heavy minerals (e.g., Cr-spinel in Simme Flysch, olivine in Lanzo unit). SRD= Source Rock Density index.*

	N°	**Q**	**F**	**Lv**	**Lcc**	**Lcd**	**Lp**	**Lch**	**Lms**	**Lmv**	**Lmf**	**Lmb**	**Lu**	Ms	Bt	**HM**	total	MI	HMC
SHALLOW LEVEL																			
Flysch units	22	**16**	**4**	**0**	**35**	**3**	**17**	**1**	**21**	**0**	**2**	**0**	**0**	**0**	**0**	**0**	100,0	**88**	**0.2**
		9	*1*	*0*	*12*	*3*	*6*	*1*	*4*	*0*	*1*	*0*	*0*	*0*	*0*	*0*		*12*	*0.4*
Briançonnais covers	1	25	10	0	21	15	5	1	20	1	2	0	0	0	0	0	100,0	135	0.3
Totalp and Chenaillet ophiolites	2	**1**	**1**	**6**	**1**	**2**	**0**	**0**	**0**	**1**	**1**	**1**	**57**	**0**	**0**	**29**	100,0	**92**	**51.7**
		1	*1*	*9*	*1*	*3*	*0*	*0*	*2*	*1*	*1*	*9*	*9*	*0*	*0*	*19*			*39.7*
INTERMEDIATE LEVEL																			
Calcschist units	27	**27**	**4**	**0**	**22**	**2**	**5**	**0**	**6**	**1**	**24**	**1**	**1**	**2**	**1**	**3**	100,0	**280**	**4.1**
		5	*1*	*0*	*9*	*1*	*3*	*0*	*3*	*1*	*8*	*1*	*1*	*1*	*0*	*2*		*46*	*3.9*
Briançonnais covers	9	**33**	**6**	**0**	**7**	**5**	**1**	**0**	**18**	**2**	**24**	**1**	**0**	**0**	**0**	**1**	100,0	**262**	**2.4**
		6	*6*	*1*	*8*	*6*	*1*	*1*	*9*	*1*	*11*	*1*	*0*	*0*	*0*	*1*		*37*	*1.5*
Continental Penninic basements	25	**40**	**16**	**0**	**1**	**0**	**0**	**0**	**1**	**2**	**21**	**3**	**0**	**4**	**5**	**6**	100,0	**380**	**7.9**
		7	*4*	*0*	*1*	*0*	*0*	*0*	*1*	*2*	*11*	*3*	*0*	*1*	*3*	*5*		*14*	*6.6*
Dent Blanche Unit	1	30	24	0	1	0	0	0	0	2	19	5	0	1	4	13	100,0	363	16
Malenco ophiolite	1	0	0	0	0	0	0	0	0	0	0	0	65	0	0	35	100,0	n.d.	57
DEEP LEVEL																			
Sesia-Lanzo Unit	8	**40**	**15**	**0**	**0**	**0**	**0**	**0**	**1**	**3**	**18**	**1**	**0**	**8**	**2**	**11**	100,0	**387**	**15.6**
		6	*5*	*0*	*0*	*0*	*0*	*0*	*1*	*1*	*4*	*2*	*0*	*3*	*1*	*3*		*19*	*4.8*
Texel, Saualpe-Koralpe, Pohorje	15	**38**	**7**	**0**	**0**	**3**	**0**	**0**	**0**	**0**	**16**	**1**	**0**	**10**	**7**	**18**	100,0	**404**	**22.7**
		8	*0*	*0*	*0*	*3*	*0*	*0*	*0*	*0*	*10*	*1*	*0*	*3*	*3*	*3*		*12*	*7.3*
Internal Massifs	8	**49**	**15**	**0**	**0**	**0**	**0**	**0**	**0**	**1**	**14**	**0**	**0**	**8**	**5**	**6**	100,0	**390**	**8.9**
		8	*7*	*0*	*0*	*0*	*0*	*0*	*0*	*1*	*6*	*0*	*0*	*4*	*1*	*3*		*11*	*4.7*
Lepontine Dome	13	**49**	**23**	**0**	**0**	**0**	**0**	**0**	**0**	**1**	**3**	**1**	**0**	**7**	**8**	**8**	100,0	**436**	**9.4**
		7	7	0	0	0	0	0	0	1	5	1	0	3	4	4		*31*	*3.9*
Voltri-Zermatt metaophiolites	9	**8**	**10**	**0**	**1**	**1**	**0**	**0**	**0**	**2**	**6**	**6**	**29**	**1**	**0**	**35**	100,0	**350**	**34.4**
		3	*6*	*0*	*1*	*0*	*0*	*0*	*1*	*2*	*5*	*6*	*8*	*1*	*0*	*19*		*15*	*17.1*

	Zrn	Tur	Rt	Ttn	Ap	TiOx	Hbl	Act	Na A	Cpx	Opx	Ep	Cld	Grt	St	Ky	Sil	&tHM	total
SHALLOW LEVEL																			
Flysch units	**11**	**17**	**7**	**1**	**6**	**5**	**13**	**1**	**0**	**2**	**1**	**16**	**0**	**15**	**1**	**1**	**0**	**2**	###
	11	*9*	*3*	*1*	*8*	*10*	*8*	*1*	*0*	*3*	*1*	*5*	*0*	*16*	*2*	*1*	*0*	*4*	
Briançonnais covers	9	15	6	0	13	12	4	1	0	0	0	39	1	1	0	0	1	0	###
Totalp and Chenaillet ophiolites	**0**	**0**	**0**	**1**	**1**	**0**	**10**	**7**	**0**	**45**	**0**	**35**	**0**	**0**	**0**	**0**	**0**	**0**	###
	0	*0*	*0*	*0*	*2*	*0*	*14*	*3*	*0*	*17*	*0*	*2*	*0*	*0*	*0*	*0*	*0*	*0*	
INTERMEDIATE LEVEL																			
Calcschist units	**1**	**9**	**3**	**2**	**1**	**1**	**19**	**7**	**2**	**2**	**0**	**40**	**7**	**5**	**0**	**0**	**0**	**0**	###
	1	*9*	*3*	*1*	*1*	*1*	*16*	*7*	*3*	*2*	*0*	*15*	*6*	*3*	*0*	*0*	*0*	*1*	
Briançonnais covers	**8**	**3**	**1**	**1**	**1**	**2**	**16**	**2**	**4**	**2**	**1**	**50**	**1**	**5**	**0**	**0**	**1**	**1**	###
	7	*3*	*2*	*1*	*2*	*3*	*11*	*2*	*8*	*2*	*1*	*15*	*1*	*8*	*1*	*1*	*1*	*1*	
Continental Penninic basements	**1**	**0**	**2**	**3**	**0**	**0**	**29**	**5**	**1**	**0**	**0**	**43**	**4**	**11**	**0**	**0**	**0**	**0**	###
	1	*1*	*1*	*2*	*0*	*0*	*15*	*2*	*2*	*1*	*1*	*12*	*7*	*11*	*0*	*0*	*0*	*0*	
Dent Blanche Unit	0	0	1	1	0	0	11	1	0	8	6	23	0	41	0	0	7	0	###
Malenco ophiolite	0	0	0	5	0	0	3	0	0	52	8	25	0	7	0	0	0	0	###
DEEP LEVEL																			
Sesia-Lanzo Unit	**0**	**0**	**1**	**3**	**0**	**0**	**8**	**4**	**3**	**1**	**0**	**58**	**0**	**21**	**0**	**0**	**0**	**0**	###
	1	*0*	*1*	*1*	*0*	*0*	*6*	*2*	*4*	*1*	*0*	*12*	*1*	*7*	*0*	*0*	*0*	*0*	
Texel, Saualpe-Koralpe, Pohorje	**0**	**1**	**2**	**3**	**0**	**1**	**30**	**5**	**0**	**1**	**0**	**16**	**0**	**38**	**2**	**1**	**0**	**0**	###
	0	*1*	*0*	*2*	*0*	*0*	*14*	*4*	*0*	*1*	*0*	*7*	*0*	*24*	*3*	*2*	*0*	*0*	
Internal Massifs	**1**	**1**	**2**	**2**	**0**	**0**	**5**	**2**	**1**	**1**	**0**	**40**	**3**	**42**	**0**	**1**	**0**	**0**	###
	1	*0*	*1*	*1*	*0*	*0*	*3*	*1*	*1*	*1*	*0*	*24*	*1*	*27*	*0*	*2*	*0*	*0*	
Lepontine Dome	**1**	**0**	**1**	**1**	**0**	**0**	**49**	**4**	**0**	**3**	**1**	**17**	**0**	**19**	**1**	**1**	**1**	**1**	###
	1	*1*	*1*	*1*	*0*	*0*	*15*	*3*	*1*	*1*	*1*	*12*	*0*	*10*	*1*	*1*	*1*	*1*	
Voltri-Zermatt metaophiolites	**0**	**0**	**0**	**1**	**0**	**0**	**11**	**14**	**1**	**10**	**13**	**46**	**0**	**1**	**0**	**0**	**0**	**2**	###
	0	*0*	*1*	*0*	*0*	*0*	*7*	*12*	*1*	*13*	*25*	*25*	*1*	*2*	*0*	*1*	*0*	*2*	

The extremely-rich heavy-mineral suite consists of opaques, diopsidic clinopyroxene, epidote-group minerals, orthopyroxene, garnet (grossular, andradite), titanite, and vesuvianite.

Eclogitic remnants of the European continent-ocean transition subducted in the Eocene (Voltri, Monviso, Zermatt-Saas units; figure 5.6H) shed lithic to feldspatholithic/ feldspathoquartzolithic ultramaficlastic detritus with exclusive antigorite-serpentineschist grains. Metabasite and plagioclase grains derived from crustal protoliths are subordinate. Locally associated metasedimentary covers supply quartz, quartz-mica, and carbonate grains. Extremely-rich heavy-mineral suites include epidote, zoisite, actinolite and barroisitic hornblende, reflecting widespread greenschist-facies retrogression. Glaucophane may document relict high-pressure parageneses. Lanzo lherzolites shed heavy-mineral-dominated sand with an enstatite-clinopyroxene suite including epidote-group minerals and olivine.

5.6 Axial Belt Provenance revisited

5.6.1 Detrital fingerprints of Axial Belt detritus

Petrography and mineralogy of axial-belt detritus vary markedly and consistently with metamorphic grade and structural level within the fossil continental-subduction zone.

Lithic to quartzolithic sedimentaclastic sands yielding very-poor suites with ultrastable minerals characterize continental-margin to remnant-ocean sedimentary source-rocks offscraped at shallow levels. Quartzolithic sands with low to medium-rank metacarbonate, metapelite and metapsammite grains, yielding poor to moderately-rich epidote-amphibole suites with chloritoid and ultrastable minerals, characterize metasedimentary source-rocks subcreted at intermediate levels. Polymetamorphic basements of the intermediate structural level shed feldspathoquartzolithic to feldspatholithoquartzose medium-rank to high-rank metamorphiclastic detritus including moderately-rich to rich epidote-amphibole-garnet suites. pressure/temperature conditions met during tectonic exhumation of source rocks (amphibolite-facies re-equilibration versus greenschist-facies retrogression). Eclogitic metaophiolites supply lithic to feldspathoquartzolithic detritus with abundant antigorite-serpentineschist grains and extremely-rich epidote-amphibole-pyroxene suites, reflecting widespread greenschist-facies retrogression.

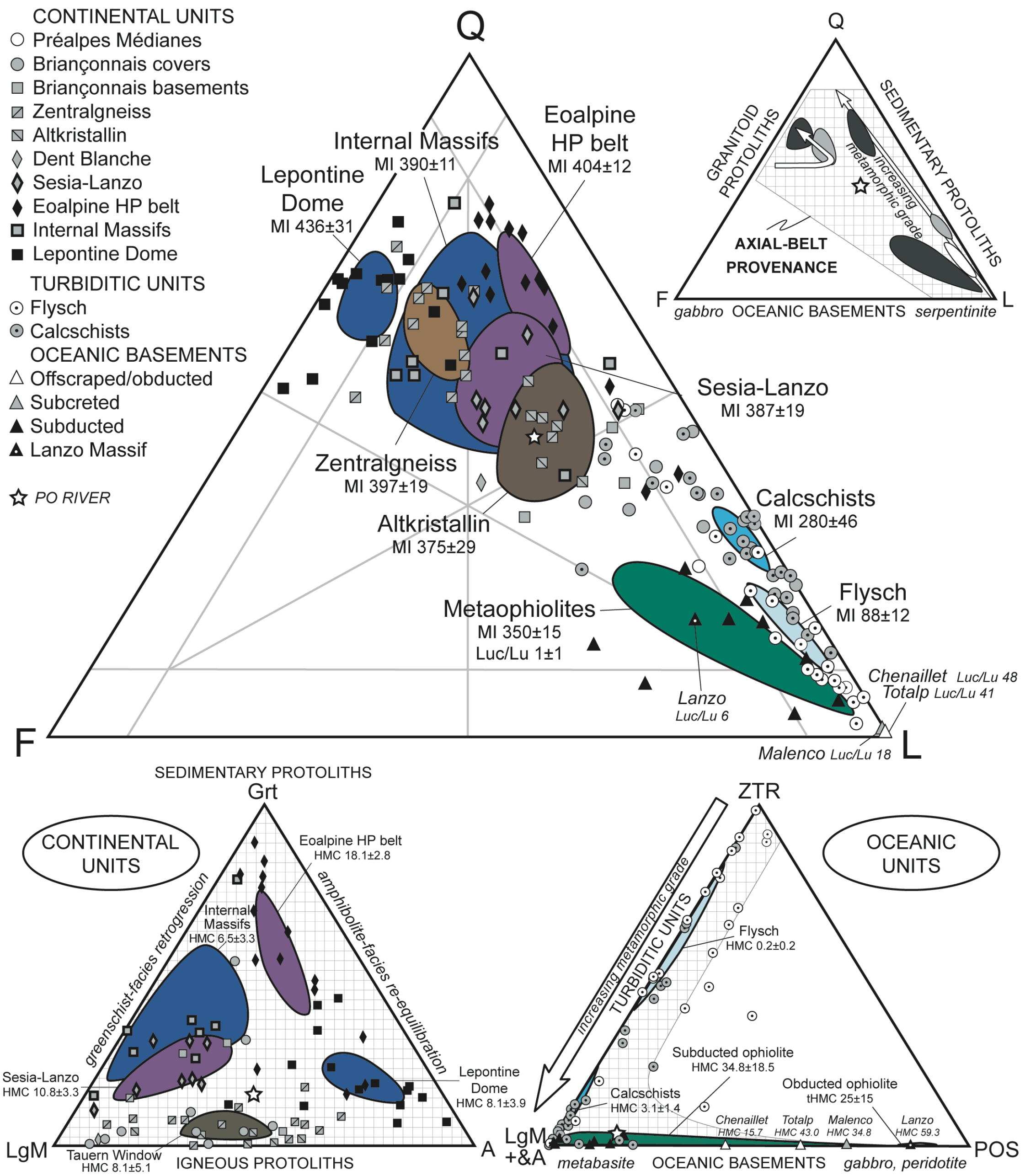

Figure 5.7. *Fingerprints of Axial Belt Provenance. Detrital modes depend on protolith type, structural level, and thermal gradients during exhumation (greenschist-facies retrogression versus amphibolite-facies re-equilibration). Arrows indicate increasing* metamorphic grade. *Note that Axial-Belt field roughly corresponds to "Recycled Orogen" field of Dickinson (1985). Obducted-ophiolite field after Garzanti et al. (2000; 2002). Open symbols, light-grey symbols, and full symbols for shallow-level, intermediate-level, and deep-level units, respectively; grey symbols with thick black outline for retrogressed deep-level units. All fields are 90% confidence regions about the mean. The lithic pole L includes carbonate grains; POS= pyroxene, minor olivine and spinel; other parameters as in table. 5.1.*

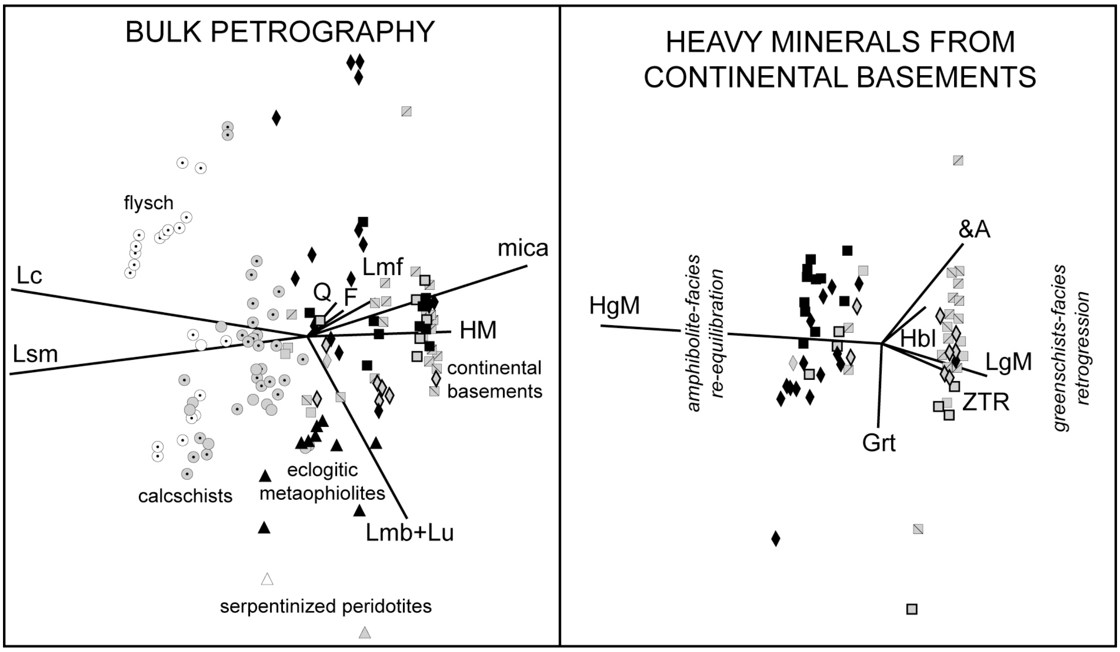

Figure 5.8. *Axial Belt subprovenances discriminated with compositional biplots.* ***Left panel****: Shallow-level turbidite and intermediate-level metaturbidite are distinguished from continental-basement and oceanic-basement sources.* ***Right panel****: Heavy-mineral data allow further discrimination bewteen retrogressed greenschist-facies and re-equilibrated amphibolite-facies continental basements.*
The first and second principal components account for 65% and 11% (left panel) and for 69% and 15% (right panel) of total variance. Symbols as in Fig. 5.6. Lc= carbonate grains; Lsm= other sedimentary and metasedimentary grains. ZTR= zircon, tourmaline, rutile; A= amphiboles (Hbl= hornblende; &A= actinolite, glaucophane); Grt= garnet; LgM= epidote, chloritoid, minor prehnite, pumpellyite, lawsonite, carpholite; HgM= staurolite, andalusite, kyanite, sillimanite; other parameters as in Table 5.2.

Heavy-mineral-dominated sand with enstatite, clinopyroxene and some olivine is produced from preserved lherzolite. Subcreted and accreted or obducted lithospheric sections of continent-ocean transitions shed lithic ultramaficlastic sands with both lizardite-serpentinite and antigorite-serpentineschist grains, yielding extremely-rich clinopyroxene-opaque suites with epidote-group minerals, orthopyroxene or actinolite. Cr-rich spinel was detected only locally (Totalp sand), confirming that its relative abundance in ophiolite and metaophiolite detritus is invariably negligible, and less than in sand recycled from remnant-ocean turbidites (Garzanti and Andò 2007b).

5.6.2 Rock fragment textures and structural level

Determination of the MI (Garzanti and Vezzoli 2003) is an empirical but effective way to assess petrographically the average metamorphic grade of source rocks (Garzanti et al. 2006). In this study, the MI proved to be the most efficient petrologic parameter, sufficient by itself to statistically discriminate the structural level of axial-belt sources (Figure 5.9).

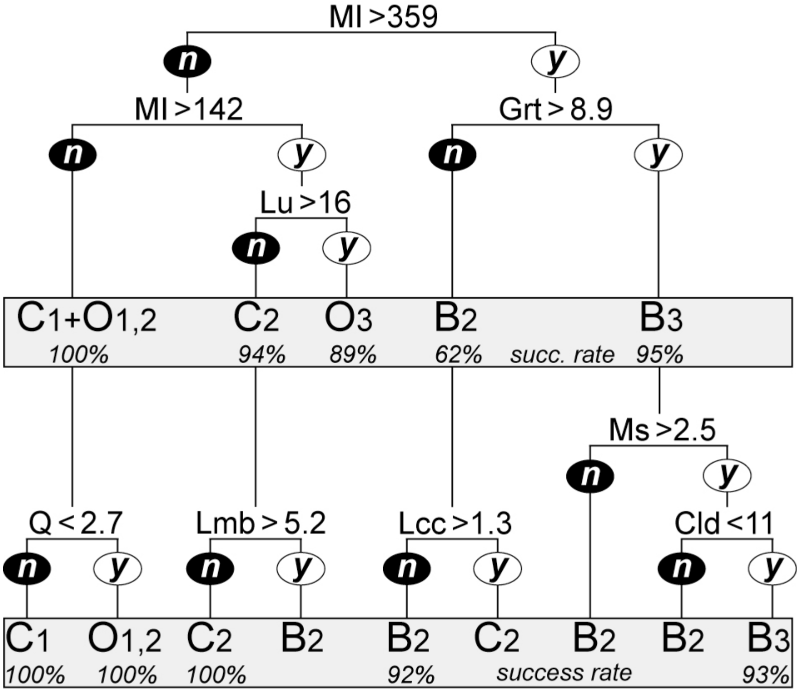

Figure 5.9. *Axial Belt subprovenances discriminated with decision trees. Accreted cover (C1), subcreted cover (C2), subcreted basement (B2), eclogitic continental basement (B3), and eclogitic ophiolite (O3) detrital sources are effectively distinguished with three parameters only. Because of exclusive* ultramafic rock fragments, detritus from accreted ophiolite (O1) and subcreted ophiolite (O2) fails the MI test and is lumped together with detritus from accreted covers (upper part of the diagram). More sophisticated discrimination can be obtained by adding branch levels (lower part of the diagram), with further increase of success rate (percentages of successful discrimination are given). Parameters as in Table 5.2.

Boundaries between very-low rank detritus from shallow-level anchimetamorphic sediments, medium-rank detritus from intermediate-level low-grade metasediments, and high-rank detritus from deep-level continental eclogites are set objectively by decision-tree analysis at MI ~150 and MI ~350.

In detail, the MI is typically ≤100 for offscraped remnant-ocean turbidites or Briançonnais continental-margin successions, ranges from ~200 (Engadine window) to ~300 for subcreted calcschists (Piedmont zone, N Graubünden, Tauern window), and reaches ~375 for subcreted Briançonnais and Altkristallin basements.

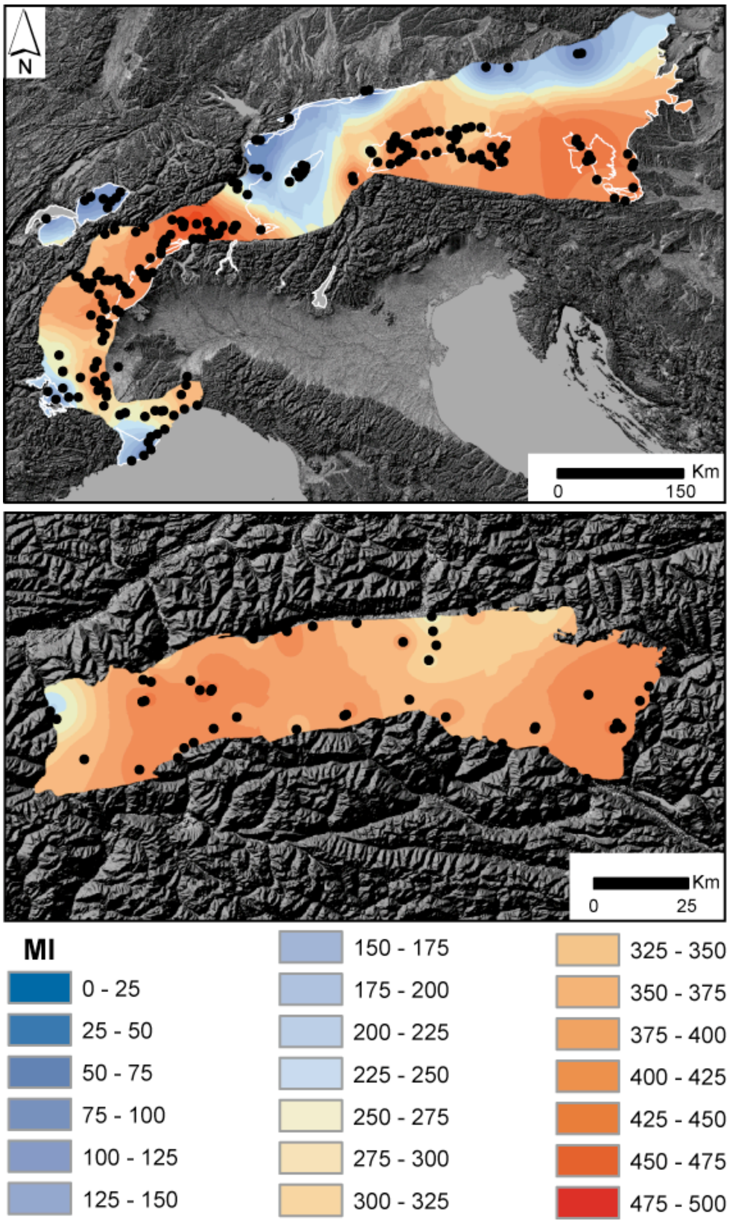

Figure 5.10. *Inverse weighted distance of MI values from samples from the Cretaceous and Eocene axial belts (upper panel) and Tauern window (lower panel)*

MI ~400 characterizes detritus from continental eclogites of both Eocene and Cretaceous axial belts, and from the Zentralgneiss. Significantly higher MI characterizes units affected by late-stage amphibolite-facies re-equilibration, largely adjacent to Periadriatic intrusions north of the Insubric Fault. MI as high as 480-490 is reached for upper-amphibolite-facies source rocks in the southeastern part of the Lepontine dome. Within the Tauern-window, the MI reaches ~430 at the core of the Hochalm and Zillertal gneiss domes.

The MI can be obtained from metapelite, metapsammite/metafelsite, metacarbonate and metabasite, but not from ultramafic rock fragments. In order to assess structural level of ultramafic source rocks, we can use instead the Luc/Lu ratio, expressing the abundance of cellular serpentinite on total serpentinite grains. Comprehensive studies of Tethyan ophiolites from the Alps to the Himalaya showed that eclogitic metaophiolites shed detritus dominated by foliated serpentineschist grains (Luc/Lu <10), whereas accreted or obducted ophiolites shed detritus with abundant cellular serpentinite grains (Luc/Lu ≥40; Garzanti et al. 2000; 2002). This petrographic index is confirmed here to discriminate detritus from eclogitic metaophiolites (Luc/Lu 1±1; Luc/Lu 6 for Lanzo), from Malenco metaophiolite subcreted under epidote-amphibolite-facies conditions (Luc/Lu 18), and from offscraped/obducted Chenaillet and Totalp ophiolites (Luc/Lu 45±5). Detritus from serpentinite bodies embedded in subcreted Piemontese and Engadine calcschists yielded Luc/Lu≤11 and Luc/Lu 14±3, respectively.

5.6.3 Heavy-mineral concentration and structural level

In the over 4 Ga-long geological evolution of the Earth, gravity has progressively and efficiently segregated less dense rocks towards the surface. Even within the continental crust, an heterogeneous rock stack assembled through several orogenic cycles (Taylor and McLennan 1985), a general subdivision in superposed tectonostratigraphic layers with upward decreasing density can be ideally envisaged (Handy 1990). These include lower crustal granulites (δ ~3.0 g/cm^3), mid-crustal kinzigites (δ ~2.85 g/cm^3), and upper crustal gneisses, schists and granitoids (δ ~2.7 g/cm^3).

The abundance of heavy minerals in a particular source rock is a function of its density. Denser rocks equilibrated at greater depths and higher-pressure conditions contain, and thus shed, more heavy minerals than less dense shallower-level rocks. In the absence of hydrodynamic size-density sorting (which can markedly enhance heavy-mineral concentration during deposition; Garzanti et al. 2009) and of diagenetic dissolution (which can drastically reduce heavy-mineral concentration in ancient sediments; Garzanti and Andò 2007a), the average density of source rocks is faithfully mirrored by HMC, tHMC and SRD indices. All indices steadily increase with crustal depth. In detritus eroded from an ideal vertical section of continental crust, HMC and tHMC increase by an order of magnitude from slate-derived to schist- or gneiss-derived sand, and by another order of magnitude in kinzigite- and granulite-derived sand (Garzanti et al. 2006).

For fossil continental-subduction zones, HMC and tHMC are similarly observed to increase by an order of magnitude (figures 5.11 and 5.12) from detritus shed by offscraped anchimetamorphic sequences to detritus shed by subcreted metasediments, and by another order of magnitude in detritus shed by continental or strongly serpentinized oceanic eclogites.

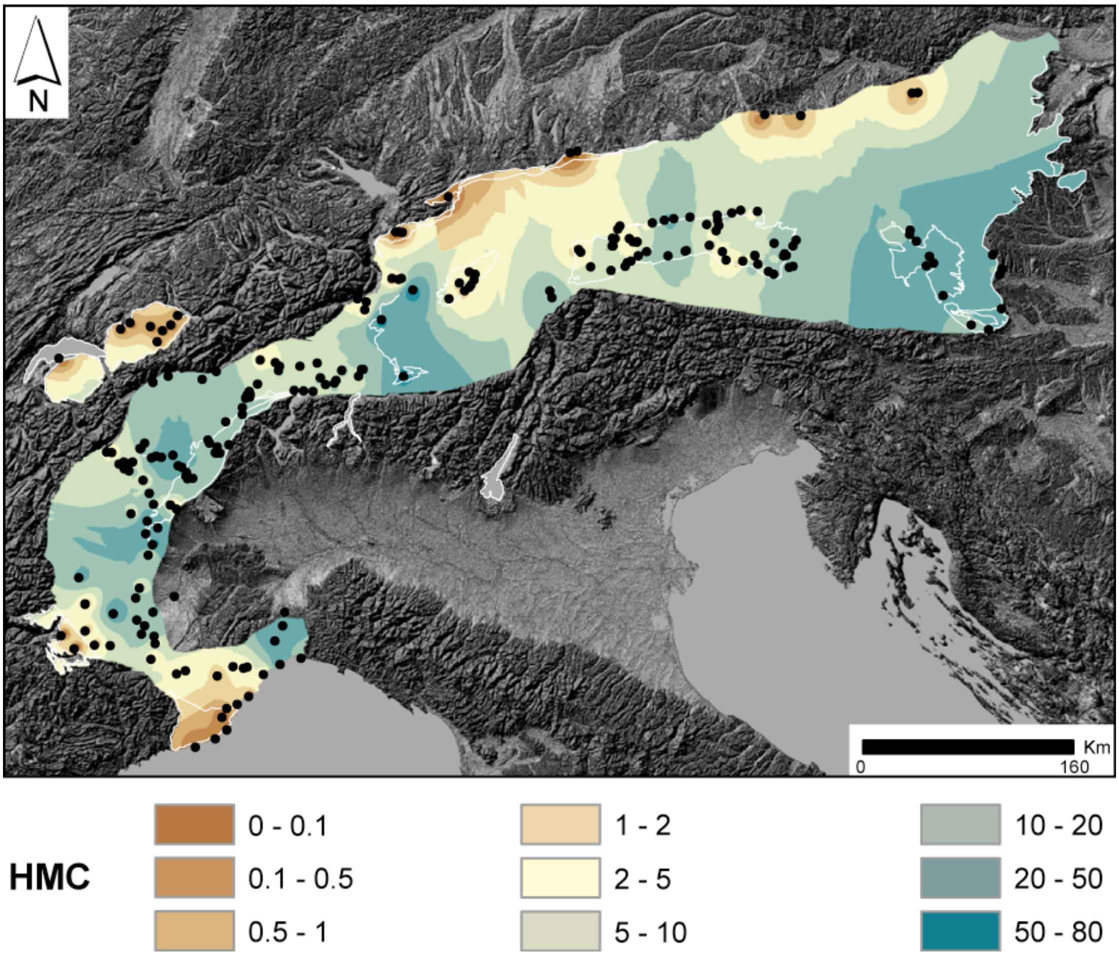

Figure 5.11. *Inverse weighted distance of HMC values calculated from samples of the Cretaceous and Eocene axial belts.)*

Significant variability, however, is associated with lithology (denser mafic and ultramafic rocks contain, and therefore supply, more heavy minerals than felsic rocks), pervasive retrogression or re-equilibration during exhumation, and degree of serpentinization. Density anomalies in source rocks are readily highlighted by SRD values. Within the shallow structural level, SRD <2.7 characterizes detritus from offscraped sedimentary sequences (unless dolostone is locally dominant), but SRD reaches as high as 3.2 in detritus from unmetamorphosed peridotite (Totalp unit). Within the intermediate structural level, SRD typically ranges from 2.7 to 2.75, but reaches 2.8 in detritus from more mafic basement rocks (Altkristallin), and as high as 3.2 in detritus from the Malenco serpentinized peridotite. Within the deep structural level, SRD ranges from 2.7 (Gran Paradiso) to 2.8 (Dora Maira) for Eocene continental eclogites, and from 2.8 (Sesia-Lanzo) to 3.0 (Koralpe-Saualpe) for Cretaceous continental eclogites. Lower values are observed for largely metagranitoid (Gran Paradiso) and pervasively retrogressed (Sesia-Lanzo) source rocks; higher values characterize denser metapelitic source rocks (Koralpe-Saualpe). With increasing pressure deeper and deeper in the subduction zone, rock density increases in fact much less for quartzofeldspathic granitic bodies than for metapelites, where garnet-kyanite parageneses develop. In detritus from eclogitic metaophiolites, SRD ranges from 2.9 in case of pervasive serpentinization (Voltri), to 3.1 where peridotite is largely preserved (Lanzo).

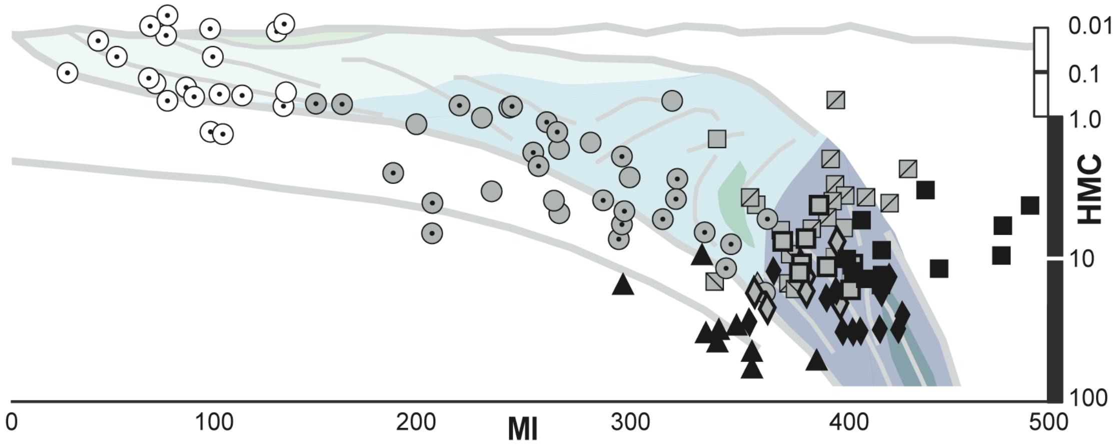

__Figure 5.12.__ Petrologic indices of detritus from fossil continental-subduction zones. Structural level and metamorphic grade of axial-belt sources can be inferred by Metamorphic Index MI and Heavy-Mineral Concentration index HMC. Denser rocks produced deeper in the subduction zone contain, and thus shed, more heavy minerals. Instead, the MI largely reflects thermal gradients during exhumation (greenschist-facies retrogression versus amphibolite-facies re-equilibration). Symbols as in Fig. 5.7. Change of scale in the ordinate for graphic reasons only.

Simple indices as HMC, tHMC and SRD do not only represent indicators of structural level, but are particularly sensitive and thus useful by themselves to reveal occurrence of ultradense rocks in source areas (Garzanti and Andò 2007a). If hydraulic concentration can be excluded (e.g., when replicate samples are collected at different times, sites, and hydraulic conditions), then high HMC, tHMC, and SRD indices may reveal occurrence of ultradense eclogitic sources even where eclogitic parageneses are preserved only within small volumes of total rock mass. An example is provided by rivers Tauernbach and Frossnitzbach draining the southern flank of the Tauern window where the Eclogite zone is exposed, which carry garnet-rich sands with HMC and tHMC values that are twice the average value for either Bündnerschiefer or Zentralgneiss units.

5.6.4 Hornblende colour and peak temperatures

The HCI is a useful empirical statistical indicator in provenance studies. In hornblende-rich sands derived from the Lepontine dome, the HCI is observed to correlate well with peak metamorphic temperatures reached by source rocks during Barrovian re-equilibration (Garzanti et al. 2004a).

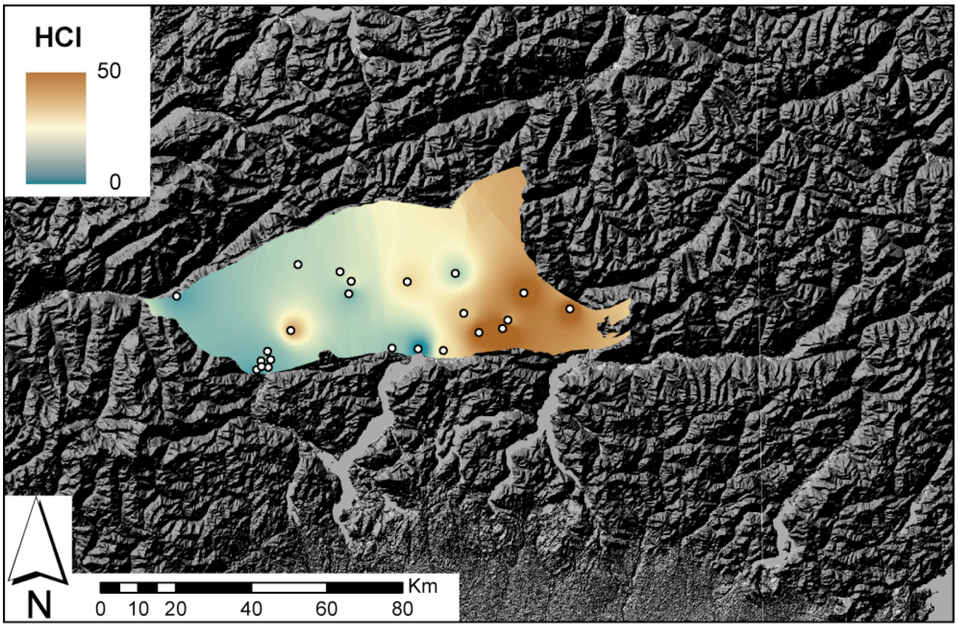

Figure 5.13. *Inverse weighted distance of HCI values from samples from the Lepontine Dome*

Dominant blue-green hornblende in rivers draining rocks below the 600°C isograd at the periphery of the Lepontine dome (HCI <10) is progressively replaced by green hornblende in rivers draining rocks above the 600°C isograd (HCI 10-20), by green-brown hornblende in rivers draining rocks above the 625°C isograd (HCI 20-30), and by brown hornblende in rivers draining sillimanite-bearing rocks above the 650°C isograd (HCI 30-50). Highest values are reached in detritus from granulites exposed at the southeastern tip of the dome (HCI 52; Gruf Complex).

The Lepontine dome is the only region within Alpine axial belts that has undergone such high-temperature re-equilibration during late orogenic stages (Todd and Engi 1997). In the Tauern window, widespread overprint not exceeding lower amphibolite-facies (~575°C) is indicated by invariably dominant blue-green hornblende in detritus from Zentralgneiss and Altkristallin units (HCI ≤ 10). The HCI is invariably ≤ 15 in detritus from eclogitic continental basements of both Cretaceous (Pohorje, Koralpe-Saualpe, Texel) and Eocene axial belts (Internal Massifs). Similar values characterize detritus from Briançonnais basements of the intermediate structural level, whereas higher HCI characterizes detritus from relict high-grade Paleozoic rocks in Austroalpine units of the Western Alps (HCI ≤ 28 for Sesia-Lanzo, HCI 57 for Dent Blanche).

5.6.5 Matryoshka orogens and the discrimination of neometamorphic versus paleometamorphic detritus

Orogenic belts contain abundant polymetamorphic rocks, the legacy of past orogenic cycles. Beside the Austroalpine Cretaceous and Penninic Eocene axial belts, the Alps also comprise a Variscan Carboniferous axial belt, and an even older fossil continental-subduction zone including Ordovician eclogite (Gebauer 1993). Deformed remnants of the Ordovician belt are found in the Variscan belt; Variscan units were partly involved in both Cretaceous and Eocene continental-subduction zones; and western Austroalpine units (Sesia-Lanzo, Dent Blanche) were involved in the Eocene continental-subduction zone. Such nested orogenic roots of successive ages now display roughly subparallel E-W trend. The Cretaceous axial belt is exposed south of, and structurally above the Eocene axial belt, and the Variscan axial belt is still well preserved in the Southalpine domain farther south at an even higher structural position. The Alps can thus be considered as formed by a series of fossil continental-subduction zones, each of which originally developed beneath an older fossil continental-subduction zone, subsequently accreted to the upper plate, and finally exhumed.

In the Southern Alps, thermally affected more by Early Permian and Late Triassic rift events than by Late Cretaceous to Tertiary fold-thrust deformation, the original structure of the Variscan orogen can be followed from lower-crustal Ivrea-Verbano granulites in the west, to mid-crustal amphibolite-facies Serie dei Laghi metasediments, to upper-crustal greenschist-facies basements of the Dolomites, and finally to epimetamorphic and anchimetamorphic offscraped turbidites of the Paleocarnic Range in the east (Vai et al. 1984; Garzanti et al. 2006). The compositional signatures of metamorphiclastic detritus from the Variscan axial belt are varied, and overlap those of younger axial belts. Therefore, petrographic and mineralogical methods can hardly discriminate detritus from Eocene, Cretaceous or Variscan axial belts found mixed in major Alpine rivers (e.g., Po, Adige, Drava). Detrital-geochronology techniques are required for this task (von Eynatten et al. 1996; DeCelles et al. 2005).

Although unable to identify paleometamorphic versus neometamorphic detrital grains, petrographic techniques can still help discriminate detritus from axial-belt and external-belt sources at a larger sampling scale (Ingersoll 1990). Because continental collision is followed by focused rapid erosion, Cretaceous and Eocene Alpine axial belts have long been stripped of their shallow-level covers, now preserved only along the orogen's front. The Variscan axial belt, instead, is still largely buried beneath thick sediments deposited during subsequent Permo-Mesozoic rift-drift evolution. As a consequence, major Southalpine rivers today carry lithic to feldspathoquartzolithic sedimentaclastic sands (undissected to undissected/transitional Continental Block subprovenances), which are markedly different from feldspatholithoquartzose/lithofeldspathoquartzose detritus carried by Alpine rivers draining the axial belt (Axial Belt Provenance; Garzanti et al. 2007).

5.7 Conclusions

Collision orogens such as the Alps or the Himalayas, generated by convergence and attempted subduction of thinned continental margins, are the most prominent product of plate tectonics, shedding huge volumes of detritus to associated sedimentary basins. The Alps, perhaps the best studied mountain chain of all, can be conceived as a nested set of subparallel belts, each representing a zone of continental subduction eventually aborted and exhumed: the Ordovician, Carboniferous, Cretaceous, and Eocene axial belts. Focusing on the Cretaceous and Eocene continental-subduction zones, representing the backbone of the modern orogen, we ideally distinguish three structural levels, and investigate the detrital fingerprints of each. The shallow level, chiefly consisting of offscraped remnant-ocean turbidites and unmetamorphosed continental-margin sediments, supplies lithic to quartzolithic sedimentaclastic sands yielding very-poor heavy-mineral suites including ultrastable minerals. The intermediate level, consisting of subcreted low-grade metasedimentary covers and polymetamorphic basements, supplies quartzolithic to feldspatholithoquartzose medium-rank metamorphiclastic sands yielding moderately-rich epidote-amphibole suites with chloritoid or garnet. The deep level, consisting of eclogitic remnants of continent-ocean transitions, supplies feldspatholithoquartzose/ feldspathoquartzose high-rank metamorphiclastic or lithic ultramaficlastic sands yielding rich to extremely-rich suites dominated by garnet, hornblende, or epidote depending on protolith (sedimentary vs. igneous, continental vs. oceanic) and pressure/temperature conditions met during exhumation (amphibolite-facies re-equilibration versus greenschist-facies retrogression).

Axial-belt provenance can be identified and structural level deduced by the use of appropriate compositional parameters, although complementary detrital-geochronology techniques are indispensable to distinguish neometamorphic and paleometamorphic detritus. In the absence of hydraulic-sorting effects, the Heavy Mineral Concentration index (HMC) directly mirrors source-rock density, and thus reveals the occurrence of ultradense lithologies (continental eclogite, obducted or subducted ophiolite) in catchment areas. The Metamorphic Index (MI), based on texture and mineralogy of sedimentary/metasedimentary and igneous/metaigneous rock fragments, coupled with the Hornblende Colour Index (HCI), provide accurate information on metamorphic grade of source rocks. In modern sands derived from thermal domes, the MI and HCI faithfully mirror isograd patterns, documenting lower-amphibolite-facies conditions at ~600°C within the Tauern window but up to granulite facies at the southeastern tip of the Lepontine dome. HMC thus retains memory of the baric peak reached at depth within the subduction throat, whereas the MI and HCI chiefly reveal the thermal peak reached at later stages, when subduction is throttled by the arrival of thicker continental crust and geothermal gradients rapidly increase. In the case of ophiolite and metaophiolite source rocks, structural level can be inferred from relative abundance of cellular lizardite-serpentinite versus foliated antigorite-serpentineschist rock fragments (Luc/Lu ratio).

The detailed knowledge acquired in the investigation of modern Alpine detritus can be applied, expanded, and refined by similar provenance studies on other mountain belts produced by attempted continental subduction (collision orogens). Guided by the experience gained from modern sediments, and armed with suitable petrographic and geochronological tools, we may eventually become able to unravel the innumerable pieces of information stored in the sedimentary record, and to reconstruct orogenic events of the past with unsuspected accuracy and precision.

PART 2

DETRITAL FISSION-TRACK ANALYSIS IN PROVENANCE STUDIES:

determining long- and short term erosion rates

6 Fission-track analysis

6.1 Fission tracks formation

Fission tracks are damage features produced by charged nuclear particles that travel through insulating solids. The most widely accepted model for fission tracks formation is the ion spike explosion model (Fleischer et al., 1975; figure 6.1). Although it is able to explain why tracks only form within insulators and not in conductors, this model fails to consider the possibility of discontinuities in the track structures, and it has to be considered only a first approximation of the real track-forming process (Gallagher et al., 1998 and reference therein).

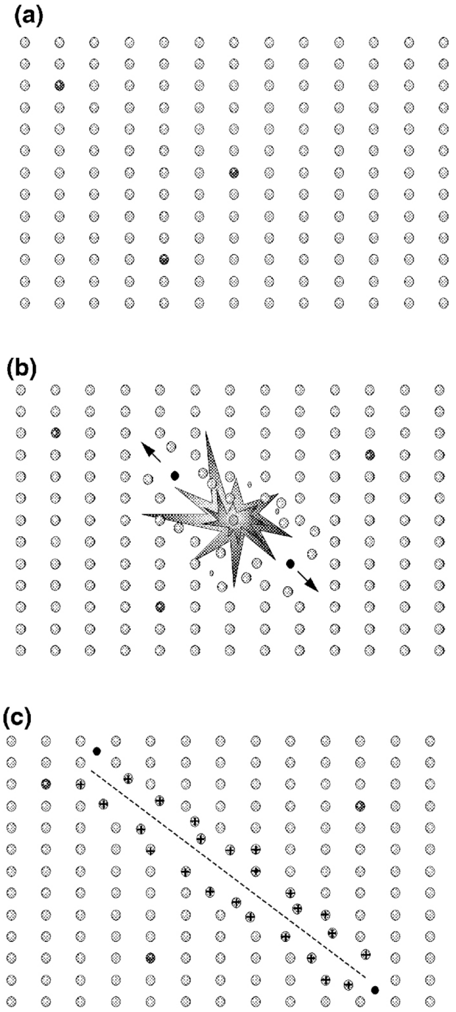

Figure 6.1. *Cartoon representation of the "ion-spike explosion" model and the formation of fission-tracks in a mineral. (Gallagher et al., 1998)*

a) trace amounts of ^{238}U *are present in the crystal lattice (dark circles);*

b) ^{238}U *nuclei are unstable and experience spontaneous fission which produces two highly charged particles. The charged particles recoil due to Coulomb repulsion and interact with other atoms in the lattice;*

c) the fission-produced particles slow down and stop, leaving a trail of disrupted crystal lattice, or a fission-track.

Natural tracks in geological samples are produced nearly exclusively by the spontaneous fission of ^{238}U, as the fission half-lives of all other naturally occurring heavy isotopes such as ^{235}U and ^{232}Th are too long to produce a significant number of tracks.

Table 6.1. *Half life and decay constant of Th and U isotopes*

Isotope	**Abundance**	**Half-Life**	**Decay Constant**	**Thermal Neutron Capture Cross Section**
	(%)	(yr)	(yr^{-1})	(10^{-24} cm^2)
^{232}Th	100.0000	1.41×10^{10} (α)	4.916×10^{-11}	7.4
^{234}U	0.0056	2.47×10^{5} (α)	2.806×10^{-6}	100
^{235}U	0.7200	0.7038×10^{9} (α)	9.8485×10^{-10}	580
^{238}U	99.2743	4.468×10^{9} (α) 1.3×10^{16} (s.f.)	1.55125×10^{-10} 7.5×10^{-17}	2.7

α indicate alpha-decay; s.f. spontaneous fission

data after Lederer et al., 1967; Steiger and Jäger, 1977; Friedlander et al., 1981

For such reasons, fission-track analyses are applied only to minerals that contain enough ^{238}U to produce a detectable number of fission events. On the other hand too high concentrations of ^{238}U can result in so much fission induced that is hard if not impossible to distinguish individual tracks. The appropriate range of concentration for accumulation over geological times can be estimated between 1 and 1000 ppm. Fortunately such a concentration is typical of some relatively common minerals such as apatite ($Ca_5(PO_4)_3(F,Cl,OH)$), zircon ($ZrSiO_4$), and sphene ($CaTiO(SiO_4)$).

Natural uranium is composed of three isotopes ^{234}U, ^{235}U, and ^{238}U. ^{238}U experiences nuclear decay by two different processes: α-decay and spontaneous fission.

A-decay (emission of a ^{4}He nucleus) is by far the dominant process, and it is composed of a complex sequence of individual α-particle emitting nuclear reactions that leads to the formation of a stable ^{206}Pb nucleus.

Spontaneous fission of the ^{238}U nucleus forces the unstable nucleus to split into two fragment nuclei and 2 or 3 high-energy neutrons (Friedlander et al., 1981).

On average, every two million ^{238}U nuclei that undergo α-decay, only a single ^{238}U nucleus will experience spontaneous fission.

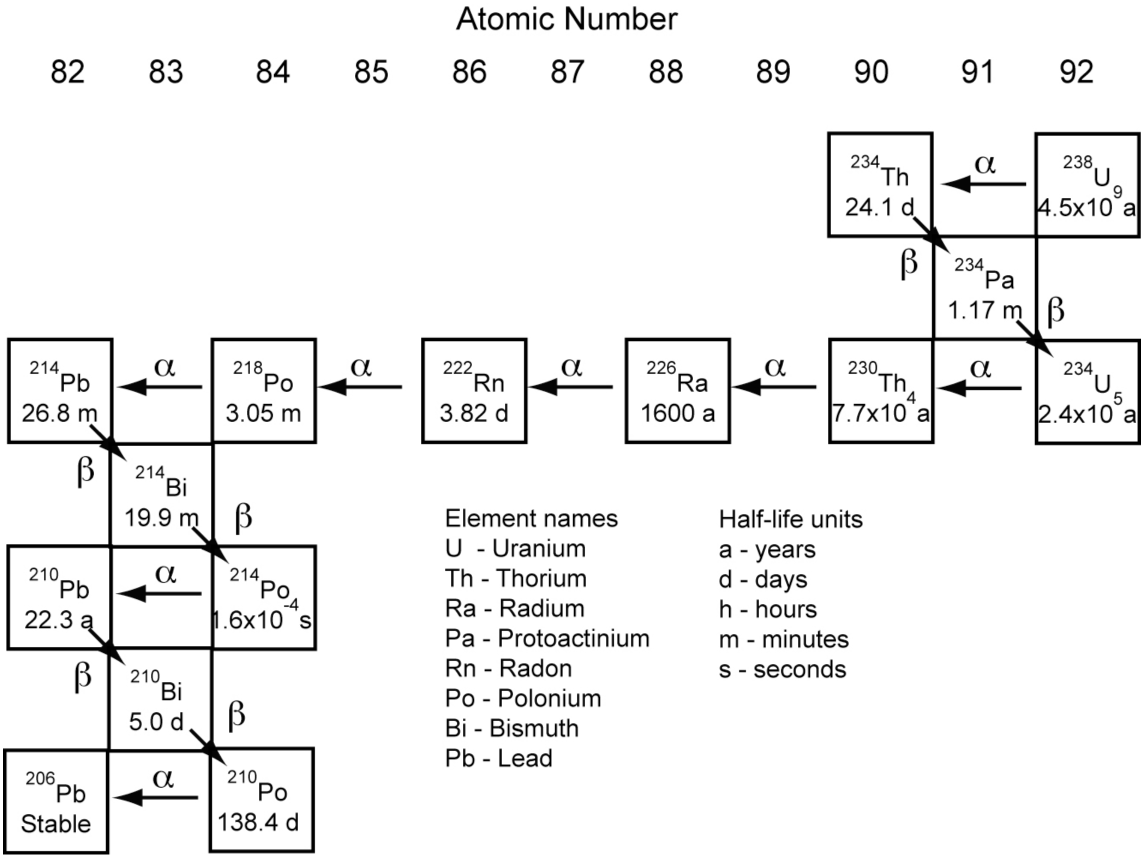

Figure 6.1. *^{238}U decay chain*

6.2 Fission track annealing

Fission tracks are metastable features that can self-repair and eventually disappear by a natural process known as annealing, which is fundamentally driven by time and temperature. Fission tracks are completely healed and removed from the host crystal lattice at high temperatures (higher than the “closure temperature”, which set the upper limit for the application of fission tracks analysis) while they are quite stable features at relatively low temperature conditions. The temperature interval between total resetting and relative stability is known as the “partial annealing zone” (PAZ). Typical PAZ temperature ranges for heating durations of 10^7 yr are 60-110°C for apatite (Gleadow & Duddy, 1981; Gleadow & Brown, 1999), 170-330°C for zircon (Zaun & Wagner, 1985; Yamada et al., 1995), and 265-310°C for titanite (Coyle & Wagner, 1998). This feature allows fission-track analysis not only to date the moment at which the host crystals reached the “closure temperature” but also to record their cooling history through the PAZ, giving insight on the sub-surface exhumation path of crustal rocks and on sedimentary basins thermal evolution. Annealing processes primarily depend on temperature and time but also on host crystal mineralogy, chemical composition, crystallographic orientation (see Ketcham et al., 2007), heating rate and duration (see Wagner & Van den Haute, 1992), and possibly pressure (Wendt et al., 2002).

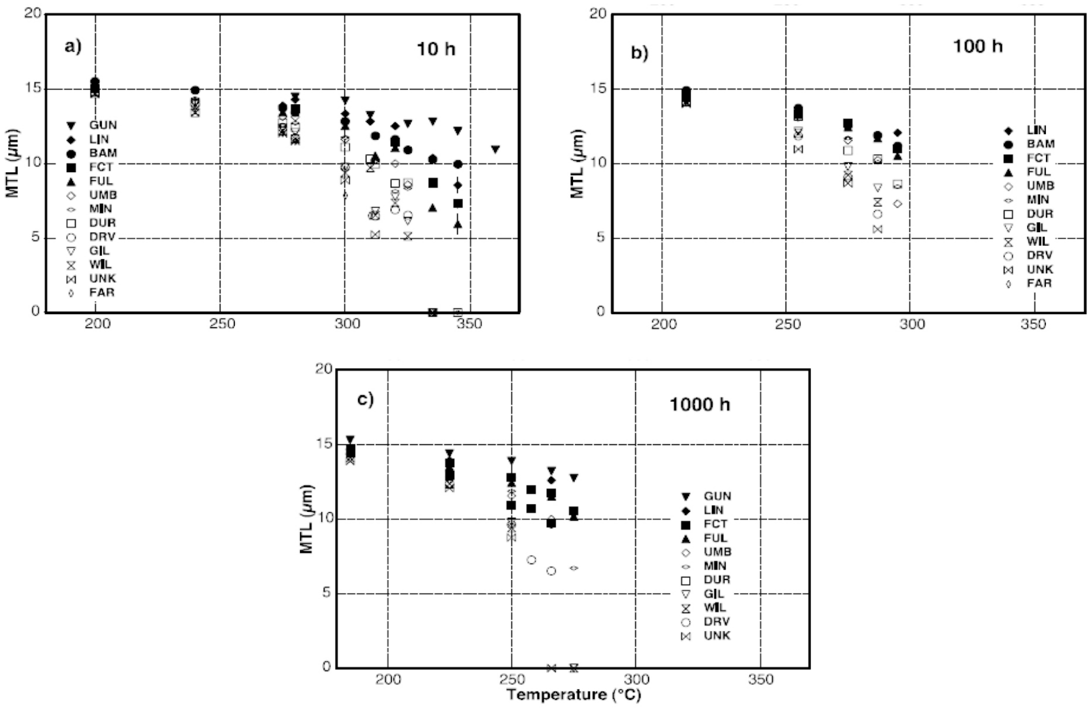

Figure 6.2. *Results from fission-track annealing experiments at various temperatures for 10h (a), 100h (b), and 1000h (c). Data from Barbarand et al., 2003.*

6.3 Determination of parent and daughter nuclei concentrations

In order to be used as geochronometers, isotopic dating methods need two parameters to be known: i) the concentration of the daughter nuclei (the products of the isotopic decay) and ii) the concentration of the parent isotope.

In fission track analysis the measurement of daughter nuclei concentrations is replaced by the measure of the effects of spontaneous fission events, which leave trails of disrupted atoms inside the crystals lattice. Those tracks, only 3 to 14 nm in width, can be observed only with a transmission electron microscope (Paul & Fitzgerald, 1992) and are referred to as “latent tracks”. The damaged material of latent tracks however is in an higher free-energy state with respect to the undamaged surroundings, thus being much more chemically reactive. Latent tracks can be chemically etched (e.g. in 5.5 M HNO_3 for 20 s at 21°C for apatite) and enlarged sufficiently to detect etched tracks under an optical microscope, although under high magnification (~1200X).

Currently two techniques are available for measuring the concentration of ^{238}U in crystals: LA-ICP-MS direct measurements of uranium concentration and induced fission tracks measures.

- LA-ICP-MS direct measurement of ^{238}U concentration:

In 2004 the first efforts to directly determine ^{238}U concentration in single apatite crystals using Laser Ablation-Inductively Coupled Plasma-Mass Spectroscopy were performed (Hasabe et al., 2004).

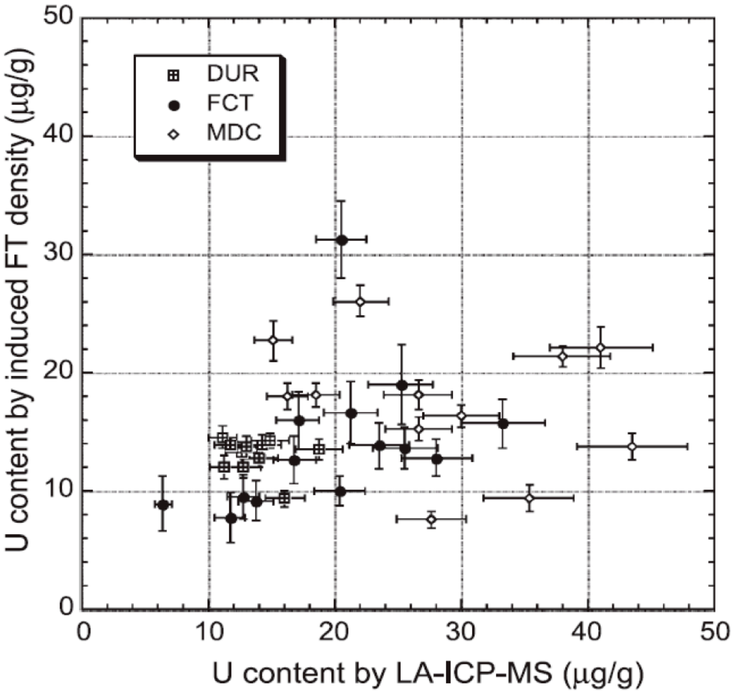

Figure 6.3. *Uranium contents in μg/g of individual apatite grains determined by LA-ICP-MS and neutron-induced fission-track density. DUR**= Durango;** FCT**= Fish Canyon Tuff;** MDC**= Mount Dromedary Complex.***
From Hasabe et a., 2004

Although results from this approach proved to be consistent, up to now, no further experiment or application of this technique have been made. The application of such a technique has no clear real advantage because, as the standard technique does (see below), it depends on the availability of very sophisticated instruments.

- **Induced fission-track density measures (external detector method):**

Induced fission track analysis is by far the most common procedure in use. It is based on the large thermal-neutron capture cross section of ^{235}U with respect to those of ^{238}U, ^{234}U, and ^{232}Th. Exposing a crystal containing U and Th to a flux of thermal neutrons in a nuclear fission reactor, ^{235}U, due to its physical properties, will experience fission while the other uranium and thorium isotopes will be nearly unaffected. Since the ^{238}U/^{235}U natural ratio is conventionally set to 137.88 (Steiger and Jäger, 1977), ^{238}U concentration can be deduced from the ^{235}U abundance, proportional to the induced fission-tracks density (figure 6.5).

Since the amount of induced fission track depends both on ^{235}U content and thermal neutron flux, two silicate glass standards of known uranium concentration are irradiated at either end of the samples stack in the reactor to interpolate the effective neutron flux through the samples. Induced fission tracks on the grain surface are recorded on a muscovite sheet located on the sample surface.

6.4 Fission track age equations

Using the external detector method, fission-tracks age of single apatite grains is given by:

$$t_i = \frac{1}{\lambda_d} \ln\left(1 + \lambda_d \zeta g \rho_d \frac{\rho_{s,i}}{\rho_{i,i}} \right) \qquad 1$$

where subscript i refers to i-th grain, t_i is the fission-tracks age of grain i, λ_d is the total decay constant of ^{238}U, ζ is the zeta calibration factor based on age-standard analysis, g is a geometry factor for spontaneous fission-tracks registration, ρ_d is the induced fission-tracks density for an glass standard corresponding to the sample position during irradiation, $\rho_{s,i}$ is the spontaneous fission-tracks density for grain i, which is the ratio between the number of spontaneous fission-tracks ($N_{s,i}$) counted over a crystal portion (Ω_i), $\rho_{i,i}$ is the induced fission-tracks density for grain i which equals

($N_{i,i}/\Omega_i$) where $N_{i,i}$ is the number of induced fission-tracks counted over an area Ω_i on the mica sheet.

The symmetrical error of single grain fission-tracks age determination is given by:

$$\sigma_i = \left[\frac{1}{N_{s,i}} + \frac{1}{N_{i,i}} + \frac{1}{N_d} + \left(\frac{\sigma_\zeta}{\zeta} \right)^2 \right]^{0.5} \qquad 2$$

where N_d is the number of the fission-tracks induced in the dosimeter used to calculate ρ_d, σ_ζ is the error of ζ.

The ζ–calibration is of crucial importance for obtaining reliable age-determinations among different operators, because it absorbs many of the vagaries of the observation processes. It is calculated by analyzing samples of known age and rearranging equation 1 in order to calculate the ζ value. Usually each operator should undertake 20-50 calibrations to stabilize its own ζ value.

The other important parameter in equation (1) is the geometric factor g. Fission-tracks density depends on the position of the analyzed polished surface within the crystal. Natural grain surfaces intersect fission tracks derived only from the crystal interiors, determining a 2π geometry (g=1.0), whereas randomly oriented surfaces inside crystals have a 4π geometry (g=0.5) because they are intersected by fission tracks originated from both sides of the surfaces. This is the reason why it is generally recommended to analyze fission tracks in areas at least at 10μm away from the crystal boundary, because near the crystal edges there’s the transition from 2π to 4π geometry.

6.5 Apatite fission track analysis

Apatite is a very suitable mineral for FT analysis. Its main advantages are: 1) its nearly ubiquitous natural occurrence in many common crustal rock types, 2) its physical properties, 3) its chemical composition, and 4) its ability to retain fission tracks in the geological environments.

1 – Natural occurrence:

Apatite is a nearly ubiquitous accessory mineral, found in many types of igneous, metamorphic and sedimentary rocks. Generally apatite grains composed of whole

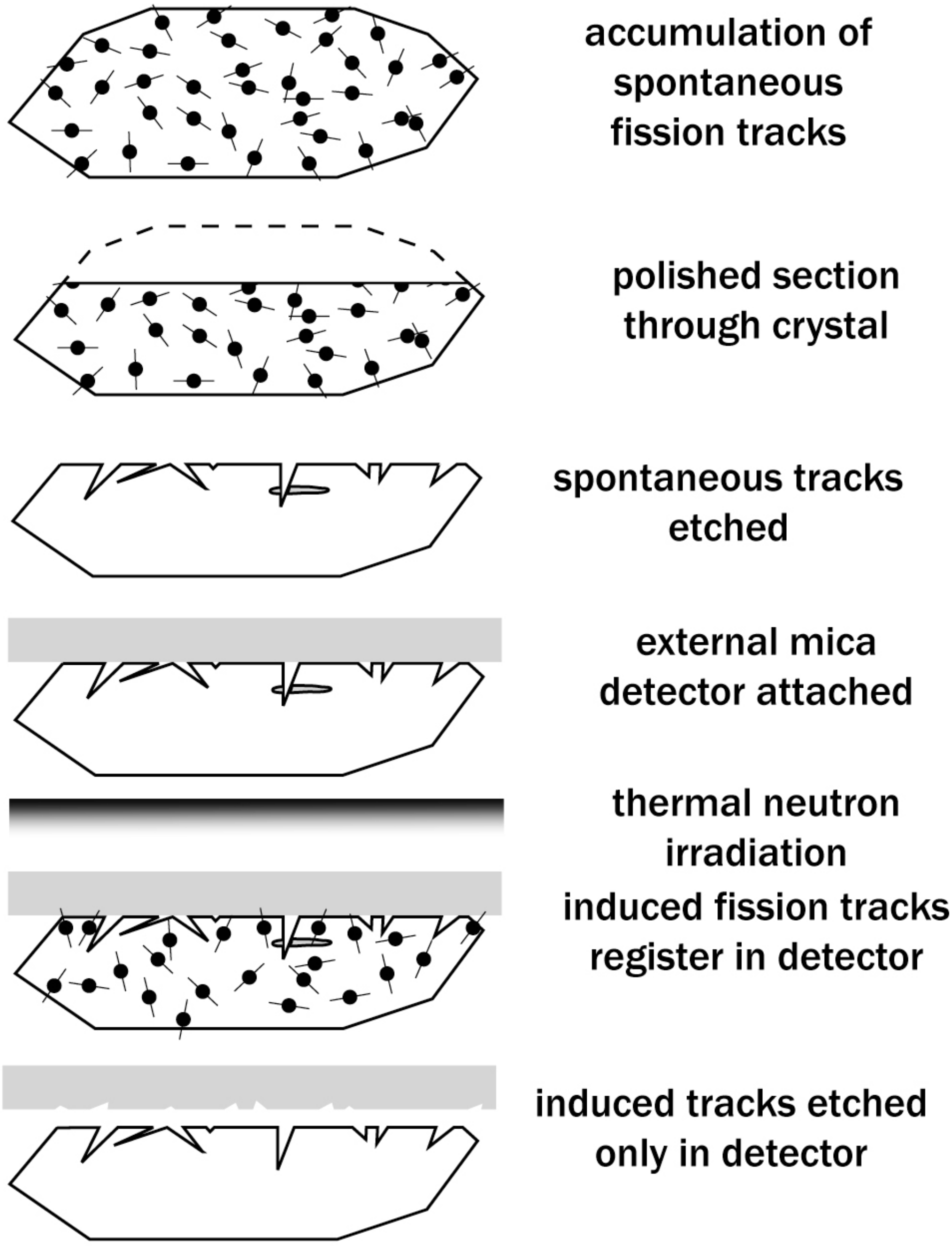

plan view

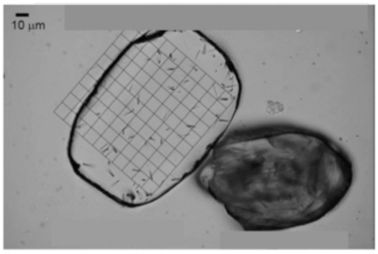

grain mount showing spontneous tracks

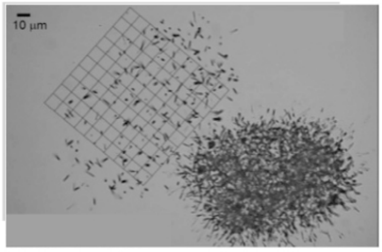

external detector showing induced tracks crystals or crystal fragments occur as anhedral to euhedral accessory grains in igneous rocks, sub-euhedral to well rounded detrital grains in clastic sedimentary rocks, primary and secondary grains in shales, limestones, and coals, primary grains or porphyroblasts in metamorphic rocks including marbles.

Apatite usually occurs as small sand-sized grains, typically <300 μm across the short diameter, in amount less than 1% of the total rock volume. AFT analysis methods generally require apatite grain to have a minimum diameter of approximately 50 μm (very fine sand), although finer grains can be used.

2 – Physical properties

Apatite is a member of the 6/m-hexagonal dipyramidal cristal class (Deer et al., 1969), the known exception being the uncommon, near end-member chlorapatite, which is monoclinic (Hughes et al., 1989). Apatite possesses a weak partitioning perpendicular to the crystallographic c-axis, but possesses no strong cleavage. Except for possible interaction with natural acidic solutions (humic acids in tropical weathering regimes), apatite commonly survives surface and near surface geological processes.

Apatite has a specific gravity between 3.15-3.20 g/cm^3.

3 – Mineral chemistry

Apatite is the most common phosphorous bearing mineral in the Earth's crust. The chemical formula for apatite is generally written as $Ca_5(PO_4)_3[F,Cl,OH]$ (Deer et al., 1969). The three anions F^{-1}, Cl^{-1}, and OH^{-1} are believed to substitute for one another between the various end-compositions fluoroapatite, chloroapatite, and hydroxyapatite, respectively. Additional substitutions include Mn, Sr, Fe, Na, and rare-earth elements (particularly Ce) in the Ca-site and Si, S, and C in the P-site. Near end member calcian-fluoroapatite is the dominant apatite variety in most crustal rocks. Minor components, present as trace elements, are U and Th, that make apatite a suitable

Figure 6.4. *The external detector method (Hurford, 1990).*
a) crystal surfaces are intersected by tracks originated within the crystal, while inside the crystal, each surface is cross-cutted by tracks originated on both sides (b);
c) crystal polished surface is chemically etched to reveal latent fission tracks. Revealed tracks can intersect the polished surface or be confined within the crystal. Confined tracks are classifies as Track-IN-Track, Track-IN-CLEavage, or Track-IN-DEFect; d) low-uranium track-free muscovite sheet (external detector) is applied to the grain mount; e)exposition to a thermal neutron flux induce ^{235}*U fission which leaves latent tracks also on muscovite; f) muscovite sheet is removed and etched to reveal induced tracks; g) spontaneous fission-tracks density is measured on the grain mount, while induced fission tracks are measured on the external detector.*
After Hurford and Carter, 1991.

mineral both for fission-tracks and (U-Th)/He analysis. Uranium content generally ranges between 1 and 200 ppm.

4 – Fission track retention in the geological environment

As stated above, fission tracks are metastable features. Apatite PAZ ranges from 120° to 60°C.

Fission-tracks annealing in apatite is faster for tracks orientated perpendicular to crystal's *c*-axis than for tracks parallel to *c*-axis (Donelick, 1991) (figure 6.6).

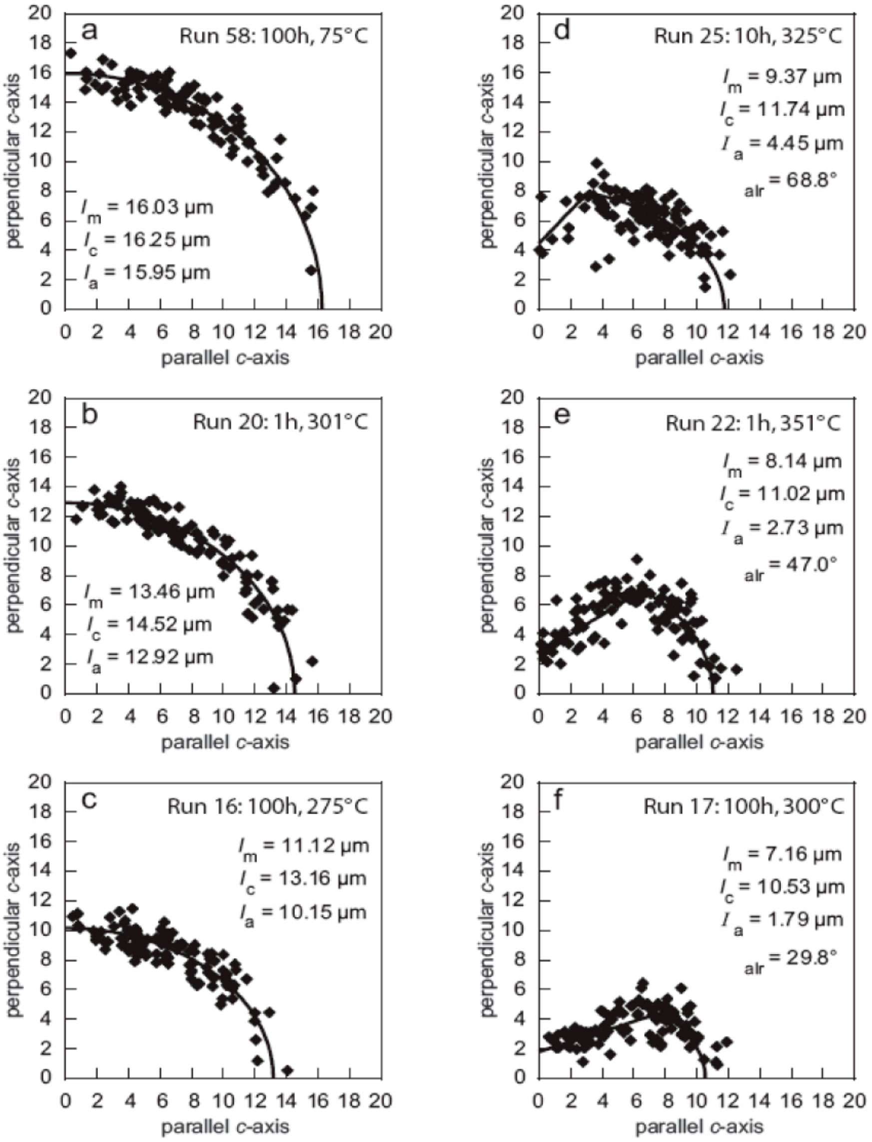

Figure 6.6. *Polar coordinate plots for fission-track lengths (Durango apatite, Donelick et al., 1999).*

6.6 Sample preparation for apatite fission-tracks analyis

Apatite-fission tracks sample preparation involves a number of procedures that have been developed and refined through more than 40 years of applications.

First of all, provided that the samples of interest do contain apatite, if they consist of solid rocks, they need to be disaggregated into constituent grains using disk mills and/or jaw-crusher until obtaining a sand-sized material. The resulting grains are then sieved using a 250μm sieve cloth and the <250μm is processed further. To obtain a sufficient number of apatites to be dated, at least 500g of <250μm are needed. If the samples consist of loose sand, sieving procedures require particular care in order to correctly identify and recover the correct grain-size fraction. Transport and deposition processes can significantly alter sediment composition, leading to a intra-sample compositional variability, strongly size-dependent (Garzanti et al., 2009).

Since apatite has a specific gravity ranging from 3.15-3.20 g/cm^3, it can be separated from the bulk of mineral and rock fragments which commonly have specific gravity <3.0 g/cm^3. Once the samples are sieved, the 63-125 and 125-250μm fraction (or a more suitable fraction), run through an hydrodynamic separation process using a shaking table to remove light minerals and rock fragments. The resulting fraction is then treated with dense liquids (usually bromoform or Na-polytungstate) to concentrate minerals with a specific density higher than 2.90 g/cm^3.

The heavy minerals fraction is processed with a Franz Isodynamic Separator to extract dia-magnetic from magnetic crystals. The resultant material needs a further separation step to concentrate apatite from zircon crystal, using diiodiomethane (ρ=3.2 g/cm^3).

Apatite separates are finally mounted in epoxy and then polished to reveal grains internal surfaces using a lap wheel. Polished mounts are etched to reveal spontaneous fission track intersecting the exposed mineral surfaces. The most common technique for etching tracks is to immerge grain mounts in 5.0 M HNO_3 for 20s (±0.5s) at 21°C (±1°C).

A muscovite sheet is applied on the polished surface to record induced-fission events. Samples are exposed in a nuclear reactor to a thermal neutron flux. Since the amount of induced fission events depends both on ^{235}U content and neutron flux intensity, two standard glasses, of known U content, are irradiated at both ends of the sample stack.

After irradiation, mica sheet are removed from the grain mounts and etched with HF 40% for 45 minutes to reveal induced tracks.

6.7 Sample analysis

Irradiated grain mounts and mica sheets must be observed under high magnification (~1200X) under transmitted and reflect light to calculate spontaneous and induced fission track densities (ρ_s and ρ_i, respectively). A preliminary spatial referencing operation is required to count the induced fission tracks on specific areas on the external detectors, corresponding to the analyzed areas on the grain mount.

Track density measures must be supported by simple morphometric observations on apatite grains shape, axis lengths, rounding and corrosion features, abundance of defects and fluid inclusions to better constrains age-determinations for different grain populations that may be present within the samples.

Since fission-tracks can be used not merely as a geochronometer but also as an effective thermocronometer, track length must be measured to reconstruct samples thermal history. Track lengths are measured from etched, horizontal, confined fission tracks. Confined tracks are tracks for which both ends are confined within the volume of polished and etched crystals and are reached by the chemical etchant via other etched features that intersect the polished surface. Confined fission tracks (figure 6.7) are usually described as TINT (Track-IN-Track), TINCLE (Track-IN-CLEavage; Lal et al., 1969) or TINDEF (Track-IN-DEFect or fluid or soluble mineral inclusion; Donelick et al., 2005). However, only TINT confined track lengths should be measured (Carlson et al., 1999), because TINCLE and TINDEF tracks have anomalous response to annealing processes (Barbarand et al., 2003; Jonckjeere & Wagner, 2000).

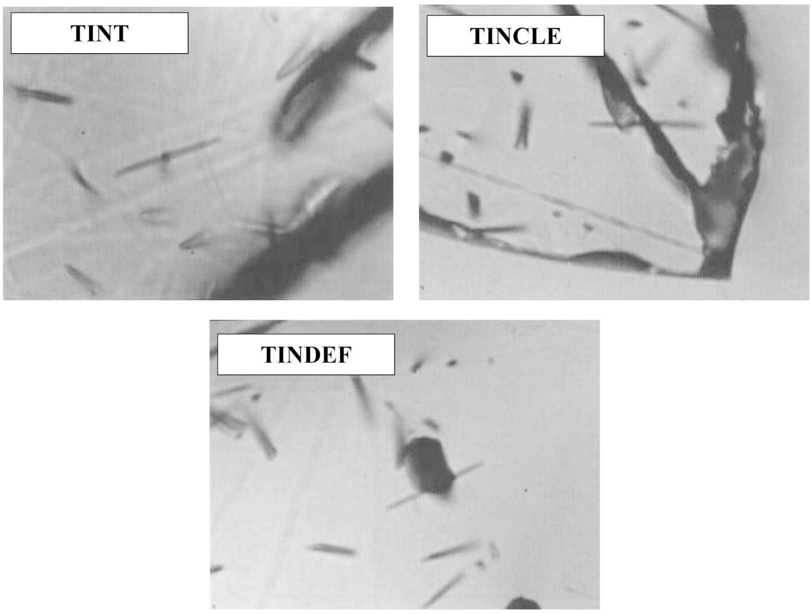

Figure 6.7. *Types of etched, confined fission tracks in apatite. Photos from Donelick et al., 2005.*

Annealing processes are not fully understood also for TINT tracks, but is well known that they depend on temperature, crystallographic orientation and apatite chemical composition (Figure 6.8). For these reasons for each samples at least 100 confined fission track lengths have to be measured, together with their orientation with respect to the crystallographic c-axis and D_{par}, a parameter that can be correlated with annealing kinematics. D_{par} is simply the mean maximum diameter of etch-pits parallels to c-axis. Apatite grains with low D_{par} values (≤1.75μm) anneal rapidly, while apatite grains with high D_{par} values (>1.75μm) anneal more slowly. D_{par} is also positively correlated with Cl wt% and OH wt% and negatively correlated with F wt% (Donelick 1993).

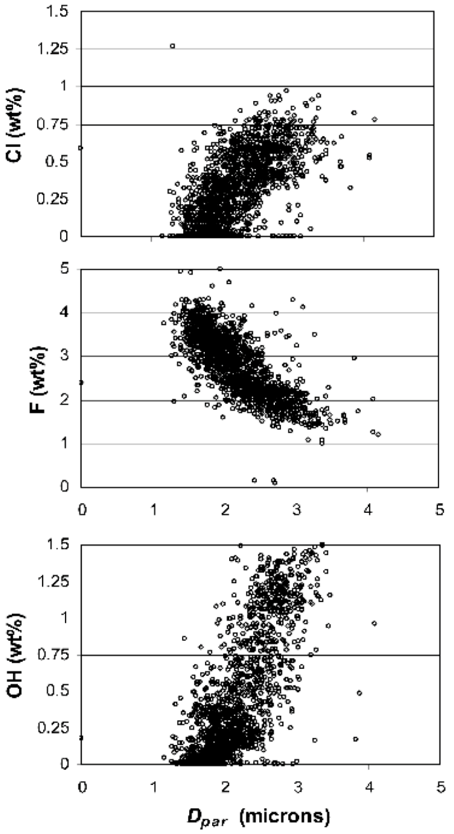

Figure 6.8. *Correlation of kinetic parameter D_{par} with Cl (wt%), F (wt%) and OH (wt%). Donelick et al., 2005*

6.8 Data visualization and interpretation

Single grain ages, calculated from equation (1) contain little information. Fission track ages are generally reported as some kind of average estimate of the individual single grain ages or groups of single grains ages. There are three “mean” age estimates in common use: the “mean age” is simply the arithmetic mean of the individual ratios of spontaneous to induced tracks; the “pooled age” is the sum of spontaneous tracks divided by the number of induced tracks; the “central age” is the weighted mean of the log-normal distribution of single grain ages (Galbraith & Laslett, 1993). When the variation of the count population is consistent with a Poisson distribution, then all three age estimates are essentially the same.

Grain-age distributions usually consist of more than single component, especially in detrital grain analysis. Such “mixed ages” have to be statistically manipulate in order to decompone their age-distribution into a set of “homogeneous” grain-age sub-populations. Several statistical procedures have been proposed for this task. Seward and Rhoades (1986) used cluster analysis, Galbraith (1988) introduced a maximum-likelyhood procedure to find best-fit solutions assuming binomially distributied component, while Brandon (1992) adopted a non linear least-square procedure assuming a Gaussian distribution.

Another way to display grain-age populations was introduced by Gailbraith (1988, 1990) with his “radial plot” (figure 6.9). This graph allows the simultaneous display of multiple grain age taking into account the effects of their different standard errors.

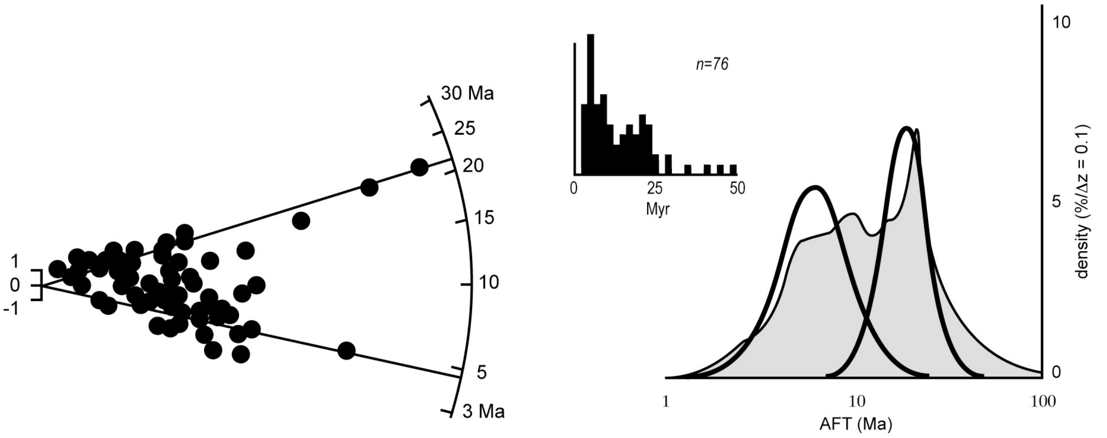

Figure 6.9. *Radial plot (left), single grain age histogram (centre), and probabilità distribution function and its decomposition (right). Radial plots are designed to graphically display single grain ages an their standard errors (Galbraith, 1988; 1990).*
Single grain ages (t) with standard error (σ) are plotted into x-y plot diagram according to precision (x-axis) = $1/\sigma$ and standard estimate (y-axis) = $(t-t_0)/s$, where t_0 is the central age. The error attached to each point is standardized on the y-scale. Grain age values and 2 σ errors can be read off the age scale, projecting points and 2σ bars onto the age scale. This implies that more precise age determination will plot farther from the origin.

7 Sediment budgets by detrital apatite fission tracks (Rivers Dora Baltea and Arc, Western Alps)

*submitted for publication in Geological Society of America Special Volume on Provenance Studies as "*Sediment budgets by detrital apatite fission tracks (Rivers Dora Baltea and Arc, Western Alps)*" by Alberto Resentini and Marco G. Malusà.*

7.1 Introduction

The idea that very small areas can be the source of huge sediment volumes, and that erosion can be focused both in space and time, has been recently documented by independent techniques in different orogenic belts (Beaumont et al., 2001; Zeitler et al., 2001; Finlayson et al., 2002; Garzanti et al., 2004; Zeilinger and Schlunegger, 2007; Garzanti and Malusà, 2008).

Surface erosion results from complex interactions among diffusive hill-slopes runoff, landsliding, weathering, and glacial grinding (Burbank, 2002; Korup, 2005; Koppes and Montgomery, 2009), whereas streams are the preferential ways to evacuate detritus (Milliman and Meade, 1983; Syvitski et al., 2003). For such reasons, detecting sources of (paleo-)river sediments is an invaluable tool to reconstruct magnitude and distribution of erosional processes over wide areas, and to assess the potential occurrence of focused erosional processes.

Sediments provenance can be proficiently assessed by sandstone/sand framework petrography (Ingersoll, 1990; Arribas et al., 2000; von Eynatten et al., 2003; Garzanti et al., 2007a), heavy mineral analysis (Morton and Hallsworth, 1994; Mange-Rajetzky, 1995), and geochronological analysis on detrital grains (Hurford and Carter, 1991a; Bernet et al., 2004a,b; Foster and Carter, 2007; Vermeesch et al., 2010).

This study presents a new quantitative approach to assess sediment provenance based on fission-track analysis of detrital apatites. It is applied to the modern sands of Rivers Arc and Dora Baltea, which drain the Western European Alps and flow in opposite directions towards the European foreland and the Adriatic retroforeland, respectively. These rivers cut the same tectonic stack, and represent an excellent natural laboratory to investigate relationships and feedbacks between exogenic and endogenic processes.

7.2 Geological setting

The Western Alps are a thick-skinned orogen welding the European and Adriatic plates (Figure 7.1). Tertiary metamorphic units are exposed in the axial belt, delimited by the Insubric Fault to the southeast and the Frontal Pennine Fault to the northwest (Polino et al. 1990, Schmid and Kissling, 2000). They record attempted subduction of Tethyan oceanic crust and thinned European continental crust within a fossil subduction zone (Agard et al., 2009, Garzanti et al., 2010a), developed in Eocene times beneath the Adriatic margin and the remnants of a Late Cretaceous orogenic wedge.

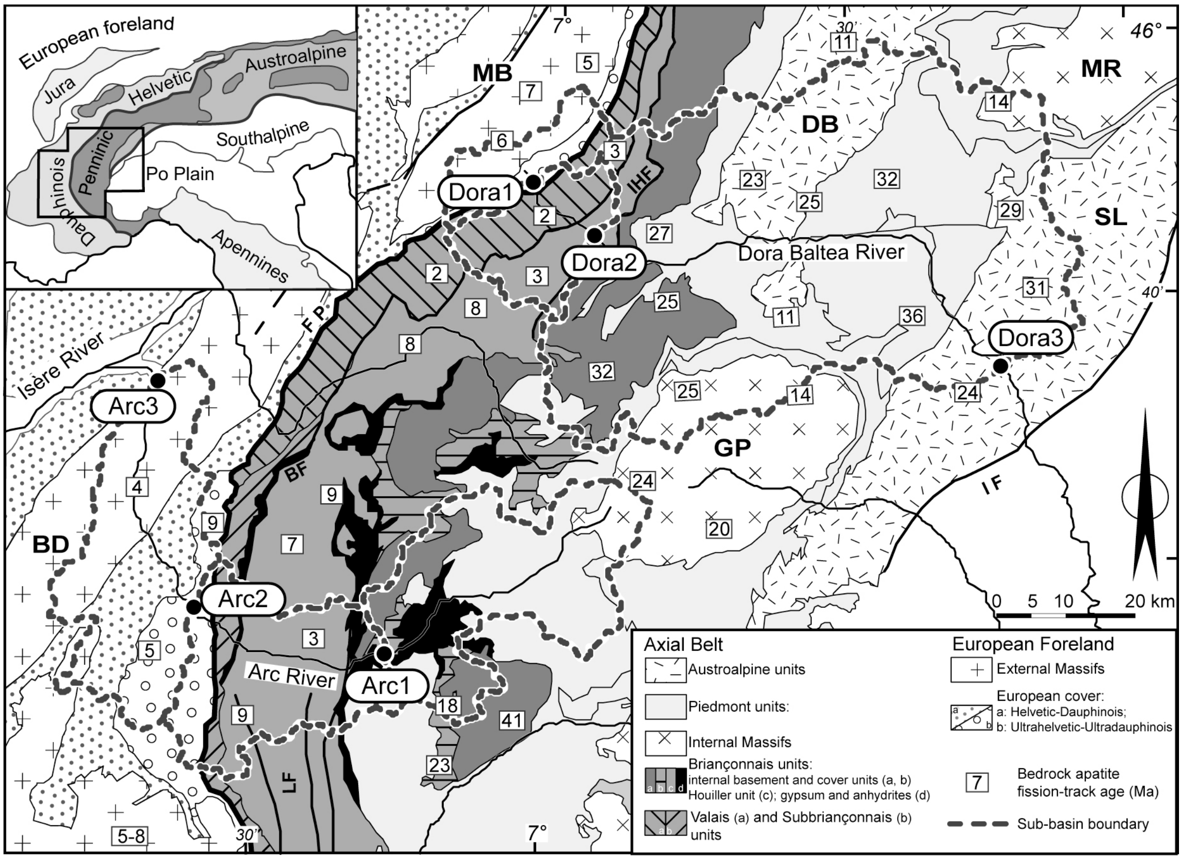

Figure 7.1. *Tectonic map of the study area and sample location. Inset: tectonic map of the European Alps. Samples were collected at the end of sub-basins indicated by dashed lines. Major faults are: BF, Briançonnais Fault; FP, Frontal Pennine Fault; IHF, Internal Houiller Fault; IF, Insubric Fault; LF, Longitudinal Faults. Tectonic units: BD, Belledonne Massif; DB, Dent Blanche; GP, Gran Paradiso; MB, Mont Blanc; MR, Monte Rosa; SL, Sesia-Lanzo. Arc and Dora Baltea basins and sub-basins based on ArcHydro toolset delineations on 90m SRTM DEM. River samples locations are as follows: Arc1: Arc@Avrieux; Arc2: Arc@Saint Jean de Maurienne; Arc3: Arc@Aiguebelle; Dora1: Dora Baltea@La Saxe; Dora2: Dora Baltea@La Salle; Dora3: Dora Baltea@Quassolo. Bedrock apatite fission-track data simplified after Malusà et al. (2005b) and Vernon (2009) and references therein.*

The fossil subduction zone of the Western Alps includes, west of the Sesia-Lanzo unit (Babist et al., 2006), Penninic units of oceanic and continental-margin affinity, which were dragged to deep subcrustal levels (Chopin 2003; Groppo et al., 2009), detached and subcreted at intermediate crustal levels (Desmons, 1992; Malusà et al., 2002), or offscraped at shallow structural levels and thus escaping significant metamorphism (Polino et al., 1983; Chalot-Prat, 2005). After undergoing subduction, basement and cover rocks were retrogressed at variable pressure and temperature, and finally reached the Earth's surface. Major tectonic discontinuities run sub-parallel to the orogen trend.

In the study area, eclogite units are exposed northwest of the Insubric Fault, and consist of oceanic slivers (e.g. Zermatt-Saas unit, Bearth, 1967; Rubatto et al., 1998) enveloping the continental basement of the Internal Massifs (e.g. Monte Rosa and Gran Paradiso units, Dal Piaz and Lombardo, 1986; Gabudianu Radulescu et al., 2009). Sedimentary thrust-sheets and subcreted greenschist-facies to blueschist-facies units are exposed in a more external, Europe-side position, and form a double-vergence accretionary wedge classically referred to as Briançonnais tectonic fan (Fabre, 1961; Goguel, 1962). It includes metaturbidite sequences (e.g. Combin unit, Caron, 1977), basement slivers (e.g. Ambin and Leverogne units, Desmons, 1992, Malusà et al., 2005a), Permo-Carboniferous metasediments (Houiller unit - Ellenberger, 1958; Bertrand et al., 1998), and Valaisan and Subbriançonnais sequences (Elter and Elter, 1965; Bousquet et al., 2002). West of the axial belt, the European basement is exposed in the Mont Blanc and Belledonne External Massifs, consisting of Upper Carboniferous granitoids intruded into amphibolite-facies metasediments and migmatites (von Raumer et al., 1993). Their chiefly carbonate cover sequences, which are classically referred to as Helvetic-Ultrahelvetic and Dauphinois-Ultradauphinois successions (Barbier, 1948), are largely preserved in the Arc catchment, but quite limited in the Dora Baltea basin.

7.3 Bedrock fission-track ages

Geochronological work over the last three decades has provided detailed information on timing and distribution of exhumation processes in the Western Alps (e.g. Hurford et al., 1991b; Seward and Mancktelow, 1994; Fügenschuh and Schmid, 2003; Tricart et al., 2007). Available data sets show a systematic decrease in fission-track ages towards the European foreland (Figure 7.1), with major breaks occurring across major faults (Malusà et al., 2005b; Malusà and Vezzoli, 2006). Contrasting fission-track ages are observed in fault-bounded crustal blocks pointing to differential exhumation rates over a long-term (10^6-10^7a) timescale (Figure 7.2).

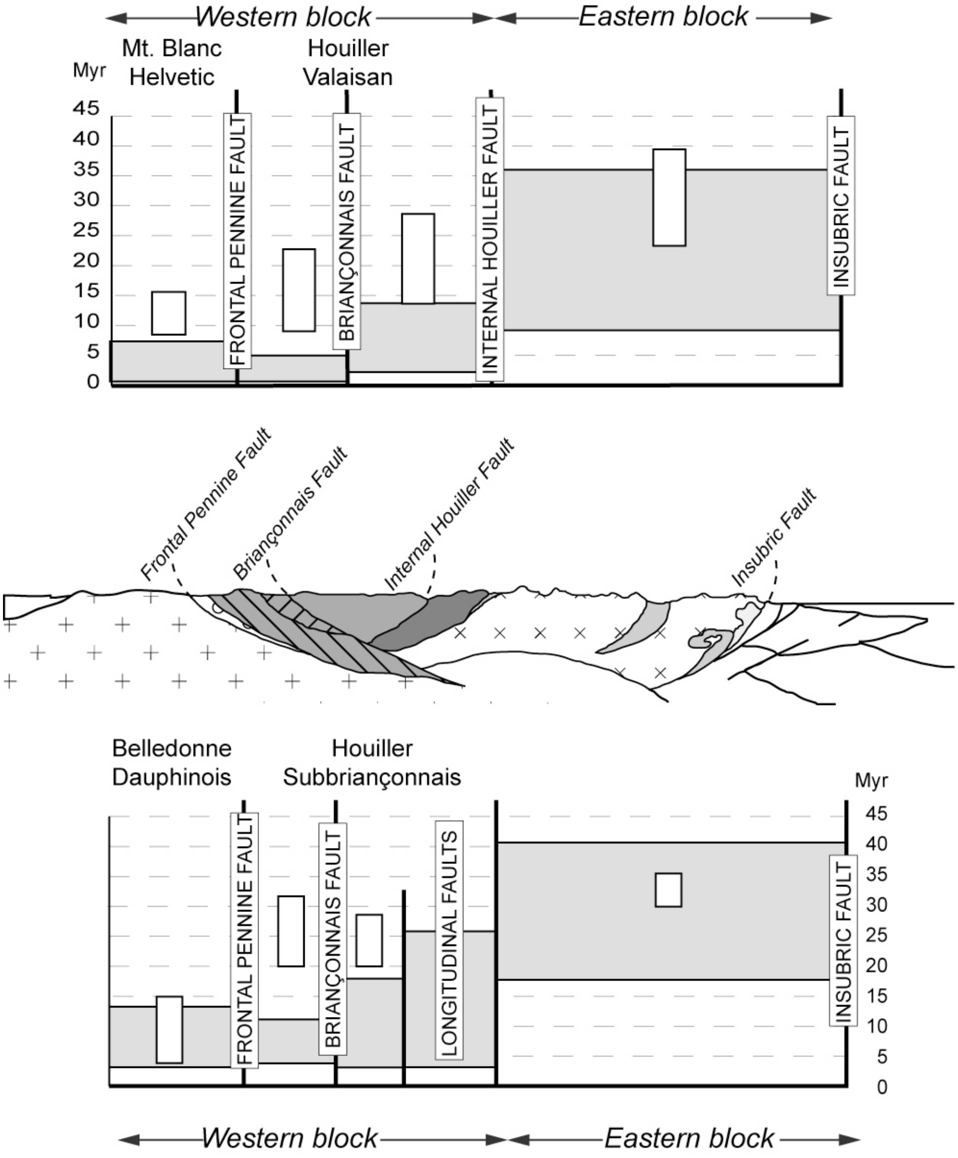

__Figure 7.2.__ Crustal scale section of the Western Alps (same patterns as in figure 1) and synthesis of bedrock zircon and apatite fission-track data in major fault-bounded blocks (simplified after Malusà et al., 2005b).

The Eastern Block comprises most of the axial units, and yields fission-track ages older than 10 Ma on apatite and older than 20 Ma on zircon. It is bounded to the east by the Insubric Fault. To the west, it is delimited by the Internal Houiller Fault, along the Aosta

Valley transect, and by the Longitudinal Faults along the Arc Valley transect. Younger fission-track ages, generally younger than 10 Ma on apatite and younger than 20 Ma on zircon, are observed in the Western Block, which includes the Houiller, Valais and Subbriançonnais units, delimited to the west by the Frontal Pennine Fault, and the External Massifs and the overlying cover sequences. Average long-term exhumation rates for these blocks were estimated by Malusà et al. (2005b) as 0.1 km/Ma in the Eastern Block and 0.5-0.9 km/Ma in the Western Block.

The Dora Baltea river cuts across the whole nappe stack, from the Mont Blanc to the Insubric Fault, cutting across the Western and the Eastern Blocks. The Arc river is sourced inside the Eastern Block, and cuts the axial units to the west finally crossing the Belledonne Massif in the Western Block.

7.4 Sampling strategy

The Arc and Dora Baltea catchments were considered as subdivided into three sub-basins, corresponding to (i) the axial units of the Eastern Block, (ii) the Houiller and Valaisan-Subbriançonnais units of the Western Block and (iii) the External Massifs and overlying sedimentary rocks (Figure 7.1). These blocks are delimited by major tectonic boundaries detected inside the Western Alps: the Insubric Fault, the Internal Houiller and Longitudinal Faults, the Frontal Pennine Fault. Samples for bulk-petrography and fission-track analysis were collected at the end of each sub-basin, in order to investigate how the detrital signal evolves when detritus from different sub-basins is progressively added to the system.

Sample Dora1 includes detritus from the upper sub-basin of the Dora Baltea catchment, comprising the Mont Blanc basement and the Ultrahelvetic cover units. Sample Dora2 also includes detritus from the Valaisan and Houiller units, whereas sample Dora3 includes detritus from the whole nappe stack.

In the Arc catchment, sample Arc1 entirely consists of detritus from the Penninic units of the Eastern Block. Sample Arc2 includes detritus from the Houiller and Subbriançonnais units, whereas sample Arc3 includes also detritus from the Belledonne basement and the Dauphinois-Ultradauphinois cover sequences.

7.5 Bulk petrography

7.5.1 Methods

Thin sections for petrographic analysis were prepared from the whole sand fraction (63-2000 μm), impregnated with araldite and stained with Alizarine-red to distinguish dolomite from calcite. For each thin section, 400 points were counted according to the Gazzi-Dickinson method (Ingersoll et al., 1984). Metamorphic Index (MI), ranging from 0 (no metamorphic rock fragments) to 500 (exclusively high-grade metamorphic rock fragments), provided an estimate of source-rock metamorphic grade (Garzanti and Vezzoli, 2003). Forward mixing models (Draper and Smith, 1998) were applied to assess the relative contribution of specific source units to the total bedload of the Arc and Dora Baltea rivers. Goodness of fit was assessed by the coefficient of multiple correlation (R in Vezzoli and Garzanti, 2009).

7.5.2 Results

Sample Dora1 consists of quartzofeldspathic sand with minor calcareous rock fragments (table 7.1). Carbonatic-grains slightly increase downstream because of the contribution from the Houiller-Valaisan units (sample Dora2).

Sample Dora3 (whole Dora Baltea catchment) consists of quartz, feldspars, metafelsite/metabasite grains, few serpentine-schist fragments, and very rich heavy-mineral assemblages. Comparison between such modal compositions and those reported by Vezzoli et al. (2004) yielded R values of 0.99, testifying to samples reproducibility.

Mixed sample compositions were compared to source-rocks detrital signatures, according to the end-member compositions in Vezzoli et al. (2004) (Figure 7.3). Dora Baltea sands at La Salle (sample Dora2) derive about 85% from the Mont Blanc-Helvetic units and 15% from the Houiller-Valais units (R=0.99). Contribution at Quassolo (sample Dora3) is calculated as 25% from the Mont Blanc-Helvetic units, 4% from the Houiller-Valais units and 71% from Eastern Block units (R=0.99).

Detritus from the Eastern Block (Arc1) chiefly consists of calcareous rock fragments from Piedmont calcschists, quartz and metafelsite/metapsammite rock fragments from the Gran Paradiso and Briançonnais basements, and minor serpentine-schist grains from Piedmont metaophiolites. A MI value of 275 is consistent with provenance from low- to medium-grade units (Garzanti et al., 2010a). Sample Arc2, derived from the

Eastern Block and the inner parts of the Western Block, shows dominant carbonate and quartz grains. Relative to sample Arc1 low-rank metapelite fragments increase slightly at the expense of higher-rank metamorphic rock fragments, reflecting detrital contribution of low-grade metasediments of the Houiller-Subbriançonnais units. Sample Arc3 (whole Arc catchment) consists of abundant carbonates and quartz and minor pelitic grains, with a slight increase in feldspar. The low MI value (126) testifies to major contributions from very low-grade Dauphinois sequences.

Table 7.1. *Composition of Dora Baltea and Arc River sands and source-rocks end-member compositions. Q: quartz, KF: K-feldspar, P: plagioclase, L: lithic fragments (Lv: volcanic, Lcc: calcareous, Lcd: dolostone, Lp: terrigenous; Lmv: low-rank metavolcanic; Lms: low-rank metasedimentary, Lmf: felsic medium- to high-rank metamorphic, Lmb: metabasite, Lu: ultramafic); HM: heavy minerals, MI: metamorphic index (Garzanti and Vezzoli, 2003).*

	Q	**KF**	**P**	**Lv**	**Lcc**	**Lcd**	**Lp**	**Lmv**	**Lms**	**Lmf**	**Lmb**	**Lu**	**mica**	**HM**	total	**M.I.**
Dora Baltea																
Sample																
Dora1	47	16	21	0	5	1	0	0	1	2	1	0	1	4	*100,0*	316
Dora2	50	13	17	0	10	2	0	0	1	3	0	0	1	2	*100,0*	325
Dora3	31	6	10	0	8	4	1	0	0	10	4	4	3	18	*100,0*	357
compositional end-members																
Mont Blanc-Helvetic	35	14	19	0	11	0	2	0	8	6	1	0	2	1	*100,0*	253
Houiller-Valaisan	34	1	3	0	27	1	2	1	9	19	1	0	3	1	*100,0*	322
Briançonnais basements	43	2	3	0	0	0	0	1	0	40	0	0	7	4	*100,0*	403
Internal Massifs	52	8	9	0	0	0	0	1	0	11	0	0	14	5	*100,0*	391
Pimontese calcschists	26	0	3	0	12	10	4	4	9	14	1	3	5	9	*100,0*	348
Metaophiolites	10	1	6	0	2	1	1	5	1	3	2	29	2	39	*100,0*	342
Austroalpine units	35	4	14	0	0	0	0	3	0	18	3	0	11	11	*100,0*	387
Arc																
Sample																
Arc1	36	2	3	0	24	6	6		1	13	0	2	4	3	*100,0*	275
Arc2	24	2	3	0	37	9	3		8	10	0	0	1	2	*100,0*	242
Arc3	26	3	4	0	35	4	13		9	3	0	0	1	1	*100,0*	126
compositional end-members																
Eastern Block	36	2	3	0	24	6	6		1	13	0	2	4	3	*100,0*	275
Houiller-Subbriançonnais	31	1	0	2	20	16	3		16	9	0	0	0	0	*100,0*	198
Belledonne-Dauphinois	36	9	8	0	12	3	15		6	2	1	0	2	6	*100,0*	100

The Arc samples thus show very similar compositions, dominated by quartz and carbonate fragments, mainly due to a general homogeneity of end-member compositions, invariably consisting of felsic (Gran Paradiso / Belledonne Massif) and calcareous (Combin / Subbriançonnais / Dauphinois units) source-rocks. The MI index provides a key to distinguish differerent sub-basins, showing a general decrease in rank from east to west. In the westernmost sub-basin feldspars are few, reflecting wide exposure of Dauphinois cover rocks. Such a general homogeneity in detrital modes of Arc river sediments derives from very similar end-member compositions. Since quantification of detrital contributions from different sources is accurate only if contributing end-member compositions are mineralogically distinct, unmixing of Arc river samples results difficult to determine (Figure 7.3).

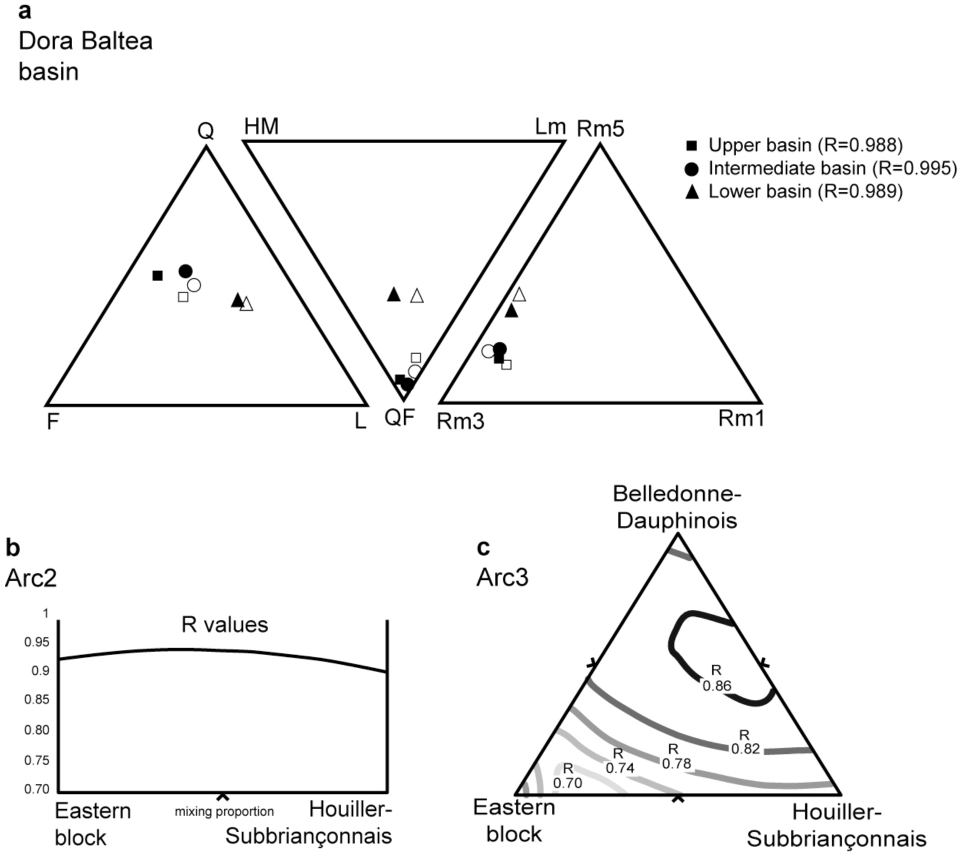

Figure 7.3. *Upper panel (a) compares compositions of our Dora Baltea samples (black symbols) with data from previous samples collected in same locations (open symbols, data from Vezzoli et al., 2004). R values are also reported. Same symbols as in Table 7.1.*
Rm1: very low to low-rank metamorphic rock fragments; Rm3: intermediate-rank metamorphic rock fragments; Rm5: high-rank metamorphic rock fragments (Garzanti and Vezzoli, 2003).
Panels b and c describe composition of Arc River multi-sourced samples as a mixture of the contributing sources. Quantification of the relative contributions from the different sources is obtained comparing samples with compositions generated by mixing their sources in various proportions. R parameter (Vezzoli and Garzanti, 2009) gives a statistical estimation of the similarity between real and modelled compositions, ranging from 0 -no similiarity- to 1-perfect similarity. Panel (b) shows R values for sample Arc2 according to different mixing proportions of Eastern Block (left) and Houiller-Subbriançonnais (right) end members. Contour lines in lower panel (c) show variations in R-value as the three contributing sediment sources are combined in different proportions.

Best fit is obtained with sub-equal proportions of Eastern Block and Houiller-Subbriançonnais detritus for sample Arc2, and dominant contributions from the Belledonne and Dauphinois rocks for sample Arc3.

7.6 Fission-track data from detrital apatites

Fission-track analysis of detrital apatites represents an effective complementary tool to quantify sediment provenance from subcatchments with similar detrital signatures but where source-rocks experienced contrasting exhumation paths. This latter pre requisite is fully met in the study area, because the Eastern and Western blocks experienced different long-term exhumation rates during the Neogene (Malusà et al., 2005b).

7.6.1 Methods

In order to retrieve the maximum amount of apatite grains, apatites were concentrated from the 63-250 μm (4-2ϕ) sand fraction, selected according to the mean grain-size of our samples (2.0÷3.1ϕ in the Arc and 2.1÷2.5ϕ in the Dora Baltea) and the expected size-shift of apatite relative to quartz in well sorted sediments (0.20÷0.25ϕ; Garzanti et al., 2008). Because of poor sorting (0.8÷1.2 ϕ), only 53% to 75% of total apatites was expected to fall in this size window, while loosing 40% to 16% of apatite grains in the > 250 μm window and 2% to 25% of apatite grains in the < 63 μm window (that would have been hard to count anyway).

Detrital apatites were concentrated using standard hydrodynamic, magnetic and dense-liquid techniques and prepared for irradiation according to the external-detector method (Hurford, 1990; Wagner and Van den Haute, 1992). Samples were irradiated in the TRIGA-II reactor at the Oregon State University, and analyzed in the Laboratory for Provenance Studies at Milano-Bicocca University. Grain age was calculated by using the "Trackkey" software (Dunkl, 2002). Beside track density, several features including size, shape, roundness and occurrence of fluid inclusions were recorded for each grain. Potential relationships between these features and fission-track age were inspected with the software “Radial Plotter” (Vermeesch, 2009). Decomposition of grain-age distributions was finally performed with the programs "Popshare" (Dunkl and Székely, 2002) and "Binomfit" (Brandon, 2002).

7.6.2. Results

The obtained detrital age populations (Figures 7.4 and 7.5) closely reflect bedrock fission-track ages in source areas (Figure 7.1). In the Dora Baltea basin, samples

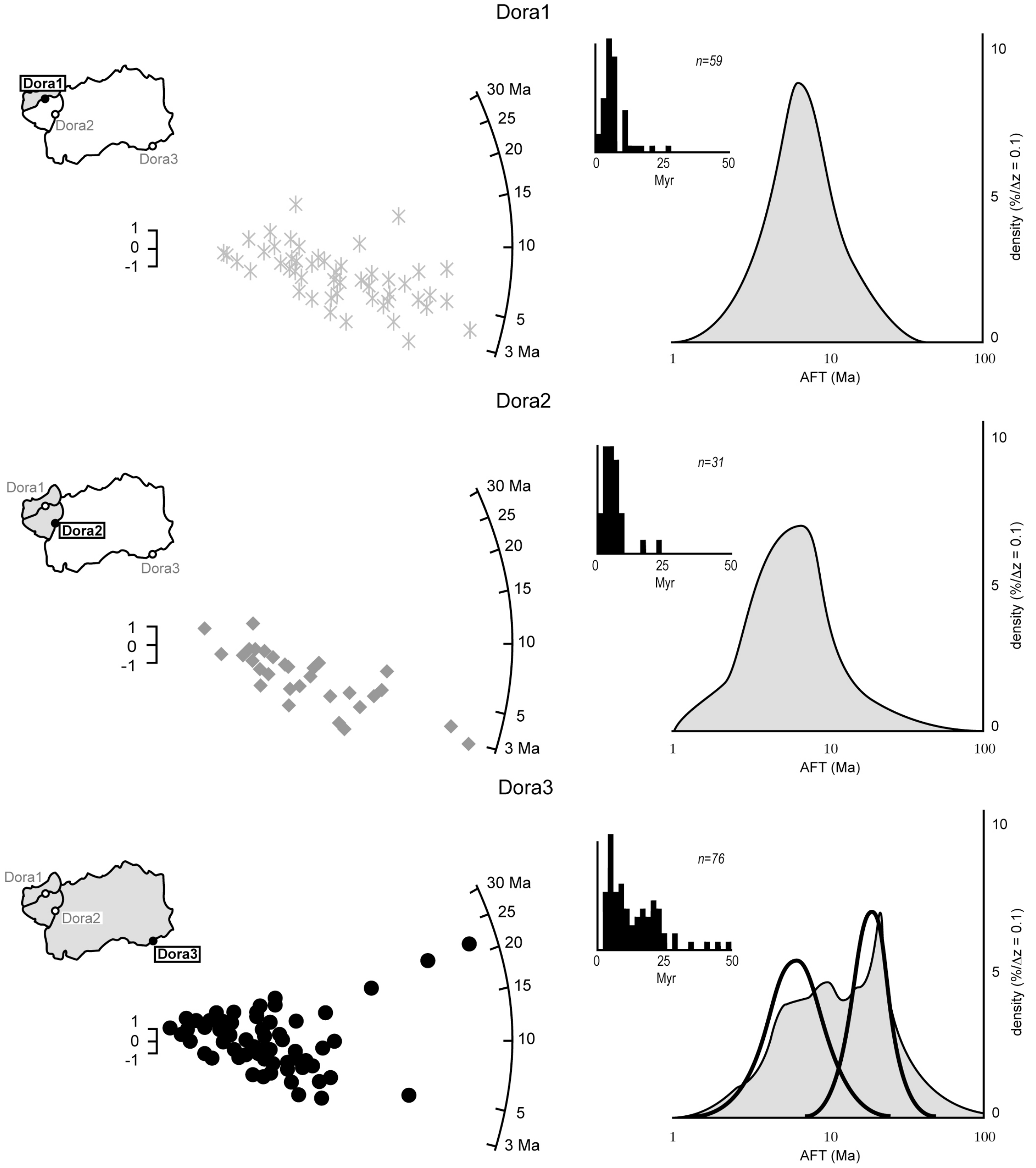

Figure 7.4. *Grain-age distribution for detrital apatite fission tracks from the Dora Baltea catchment, indicated in radial plot (left), histogram (middle), and probability density distribution (right).*

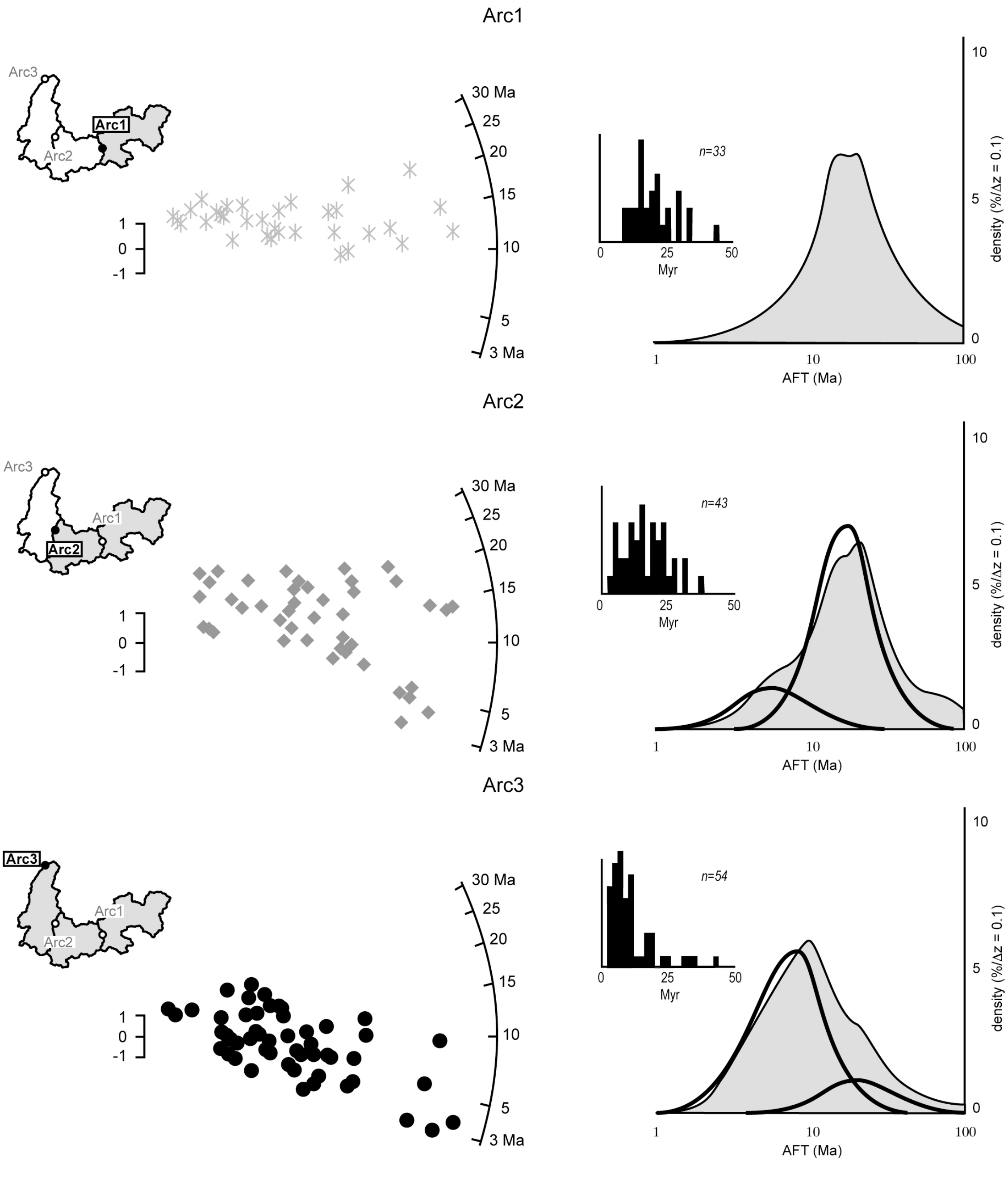

Figure 7.5. *Grain-age distribution for detrital apatite fission tracks from the Arc catchment, indicated in radial plot (left), histogram (middle), and probability density distribution (right).*

Dora1 and Dora2 yielded young ages (7.0 ± 0.6 Ma in sample Dora1, and 5.9 ± 0.8 in sample Dora2), consistent with those observed in the Western Block. Sample Dora3 yielded two distinct populations (5.7 ± 2.6 Ma and 18.5 ± 6.9), consistent with bedrock fission-track ages observed in the Western and Eastern blocks, respectively.

In the Arc River, sample Arc1 yields scattered old ages (16.5 ± 2.2 Ma) reflecting the slow exhumation history of the Eastern Block.

In sample Arc2, collected west of the Internal Houiller Fault, decomposition of grain-age distributions highlights two distinct populations (7.9 ± 4.1 Ma and 19.4 ± 6.4 Ma), consistent with bedrock ages in the Eastern Block and in the Houiller-Subbriançonnais units, respectively. Populations in sample Arc3 are similar to sample Arc2 (6.9 ± 3.3 Ma and 19.4 ± 8.7 Ma) but with different relative size (71 vs. 32% and 29 vs. 68%, respectively, see Table 7.2).

None of the samples collected in the Dora Baltea and Arc catchments show any correlation of grain age with grain size (R^2=0.05) (Figure 7.6), making the geochronological signature robust with respect to hydraulic-sorting effects.

Fission-track grain-age distributions provide not only information on long-term exhumation patterns, which are based on the age of the peaks in the grain-age distribution, but also on short term erosion patterns at 10^2-10^4 timescales (Malusà et

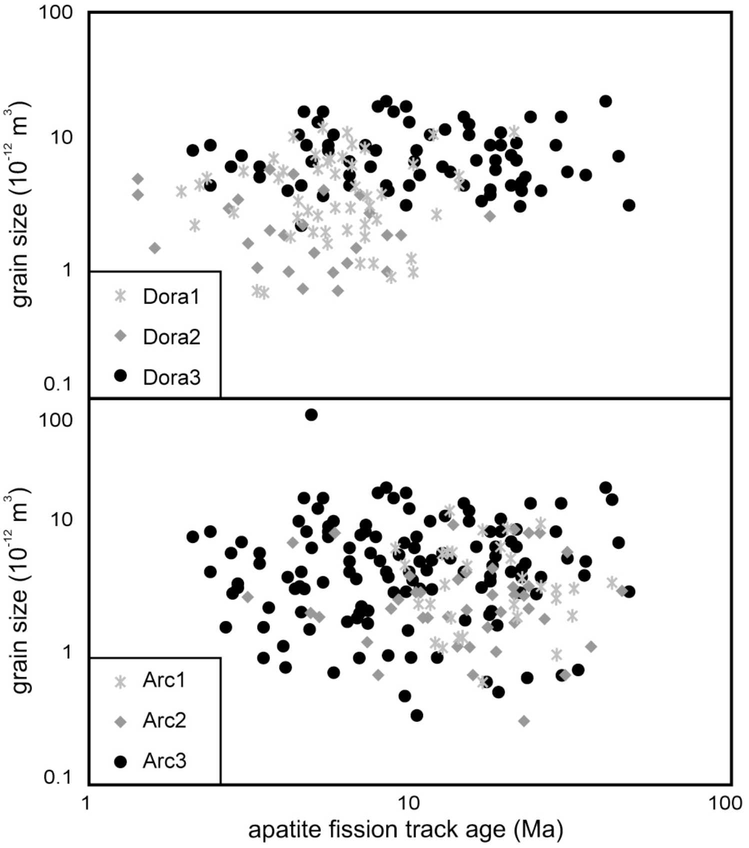

Figure 7.6. *Grain-size vs. grain-age plot. Analyzed samples show no correlation between age and crystal size, thus minimizing the effects of size-sorting on single grain age distribution.*

al., 2009a). Comparison between the size of the peaks in the grain-age distribution, and the size of the potential source areas, provides in fact firm constraints on short-term erosion rates.

In the Dora Baltea basin, detrital-apatite contribution from the Western Block represents 43% of the entire apatite flux, whereas the Eastern Block contributes for the remaining 57%. Our geochronological dataset does not allow any discrimination between contributions from the Mont Blanc-Ultrahelvetic and the Houiller-Valaisan units, because they are both characterized by young fission-track ages < 10 Ma. A finer subdivision is allowed by bulk petrography data.

In the Arc River, upstream of the Frontal Pennine Fault, apatite contribution from the Houiller and Subbriançonnais units of the Western Block represents 32% of the total apatite flux, whereas the Eastern block contributes for the remaining 68%. Total contribution of the Western Block at the mouth of the Arc valley increases markedly to 71% of the total apatite flux, reflecting major supply from the Belledonne Massif and overlying Dauphinois-Ultradauphinois cover. The relative contribution from the Houiller-Subbriançonnais units and Belledonne-Dauphinois units is assessed at 14% and 57%, respectively. Contribution from the Eastern Block is only 29% of the whole Arc River apatite flux (Table 7.2).

Table 7.2 *Apatite grain-age populations (mean ages and standard deviations in Ma) and relative apatite budget*

Sample	Young population			Old population		
	Mean age	St. dev	%	Mean age	St. dev	%
Dora 1	7.0	0.6	100	-	-	-
Dora 2	5.9	0.8	100	-	-	-
Dora 3	5.7	2.6	43	18.5	6.9	57
Arc 1	-	-	-	16,5	2,2	100
Arc 2	7,9	4,1	32	19,4	6,4	68
Arc 3	6,9	3,3	71	19,4	8,7	29

7.7 From apatite budgets to erosion rates

7.7.1 Calculating apatite fertility

Relative apatite budgets retrieved from fission-track analyses do not reflect only short-term erosion rate (Amidon et al., 2005; Weltje and von Eynatten, 2004), but also the size of specific sub-basins and the mean apatite abundance in source-rocks (often referred to as fertility, Moecher and Samson, 2006; Dickinson, 2008). This implies that a slowly-eroding apatite-rich unit can supply the same amount of apatite as an apatite-poor fast-eroding unit of comparable exposure.

We can assess apatite fertility in source-rocks by measuring apatite content in sediments, provided that sediment mineralogy is not significantly modified by hydrodynamic processes (e.g., selective entrainement, Komar, 2007, Garzanti et al., 2009). Sorting during transport and deposition, or inaccurate sampling and treatment in the laboratory, can in fact severely alter the original provenance signature (Garzanti et al., 2008). Placer deposits are strongly enriched in heavy minerals (Slingerland, 1984; Garzanti and Andò, 2007) thus providing plenty of species to analyze and expediting mineral concentration procedures. However, placers must be carefully avoided when evaluating contribution from different sources, unless hydraulic sorting effects can be quantified and corrected.

Sediment geochemistry is an invaluable tool to readily check for anomalous mineral concentrations, because high concentrations of Y, REE, Th, U, Ti, Zr, Hf, Nb, Ta, and Cr immediately reveal deposits strongly enriched in ultradense minerals (Garzanti et al., 2010b).

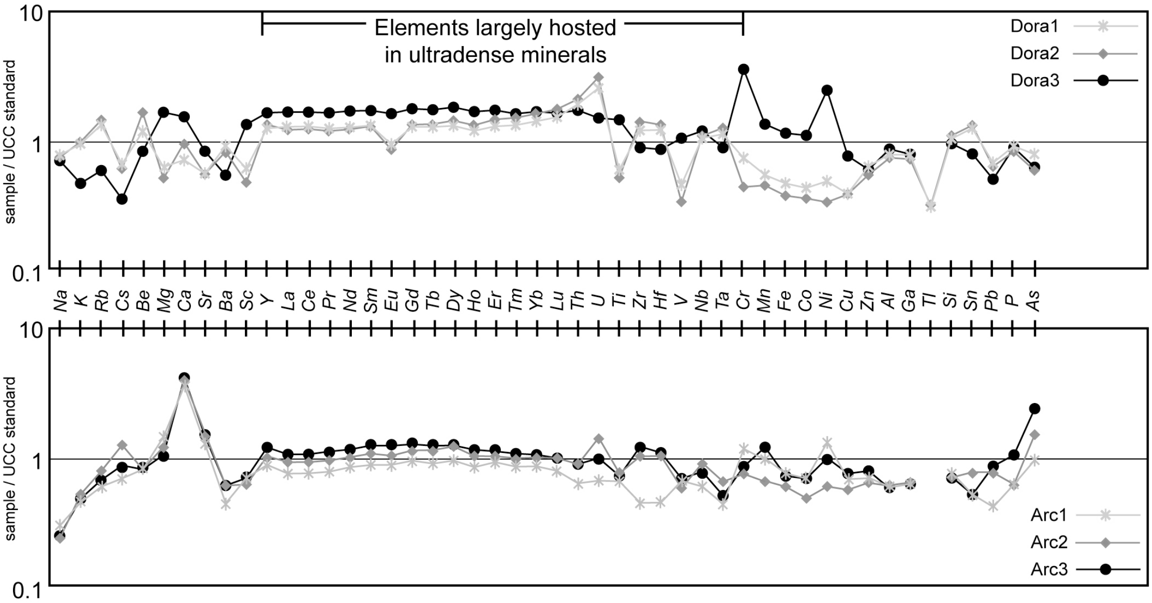

Figure 7.7. *Geochemistry of Dora Baltea and Arc sediments. Multielement diagram arranged according to the periodic table (cf. Garzanti et al., 2010b). Very close concentrations to UCC for elements including Y, REE, Th, U, Zr, Hf, Nb, Ta, and Cr testify to minor hydraulic sorting effects.*

We thus analyzed a quartered sand-fraction of each sample at ACME Analytical Laboratories by ICP-emission spectrometry, after lithium meta-borate/tetra-borate fusion (for detailed information on adopted analytical procedures, standards used, and reproducibility of results for GROUP 4A-4B, see http://acmelab.com). Concentrations were normalized against upper continental crust standards (UCC, Taylor and McLennan, 1985; 1995). Results do not reveal major compositional anomalies, especially for elements listed above, largely hosted in ultradense minerals, thus granting that source-rocks distribution in the basin is faithfully reflected by detrital assemblages (Figure 7.7).

We can thus determine apatite fertility (F) in source-rocks by measuring apatite abundance in processed sediments (table 3), taking also into account the amount of apatite grains lost in finer and coarser size windows and an hydraulic correction factor R (which is equal to 1 in our case, since no hydraulic sorting occurred during sediment deposition and sample treatement):

$$F = \frac{\mathbf{Apw(63 - 250\mu m)} + \mathrm{Apw}(< 63\mu m) + \mathrm{Apw}(> 250\mu m)}{\mathrm{Sediment_w}} + R \qquad (1)$$

Table 7.3. *Determination of mean apatite fertility in sediments. Apatite abundance can be calculated from samples preparation routines.*

Sample	Dm (φ)	Selected grain size (μm)	% on bulk sediment	Processed material (g)	retrieved material after: Gemini shaking-table (g)	Na metatungstate ρ>2.9 g/cm³ (g)	Frantz isodynamic magnetic separation (g)	diiodiomethane ρ<3.2 g/cm³ (g)	Apatite vs. non apatite grains on mount (%)	Apatite (g)	Apatite fertility in 63-250μm (ppm)	Theoretical apatite >250μm	Theoretical apatites 63-250μm	Theoretical apatite <63μm	Theroretical apatite fertility in bulk sediment (ppm)
Dora 1	2,1	63-250	45	406	15,29	7,74	0,67	0,36	70	0,25	**262,0**	40	53	7	**494,4**
Dora 2	2,5	63-250	73	893	32,78	6,13	0,77	0,45	80	0,36	**523,7**	20	72	8	**727,4**
Dora 3	2,1	63-250	47	620	43,28	19,94	0,69	0,25	50	0,13	**193,2**	40	58	2	**333,2**
Arc 1	2,0	63-250	43	371	10,63	7,53	0,34	0,27	25	0,07	**79,1**	42	56	2	**141,3**
Arc 2	2,6	63-250	68	873	51,07	7,09	0,61	0,41	25	0,10	**81,0**	18	75	7	**108,0**
Arc 3	3,1	63-250	51	321	12,96	4,05	0,20	0,13	25	0,03	**51,5**	16	59	25	**87,2**

7.7.2 Calculating sediment budgets

Once sediment composition has been thoroughly checked to highlight potential anomalous mineral concentrations and source-rock mean apatite fertility has been calculated, the relative apatite budget retrieved from fission-track analysis can be converted into a relative sediment budget.

For any given quantity of detrital apatites, fertility estimates can be used to calculate the corresponding amount of sediment needed to provide such an amount of apatites.

For any composite catchment (x+y), formed by sub-basins x and y with fertility F(x) and F(y) and contributing for a proportion *m* and *n* to the total apatite load, sediment partitioning can be expressed as:

$$\frac{\text{Apatite (x + y)}}{\text{F (x + y)}} = \frac{m\text{Apatite (x + y)}}{\text{F(x)}} + \frac{n\text{Apatite (x + y)}}{\text{F(y)}} \qquad (2)$$

Ratios in equation (2) are equal to sediment load in whole catchment, and in sub-basins x and y, respectively. Such an equation allows to combine information retrieved from fission-track analysis and fertility estimates to calculate a relative sediment budget. This approach can be iteratively applied in the case of basins consisting of three sub-basins or more.

7.7.3 Calculating short-term mean erosion rates

This relative sediment budget can be converted into a quantitative budget, allowing erosion rates calculation, provided that the sediment flux through the catchment is known.

In the Dora Baltea basin, annual sediment load is estimated to be ~10^6 tons/yr (Autorità di Bacino Fiume Po, 2001). Sediment load was partitioned between relative contributions of the Western and Eastern blocks. We found that 29% of the sediment load derives from the Western Block, and the remaining 71% derives from the Eastern Block. Sediment yield (i.e. sediment load divided by the area of the basin) is 620 tons/km^{2}yr in the Western Block, and 256 tons/km^{2}yr in the Eastern Block. Average short-term erosion rates were calculated from the sediment yield divided by the density of the material removed, assumed to be 2.72 g/cm^3 (Table 4). Erosion rate calculated for the Western block is 0.23 mm/yr, more than twice the erosion rate in the Eastern block, which is 0.09 mm/yr.

Rivers Arc and Dora Baltea in the easternmost part of their catchment, flow very close to each other, draining the same units and making reasonable the assumption of common erosion rates for the Eastern Block in both drainages. This allows the calculation of mean erosion rates in other sub-basins of the Arc catchment even in the lack of quantitative sediment load estimates for the Arc River.

Results indicate a mean denudation rate of 0.25 mm/yr in the Western Block within the Arc catchment, with higher values in the Belledonne Massif and Dauphinois cover (~ 0.36 mm/yr), and lower values in the Houiller-Subbriançonnais units (~ 0.11 mm/yr).

Table 7.4. *Average long-term (10^6-10^7 a) and short-term (10^2-10^4 a) erosion rates in the Arc and Dora Baltea Valleys. Long-term erosion rates were calculated from detrital apatite populations fission ages, assuming an annealing temperature of 100-120°C and a thermal gradient of 30°/km. Short-term erosion rates are reported according to both fission-track and and bulk petrography estimates.*

Sub-basin	Fission track analysis		Sand petrography
	long-term erosion rates	short-term erosion rates	short-term erosion rates
Dora Baltea River			
Eastern block	**0.16-0.22**	**0.09**	**0.09**
Western block	**0.43-0.68**	**-**	**0.23**
Houiller-Valaisan	-	0.06	0.06
Mont Blanc/Helvetic	-	0.48	0.48
Arc River			
Eastern block	**0.15-0.24**	**0.09**	**0.09**
Western block	**0.38-0.58**	**-**	**0.22**
Houiller-Subbriançonnais	-	0.11	0.12
Belledonne/Dauphinois	-	0.36	0.30

Similarity between erosion rate estimates based on geochronological analyses of accessory minerals with those based on sediment budgets on bulk sediment attests the reliability of our results.

7.8 Erosion patterns and underlying mechanisms

Integrated apatite fission track and petrographic data confirm that erosion rates, both at long-term and short-term timescales, are markedly different in different areas of the Western Alps (Malusà et al., 2005b; Malusà and Vezzoli, 2006). Fission-track analysis of modern sands provides a deeper insight in this issue. Data from the Arc catchment show that the Western Block, although acting as a unique block on a long-term perspective, can be subdivided into two parts with different short-term erosion rates. To the west, the External Massifs and overlying cover sequences display much higher erosion rates than the crustal block bounded by the Frontal Pennine Fault and the Internal Houiller – Longitudinal Faults. Low short-term erosion rates are observed at the core of the belt, in the Eastern Block. The Houillier-Subbriançonnais-Valaisan units, that experienced fast erosion on long-term timescales, confirmed by the age of the peaks in the grain-age distribution, are characterized by much lower erosion rates on a short-term timescale, pointing to a westward migration of erosion foci through time.

The peculiar short-term erosion pattern we document in the northwestern Alps may be determined by a variety of potential exhogenic controlling factors, such as lithology, relief and climate (Schaller et al., 2001; Montgomery and Brandon, 2002; Whipple, 2009).

In the Arc and Dora Baltea catchments lithologies are varied and so is their mean erodibility. However, major variations in lithology can be found within each sub-basins (largely consisting of metagranitoids, schists, and calcareous rocks) rather than among different sub-basins, thus qualititatively averaging out mean erodibility.

If local morphology is invoked as the dominant controlling factor on erosion, this should result in some correlation between erosion patterns and relief or slope. This is not observed in the Dora Baltea and Arc catchments.

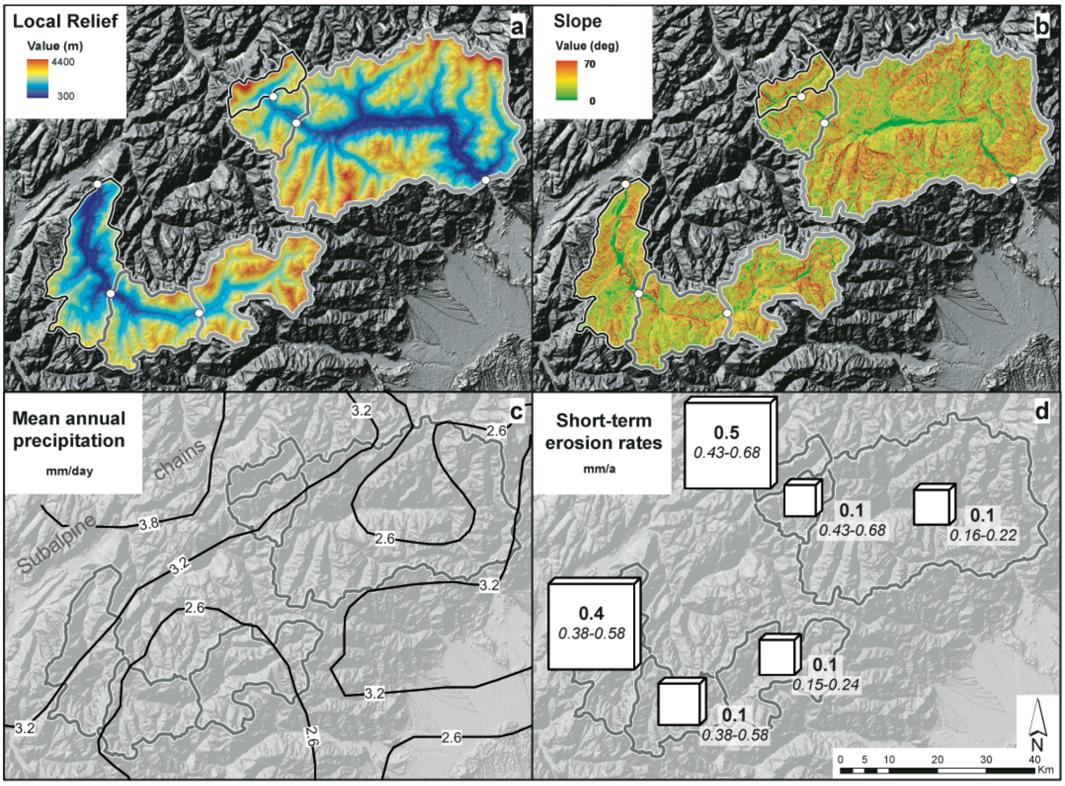

Figure 7.8. *Short term erosion patterns and potential exhogenic controlling factors. Local relief for 1-km radius (a) and local slope (b) from 90m SRTM DEM; precipitation distribution after Frei and Schär, 1998 (c); estimated erosion rates (d) on short-term (10^2-10^4 a) timescales, in bold, and long-term (10^6-10^7 a) timescales, in italics.*

In the Arc Valley, local relief is higher in the Eastern Block (Figure 7.8a), which roughly corresponds to the core of the Alpine belt, and progressively decreases towards the European foreland (mean local relief: 2500 m in the Eastern Block, with a maximum height range of 2670 m; 2050 m for the Houiller-Subbriançonnais units, and a range of 2950 m; and 1550 m in the Belledonne-Dauphinois units, with a maximum vertical drop of 3000 m). Estimated erosion rates show an opposite trend, with erosion focused in the western part of the valley. In the Aosta Valley, relief is more evenly distributed, with the highest peak (Mt. Blanc, 4810 m a.s.l.) located in the Mont Blanc-Helvetic units (mean relief 2600 m, vertical drop 3350 m), whereas the Houiller-Valais units (2150 m mean relief and 2570 m vertical range) and the Eastern Block (2050 m mean relief and 4350 m of vertical height drop) show remarkably lower erosion rates.

Local slopes (Figures 7.8b and 7.9), derived from 90m SRTM DEM, are uniformly distributed within each sub-basin in both the Arc and Dora Baltea catchments, with no clear correlation with estimated erosion rates.

Local slope distribution within the sub-basins is similar in both catchments: in the Dora Baltea basin the westernmost sub-basin (Mont Blanc and Helvetic units) shows slighty higher mean slope angles, whereas in the Arc catchment slope distribution is almost uniform in the whole basin, with the Belledonne-Dauphinois units, yielding higher erosion rates, characterized by the occurrence of wide areas of flat alluvial plains along the Arc River trunk.

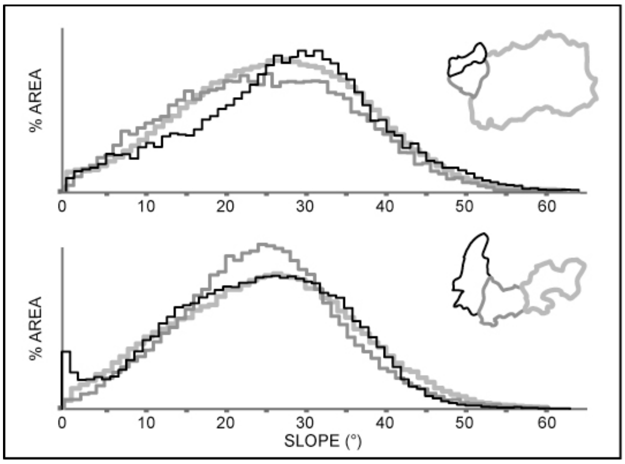

Figure 7.9 *Slope distribution in the three sub-basins in which Dora Baltea (upper panel) and Arc River (lower panel) were subdivided.*

An uneven distribution of precipitations (e.g. Grujic et al., 2006) may alternatively explain the peculiar short-term erosion pattern observed in the Western Alps. Frei and

Schär (1998) document a slight increase in mean annual precipitation west of the External massifs, which represents a major topographic barrier intercepting most of the Atlantic storms headed towards the Alps. Such an increase, however, is less than 1 mm/day in mean annual precipitations, with a maximum concentrated in the Subalpine chains, and thus can hardly explain the sharp change in sediment yield between the External Massifs and the axial belt.

Glaciers are another effective erosional agent (Hallet et al., 1996), but their distribution shows a weak correlation with the erosion pattern. In the Dora Baltea catchment, glaciers are concentrated in the rapidly eroding Mont Blanc massif belonging to the Western Block. In the Arc catchment, instead, small glaciers are concentrated in the Eastern Block, whereas the highest erosion rates are observed in the virtually glacier-free Western Block, where erosion rates are very close to that inferred for the Mont Blanc Massif. The coupled effects of glaciers and relief seem thus to represent a minor controlling factor on erosion rates, as exemplified by erosion rates distribution in the Arc catchment.

A possible control exerted by tectonics on erosion patterns has been recently suggested for long-term timescales (Malusà and Vezzoli, 2006). Progressive westward shift in the Western Alps of both contractional tectonics (Malusà et al 2009b) and erosional foci (this work), now located in the External Massifs, might suggest a tectonic control on erosion patterns also on short-term timescale, but such kind of analysis is beyond the aims of our work.

7.9 Conclusions

Quantification of sediment generation in modern sands, as well as in ancient clastic wedges, represents a fundamental tool to reconstruct basin-wide erosion patterns and sediment yield. Sedimentary petrography represents a fundamental key to unravel sediment mixing because it considers the whole detrital spectrum and readily allows identification of main detrital sources. In complex geological settings, however, where sources are mixed and end-members may not distinct enough mineralogically to allow sufficiently accurate unmixing calculations, may be hard to discriminate by a petrographical/mineralogical approach alone. Detrital geochronology coupled with geochemistry provides a powerful integration tool to check and improve robustness in quantitative sediment budgets, provided that age-signatures in the sources are spread enough to be statistically discriminated, and “fertility” and hydraulic sorting effects are properly taken into account.

The application of such an approach to the northwestern Alps allowed us to unravel a short-term erosion pattern characterized by focused erosion in the External Massifs, both in the eastward-draining Dora Baltea basin and in the westward draining Arc catchment. No clear relationship between erosion and climate or relief is observed in this sector of the belt, where endogenic forces may represent the main controlling factor on both long-term and short-term erosion rates.

References cited:

- Agard, P., Yamato, P., Jolivet, L., and Burov, E., 2009. Exhumation of oceanic blueschists and eclogites in subduction zones: timing and mechanisms. Earth Sci. Rev., 92, 53-79.
- Aitchison, J., 1982. The statistical analysis of compositional data (with discussion). Journal of the Royal Statistical Society, 44, 139-177.
- Aitchison, J., 1986. The statistical analysis of compositional data. Monographs on Statistics and Applied Probability. London, Chapman & Hall, 416 p.
- Aitchison, J., 1989. Measures of location of compositional data sets. Math. Geol., 21, 787-790.
- Aitchison, J., 1997. The one-hour course in compositional data analysis or compositional data analysis is simple. *in* Pawlowsky-Glahn, V., ed. Proceedings of IAMG'97—The third annual conference of the International Association for Mathematical Geology, Volume I, II and addendum, International Center for Numerical Methods in Engineering (CIMNE), Barcelona, 1100 p.
- Aitchison, J., and Greenacre, M., 2002. Biplots of compositional data. Appl. Stat., 51, 375-392.
- Aitchison, J., Barcelo-Vidal, C., Martin-Fernandez, J.A., and Pawlowsky- Glahn, V., 2000. Logratio analysis and compositional distance. Math. Geol. 32, 271-275.
- Allen, R.. Carter, A.. Najman, Y.. Bandopadhyay, P.C.. Chapman, H.J.. Bickle, M.J.. Garzanti, E.. Vezzoli, G.. Andò, S.. Foster, G.L.. and Gerring, C. 2008. New constraints on the sedimentation and uplift history of the Andaman-Nicobar accretionary prism, South Andaman Island. In Draut, A.E.. Clift, P.D.. and Scholl, D.W., eds. Formation and applications of the sedimentary record in arc collision zones. Geol. Soc. Am. Spec. Pap. 436, p. 223-255.
- Amidon, W.H., Burbank, D.W., and Geherels, G.E., 2005. U-Pb zircon ages as a sediment mixing tracer in the Nepal Himalaya. Earth Planet. Sci. Letters, 235, 244-260.
- Andò, S., Bersani, D., Vignola, P., and Garzanti, E., 2009. Raman spectroscopy as an effective tool for high-resolution heavy-mineral analysis : examples from major Himalayan and Alpine fluvio-deltaic systems. Spectrochimica Acta (A), 73, 450-455.
- Arribas, J., Critelli, S., Le Pera, E., and Tortosa, A., 2000. Composition of modern stream sand derived from a mixture of sedimentary and metamorphic source-rocks (Henares River, Central Spain). Sed. Geol., 133, 27-48.
- Artini, E., 1891. Intorno alla composizione mineralogica delle sabbie del Ticino. Giornale di Mineralogia, Cristallografia e Petrologia, 2, 177-195.
- Autorità di Bacino del Fiume Po, 2001. Progetto di piano stralcio per l'assetto idrogeologico (PAI). Parma, Supplemento Straordinario della Gazzetta Ufficiale 166.
- Babist, J., Handy, M.R., Konrad-Schmolke, M., and Hammerschmidt, K., 2006. Precollisional, multistage exhumation of subducted continental crust: the Sesia Zone, western Alps. Tectonics, 25, 1-25.
- Barbarand, J., Carter, A., Wood, I., Hurford, T., 2003. Compositional and structural control of fission-track annealing in apatite. Chem. Geology, 198, 107-137.
- Barbier, R., 1948. Les Zones Ultra-Dauphinoise et Subbriançonnaise entre l'Arc et l'Isère. mémoire pour servir à l'explication de la carte géologique détaillée de la France ». Rapport technique, Ministère de la Production Industrielle.
- Barfety, J.C., Lemoine, M., Mercier, D., Polino, R., Nievergelt, P., Bertrand, J., Dumont, T., Amaudric du Chaffaut, S., Pecher, A., and

Monjuvent, G. 1996. Carte géologique de France (1/50.000), feuille Briançon (823). Orléans, B.R.G.M., 180 p.

- Barrell, J., 1908. Relations between climate and terrestrial deposits. J. Geol. 16, 159-190. 255-295. 363-384.
- Basu, A., 1976. Petrology of Holocene fluvial sand derived from plutonic source rocks – implications to paleoclimatic interpretation. J. Sed. Petrol., 46, 694-709.
- Basu, A., 1985. Influence of climate and relief on compositions of sands released at source areas. *in* Provenance of arenite. G.G. Zuffa (ed), NATO-ASI serie C, 148, Dordrecht, 408 p.
- Basu, A., 1985. Reading provenance from detrital quartz. *in* Provenance of arenite. G.G. Zuffa (ed), NATO-ASI serie C, 148, Dordrecht, 408 p.
- Bearth, P., 1967. Die Ophiolite der Zone von Zermatt-Saas-Fee. Beitr. Geol. Karte Schweiz 132, 1-130.
- Beaumont, C., Jamieson, R.A., Nguyen, M.H., and Lee, B., 2001. Himalayan tectonics explained by extrusion of a low-viscosity crustal channel coupled to focused surface denudation. Nature, v. 414, p. 738-742.
- Beaumont, C.. Jamieson, R.A.. Butler, J.P.. and Warren, C.J. 2009. Crustal structure: a key constraint on the mechanism of ultra-high-pressure rock exhumation. Earth Pl. Sci. Lett., 287, 116-129.
- Bernet, M., Brandon, M.T., Garver, J.I., and Molitor, B., 2004a. Downstream changes of Alpine zircon fission-track ages in the Rhône and Rhine Rivers. J. Sediment. Res., 74, 82-94.
- Bernet, M., Brandon, M.T., Garver, J.I., and Molitor, B., 2004b. Fundamentals of detrital zircon fission-track analysis for provenance and exhumation studies with examples from the European Alps. in Bernet, M. and Spiegel, C. eds. Detrital thermochronology-Provenance analysis, exhumation, and landscape evolution of mountain belts. Boulder, Colorado. Geological Society of America Special Paper, 378, 25-36.
- Bernoulli, D., and Weissert, H. 1985. Sedimentary fabrics in Alpine ophicalcites, South Pennine Arosa Zone, Switzerland. Geology, 13, 755-758.
- Bertrand, J.M., Guillot, F., Laterrier, J., Perruchot, M.P., Aillères, L., and Macaudière, J., 1998. Granitoids from the “Zone Houillère Briançonnaise” (Savoie and Valle d'Aosta, western Alps): geology and U-Pb geochronology. Geodinamica Acta, v. 11, p. 33-49.
- Bhatia, M.R., and Crook, K.A.W., 1986. Trace element characteristics of greywackes and tectonic discrimination of sedimentary basins. Contrib. Mineral. Petrol., 92, 181-193.
- Billheimer, D., Guttorp, P., and Fagan, W., 2001. Statistical interpretation of species composition. Journal of the American Statistical Association, 96, 1205-1214.
- Blatt, H., 1967. Provenance determinations and recycling of sediments. J. Sed. Petrol., 37, 1031-1044.
- Bousquet, R.. Oberhänsli, R.. Goffé, B.. Jolivet, L.. and Vidal, O. 1998. High pressure-low temperature metamorphism and deformation in the Bündnerschiefer of the Engadine window: implications for the regional evolution of the eastern Central Alps. J. metamorphic Geol., 16, 657-674.
- Bousquet, R., Goffé, B., Vidal, O., Oberhänsli, R., and Patriat, M., 2002. The tectono-metamorphic history of the Valaisan domain from the Western to the Central Alps: new constraints on the evolution of the Alps. Geol. Soc. Am. Bull., 114, 207-225.
- Brandon, M.T., 1992. Decomposition of fission-track grain age distributions. Am. J. Sci., 292. 535-564.

- Brandon, K., 2002. Decomposition of mixed grain age distributions using binomfit. On Track, 24, 13-18.
- Breiman, L.. Friedman, J.H.. Olshen, R.. and Stone, C. 1984. Classification and Regression Trees. Belmont, Wadsworth, 358 p.
- Briggs, L.I., 1965. Heavy mineral correlations and provenances. J. Sed. Petrol., 35, 939-955.
- Buccianti, A., Mateu-Figueras, G., and Pawlowsky-Glahn, V., 2006. Compositional data analysis in the geosciences: from theory to practice. Geol. Soc. Lond. Spec. Publ., 264, 224 p.
- Burbank, D.W., 2002. Rates of erosion and their implications for exhumation. Mineralogical Magazine, 66, 25-52.
- Butler, J.C., 1979. Trends in ternary petrologic variation diagrams – facts or fantasy? Am. Mineral., 64, 1115-1121.
- Carlson, W.D., Donelick, R.A., Ketcham, R.A., 1999. Variability of apatite fission-tracks annealing kinetics: I. Experimental results. Am. Mineral., 84, 1213-1223.
- Caron, J.M., 1977. Lithostratigraphie et tectonique des schistes lustrés dans les Alpes Cottiennes septentrionales et en Corse orientale. Sciences Géologiques (Strasboug), 48, 1-326.
- Cavazza, W., 1986. Miocene sediment dispersal in the central Espanola basin, Rio Grande rift, New Mexico, USA. Sediment. Geol., 51, 119-135.
- Cayeux, L., 1929, Les roches sedimentaires de France. Roches siliceuses: Paris, Imprimerie Nationale, 696 p.
- Chalot-Prat, F., 2005. An undeformed ophiolite in the Alps: field and geochemical evidences for a link between volcanism and shallow plate tectonic processes. *in* Foulger, G.R., Natland, J.H., Presnall D.C., and Anderson, D.L. (eds). Plates Plumes and Paradigms: Geological Society of America, Special Paper 388, 751-780.
- Chayes, F., 1960. On correlation between variables of constant sum. J. Geophys. Res., 6, 4185-4193.
- Chayes, F., 1971. Ratio correlation: a manual or students of petrology and geochemistry. Chicago University Press, 99 p.
- Chayes, F., and Velde, D., 1965. On distinguishing basaltic lavas of circum- oceanic and oceanic-island type by means of discriminant functions. Am. J. Sci., 263, 206–222.
- Chopin, C. 1984. Coesite and pure pyrope in high-grade blueschists of the Western Alps: a first record and some consequences. Contrib. Mineral. Petrol. 86,107-118.
- Chopin, C., 2003. Ultrahigh-pressure metamorphism: tracing continental crust into the mantle. Earth Planet. Sci. Lett., 212, 1-14.
- Clift, P.D., Shimizu, N., Layne, G.D., Blusztajn, J.S., Gaedicke, C., Schlüter, H.-U., Clark, M.K., and Amjad, S., 2001. Development of the Indus Fan and its significance for the erosional history of the western Himalaya and Karakoram. Geol. Soc. Am. Bull. 113, 1039-1051.
- Compagnoni, R.. Elter, G.. and Lombardo, B. 1974. Eterogeneità stratigrafica del complesso degli “Gneiss Minuti” nel massiccio cristallino del Gran Paradiso. Mem. Soc. Geol. It., 13, 227-239.
- Compagnoni, R.. Dal Piaz, G.V.. Hunziker, J.C.. Gosso, G.. Lombardo, B.. and Williams, P.F. 1977. The Sesia-Lanzo Zone, a slice of continental crust with Alpine high pressure-low temperature assemblages in the Western Italian Alps. Rend. Soc. It. Miner. Petrol., 33, 281-334.
- Compagnoni, R.. Hirajima, T.. and Chopin, C. 1995. Ultra-high pressure metamorphic rocks in western Alps. In Coleman, R.G., and Wang, X., eds. Ultrahigh-Pressure Metamorphism. New York, Cambridge Univ. Press, p. 206-243.
- Coyle, D.A., Wagner, G.A., 1998. Positioning the titanite fission track

partil annealing zone. Chem. Geol., 149, 117-125.

- Critelli, S., Arribas, J., Le Pera, E., Tortosa, A., Marsaglia, K.M., and Latter, K.K., 2003. The recycled orogenic sand provenance from an uplifted thrust belt, Betic Cordillera, Southern Spain. J. Sed. Res., 73, 72-81.
- Crook, K. A. W. 1960. Classification of arenites. Am. J. Sci., 258, 419-428.
- Crook, K.A.W., 1974. Lithogenesis and geotectonics: the significance of compositional variations in flysch arenites (graywackes). *in* Dott, J.R., and Shaver, R.H., (eds). Modern and ancient geosynclinals sedimentation. Soc. Econ. Pal. Mineral. Spec. Publ., 19, 304-310.
- Dal Piaz, G.V. 1993. Evolution of Austro-Alpine and Upper Penninic basement in the northwestern Alps from Variscan convergence to post-Variscan extension. In von Raumer, J. F., and Neubauer, F., eds. Pre-Mesozoic geology in the Alps. Berlin, Springer, p. 249-265.
- Dal Piaz, G.V., and Lombardo, B., 1986. Early Alpine eclogite metamorphism in the Penninic Monte Rosa-Gran Paradiso basement nappes of the northwestern Alps. Geol. Soc. Am. Mem., 164, 249-265.
- Daunis-I-Estadella, J., Barcélo-Vidal, C., and Buccianti, A., 2006. Exploratory compositional data analysis. Geol. Soc. London Spec. Publ., 264, 161-174.
- Davis, J.C., 1986. Statistics and data analysis in geology. 2nd edition, Wiley, New York, 646 p.
- DeCelles, P.G., and Hertel, F. 1989. Petrology of fluvial sands from the Amazonian foreland basin, Peru and Bolivia. Geol. Soc. Am. Bull., 101, 1552-1562.
- DeCelles, P.G., Gehrels, G.E., Quade, J., Ojha, T.P., Kapp, P.A., and Upreti, B.N., 1998. Neogene foreland basin deposits, erosional unroofing, and the kinematic history of the Himalayan fold-thrust belt, western Nepal. Geol. Soc. Am. Bull., 110, 2-21.
- DeCelles, P.G.. Gehrels, G.E.. Najman, Y.. Martin, A.J.. Carter, A.. and Garzanti, E. 2005. Detrital geochronology and geochemistry of Cretaceous-Early Miocene strata of Nepal: implications for timing and diachroneity of initial Himalayan orogenesis. Earth Planet. Sci. Lett., 227, 313-330.
- Deer, W.A., Howie, R.A., Zussmann, J., 1969. An introdiction to the rock-forming minerals. John Wiley and sons, New York.
- Desmons, J. 1992. The Briançon basement (Pennine Western Alps): mineral composition and polymetamorphic evolution. Schweiz. Mineral. Petrogr. Mitt., 72, 37-55.
- Di Giulio, A. 1992. The evolution of the western Ligurian Flysch Units and the role of mud diapirism in ancient accretionary prisms (Maritime Alps, Northwestern Italy). Geol. Rundsch., 81, 655-668.
- Di Giulio, A., Tribuzio, R., Ceriani, A., and Riccardi, M.P., 1999. Integrated analyses constraining the provenance of sandstones, a case study: the Section Peak Formation (Beacon Supergroup, Antarctica). Sed. Geol., 124, 169-183.
- Di Giulio, A., Carrapa, B., Fantoni, R., Gorla, L., and Valdisturlo, A., 2001. Middle Eocene to Early Miocene sedimentary evolution of the western Lombardian segment of the South Alpine foredeep (Italy). Int. J. Earth Sciences, 90, 534-548.
- Di Giulio, A., Ceriani, A., Ghia, E., and Zucca, F., 2003. Composition of modern stream sands derived from sedimentary source rocks in a temperate climate (Northern Apennines, Italy). Sed. Geology, 158, 145-161.
- Dick, A.B., 1887. On zircon and other minerals contained in sands. Nature, 36, 1-92.
- Dickinson, W.R., 1970. Interpreting detrital modes of greywacke and arkose. J. Sed. Petrol., 40, 695-707.

- Dickinson, W.R., 1974. Plate tectonics and sedimentation. *in* Dickinson, W.R. (ed). Tectonics and sedimentation. Soc. Econ. Pal. Mineral. Spec. Publ., 22, 1-27.
- Dickinson, W.R. 1985. Interpreting provenance relations from detrital modes of sandstones. In Zuffa, G.G., ed. Provenance of arenites. NATO ASI Series 148. Dordrecht, Reidel, p. 333-361.
- Dickinson, W.R., 2008. Impact of differential zircon fertility of granitoid basement rocks in North America on age populations of detrital zircons and implications for granite petrogenesis. Earth Planet. Sci. Letters, 275, 80-92.
- Dickinson W.R., and Rich, E.I., 1972. Petrologic intervals and petrofacies in the Great Valley sequence, Sacramento Valley, California, Geol. Soc. Amer. Bull., 83, 3007–3024.
- Dickinson, W.R., and Suczek, C.A., 1979. Plate tectonics and sandstone composition. Am. Ass. Petrol. Geol. Bull., 63, 2164-2172.
- Dickinson, W. R., and Valloni, R., 1980. Plate settings and provenance of sands in modern ocean basins. Geology, 8, 82-86.
- Doglioni, C. 1994. Foredeep versus subduction zones. Geology, 22, 271-274.
- Doglioni, C.. Carminati, E.. Cuffaro, M.. and Scrocca, D. 2007. Subduction kinematics and dynamic constraints. Earth Sci. Rev., 83, 125-175.
- Doglioni, C.. Harabaglia, P.. Merlini, S.. Mongelli, F.. Peccerillo, A.. and Piromallo, C. 1999. Orogens and slabs vs. their direction of subduction. Earth Sci. Rev., 45, 167-208.
- Donelick, R.A., 1991. Crystallographic orientation dependence of mean etchable fission-track length in apatite: an empirical model and experimental observation. Am. Mineral., 76, 83-91.
- Donelick, R.A., 1993. A method of fission-track analysis utilizing bulk chemical etching of apatite. Patent 658800 USA.
- Donelick, R.A., Ketcham, R.A., Carlson, W.D., 1999. Variability of apatite fission track kinetics: II. Crystallographic orientation effects. Am. Mineral., 84, 1224-1234.
- Donelick, R.A., O'Sullivan P.B., Ketchm, R.A., 2005. Apatite fission-tracks analyis. Rev. Mineral. Geochem., 58, 49-94.
- Dorsey, R.J., 1988. Provenance evolution and unroofing history of a modern arc-continent collision: evidence from petrography of Plio-Pleistocene sandstones, eastern Taiwan. J. Sed. Petrol., 58, 208-218.
- Draper, N.R., and Smith, H., 1998. Applied regression analysis. New York, Wiley, 736 p.
- Dryden, A.L., 1931. Accuracy in percentage representation of heavy mineral frequencies. Proceedings of the Natinal Academy of Sciences, 17, 233-238.
- Dunkl, I., 2002. Trackkey: a Windows program for calculation and graphical presentation of fission track data. Computers and Geosciences, 28, 3-12.
- Dunkl, I., and Székely, B., 2002. Component analysis with visualization of fitting – PopShare, a Windows program for data analysis. Goldschmidt Conference Abstracts 2002, Geochimica et Cosmochimica Acta 66/A: 201.
- Dutta, P.K., and Suttner, L.J., 1986. Alluvial sandstone composition and paleoclimate, II Authignic mineralogy, J. Sed. Petrol., 56, 346-358.
- Eckart, C., Young, G., 1936. The approximantion of a matrix by another of lower rank. Phsychometrika, 1, 211-218.
- Edelman, C.H. 1931. Over bloedverwantschap van sedimenten verband met het zware mineralen onderzoeck. Geol. Minjb., 10, 122-124.
- Edelman, C.H. 1933. Petrologische provincies in het nederlandsche

Kwatair. Ph.D. Thesis, Centen’s Uitg. Mij., Amsterdam, 104pp.

- Einsele, G.. Ratschbacher, L.. and Wetzel, A. 1996. The Himalayan-Bengal Fan denudation-accumulation system during the past 20 Ma. J. Geol., 104,163-184.
- Ellenberger, F., 1958. Etude géologique du pays de Vanoise (Savoie). Mém. Service Carte Géol. France, 50, 561 p.
- Elter, G., and Elter, P., 1965. Carta geologica della regione del Piccolo S. Bernardo (versante italiano). Note illustrative. Mem. Ist. Geol. Min. Univ. Padova, 25, 53 p.
- Elter, G.. Elter, P.. Sturani, C.. and Weidmann, M. 1966. Sur la prolongation du domaine ligure de l' Apennin dans le Monférrat et les Alpes et sur l' origine de la nappe de la Simme s.l. des Préalpes romandes et chablaisiennes. Archives des Sciences, 19, 279-374.
- Engi, M.. Bousquet, R.. and Berger, A. 2004. Explanatory notes to the map: metamorphic structure of the Alps. Central Alps. Mitt. Österr. Miner. Ges., 149, 157-173.
- Ernst, W.G.. Maruyama, S.. and Wallis, S. 1997. Buoyancy-driven, rapid exhumation of ultrahigh-pressure metamorphosed continental crust. Proc. Natl. Acad. Sci. USA, 94, 9532-9537.
- Fabre, J., 1961. Contribution a l'étude de la Zone Houillère en Maurienne et en Tarentaise (Alpes de Savoie). Mem. B.R.G.M., 2, 1-315.
- Faupl, P., and Wagreich, M. 1999. Late Jurassic to Eocene palaeogeography and geodynamic evolution of the Eastern Alps. Mitt. Österr. Miner. Ges., 92, 79-94.
- Filzmoser, P., Hron, H., and Templ, M., 2009. Discriminant analysis for compositional data and robust parameter estimation. http://www.statistik.tuwien.ac.at.
- Finlayson, D.P., Montgomery, D.R., and Hallet, B., 2002. Spatial coincidence of rapid inferred erosion with young metamorphic massifs in the Himalayas. Geology, 30, 219-222.
- Fleet, W.F., 1926. Petrological notes on the Old Red Sandstone of the West Midlands. Geol. Mag., 63, 505-519.
- Fleischer, R.L., Price, P.B., Walker, R.M., 1975. Nuclear tracks in solids. University of California Press, Berkeley.
- Folk, R.L., 1954. The distiction between grain size and mineral composition in sedimentary rocks nomenclature. J. Geol., 62, 344-359.
- Folk, R.L., 1974. Petrology of sedimentary rocks. Hephill Publishing Co., Austin, 184 p.
- Fontana, D., Zuffa, G.G., and Garzanti, E., 1989. The interaction of eustasy and tectonism from provenance studies of the Eocene Hecho Group Turbidites (South-Central Pyrenees, Spain). Basin Research, 2, 223-237.
- Foster, G.L., and Carter, A., 2007. Insights into the pattern and locations of erosion in the Himalaya. A combined fission-track and in situ Sm-Nd isotopic study of detrital apatite. Earth Planet. Sci. Lett., 257, 407-418.
- Friedlander, G., Kennedy, J.W., Macias, E.S., Miller, J.M., 1981. Nuclear and radiochemistry. John Wiley and sons, New York.
- Frei, C., and Schär, C., 1998. A precipitation climatology of the Alps from high-resolution rain-gauge observation. Int. J. Climatol., 18, 873-900.
- Frey, M.. Desmons, J.. and Neubauer, F. 1999. The new metamorphic map of the Alps. Schweiz. Mineral. Petrogr. Mitt., 79, 1-209.
- Fuentes, F., DeCelles, P.G., and Gehrels, G.E., 2009. Jurassic onset of foreland basin deposition in northwestern Montana, USA: implications for along-strike synchroneity of Cordilleran orogenic activity. Geology, 37, 379-382.
- Fügenschuh, B., and Schmid, S.M., 2003. Late stages of deformation

and exhumation of an orogen constrained by fission-track data: a case study in the Western Alps. Geol. Soc. Am. Bull., 115, 1425-1440.

- Gabriel, K.R., 1971. The biplot – a graphic display of matrices with application to principal components analysis. Biometrika, 58, 453-467.
- Gabudianu Radulescu, I., Rubatto, D., Gregory, C., and Compagnoni, R., 2009. The age of HP metamorphism in the Gran Paradiso Massif, Western Alps: a petrological and geochronological study of the "slivery micaschists". Lithos, 110, 95-108.
- Galbraith, R.F., 1988. Graphical display of estimates having differing standard errors. Technometrics, 30, 271-281.
- Galbraith, R.F., 1990. The radial plot: graphical assessment of spread in ages. Nucl. Tracks, 17, 207-214.
- Galbraith, R.F., Laslett, G.M., 1993. Statistical models for mixed fission track ages. Nucl. Tracks, 21, 459-470.
- Galehouse, J.S., 1969. Counting grain mounts: number percentages vs. number frequency. J. Sed. Res., 39, 812-815.
- Galehouse, J.S. 1971. Point counting, In: Carver, R.E., ed. Procedures in sedimentary petrology. New York, Wiley, p. 385-407.
- Gallagher, K., Brown, R., Johnson, C., 1998. Fission track analysis and its applications to geological problems. Annu. Rev. Earth Planet. Sci., 26, 519-572.
- Gansser, A. 1982. The morphogenic phase of mountain building. In: Hsü, K.J., ed. Mountain building processes. London, Academic Press, p. 221-228.
- Garzanti, E., 1991. Non-carbonate instrabasinal grains in arenites: ther recognition, significance, and reltionship to eustatic cycles and tectonic setting. J. Sedim. Petrol., 61, 959-975.
- Garzanti, E., and Vezzoli, G., 2003. A classification of metamorphic grains in sands based on their composition and grade. J. Sediment. Res., 73, 830-837.
- Garzanti, E., and Andò, S. 2007a. Heavy-mineral concentration in modern sands: implications for provenance interpretation. In Mange, M., and Wright, D., eds. Heavy Minerals in Use. Developments in Sedimentology Series 58. Amsterdam, Elsevier, p. 517-545.
- Garzanti, E., and Andò, S. 2007b. Plate tectonics and heavy-mineral suites of modern sands. In Mange, M., and Wright, D., eds. Heavy Minerals in Use. Developments in Sedimentology Series 58. Amsterdam, Elsevier, p. 741-763.
- Garzanti E., and Malusà, M.G., 2008. The Oligocene Alps: domal unroofing and drainage development during early orogenic growth. Earth Planet. Sci. Lett., 268, 487-500.
- Garzanti, E., Andò, S. and Scutellà, M., 2000. Actualistic ophiolite provenance: the Cyprus case. J. Geol., 108, 199-218.
- Garzanti, E., Vezzoli, G., and Andò, S., 2002. Modern sand from obducted ophiolite belts (Oman, U.A.E.). J. Geol., 110, 371-391.
- Garzanti, E., Vezzoli, G., Lombardo, B., Andò, S., Mauri, E., Monguzzi, S., 2004a. Collision-orogen provenance (western Alps).: detrital signatures and unroofing trends. J. Geol., 112, 145-164.
- Garzanti, E., Vezzoli, G., Andò, S., France-Lanord, C., Singh, S.K., and Foster, G., 2004b. Sand petrology and focused erosion in collision orogens: the Brahmaputra case. Earth. Planet. Sci. Lett., 220, 157-174.
- Garzanti, E., Vezzoli, G., Andò, S., Paparella, P., and Clift, P.D., 2005. Petrology of Indus River sands: a key to interpret erosion history of the Western Himalayan Syntaxis. Earth Planet. Sci. Letters, 229, 287-302.
- Garzanti, E., Andò, S., and Vezzoli, G., 2006a. The continental crust as a source of sand (Southern Alps

cross section, northern Italy). J. Geol., 114, 533-554.

- Garzanti, E., Andò, S., Vezzoli, G., Ali Abed Megid, A., and El Kammar, A., 2006b. Petrology of Nile river sands (Ethipia and Sudan): sediment budget and erosion patterns. Earth and Planet. Sci. Letters, 252, 327-341.
- Garzanti, E., Doglioni, C., Vezzoli, G., and Andò, S., 2007a. Orogenic belts and orogenic sediments provenances. J. Geol., 115, 315-334.
- Garzanti, E., Vezzoli, G., Andò, S., Lavé, J., Attal, M., France-Lanord, C., and DeCelles, P., 2007b. Quantifying sand provenance and erosion (Marsyandi River, Nepal Himalaya). Earth Planet. Sci. Lett., 258, 500-515.
- Garzanti, E., Andò, S., and Vezzoli, G., 2008. Settling equivalence of detrital minerals and grain-size dependence of sediment composition. Earth Planet. Sci. Lett., 273, 138-151.
- Garzanti, E., Andò, S., and Vezzoli, G., 2009b. Grain-size dependence of sediment composition and environmental bias in provenance studies. Earth Planet. Sci. Lett., 277, 422-432.
- Garzanti, E., Resentini, A., Vezzoli, G., Andò, S., Malusà, M.G., Padoan, M., and Paparella, P., 2010a. Detrital fingerprints of fossil continental-subduction zones (Axial Belt Provenance, European Alps). J. Geol., 118, 341-362.
- Garzanti, E., Andò, S., France-Lanord, C., Vezzoli, G., Censi, P., Galy, V., and Najman, Y., 2010b. Mineralogical and chemical variability of fluvial sediments. 1. Bedload sand (Ganga-Brahmaputra, Bangladesh). Earth. Planet. Sci. Lett., 220, 157-174.
- Gazzi, P., 1966. Le arenarie del flysch sopracretaceo dell’Appennino modenese: correlazioni con il flysch di Monghidoro. Miner. Petrogr. Acta, 12, 69-97.
- Gebauer, D. 1993. The pre-Alpine evolution of the continental crust of the Central Alps: an overview. In von Raumer, J. F., and Neubauer, F., eds. Pre-Mesozoic geology in the Alps. Berlin, Springer, p. 93-117.
- Gilbert, C.M., 1954. Sedimentary rocks. *in* Williams, H., Turner, F.J., and Gilbert, C.M., (eds). Petrography. San Francisco, W.H. Freeman and Co, 406 p.
- Girty, G.H., Hanson, A.D., Yoshinobu, A.S., Knaack, C., and Johnson, D., 1993. Provenance of Paleozoic mudstones in a contact metamorphic aureole determined by rare earth elements, Th, and Sc analyses, Sierra Nevada, California. Geology, 21, 363-366.
- Gleadow, A.J.W., Brown R.W., 1999. Fission track thermochronology and long term denudational respond to tectonics. In Geomorphology and Global Tectonics, M.A. Summerfeld (ed), John Wiley and sons, New York.
- Gleadow, A.J.W., Duddy, I.R., 1981. a natural long-term track annealing experiment for apatite. Nucl. Tracks Radiat. Meas., 5, 169-174.
- Glodny, J.. Ring, U.. Kühn, A.. Gleissner, P.. and Franz, G. 2005. Crystallization and very rapid exhumation of the youngest Alpine eclogites (Tauern Window, Eastern Alps) from Rb/Sr mineral assemblage analysis. Contrib. Mineral. Petrol., 149, 699–712.
- Goguel., J., 1962. Tectonics. San Francisco, Freeman. 384 p.
- Gorelikova, N., Tolosana-Delgado, R., Pawlowsky-Glahn, V., Khanchuk, A., and Gonevchuk, V., 2006. Discriminating geodynamical regimes of tin ore formation using trace element composition of cassiterite: the Sikhote’Alin case (Far Eastern Russia). *in* A. Buccianti, A., G. Mateu-Figueras, G., and Pawlowsky-Glahn, V., (eds), Compositional data analysis in the geosciences: from theory to practice, 43–57. Geological Society, London.
- Graham, S.A.. Dickinson, W.R.. and Ingersoll, R.V. 1975. Himalayan-Bengal model for flysch dispersal in

the Appalachian-Ouachita system. Geol. Soc. Am. Bull., 86, 273-286.

- Grantham, J.H., and Velbel, M.A., 1988. The influence of climate and topography on rock fragments abundance in modern fluvial sands of the southern Blue Ridge Mountains, North Carolina. J. Sed. Petrol., 58, 219-227.
- Groppo, C., Beltrando, M., and Compagnoni, R., 2009. P-T path of the UHP Lago di Cignana and adjoining meta-ophiolitic units: insights into the evolution of subducting tethyan slab. J. Metam. Geol., 27, 207-231.
- Grujic, D., Coutand, I., Bookhagen, B., Bonnet, S., Blythe, A., Duncan, C., 2006. Climatic forcing of erosion, landscape, and tectonics in the Bhutan Himalayas. Geology, 34, 801-804.
- Habler, G.. Thöni, M.. and Sölva H. 2006. Tracing the high pressure stage in the polymetamorphic Texel Complex (Austroalpine basement unit, Eastern Alps): P–T–t–d constraints. Miner. Petrol., 88, 269-296.
- Hacker, B.R.. McClelland, W.C.. and Lihou, J.C. 2006. Ultrahigh-pressure metamorphism: deep continental subduction. Geol. Soc. Am. Special Paper 403, 206 p.
- Hallet, B., Hunter, L., and Bogen, L., 1996. Rates of erosion and sediment evacuation by glaciers: a review of field data and their implications. Glob. Planet. Change, 12, 213-235.
- Handy, M.R. 1990. The exhumation of cross sections of the continental crust: structure, kinematics and rheology. In Salisbury, M.H., and Fountain, D.M., eds. Exposed cross-sections of the continental crust. Amsterdam, Kluwer, p. 485-507.
- Hasabe, N., Barbarand, J., Jarvis, K., Carter, A., Hurford, A.J., 2004. Apatite fission-track chronometry using laser ablation ICP-MS. Chem. Geol. 207, 135-145.
- Hastie, T., Tibshirani, R., Friedman, J.H., 2001. The elements of statistical learning: data mining, inference, and prediction. Springer, Berlin, 552 p.
- Heberer, B., Roser, G., Behrmann, J.H., Rahn, M., and Kopf, A., 2010. Holocene sediments from the Southern Chile Trench: a record of active margin magmatism, tectonics, and palaeoseismicity. J. Geol. Soc. London, 167,539-553.
- Hoinkes, G.. Koller, F.. Rantisch, G.. Dacks, A.V.. Höck, V.. Neubauer, F.. and Schuster, R. 1999. Alpine metamorphism of the Eastern Alps. Schweiz. Mineral. Petrogr. Mitt., 79, 155-181.
- Howaed, J.L., 1994. A note on the use of statistics in reporting detrital clastic compositions. Sedimentology, 41, 747-753.
- Hughes, J.M., Cameron, M., Crowley, K.D., 1989. Structural variation in natural F, OH, and Cl apatites. Am. Mineral., 88, 817-829.
- Hurford, A.J., 1990. Standardization of fission-track dating calibration: reccomendation by the Fission Track Working Group of the I.U.G.S. Subcommission on Geochronology. Chemical Geology, 80, 171-178.
- Hurford, A.J., Carter, A., 1991a. The role of fission track dating in discrimination of provenance. in Morton, A.C., Todd, S.P., and Haughton, P.D.W., eds. Developments in Sedimentary Provenance Studies. Geological Society Special Publication 57.
- Hurford, A.J, Hunziker, J.C., and Stockhert, B., 1991b. Constraints on the late thermotectonic evolution of the Western Alps. Evidences for episodic rapid uplift. Tectonics, 10, 758-769.
- Inger, S.. Ramsbotham, W.. Cliff, R.A.. and Rex, D.C. 1996. Metamorphic evolution of the Sesia-Lanzo Zone, Western Alps: time constraints from multi-system geochronology. Contrib. Mineral. Petrol., 126, 152-168.
- Ingersoll, R.V. 1983. Petrofacies and provenance of Late Mesozoic forearc basin, northern and central California. Am. Ass. Petr. Geol. Bull., 67, 1125-1142.

- Ingersoll, R.V., 1990. Actualistic sandstone petrofacies: discriminating modern and ancient source-rocks. Geology, 18, 733-736.
- Ingersoll, R.V., and Suczek, C.A. 1979. Petrology and provenance of Neogene sand from Nicobar and Bengal Fans, DSDP Sites 211 and 218. J. Sediment. Petrol., 49, 1217-1228.
- Ingersoll, R.V., Bullard, T.F., Ford, R.L., Grimm, J.P., Pickle, J.D., and Sares, S.W., 1984. The effect of grain size on detrital modes: a test of the Gazzi-Dickinson point-counting method. J. Sediment. Petrol., 54, 103-106.
- Ingersoll, R.V., Kretchmer, A.G., and Valles, P.K., 1993. The effect of sampling scale on actualistic sandstone petrofacies. Sedimentology, 40, 937-953.
- Ingersoll, R.V.. Dickinson, W.R.. and Graham, S.A. 2003. Remnant-ocean submarine fans: largest sedimentary systems on Earth. In Chan, M.A., and Archer, A.W., eds. Extreme depositional environments: mega end-members in geologic time. Geol. Soc. Am. Spec. Pap. 370, p. 191-208.
- Jonckheere, R.C., Wagner, G.A., 2000. On the occurrence of anomalous fission tracks in apatite and titanite. Am. Mineral., 85, 1744-1753.
- Kerckhove, C. 1969: La “zone du Flysch” dans les nappes d’Embrunais-Ubaye. Géol. Alpine, 45, 5-204.
- Ketcham, R.A., Carter, A., Donelick, R.A., Barbarand, J., Hurford, A.J., 2007. Improved modelling of fission-track annealing in apatite. Am. Mineral., 92, 799-810.
- Komar, P.D., 2007. The entrainment, transport and sorting of heavy minerals by waves and currents. In Mange, M., and Wright, D., eds. Heavy minerals in use. Developments in Sedimentology Series 58. Amsterdam, Elsevier.
- Koppes, M.N., and Montgomery D.R., 2009. The relative efficiency of fluvial and glacial erosion over modern to orogenic timescales. Nature Geoscience, 2, 644-647.
- Korup, O., 2005 Large landslides and their effect on sediment flux in South Westland, New Zealand. Earth Surf. Process. Landforms, 30, 305-323.
- Kovacs, L.O., Kovacs, G.P., Martin-Fernandez, J.A., and Barcelo-Vidal, C., 2006. Major-oxide compositional discrimination in Cenozoic volcanites of Hungary. *in* Buccianti, A., Mateu-Figueras, G., and Pawlowsky-Glahn, V., (eds), Compositional data analysis in the geosciences: from theory to practice, 11–23. Geological Society, London.
- Krumbein, W.C., 1962. Open and closed number systems in stratigraphic mapping. Am. Assoc. Petroleum Geol. Bull., 46, 2229-2245.
- Krynine, P.D., 1935. Arkose deposits in the humid tropics. A study of sedimentation in southern Mexico. Amer. J. Sci., 29, 353-363.
- Krynine, P.D., 1936. Geomorphology and sedimentation in the humid tropics. Amer. J. Sci., 32, 292-306.
- Krynine, P.D., 1941. Paleogeogtaphic and tectonic significance of arkoses. Geol,. Soc. Amer. Bull., 52, 1918-1919.
- Krynine, P.D., 1948. The megascopic study and field classification of sedimentary rocks. J. Geol. 56, 130-165.
- Krzanowski, W.J., 1988. Principles in multivariate analysis: a user’s perspective. Oxford statistical series, 3. Clarendon Press, Oxford, 587 p.
- Kurz, W.. Neubauer, F.. Genser, J.. and Dachs, E. 1998. Alpine geodynamic evolution of passive and active continental margin sequences in the Tauern Window (eastern Alps, Austria, Italy): a review. Geol. Rundsch., 87, 225-242.
- Lal, D., Rajan, R.S., Tamhane, A.S., 1969. Chemical composition of nuclei of Z>22 in cosmic rays using

meteoric minerals as detectors. Nature, 221, 33-37.

- Le Pera, E., Critelli, S., Sorriso-Valvo, M., 2001a. Weathering of gneiss in Calabria, Southern Italy. Catena, 42, 1-15.
- Le Pera, E., Arribas, J., Critelli, S., Tortosa, A., 2001b. The effects of source rocks and chemical weathering on the petrogenesis of siliciclastic sand from the Neto River (Calabria, Italy): implications for provenance studies. Sedimentology, 48, 357-378.
- Lederer, C.M., Hollander, J.M., Perlman, I., 1967. Table of isotopes, 6th Edition. John Wiley, New York.
- Lemoine, M., and de Graciansky, P.C. 1988. Histoire d'une marge continentale passive: les Alpes occidentales au Mésozoıque—introduction. Bull. Soc. Géol. Fr., 8, 597-600.
- Lihou, J.C., and Allen, P.A. 1996. Importance of inherited rift margin structures in the early North Alpine Foreland Basin, Switzerland. Basin Research, 8, 425-442.
- Lombardo, B.. Nervo, R.. Compagnoni, R.. Messiga, B.. Kienast, J.R.. Mevel, C.. Fiora, L.. Piccardo, G.B.. and Lanza, R. 1978. Osservazioni preliminari sulle ofioliti metamorfiche del Monviso (Alpi occidentali). Rend. Soc. It. Miner. Petrol., 34, 253-305.
- Malusà, M.G. and Vezzoli, G., 2006. Interplay between erosion and tectonics in the Western Alps. Terra Nova, 18, 104-108.
- Malusà, M.G., Mosca, P., Borghi, A., Dela Pierre, F., and Polino, R., 2002. Approccio multidisciplinare per la ricostruzione dell'assettotettono-stratigrafico e dell'evoluzione metamorfico-strutturale di un settore di catena orogenica: l'esempio dell'Alta Val di Susa (Alpi occidentali). Mem. Soc. Geol. Ital., 59, 249-257.
- Malusà, M.G., Polino, R., and Martin, S., 2005a. The Gran San Bernardo nappe in the Aosta valley (western Alps): a composite stack of distinct continental crust units. Bull. Soc. Geol. France, 176, 417-431.
- Malusà, M.G., Polino, R., Zattin, M., Bigazzi, G., Martin, S., and Piana, F., 2005b. Miocene to Present differential exhumation in the Western Alps: Insights from fission track thermochronology. Tectonics, 24, 1-23.
- Malusà, M.G., Zattin, M., Andò, S., Garzanti, E., and Vezzoli, G., 2009a. Focused erosion in the Alps constrained by fission-track ages on detrital apatites. Geol. Soc. London Spec. Publ., 324, 141-152.
- Malusà, M.G., Polino, R., and Zattin, M., 2009b. Strain partitioning in the axial NW Alps since the Oligocene. Tectonics, 28, 1-26.
- Manatschal, G., and Bernoulli, D. 1999. Architecture and tectonic evolution of nonvolcanic margins: Present-day Galicia and ancient Adria. Tectonics, 18, 1099-1119.
- Mange-Rajetzky, M., 1995. Subdivision and correlation of monotonous sandstone sequences using high-resolution heavy mineral analysis, a case study: the Triassic of the Central Graben. Geological Society London, Spec. Publ., 89, 23-30.
- Mange, A., and Maurer, H.F.W. 1992. Heavy minerals in colour. London, Chapman and Hall, 147 p.
- Martin-Fernandez, J. A., 2001. Medidas de diferencia y clasificacion no paramétrica de datos composicionales. Ph. D. thesis, Universitat Politècnica de Catalunya, Barcelona.
- Martin-Fernandez, J.A., and Thio-Henestrosa, S., 2006. Rounded zeros: some practical aspects for compositional data. Geol. Soc. London Spec. Publ., 264, 191-201.
- Martin-Fernandez, J.A., Barcelo-Vidal, C., and Pawlowsky-Glahn, V., 1998. A critical approach to non-parametric classification of compositional data. *in* Rizzi, A., Vichi, M., and Bock, H.H. (eds.). Advances in Data Science and Classification (Proceedings of the 6th Conference of the International

Federation of Classification Societies (IFCS'98). Springer-Verlag, Berlin, 677 p.

- Martin-Fernandez, J. A., Bren, M., Barcelo-Vidal, C., and Pawlowsky-Glahn, V., 1999. A measure of difference for compositional data based on measures of divergence. *in* Lippard, S. J., Næss, A., and Sinding-Larsen , N., (eds.). Proceedings of IAMG'99. The fifth annual conference of the International Association for Mathematical Geology. Tapir, Trondheim, 784 p.
- Martin-Fernandez, J.A., Barcelo-Vidal, C., and Pawlowsky-Glahn, V., 2003. Dealing with zeros and missing values in compositional data sets using nonparametric imputation. Math. Geol., 35, 253-278.
- Meschede, M., 1986. A method of discriminating between different types of mid-ocean ridge basalts and continental tholeiites with the Nb-Zr-Y diagram. Chem. Geology, 56, 207-218.
- Miller, C.. Thöni, M.. Konzett, J.. Kurz, W., and Schuster, R. 2005. Eclogites from the Koralpe and Saualpe type-localities, Eastern Alps, Austria. Mitt. Österr. Miner. Ges., 150, 227-263.
- Milliman, J.D., and Meade, R.H., 1983. World-wide delivery of river sediments to the oceans. J. Geol., 91, 1-21.
- Milner, H.B., 1922. The nature and origin of the Pliocene deposits of Cornwall and their bearing on the Pliocene geography of the South Wales of England. Quarterly Journal of the Geological Society of London, 78, 348-377.
- Moecher, D.P., and Samson, S.D., 2006. Differential zircon fertility of source terranes and natural bias in the detrital zircon record: Implications for sedimentary provenance analysis. Earth Planet. Sci. Lett, 247, 252-262.
- Montgomery, D.R., and Brandon, M.T., 2002. Topographic controls on erosion rates in tectonically active mountain ranges. Earth Planet. Sci. Letters, 201, 481-489.
- Morton, A.C., 1991. Geochemical studies of detrital minerals and their application to provenance studies. *in* Morton, A.C., Todd, S.P., and Haughton, P.D.W. (eds). Developments in Sedimentary Provenance Studies. Geol. Soc. Spec. Publ., 57, 31-45.
- Morton, A.C., and Hallsworth, C., 1994. Identifying provenance-specific features of detrital heavy mineral assemblages in sandstones. Sed. Geol., 90, 241-256.
- Morton, A., and Chenery, S., 2009. Detrital rutile geochemistry and thermometry as guides to provenance of the Jurassic-Paleocene sandstones of the Norwegian Sea. J. Sed. Res., 79, 540-553.
- Mosar, J.. Stampfli. G.M.. and Girod, F. 1996. Western Préalpes Medianes Romandes: Timing and structure. A review. Eclogae geol. Helv., 89, 389-425.
- Nussbaum, C.. Marquer, D.. and Biino, G.G. 1998. Two subduction events in a polycyclic basement: Alpine and pre-Alpine high pressure metamorphism in the Suretta nappe, Swiss Eastern Alps. J. Metamorphic Geol., 16, 591-605.
- Packham , G.H., 1954. Sedimentary structures as an important factor in the classification of sandstones. Am. Jour. Sci., 252, 466-476.
- Parrish, R.R.. Gough, S.J.. Searle M.P.. and Waters, D.J. 2006. Plate velocity exhumation of ultrahigh-pressure eclogites in the Pakistan Himalaya. Geology, 34, 989-992.
- Paul, T., and Fitzgerald, P.F., 1992. Transmission microscope investigation of fission track in apatite. Am. Mineral., 77, 336-344.
- Pawlowsky-Glahn, V., and Egozcue, J. J., 2001. Geometric approach to statistical analysis on the simplex. Stochastic Environmental Research and Risk Assessment (SERRA) 15, 384-398.

- Pawlowsky-Glahn, V., and Egozcue, J., 2006. Analisis de datos composicionales con el coda-dendrograma. *in* Sicilia-Rodriguez, J., C. Gonzalez-Martın, J., M. A. Gonzalez-Sierra, M.A., and Alcaide, D. (eds.). Actas del XXIX Congreso de la Sociedad de Estadistica e Investigacion Operativa (SEIO'06).
- Pearce, J.A., 1976. Statistical analysis of major element patterns in basalts. J. Petrol., 17, 15-43.
- Pearson, K., 1897. Mathematical contributions to the theory of evolution. On a form of spurious correlation which may arise when indices are used in the measurement of organs. Proceedings of the Royal Society of London, LX, 489-502.
- Pearson, K., 1901. On lines and planes of closest fit to systems of points in space. Philosophical Magazine, 2, 559-572.
- Pettijohn, F.J., 1948. A preface to the classification of sedimentary rocks. J. Geol., 56, 112-117.
- Pettijohn, F.J., 1949. Sedimentary rocks. Harper and Brothers, New York, 526 p.
- Pettijohn, F.J., 1954. Classification of sandstones. J. Geol., 62, 360-365.
- Phillips, A.J., 1881. On the Constitution and History of Grits and Sandstones. Quarterly Journal of the Geological Society of London, 37, 6-28.
- Piccardo G.B.. Zanetti, A.. and Müntener, O. 2007. Melt/peridotite interaction in the Southern Lanzo peridotite: field, textural and geochemical evidence. Lithos, 94, 181-209.
- Polino, R., Monticelli, F., and Vaccaro, D., 1983. L'Unità Piemontese Chaberton-Grand Hoche (Val Susa – Alpi Occidentali): evoluzione litostratigrafica, assetto strutturale e rapporti con i complessi circostanti. Mem. Soc. Geol. Ital., 26, 489-498.
- Polino, R., Dal Piaz, G.V., and Gosso, G., 1990. An accretionary wedge model for the pre-collisional Cretaceous orogeny in the Alps. Mem. Soc. Géol. Fr., 156, 309-321.
- Rebay, G., and Spalla, M. I. 2001. Emplacement at granulite facies conditions of the Sesia-Lanzo metagabbros: an early record of Permian rifting? Lithos, 58, 85-104.
- Rencher, A.C., 2002. Methods of multivariate analysis. 2nd edition, Wiley, New York, 714 p.
- Ripley, B.D., 1996. Pattern recognition and neural networks. Cambridge University Press, Cambridge, MA, USA, 416 p.
- Rock, N.M.S., 1988. Numerical geology: a source guide, glossary and selective bibliography to geological uses of computers and statistics. Lect. Notes Earth Sci., 18, 427 p.
- Rollinson, H.R., 1995. Using geochemical data: Evaluation, presentation, interpretation. Longman Geochemistry Series. 352 p.
- Rubatto, D., and Hermann, J. 2001. Exhumation as fast as subduction? Geology, 29, 3-6.
- Rubatto, D., Gebauer, D., and Fanning, M., 1998. Jurassic formation and Eocene subduction of the Zermatt–Saas–Fee ophiolites: implications for the geodynamic evolution of the Central and Western Alps. Contrib. Mineral. Petrol., 132, 269-287.
- Rubatto, D.. Gebauer, D.. and Compagnoni, R. 1999. Dating of eclogite-facies zircons: the age of Alpine metamorphism in the Sesia-Lanzo Zone (Western Alps). Earth Planet. Sci. Lett., 167, 141-158.
- Rubey, W.W., 1933. The size distribution of heavy minerals within a water-laid sandstone. J. Sedim. Res., 3, 3-29.
- Ryan, P.D., Mange, M.A., and Dewey, J.F., 2007. Statistical analysis of high-resolution heayy mineral stratigraphic data from the Ordovician of western Ireland and its tectonic consequences. *in* Mange, M.A., Wright, D.T. (eds). Heavy Minerals in Use. Developments in

Sedimentology Series 58. Amsterdam, Elsevier, p. 465-489.

- Sarmanov, O.V., and A.B., Vistelius, 1959. On the correlation of percentage values. Doklady of the Academy of Sciences of the USSR – Earth Sciences Section, 126, 22-25.
- Sassi, R.. Mazzoli, C.. Miller, C.. Konzett, J. 2004. Geochemistry and metamorphic evolution of the Pohorje Mountain eclogites from the easternmost Austroalpine basement of the Eastern Alps (Northern Slovenija). Lithos, 78, 235-261.
- Scambelluri, M.. Müntener, O.. Hermann, J.. Piccardo, G.B.. and Trommsdorff, V. 1995. Subduction of water into the mantle: history of an alpine peridotite. Geology, 23, 459-462.
- Schaller, M., von Blanckenburg, F., Hovius, N., and Kubik, P.W., 2001. Large-scale erosion rates from in situ produced cosmogenic nuclides in European river sediments. Earth Planet. Sci. Lett., 188, 441-458.
- Schmid, S.M., and Kissling, E., 2000. The arc of the western Alps in the light of geophysical data on deep crustal structure. Tectonics, 19, 62-85.
- Schmid, S.M.. Fügenschuh, B.. Kissling, E.. and Schuster, R. 2004. Tectonic map and overall architecture of the Alpine orogen. Eclogae geol. Helv., 97, 93-117.
- Schwab, F.L., 1975. Framework mineralogy and chemical composition of continental margin-type sandstones. Geology, 3, 487-490.
- Schwartz, S.. Lardeaux, J.M.. Tricart, P.. Guillot, S.. and Labrin, E. 2007. Diachronous exhumation of HP-LT metamorphic rocks from south-western Alps: evidence from fission-track analysis. Terra Nova, 19, 133-140.
- Seaward, D., Rhoades, D.A., 1986. A clustering technique for fission track dating of fully to partially neealed minerlas and other non-unique populations. Nucl. Tracks Radiat. Meas. 11, 259-268.
- Seward. D., and Mancktelow, N.S., 1994. Neogene kinematics of the central and western Alps: evidences from fission-track dating. Geology, 22, 803-806.
- Slingerland, R., 1984. Role of hydraulic sorting in the origin of fluvial placers. J. Sediment. Petrol., 54, 137-150.
- Solomon, J.D., 1932. The heavy mineral assemblages of the Great chalky boulder-clay and Cannon-shot gravels of East Anglia, and their significance. Geol. Mag., 69, 314-320.
- Sorby, H.C., 1880. On the structure and origin of non-calcareous stratified rocks. Quarterly Journal of the Geological Society of London, 36, 46-92.
- Spalla, M.I.. Lardeaux, J.M.. Dal Piaz, G.V.. Gosso G.. and Messiga, B. 1996. Tectonic significance of Alpine eclogites. J. Geodynamics, 21, 257-285.
- Spear, F.S., and Franz, G. 1986. P–T evolution of metasediments from the eclogite zone, southcentral Tauern Window, Austria. Lithos, 19, 219-234.
- Stampfli, G.M.. Mosar, J. Marquer, D.. Marchant, R.. Baudin, T.. and Borel, G. 1998. Subduction and obduction processes in the Swiss Alps. Tectonophysics, 296, 159-204.
- Steiger, R.H., Jäger, E., 1977. Subcommission on geochronology: Convention on the use of decay constants in geo- and cosmochronology. Earth Planet. Sci. Lett. 36, 359-362.
- Stone, M., 1978. Cross validation: a review. Matematische Operationsforschung und Statistik, 9, 127-139.
- Suczek, C.A., and Ingersoll, R.V. 1985. Petrology and provenance of Cenozoic sand from the Indus Cone and the Arabian Basin, DSDP sites 221, 222, and 224. J. Sediment. Petrol., 55, 340-346.
- Suttner, L.J., 1976. Sedimentary petrographic provinces: an evaluation. *in* Ross, C.A. (ed).

Paleogeographic provinces and provinciality. Soc. Econ. Pal. Mineral. Spec. Publ., 21, 75-84.

- Suttner, L.J., and Basu, A., 1985. The effect of grain size on detrital modes – a test of the Gazzi-Dickinson point counting method – discussion. J. Sed. Petrol., 55, 616-617.
- Suttner, L.J., and Dutta, P.K., 1986. Alluvial sandstone composition and paleoclimate, I. Framework mineralogy., J. Sed. Res., 56, 329-345.
- Suttner, L.J., Basu, A., and Mack, G.H., 1981. Climate and the origin of quartz arenites. J. Sedimentary Res., 51, 1235-1246.
- Sylvester, J.J., 1889. A new proof that a general quadric may be reduced to its canonical form (that is a linear function of squares) by means of a real orthogonal substitution. Messenger of Mathematichs, 19, 42-46.
- Syvitski, J.P.M., Peckham, S.D., Hilbermann, R, and Mulder, T., 2003. Predicting the terrestrial flux of sediment to the global ocean: a planetary perspective. Sed. Geol., 162, 5-24.
- Taylor, S.R., McLennan, S.M., 1985. The Continental Crust: its composition and evolution. Oxford, Blacwell Scientific Publications, 312 p.
- Taylor, S.R., McLennan, S.M., 1995. The geochemical evolution of the continental crust. Rev. Geophys., 33, 241-265.
- Thomas, C.W., and Aitchison, J., 2006. Log-ratios and geochemical discrimination of Scottish Dalradian limestones: a case study. Geol. Soc. London Spec. Pub., 264, 25-41.
- Thöni, M. 2006. Dating eclogite-facies metamorphism in the eastern Alps–approaches, results, interpretations: a review. Mineral. Petrol., 88, 123-148.
- Thöni, M., and Jagoutz, E. 1993. Isotopic constraints for eo-Alpine high-P metamorphism in the Austroalpine nappes of the Eastern Alps: bearing on Alpine orogenesis. Schweiz. Mineral. Petrogr. Mitt., 73, 177-189.
- Thöni, M.. Miller, C.. Blichert-Toft, J.. Whitehouse, M.J.. Konzett, J.. and Zanetti, A. 2008. Timing of high-pressure metamorphism and exhumation of the eclogite type-locality (Kupplerbrunn-Prickeler Halt, Saualpe, south-eastern Austria): constraints from correlations of the Sm-Nd, Lu-Hf, U-Pb and Rb-Sr isotopic systems. J. Metamorphic Geol., 26, 561-581.
- Todd, C.S., Engi, M., 1997. Metamorphic field gradients in the Central Alps. J. Metamorphic Geol. 15, 513-530.
- Trautwein, B.. Dunkl, I.. and Frisch, W. 2001. Accretionary history of the Rhenodanubian Flysch zone in the Eastern Alps–evidence from apatite fission-track geochronology. Int. J. Earth Sciences, 90, 703-713.
- Tricart, P., Van Der Beek, P., Schwartz, S., and Labrin, E., 2007. Diachronous late-stage exhumation across the western Alpine arc: constraints from apatite fission-track thermochronology between the Pelvoux and Dora-Maira Massifs. J. Geol. Soc. London, 164, 163-174.
- Trommsdorff, V.. Montrasio, A.. Hermann, J.. Müntener, O.. Spillmann, P.. and Gieré, R. 2005. The geological map of Val Malenco. Schweiz. Mineral. Petrogr. Mitt., 85, 1-13.
- Vai, G.B.. Boriani, A.. Rivalenti, G.. and Sassi, F.P. 1984. Catena Ercinica e Paleozoico nelle Alpi Meridionali. In Cento anni di geologia italiana, vol. giub. Soc. Geol. It., p. 133-154.
- Valloni, R., 1985. Reading provenance from marine sands. *in* Provenance of arenite. G.G. Zuffa (ed), NATO-ASI serie C, 148, Dordrecht, 408 p.
- van Andel, Tj.H., 1950. Provenance, transport and deposition of Rhine sediments.
- Vanossi M.. Cortesogno L.. Galbiati B.. Messiga B.. Piccardo G.. and Vannucci, R. 1986. Geologia delle

Alpi Liguri: dati, problemi, ipotesi. Mem. Soc. Geol. It., 28, 5-75.

- Velbel, M.A. 1985. Mineralogically mature sandstones in accretionary prisms: J. Sediment. Petrol., 55, 685-690.
- Vermeesch, P., 2004. How many grains are needed for a provenance study? Earth Planet. Sci. letters, 224, 441-451.
- Vermeesch, P. 2006. Tectonic discrimination of basalts with classification trees. Geochim. CosmoChim. Acta, 70, 1839-1848.
- Vermeesch, P., 2009. RadialPlotter: a Java application for fission track, luminescence and other radial plots. Radiation Measurements, 44, 409-410.
- Vermeesch, P., Avigad, D., and McWilliams, M.O., 2010. 500 m.y. of thermal history elucidated by multi-method detrital thermochronology of North Gondwana Cambrian sandstone (Eilat area, Israel). GSA Bull., 121, 1204-1216.
- Vernon, A.J., van der Beek, P.A., and Sinclair, H.D., 2009. Spatial correlation between long-term exhumation rates and present-day forcing parameters in the western European Alps. Geology, 37, 859-862.
- Vezzoli, G., 2004. Erosion in the Western Alps (Dora Baltea basin): 2. Quantifying sediment yield. Sedimentary geology, 171, 247-259.
- Vezzoli, G., and Garzanti. E., 2009. Tracking paleodrainage in Pleistocene foreland basins. J. Geol., 117, 445-454.
- Vezzoli, G., Garzanti, E., and Monguzzi, S., 2004. Erosion in the Western Alps (Dora Baltea basin) 1. Quantifying sediment provenance. Sed. Geol., 171, 227-246.
- Vialon, P. 1966. Etude géologique du massif cristallin Dora–Maira, Alpes Cottiennes internes, Italie. Thèse d'État, Univ. Grenoble, 293 p.
- von Eynatten, H., 2004. Statistical modelling of compositional trends in sediments. Sedimentary Geology, 171, 79-89.
- von Eynatten, H.. Gaupp, R.. and Wijbrans, J.R. 1996. 40Ar/39Ar laser-probe dating of detrital white micas from Cretaceous sedimentary rocks of the Eastern Alps: evidence for Variscan high-pressure metamorphism and implications for the Alpine orogeny. Geology, 24, 691-694.
- von Eynatten, H., Barceló-Vidal, C., and Pawlowsky-Glahn, V., 2003. Sandstone composition and discrimination: a statistical evaluation of different analytical methods. J. Sedimentary Research, 73, 47-57.
- von Huene, R., and Lallemand, S. 1990. Tectonic erosion along the Japan and Peru convergent margins. Geol. Soc. Am. Bull., 102, 704-720.
- von Raumer, J.F., Ménot, R.P., Abrecht, J., and Biino, G. ,1993. The Pre-Alpine evolution of the External Massifs. in von Raumer, J. F., and Neubauer, F., eds. Pre-Mesozoic geology in the Alps. Berlin, Springer.
- Yamada, R., Tagami, T., Nishimura, S., Ito, H., 1995. Annealing kinetics of fission tracks in zircon: an experimental study. Chem. Geol., 122, 249-258.
- Wagner, G.A., and Van den Haute, P., 1992. Fission-Track dating. Dordrecht, Kluwert Academic Press., 285 p.
- Wagreich, M. 1993. Subcrustal tectonic erosion in orogenic belts-a model for the Late Cretaceous subsidence of the Northern Calcareous Alps (Austria). Geology, 21, 941-944.
- Weltje, J.G., 1995. Unraveling mixed provenance of coastal sands: the Po delta and adjacent beaches of the northern Adriatic sea as a test case. *in* Oti, M.A., Postma, G., (eds). Geology of deltas. Balkema, Rotterdam, 181-202.
- Weltje, J.G., 1998. Compositional and textural heterogeneity of detritl sediments: towards a quantitative framework for sedimentary-petrology. *in* Buccianti, A., Nardi, G., Potenza, R. (eds). Proceedings of

IAMG '98 – 4th annual conference of the International Association for Mathematical Geology. De Frede Editore, Napoli, 65-70.

- Weltje, G.J., 2002. Quantitative analysis of detrital modes: statistically rigorous confidence regions in ternary diagrams and their use in sedimentary petrology. Earth Sci. Rev., 57, 211-253.
- Weltje, G.J., and von Eynatten, H., 2004. Quantitative provenance analysis of sediments: reviews and outlook. Sedimentary Geology, 171, 1-11.
- Wendt, A.S., Olivier,V., Chadderton, L.T., 2002. Experimental evidence for the pressure dependence of fission track annealing in apatite. Earth Planet. Sci. Lett. 201, 593-607.
- Whetten, J.T., and Kelley, J.C., 1969. Characteristics of Columbia River sediment and sediment transport. J. Sedimentary Research, 39, 1149-1166.
- Whipple, K.X., 2009. The influence of climate on the tectonic evolution of mountain belts. Nature Geoscience, 2, 97-104.
- Woronov, A., 1991. Enigmas and solutions in the analyses of compositional data. J. Geol. Educ., 39, 299-302.
- Zaun, P.E., Wagner, G.A., 1985. Fission track stability in zircons under geological conditions. Nuclear Tracks and Radiation Measurements, 10, 303-307.
- Zeilinger, G., and Schlunegger, F., 2007. Possible flexural accommodation on the eastern edge of the Alptiplano in relation to focussed erosion in the Rio La Paz drainage system. Terra Nova, 19, 373-380.
- Zeitler, P.K., Meltxer, A.S., Koons, P.O., Craw, D., Hallet, B., Chamberlain, C.P., Kidd, W.S.F., Park, S.K., Seeber, L., Bishop, M., and Shroder, J., 2001. Erosion, Himalayan geodynamics, and the geomorphology of metamorphism. Geol. Soc. Am. Today, 11, 4-9.
- Zimmermann, R.. Hammerschmidt, K.. and Franz, G. 1994. Eocene high pressure metamorphism in the Penninic units of the Tauern Window (Eastern Alps): evidence from 40Ar-39Ar dating and petrological investigations. Contrib. Mineral. Petrol., 117, 175-186.
- Zuffa, G.G., 1985. Optical analysis of arenites: influence of methodology on compositional results. *in* Provenance of arenite. G.G. Zuffa (ed), NATO-ASI serie C, 148, Dordrecht, 408 p.
- Zuffa, G.G., 1987. Unravelling hinterland and offshore paleogeography from deep-water arenites. *in* Leggett, J.K., and Zuffa, G.G., (eds). Marine clastic sedimentology. Graham and Trotman, London, 39-61.
- Zuffa, G.G., 1991. On the use of turbidite arenites in provenance studies: critical remarks. *in* Morton, A.C., Todd, S.P., and Haughton, P.D.W. (eds). Developments in Sedimentary Provenance Studies. Geol. Soc. Spec. Publ., 57, 23-29.

APPENDICES

Sampling Sites of Studied Modern Sands from the Alpine Axial Belts

Sample	River	Site	GPS coordinates		Drainage basin	Drained unit
			Lat. N°	Long. E°		
SHALLOW STRUCTURAL LEVEL						
OFFSCRAPED REMNANT-OCEAN TURBIDITES						
S14	Argentina	Taggia	43°50'01"	07°51'33"	Mar Ligure	San Remo Flysch
S438	Impero	Imperia	43°53'25"	08°02'17"	Mar Ligure	San Remo Flysch
S639	Merula	Andora	43°57'00"	08°08'34"	Mar Ligure	San Remo Flysch
S15	Arroscia	Ortovero	44°01'58"	08°05'50"	Mar Ligure	San Remo Flysch
S2329	Parpaillon	La Condamine	44°27'41"	06°44'04"	Ubaye - Durance	Parpaillon Flysch
S2322	Crévoux	Crévoux	44°32'47"	06°36'36"	Durance - Rhône	Parpaillon Flysch
S3417	Hundsdrügg	Garstatt	46°35'35"	07°22'26"	Simme - Lake Thun	Simme Flysch
S3418	left trib. Färmel	Matten	46°29'43"	07°26'30"	Simme - Lake Thun	Niesen Flysch
S3578	right trib. Hero	Riedern	46°36'20"	07°33'55"	Simme - Lake Thun	Niesen Flysch
S3054	Furna	Furna	46°55'06"	09°41'00"	Rhein	Prättigau Flysch
S3053	Fideris	Fideris	46°54'45"	09°44'45"	Rhein	Prättigau Flysch
S3052	Luzein	Luzein	46°55'08"	09°46'19"	Rhein	Prättigau Flysch
S3059	Satteins	Satteins	47°13'24"	09°43'11"	Rhein	Vorarlberg Flysch
S3060	Duns	Duns	47°13'22"	09°45'09"	Rhein	Vorarlberg Flysch
S3061	Thuringerberg	Thuringerberg	47°13'18"	09°47'04"	Rhein	Vorarlberg Flysch
S3072	Bolgenbach	Obermaiselstein	47°27'00"	10°14'15"	Iller - Donau	Vorarlberg Flysch
S3079	Bichl	Bichl	47°43'08"	11°25'53"	Isar - Donau	Rheno-Danubian Flysch
S3080	Bad Heilbrunn	Bad Heilbrunn	47°43'44"	11°29'46"	Isar - Donau	Rheno-Danubian Flysch
S3365	Voeckla	Haslau	47°54'45"	13°20'36"	Traun - Donau	Rheno-Danubian Flysch
S3367	Wessenaurach	Reindlmuehl	47°53'37"	13°41'34"	Donau	Rheno-Danubian Flysch
S3375	Hiesbach	Hiesbach	47°59'28"	14°47'39"	Donau	Rheno-Danubian Flysch
S3369	Klausbach	Kogl	47°59'32"	14°50'53"	Donau	Rheno-Danubian Flysch
OFFSCRAPED BRIANÇONNAIS COVERS						
S3575	left trib. Fildrich	Grimmialp	46°33'58"	07°29'15"	Simme - Lake Thun	Préalpes Médianes + Submédianes
OFFSCRAPED/OBDUCTED OPHIOLITES						
S4027	Gimont	Rif. Gimont	44°55'48"	06°45'27"	Dora Riparia - Po	Chenaillet Ophiolite
S3731	Totalp	Wolfgang	46°50'26"	09°52'54"	Rhein	Arosa Zone
INTERMEDIATE STRUCTURAL LEVEL						
SUBCRETED CALCSCHISTS						
S2318	Aigue Blanche	Ville Vieille	44°45'26"	06°49'16"	Guil - Durance	Piemontese Zone
S2319	Guil	Ville Vieille	44°45'40"	06°49'18"	Durance - Rhône	Piemontese Zone
S3021	San Michele	San Michele	44°29'28"	07°03'41"	Maira - Po	Piemontese Zone
S2192	Gressan	Gressan	45°42'52"	07°17'29"	Dora Baltea - Po	Piemontese Zone
S2078	St. Barthelemy	Nus	45°44'24"	07°27'15"	Dora Baltea - Po	Piemontese Zone
S1853	Dora di Verney	Pre St. Didier	45°45'43"	06°59'06"	Dora Baltea - Po	Sion - Courmayeur Zone
S1854	Liconi	Morgex	45°45'32"	07°02'07"	Dora Baltea - Po	Sion - Courmayeur Zone
S3048	Rabiusa	Bonaduz	46°47'08"	09°20'53"	Rhein	Northern Graubünden Bündnerschiefer
S3046	Tartar	Tartar	46°42'44"	09°25'16"	Rhein	Northern Graubünden Bündnerschiefer
S3047	Rothenbrunnen	Rothenbrunnen	46°45'49"	09°26'05"	Rhein	Northern Graubünden Bündnerschiefer
S1753	Tasnan	Ardez	46°46'41"	10°13'31"	Inn - Donau	Engadine Bündnerschiefer (+ Tasna Unit)
S2418	Griosch	Griosch	46°52'51"	10°19'50"	Inn - Donau	Engadine Bündnerschiefer
S1756	Lavranca	Ramosch	46°49'46"	10°22'42"	Inn - Donau	Engadine Bündnerschiefer (+ Tasna Unit)
S2419	Arina	Serviezell	46°51'12"	10°25'14"	Inn - Donau	Engadine Bündnerschiefer
S2422	Mundin	Spiss	46°57'06"	10°25'32"	Inn - Donau	Engadine Bündnerschiefer
S2420	Mutller	Tschlin	46°52'06"	10°26'13"	Inn - Donau	Engadine Bündnerschiefer
S2421	Tea	Martina	46°54'08"	10°28'00"	Inn - Donau	Engadine Bündnerschiefer
S1758	Scherbeng	Schalkl	46°56'16"	10°28'46"	Inn - Donau	Engadine Bündnerschiefer
S2432	Schmirnbach	St. Jodok	47°03'50"	11°30'06"	Salzach - Inn	Tauern Bündnerschiefer
S2433	Padaster	Steinach	47°04'58"	11°28'52"	Salzach - Inn	Tauern Bündnerschiefer
S2452	Kapruner	Kesselfall	47°12'54"	12°43'28"	Salzach - Inn	Tauern Bündnerschiefer
S2459	Rauriser	Taxenbach	47°16'48"	12°58'20"	Salzach .- Inn	Tauern Window cover
S2460	Sulzbach	Fusch	47°14'14"	12°49'49"	Salzach - Inn	Tauern Bündnerschiefer
S2461	Breitebenkopf	Bad Fusch	47°12'12"	12°50'24"	Salzach - Inn	Tauern Bündnerschiefer
S1567	Grossarl	Breitenebenaim	47°16'54"	13°12'59"	Salzach - Inn	Tauern Bündnerschiefer
S2464	Möll	Franz Joseph Hohe	47°04'37"	12°44'12"	Drava	Tauern Bündnerschiefer
S2494	Val Rossa	Casere	47°03'13"	12°07'55"	Aurino-Adige	Tauern Bündnerschiefer
SUBCRETED BRIANÇONNAIS COVERS						
S2343	Pesio	Chiusa di Pesio	44°18'49"	07°40'36"	Tanaro - Po	Ligurian Briançonnais
S2344	Ellero	Villanova Mondovì	44°20'08"	07°45'32"	Tanaro - Po	Ligurian Briançonnais
S17	Tanaro	Bagnasco	44°18'10"	08°03'04"	Po	Ligurian Briançonnais
S1140	Bormida di Millesimo	Millesimo	44°21'59"	08°11'40"	Tanaro - Po	Ligurian Briançonnais
S1141	Bormida di Mallare	Ferrania	44°21'46"	08°19'17"	Tanaro - Po	Ligurian Briançonnais
S184	Neva	Cisano	44°05'20"	08°08'25"	Mar Ligure	Ligurian Briançonnais
S185	Varatello	Loano	44°07'06"	08°14'04"	Mar Ligure	Ligurian Briançonnais
S158	Porra	Finale	44°10'10"	08°20'23"	Mar Ligure	Ligurian Briançonnais
S3020	Maira	Chiappera	44°29'26"	06°55'15"	Po	Briançonnais fan
SUBCRETED CONTINENTAL PENNINC BASEMENTS						
S153	Letimbro	Savona	44°18'52"	08°28'20"	Mar Ligure	Ligurian Briançonnais
S2189	Planaval	Planaval	45°41'07"	07°06'17"	Dora Baltea - Po	Gran S. Bernardo Nappe
S1856	Dora di Valgrisenche	Ravoire	45°41'48"	07°09'01"	Dora Baltea - Po	Gran S. Bernardo Nappe
S2190	Dora di Rhêmes	Rhêmes	45°39'17"	07°09'11"	Dora Baltea - Po	Gran S. Bernardo Nappe
S1210	Liro	Mese	46°19'18"	09°23'16"	Mera - Lago di Como	Tambò - Suretta Nappes
S2441	Zemm	Ginzling	47°05'55"	11°48'11"	Ziller - Inn	Zentralgneiss
S2442	Floitenbach	Ginzling	47°06'00"	11°48'44"	Ziller - Inn	Zentralgneiss
S2443	Stillupbach	Mayrhofen	47°08'42"	11°50'10"	Ziller - Inn	Zentralgneiss
S2446	Sonderbach	In der Au	47°07'14"	12°00'24"	Ziller - Inn	Zentralgneiss

Sample	River	Site	GPS coordinates		Drainage basin	Drained unit
			Lat. N°	Long. E°		
SUBCRETED CONTINENTAL PENNINC BASEMENTS (continued)						
S2444	Hundskehlbach	Barenbad	47°07'04"	12°02'36"	Ziller - Inn	Zentralgneiss
S2445	Ziller	Barenbad	47°07'17"	12°02'56"	Ziller - Inn	Zentralgneiss
S2713	Melnikfall	Faller Tumpf	47°03'58"	13°21'45"	Lieser - Drava	Zentralgneiss
S2715	Malta	Koschach	46°59'40"	13°27'21"	Lieser - Drava	Zentralgneiss
S2716	Gossbach	Koschach	46°58'55"	13°26'39"	Lieser - Drava	Zentralgneiss
S2723	Seebach	Stappitz	46°59'45"	13°10'13"	Möll - Drava	Zentralgneiss
S2495	Griesbachthal	San Pietro	47°01'41"	12°02'57"	Aurino - Adige	Zentralgneiss
S2496	Keilbachthal	Cadipietra	46°59'47"	11°58'38"	Aurino - Adige	Zentralgneiss
S2497	Trippach	San Giovanni	46°59'02"	11°56'39"	Aurino - Adige	Zentralgneiss
S3091	Mesole	Lago di Mesole	46°56'12"	11°47'05"	Aurino - Adige	Zentralgneiss
S2450	Habach	Habach	47°15'10"	12°19'09"	Salzach - Inn	Altkristallin
S2451	Hollersbach	Hollersbach	47°15'45"	12°24'38"	Salzach - Inn	Altkristallin
S1570	Stubach	Uttendorf	47°15'56"	12°33'53"	Salzach - Inn	Altkristallin
S2710	Lieser	Tendel	47°02'39"	13°32'25"	Lieser - Drava	Altkristallin
S2714	Schlejerfall	Koschach	46°58'59"	13°28'08"	Lieser - Drava	Altkristallin
S2718	Muhldorfer	Muhldorf	46°51'58"	13°20'25"	Möll - Drava	Tauern Window basement
S2709	Mur	Schellgaden	47°04'41"	13°34'30"	Drava	Tauern Window basement
SUBCRETED AUSTROALPINE BASEMENTS						
S2077	Buthier	Thoules	45°49'32"	07°20'31"	Dora Baltea - Po	Dent Blanche
SUBCRETED OPHIOLITES						
S3430	Mallero della Val Ventin	Rifugio Porro	46°16'31"	09°46'52"	Adda - Po	Malenco Unit
DEEP STRUCTURAL LEVEL						
CONTINENTAL ECLOGITES (CRETACEOUS AXIAL BELT)						
S2194	Arnad	Arnad	45°38'18"	07°44'16"	Dora Baltea - Po	Sesia-Lanzo (Gneiss Minuti)
S2195	Rio Fer	Clapey	45°35'41"	07°45'07"	Dora Baltea - Po	Sesia-Lanzo (Eclogitic Micaschists)
S2295	Vogna	Riva Valdobbia	45°49'52"	07°57'09"	Sesia - Po	Sesia-Lanzo Unit
S2290	Sermenza	Cerva	45°49'31"	08°07'58"	Sesia - Po	Sesia-Lanzo Unit
S2293	Gronda	Rassa	45°46'15"	08°00'28"	Sesia - Po	Sesia-Lanzo Unit
S2292	Sorba	Rassa	45°46'05"	08°00'42"	Sesia - Po	Sesia-Lanzo Unit
S2294	Artogna	Otra	45°48'28"	08°01'38"	Sesia - Po	Sesia-Lanzo Unit
S2299	Riale	Piode	45°46'06"	08°03'03"	Sesia - Po	Sesia-Lanzo Unit
S3758	Rio di Salto	Pianlargo	46°49'04"	11°11'42"	Adige	Texel Unit
S3755	Valclava	Valcalva	46°46'22"	11°12'32"	Adige	Texel Unit
S2694	Lausslingbach	Obdach	47°04'04"	14°40'02"	Mur - Drava	Packalpe Unit
S2695	Kienbergbach	Kathal	47°05'43"	14°40'27"	Mur - Drava	Saualpe Unit
S2692	Lavant	Taxwirt	47°01'11"	14°43'28"	Drava	Saualpe Unit
S2689	Weissenbach	St. Margarethen	46°51'14"	14°48'10"	Drava	Saualpe Unit
S2691	Twimberg	Twimberg	46°54'54"	14°50'30"	Drava	Koralpe Unit
S2690	St. Gertraud	St. Gertraud	46°52'10"	14°52'35"	Drava	Koralpe Unit
S1527	Lavant	Effendorf	46°39'00"	14°56'22"	Drava	Saualpe + Koralpe Units
S1532	Kainach	Weitendorf	46°53'34"	15°26'40"	Drava	Koralpe Unit + Pannonian Basin
S1528	Sulm	Seggau	46°45'29"	15°29'43"	Drava	Koralpe Unit + Pannonian Basin
S1529	Lassnitz	Kaindorf	46°47'44"	15°31'32"	Drava	Koralpe Unit + Pannonian Basin
S3399	Mislinja	Mislinja	46°26'37"	15°11'17"	Drava	Pohorje Unit
S3398	Dravinja	Loska Gora	46°24'24"	15°20'44"	Drava	Pohorje Unit
S3393	Lobnica	Ruse	46°32'03"	15°29'07"	Drava	Pohorje Unit
CONTINENTAL ECLOGITES (EOCENE AXIAL BELT)						
S2414	Gilba	Brossasco	44°34'09"	07°21'01"	Varaita - Maira - Po	Dora Maira Internal Massif
S3018	Parigi	Martiniana Po	44°37'26"	07°22'33"	Po	Dora Maira Internal Massif
S3017	Croesio	Croesio	44°39'48"	07°18'03"	Po	Dora Maira Internal Massif
S2177	Stura di Vallegrande	Forno	45°21'33"	07°13'35"	Stura di Lanzo - Po	Gran Paradiso Internal Massif
S2076	Grand Eyvia	Valnontey	45°34'54"	07°20'06"	Dora Baltea - Po	Gran Paradiso Internal Massif
S3138	Valsoera	Lago La Balma	45°29'46"	07°23'48"	Orco - Po	Gran Paradiso Internal Massif
S2176	Orco	Casetti	45°25'30"	07°26'07"	Po	Gran Paradiso Internal Massif
S2395	Anza	Croppo	45°58'27"	08°06'10"	Toce - Lago Maggiore	Monte Rosa Internal Massif
S1068	Toce	Domodossola	46°08'17"	08°18'05"	Lago Maggiore	Lepontine Dome
S1876	Toce	Oira	46°10'29"	08°19'19"	Lago Maggiore	Lepontine Dome
S1877	Isorno	Montecretese	46°09'15"	08°19'57"	Toce - Lago Maggiore	Lepontine Dome
S1900	Onsernone	Sauressio	46°13'28"	08°24'04"	Toce - Lago Maggiore	Lepontine Dome
S1888	Campo	Cevio	46°18'46"	08°35'59"	Maggia - Lago Maggiore	Lepontine Dome
S1886	Maggia	Bignasco	46°20'31"	08°36'27"	Lago Maggiore	Lepontine Dome
S1054	Maggia	Tegna	46°11'01"	08°44'54"	Lago Maggiore	Lepontine Dome
S1890	Verzasca	Frasco	46°20'32"	08°47'58"	Lago Maggiore	Lepontine Dome
S1053	Verzasca	Tenero	46°10'55"	08°50'15"	Lago Maggiore	Lepontine Dome
S1893	N Cugnasco	N Cugnasco	46°10'42"	08°55'23"	Ticino - Lago Maggiore	Lepontine Dome
S1896	W Preonzo	W Preonzo	46°16'00"	08°59'37"	Ticino - Lago Maggiore	Lepontine Dome
S1049	Moesa	Arbedo	46°13'17"	09°02'44"	Ticino - Lago Maggiore	Lepontine Dome
S1902	Marmontana	Roveredo	46°13'51"	09°07'36"	Ticino - Lago Maggiore	Lepontine Dome
S1898	Calanca	Grono	46°15'02"	09°08'39"	Moesa - Ticino	Lepontine Dome
S1897	Moesa	Lostallo	46°18'54"	09°11'58"	Ticino - Lago Maggiore	Lepontine Dome
S1884	Boggia	Grondona	46°16'38"	09°21'25"	Mera - Lago di Como	Lepontine Dome
OCEANIC ECLOGITES (EOCENE AXIAL BELT)						
S148	Arrestra	Cogoleto	44°22'51"	08°37'32"	Mar Ligure	Voltri Unit
S142	Varenna	Pegli	44°25'26"	08°48'53"	Mar Ligure	Voltri Unit
S2829	Stura del Turchino	Ovada	44°38'13"	08°38'56"	Orba - Bormida	Voltri Unit
S3558	Orba	Olbicella	44°32'10"	08°34'42"	Bormida - Tanaro - Po	Voltri Unit
S175	Orba	Capriata	44°43'31"	08°39'53"	Bormida - Tanaro - Po	Voltri Unit
S3016	Po	Pian del Re	44°42'02"	07°05'12"	Mar Adriatico	Monviso Unit
S3745	Casternone	Valdellatorre	45°09'32"	07°26'05"	Stura di Lanzo - Po	Lanzo Massif
S2178	Stura di Ala	Ceres	45°18'51"	07°22'43"	Stura di Lanzo - Po	Zermatt Unit
S2193	Chalamy	Champdepraz	45°40'52"	07°39'31"	Dora Baltea - Po	Zermatt Unit

Sample	River	Site	GPS coordinates		Drainage basin	Drained unit
			Lat. N°	Long. E°		
MIXED AXIAL-BELT UNITS						
SHALLOW STRUCTURAL LEVEL						
S2069	Dranse	Vogny	46°22'02"	06°30'35"	Lac Leman	Préalpes Romandes (+ Helvetic Domain)
S3415	La Sarine	Broc	46°34'15"	07°05'22"	Aar - Rhein	Préalpes Romandes (+ Helvetic Domain)
S3416	La Jogne	Charmey	46°36'44"	07°10'40"	Sarine - Aar	Préalpes Romandes
S3419	Simme	Wimmis	46°40'07"	07°37'56"	Thuner See	Préalpes Romandes
S3057	Vilters	Vilters	47°01'36"	09°26'11"	Rhein	Mixed Flysch units
S3740	Julia	Tiefencastel	46°38'48"	09°34'47"	Rhein	Flysch unit (+ophiolite)
INTERMEDIATE STRUCTURAL LEVEL						
S1139	B. di Pallare	Carcare	44°21'28"	08°17'18"	Tanaro - Po	Ligurian Briançonnais (+ Tertiary Piedmont Basin)
S2331	Ubaye	La Barge	44°35'00"	06°49'35"	Durance - Rhône	Briançonnais covers + Piemontese Calcschists
S1861	Buthier	Castello	45°47'30"	07°18'28"	Dora Baltea - Po	Dent Blanche + Piemontese calcschists
S1862	Buthier	Roisane	45°47'07"	07°18'18"	Dora Baltea - Po	Dent Blanche + Penninic units
S1860	Artanavaz	Roisane	45°47'23"	07°18'03"	Buthier - Dora Baltea	Penninic units + Dent Blanche
S1211	Mera	Chiavenna	46°19'13"	09°24'09"	Lago di Como	Tambò Nappe (+ Bregaglia Pluton)
S2498	Aurino	Lutago	46°57'42"	11°55'15"	Isarco - Adige	Tauern Window
S3088	Pfitscherbach	S. Giacomo	46°57'57"	11°35'36"	Isarco - Adige	Tauern Window
S2448	Tux	Persal	47°09'04"	11°48'34"	Ziller - Inn	Tauern Window
S2449	Gerlos	Zell am Ziller	47°13'39"	11°53'09"	Ziller - Inn	Tauern Window
S2447	Ziller	N Hausling	47°08'40"	11°58'28"	Ziller - Inn	Tauern Window
S1574	Ziller	Ramsau	47°12'24"	11°52'01"	Inn - Donau	Tauern Window
S1572	Krimml	Wald	47°14'19"	12°12'00"	Salzach - Inn	Tauern Window
S1569	Fuschbach	Bruck a.d.Gr.	47°16'23"	12°49'41"	Salzach - Inn	Tauern Window covers
S2462	Fuscher	Ferleiten	47°10'04"	12°48'40"	Salzach - Inn	Tauern Window covers
S1568	Gasteiner	Lend	47°17'37"	13°03'29"	Salzach - Inn	Tauern Window
S2719	Reisseck	Preisdorf	46°53'00"	13°17'35"	Möll - Drava	Tauern Window
S2721	Tristenspitze	Obervellach	46°56'14"	13°11'48"	Möll - Drava	Tauern Window
S2722	Malnitzbach	Malnitz	46°59'29"	13°10'04"	Möll - Drava	Tauern Window
S2725	Fragrantbach	Innerfragrant	46°57'40"	13°03'07"	Möll - Drava	Tauern Window
S2466	Zirknitz	Grosskirchheim	46°58'26"	12°53'38"	Möll - Drava	Tauern Window
S2465	Zirm	Pockhorn	47°01'49"	12°51'37"	Möll - Drava	Tauern Window
S1516	Malta	Gmund	46°54'30"	13°31'49"	Drava	Tauern Window
S2717	Radlbach	Radl	46°54'10"	13°29'39"	Drava	Tauern Window
DEEP STRUCTURAL LEVEL						
S2080	Ayassse	Hone	45°36'43"	07°44'13"	Dora Baltea - Po	Metaophiolite + Sesia-Lanzo Unit
S2296	Sesia	Alagna	45°51'13"	07°56'17"	Po	Monte Rosa Internal Massif + metaophiolite
S1872	Anza	Piedimulera	46°01'20"	08°15'29"	Toce - Lago Maggiore	Monte Rosa + Sesia-Lanzo Units
MIXED STRUCTURAL LEVELS						
S482	Grana	S.Benigno	44°24'25"	07°26'27"	Maira . Po	Piemontese calcschsits + other Penninic units
S481	Maira	Busca	44°30'40"	07°28'25"	Po	Penninic covers + Dora Maira Internal Massif
S480	Varaita	Costigliole	44°33'32"	07°28'01"	Po	Dora Maira Internal Massif + Penninic covers
S475	Maira	Casalgrasso	44°49'15"	07°38'45"	Po	Dora Maira Internal Massif + Penninic covers
S479	Po	Staffarda	44°43'01"	07°27'04"	Mar Adriatico	Dora Maira Internal Massif + Penninic covers
S478	Pellice	Bibiana	44°48'24"	07°17'18"	Chisone - Pellice - Po	Continental + oceanic Penninic units
S477	Chisone	Pinerolo	44°52'23"	07°19'27"	Po	Dora Maira Internal Massif + Penninic covers
S554	Dora Riparia	Avigliana	45°05'29"	07°23'45"	Po	Piemontese calcschsits + other Penninic units
S2179	Stura di Viù	Fucine	45°13'56"	07°22'13"	Stura di Lanzo - Po	Lanzo ophiolite + Piemontese calcschists
S555	Stura di Lanzo	Lanzo	45°16'10"	07°28'40"	Po	Penninic units (+ Sesia-Lanzo Unit)
S556	Orco	Cuorgné	45°23'44"	07°39'03"	Po	Penninic units + Sesia-Lanzo Unit
S2175	Soana	Pont Canavese	45°25'26"	07°35'35"	Orco - Po	Penninic units + Sesia-Lanzo Unit
S2191	Savara	Molere	45°38'29"	07°11'54"	Dora Baltea - Po	Penninic units
S1857	Savara	Villeneuve	45°41'25"	07°11'48"	Dora Baltea - Po	Penninic units
S1858	Grand Eyvia	Aymaviles	45°41'59"	07°13'55"	Dora Baltea - Po	Penninic units
S910	Lys	Pont S.Martin	45°36'02"	07°48'04"	Dora Baltea - Po	Sesia-Lanzo + Penninic units
S912	Evancon	Verres	45°40'12"	07°41'33"	Dora Baltea - Po	Zermatt + other Pennininic (+ Sesia-Lanzo) units
S2081	Clavalitè	Barche	45°43'59"	07°30'11"	Dora Baltea - Po	Zermatt Unit (+ Dent Blanche)
S2079	Emilius	Pollein	45°43'52"	07°24'29"	Dora Baltea - Po	Dent Blanche + Zermatt Unit
S994	Marmore	Chatillon	45°45'03"	07°36'32"	Dora Baltea - Po	Metaophiolite + other Pennininic (+ Dent Blanche)
S2058	Borgne	Bramois	46°13'27"	07°24'33"	Rhône	Penninic covers and basements (+ Dent Blanche)
S2055	Navisence	Chippis	46°16'06"	07°33'10"	Rhône	Penninic covers and basements (+ Dent Blanche)
S2050	Vispa	Neubruch	46°15'02"	07°52'35"	Rhône	Penninic basements (+ Zermatt Unit)
S2048	Brig	Brig	46°18'14"	08°00'30"	Rhône	Penninic basements (+ calcschists)
S1873	Ovesca	Villadossola	46°04'10"	08°15'38"	Toce - Lago Maggiore	Penninic basements
S1874	Bogna	Domodossola	46°07'49"	08°17'08"	Toce - Lago Maggiore	Penninic basements
S1875	Diveria	Crevoladossola	46°09'06"	08°17'59"	Toce - Lago Maggiore	Penninic basements (+ Sesia-Lanzo)
S1878	Melezzo	Masera	46°08'10"	08°19'30"	Toce - Lago Maggiore	Penninic basements
S1895	Brenno	Biasca	46°21'44"	08°57'52"	Ticino - Lago Maggiore	Lepontine Dome + calcschists
S2391	E Ponte	Ponte	46°22'52"	08°25'27"	Toce - Lago Maggiore	Lepontine Dome + calcschists
S1887	Bavona	Fontana	46°21'52"	08°34'04"	Maggia - Lago Maggiore	Lepontine Dome + calcschists
S2477	Tauernbach	Gruben	47°02'53"	12°30'51"	Isel - Drava	Tauern Window + Eclogite Zone
S2476	Frossnitz	Gruben	47°02'42"	12°30'21"	Isel - Drava	Tauern Window + Eclogite Zone
S2474	Isel	Pragraten	47°01'04"	12°20'19"	Drava	Tauern Window + Eclogite Zone

Bulk Petrography of Modern Sands from the Alpine Axial Belts

Sample	River	Site	Operator	Q	KF	P	Lvf	Lvm	Lcc	Lcd	Lp	Lch	Lms	Lmv	Lmf	Lmb	Lu	Ms	Bt	A+POS	& HM	TOTAL	MI	Luc/Lu
SHALLOW STRUCTURAL LEVEL																								
OFFSCRAPED REMNANT-OCEAN TURBIDITES																								
S14	Argentina	Taggia	M. Russo	14	3	3	0	0	30	0	37	0	13	0	0	0	0	0	0	0	0	100,0	30	n.d.
S438	Impero	Imperia	M. Russo	7	1	2	0	0	49	3	22	0	14	0	3	0	0	0	0	0	0	100,0	79	n.d.
S639	Merula	Andora	M. Russo	11	0	1	0	0	30	8	28	0	18	1	2	0	0	0	0	0	0	100,0	53	n.d.
S15	Arroscia	Ortovero	M. Russo	16	0	0	0	0	29	0	25	1	26	1	0	0	0	0	0	0	0	100,0	100	n.d.
S2329	Parpaillon	La Condamine	A.Resentini	5	1	1	0	0	46	1	19	0	27	0	1	0	0	0	0	0	0	100,0	69	n.d.
S2322	Crévoux	Crévoux	A.Resentini	4	1	1	0	0	54	2	8	0	25	0	4	0	0	0	0	0	0	100,0	133	n.d.
S3417	Hundsdrügg	Garstatt	A.Resentini	19	1	3	0	0	24	8	20	1	19	1	2	0	0	1	0	0	0	100,0	86	n.d.
S3418	Affl. Sx. Färmel	Matten	A.Resentini	24	1	2	0	0	33	0	14	1	22	0	2	0	0	0	0	0	0	100,0	113	n.d.
S3578	trib. Dx Hero	Riedern	A.Resentini	21	1	4	0	0	46	2	10	1	14	0	0	0	0	0	0	0	0	100,0	71	n.d.
S3054	Furna	Furna	A.Resentini	8	1	1	0	0	55	1	13	0	20	0	1	0	0	0	0	0	0	100,0	77	n.d.
S3053	Fideris	Fideris	A.Resentini	9	2	2	0	0	41	2	19	0	21	0	1	0	0	0	0	0	1	100,0	70	n.d.
S3052	Luzein	Luzein	A.Resentini	8	2	2	0	0	49	0	13	0	25	0	1	0	0	0	0	1	0	100,0	102	n.d.
S3059	Satteins	Satteins	A.Resentini	5	0	0	0	0	37	5	19	1	29	0	4	0	0	0	0	0	0	100,0	99	n.d.
S3060	Duns	Duns	A.Resentini	13	1	2	0	0	30	3	17	2	29	1	1	0	0	0	0	0	0	100,0	77	n.d.
S3061	Thuringerberg	Thuringerberg	A.Resentini	7	0	1	0	0	42	1	23	4	21	0	0	0	0	0	0	0	0	100,0	45	n.d.
S3072	Bolgenbach	Obermaiselstein	A.Resentini	29	2	3	0	0	18	1	8	1	31	1	4	0	0	0	0	0	1	100,0	130	n.d.
S3079	Bichl	Bichl	A.Resentini	9	2	2	0	0	31	23	13	2	17	0	1	0	0	0	0	0	0	100,0	87	n.d.
S3080	Bad Heilbrunn	Bad Heilbrunn	A.Resentini	10	1	1	0	0	37	5	23	2	20	0	1	0	0	0	0	0	0	100,0	69	n.d.
S3365	Voeckla	Haslau	A.Resentini	36	4	4	0	0	15	3	13	5	17	1	1	0	0	0	0	0	0	100,0	91	n.d.
S3367	Wessenaurach	Reindlmuehl	A.Resentini	48	4	4	0	0	14	4	5	1	16	0	3	0	0	0	0	0	2	100,0	134	n.d.
S3375	Hiesbach	Hiesbach	A.Resentini	47	4	4	0	0	8	6	8	0	22	0	1	0	0	0	0	0	1	100,0	105	n.d.
S3369	Klausbach	Kogl	A.Resentini	40	5	5	0	0	10	2	10	2	23	0	1	0	0	0	0	0	1	100,0	101	n.d.
OFFSCRAPED BRIANÇONNAIS COVERS																								
S3575	trib. Sx Fildrich	Grimmialp	A.Resentini	25	2	8	0	0	21	15	5	1	20	1	2	0	0	0	0	0	0	100,0	135	n.d.
OFFSCRAPED/OBDUCTED OPHIOLITES																								
S4027	Gimont	Gimont	A.Resentini	1	0	1	1	12	0	0	0	0	0	3	1	2	66	0	0	7	5	100,0	252	48
S3731	Totalp	Wolfgang	A.Resentini	0	0	0	0	0	2	6	0	0	1	0	0	0	81	0	0	1	8	100,0	n.d.	41
INTERMEDIATE STRUCTURAL LEVEL																								
SUBCRETED CALCSCHISTS																								
S2318	Aigue Blanche	Ville Vieille	A.Resentini	17	0	2	0	0	15	2	6	0	6	1	45	0	3	1	0	0	1	100,0	264	11
S2319	Guil	Ville Vieille	A.Resentini	22	1	1	0	0	15	1	7	0	1	1	44	0	3	1	1	0	1	100,0	296	0
S3021	San Michele	San Michele	A.Resentini	32	0	0	0	0	4	1	1	0	6	0	54	0	0	0	0	0	0	100,0	296	nd
S2192	Gressan	Gressan	G. Vezzoli	26	0	3	0	0	12	10	4	0	9	4	14	1	3	5	0	3	6	100,0	348	0
S2078	St. Barthelemy	Nus	G. Vezzoli	33	3	6	0	0	9	3	1	0	3	4	21	3	3	3	1	3	5	100,0	346	0
S1853	Dora di Verney	Pre St. Didier	G. Vezzoli	34	0	5	0	0	22	1	1	0	9	1	21	1	0	3	0	0	1	100,0	322	nd
S1854	Liconi	Morgex	G. Vezzoli	34	1	2	0	0	31	0	2	0	8	1	17	0	0	2	1	0	1	100,0	322	nd
S3048	Rabiusa	Bonaduz	A.Resentini	25	1	2	0	0	31	1	8	0	3	0	23	1	0	1	1	0	2	100,0	254	nd
S3046	Tartar	Tartar	A.Resentini	30	0	1	0	0	30	2	3	0	2	0	30	0	0	1	1	0	1	100,0	308	nd
S3047	Rothenbrunnen	Rothenbrunnen	A.Resentini	17	1	2	0	0	36	3	10	0	3	0	26	0	0	2	1	0	1	100,0	243	nd
S1753	Tasnan	Ardez	A.Resentini	22	2	20	0	0	11	0	4	0	4	1	14	2	9	1	1	5	2	100,0	297	16
S2418	Griosch	Griosch	A.Resentini	25	0	3	0	0	22	1	8	0	8	0	26	0	0	3	1	1	2	100,0	260	nd
S1756	Lavranca	Ramosch	A.Resentini	20	0	2	0	0	47	1	13	0	4	0	9	0	3	0	0	0	0	100,0	150	11
S2419	Arina	Serviezell	A.Resentini	28	1	2	0	0	26	3	10	0	5	0	23	1	0	0	0	0	1	100,0	241	nd
S2422	Mundin	Spiss	A.Resentini	23	0	1	0	0	32	2	9	0	6	6	18	0	0	0	0	0	1	100,0	187	nd
S2420	Mutller	Tschlin	A.Resentini	14	0	2	0	0	24	2	11	0	19	1	23	1	0	0	0	2	0	100,0	205	nd
S2421	Tea	Martina	A.Resentini	12	0	1	0	0	31	1	11	0	30	0	13	0	0	0	0	0	1	100,0	161	0
S1758	Scherbeng	Schalkl	A.Resentini	20	1	3	0	0	36	2	11	0	4	1	16	3	0	0	0	1	2	100,0	205	nd
S2432	Schmirnbach	St. Jodok	A.Resentini	24	2	3	0	0	27	3	7	0	3	0	23	0	0	2	2	0	5	100,0	256	nd
S2433	Padaster	Steinach	A.Resentini	23	0	0	0	0	28	3	8	0	10	1	25	0	0	0	0	0	1	100,0	218	nd
S2452	Kapruner	Kesselfall	A.Resentini	29	0	0	0	0	35	0	3	0	4	1	17	1	0	6	3	0	0	100,0	365	nd
S2459	Rauriser	Taxenbach	A.Resentini	39	5	7	0	0	10	4	2	0	1	1	20	2	0	3	1	2	3	100,0	338	nd
S2460	Sulzbach	Fusch	A.Resentini	42	1	1	0	0	8	1	2	0	5	0	30	3	0	0	0	1	5	100,0	295	nd
S2461	Breitebenkopf	Bad Fusch	A.Resentini	35	2	3	0	0	7	1	2	0	5	0	38	0	0	2	1	0	4	100,0	316	nd
S1567	Grossarl	Breitenebenaim	M. Russo	42	1	5	0	0	12	4	0	0	6	3	15	0	0	6	1	0	4	100,0	287	nd
S2464	Moll	Franz Joseph Hohe	A.Resentini	37	4	7	0	0	26	3	2	0	0	1	7	0	0	5	1	1	7	100,0	336	nd
S2494	Val Rossa	Casere	A.Resentini	33	4	7	0	0	8	4	1	0	0	1	13	9	0	8	3	4	5	100,0	364	nd
SUBCRETED BRIANÇONNAIS COVERS																								
S2343	Pesio	Chiusa di Pesio	A.Resentini	34	8	11	0	0	3	5	0	0	15	5	17	1	0	0	0	0	1	100,0	234	n.d.
S2344	Ellero	Villanova Mondovì	A.Resentini	33	6	8	0	0	1	4	0	0	18	2	27	0	0	1	0	0	0	100,0	264	n.d.
S17	Tanaro	Bagnasco	M. Russo	39	7	1	0	0	15	0	0	0	24	1	10	0	1	0	0	0	1	100,0	281	n.d.
S1140	B. di Millesimo	Millesimo	M. Russo	30	4	2	0	0	0	0	1	0	22	1	34	3	0	1	1	0	0	100,0	300	n.d.
S1141	B. di Mallare	Ferrania	M. Russo	27	2	1	0	0	0	1	2	0	36	1	24	2	1	1	1	1	1	100,0	266	n.d.
S184	Neva	Cisano	M. Russo	22	0	0	0	0	17	8	3	2	22	0	24	0	0	0	0	0	0	100,0	229	n.d.

Sample	River	Site	Operator	Q	KF	P	Lvf	Lvm	Lcc	Lcd	Lp	Lch	Lms	Lmv	Lmf	Lmb	Lu	Ms	Bt	A+POS	& HM	TOTAL	MI	Luc/Lu
SUBCRETED BRIANÇONNAIS COVERS (continued)																								
S185	Varatello	Loano	M. Russo	44	0	0	0	0	5	11	2	1	6	0	29	0	0	0	0	0	0	100,0	266	n.d.
S158	Porra	Finale	M. Russo	35	2	3	0	0	2	1	1	0	8	2	42	4	1	1	0	0	1	100,0	319	n.d.
S3020	Maira	Chiappera	A.Resentini	31	1	0	2	0	20	16	3	0	16	0	9	0	0	0	0	0	0	100,0	198	n.d.
SUBCRETED CONTINENTAL PENNINC BASEMENTS																								
S 153	Letimbro	Savona	M. Russo	36	9	4	0	0	0	0	1	0	4	0	43	1	0	0	0	0	0	100,0	342	n.d.
S2189	Planaval	Planaval	G. Vezzoli	43	2	3	0	0	0	0	0	0	0	1	40	0	0	4	3	0	4	100,0	403	n.d.
S1856	Dora di Valgrisenche	Ravoire	G. Vezzoli	40	3	6	0	0	6	0	1	0	3	2	25	2	0	6	2	1	1	100,0	361	n.d.
S2190	Dora di Rhemes	Rhemes	G. Vezzoli	30	4	22	0	0	4	2	2	0	2	3	25	1	0	2	1	0	2	100,0	372	n.d.
S1210	Liro	Mese	L. Mattavelli	43	10	14	0	0	1	0	0	0	0	2	0	4	0	10	10	0	6	100,0	326	n.d.
S2441	Zemm	Ginzling	A.Resentini	52	7	10	0	0	0	0	0	0	0	2	13	2	0	2	3	7	2	100,0	376	n.d.
S2442	Floitenbach	Ginzling	A.Resentini	47	11	14	0	0	0	0	0	0	0	0	9	0	0	5	10	3	2	100,0	433	n.d.
S2443	Stillupbach	Mayrhofen	A.Resentini	44	7	13	0	0	0	0	0	0	0	0	20	0	0	8	7	0	1	100,0	398	n.d.
S2446	Sonderbach	In der Au	A.Resentini	46	15	21	0	0	0	0	0	0	0	0	11	0	0	2	5	1	0	100,0	424	n.d.
S2444	Hundskehlbach	Barenbad	A.Resentini	36	8	12	0	0	0	0	0	0	0	1	15	1	0	10	14	2	2	100,0	396	n.d.
S2445	Ziller	Barenbad	A.Resentini	49	9	11	0	0	0	1	0	0	0	1	16	1	0	5	7	0	0	100,0	403	n.d.
S2713	Melnikfall	Faller Tumpf	A.Resentini	32	4	9	0	0	0	0	0	0	0	1	24	3	0	6	8	6	7	100,0	398	n.d.
S2715	Malta	Koschach	A.Resentini	49	2	16	0	0	0	0	0	0	0	3	13	0	0	5	8	2	2	100,0	380	n.d.
S2716	Gossbach	Koschach	A.Resentini	60	3	16	0	0	0	0	0	0	0	1	4	0	0	2	9	3	2	100,0	413	n.d.
S2723	Seebach	Stappitz	A.Resentini	53	7	14	0	0	0	0	0	0	0	1	4	0	0	2	9	5	3	100,0	360	n.d.
S2495	Griesbachthal	San Pietro	A.Resentini	51	6	7	0	0	0	0	0	0	0	1	12	0	0	10	9	1	3	100,0	398	n.d.
S2496	Keilbachthal	Cadipietra	A.Resentini	53	5	13	0	0	0	0	0	0	0	0	9	1	0	6	11	1	2	100,0	397	n.d.
S2497	Trippach	San Giovanni	A.Resentini	50	3	19	0	0	0	0	0	0	0	1	8	2	0	2	7	3	4	100,0	387	n.d.
S3091	Mesole	Lago di Mesole	A.Resentini	55	10	11	0	0	0	0	0	0	1	1	8	1	0	2	7	2	3	100,0	394	n.d.
S2450	Habach	Habach	A.Resentini	40	5	8	0	0	0	1	0	0	0	2	17	5	0	5	8	6	3	100,0	402	n.d.
S2451	Hollersbach	Hollersbach	A.Resentini	39	1	14	0	0	0	0	0	0	0	4	12	14	0	3	5	4	4	100,0	355	n.d.
S1570	Stubach	Uttendorf	A.Resentini	37	1	13	0	0	2	1	0	0	2	11	8	7	0	3	3	6	5	100,0	339	n.d.
S2710	Lieser	Tendel	A.Resentini	32	4	12	0	0	0	0	0	0	0	4	29	6	0	1	4	7	2	100,0	377	n.d.
S2714	Schlejerfall	Koschach	A.Resentini	32	6	10	0	0	0	0	0	0	0	2	24	5	0	5	9	6	0	100,0	403	n.d.
S2718	Muhldorfer	Muhldorf	A.Resentini	28	9	11	0	0	0	0	0	0	0	2	39	4	0	2	2	3	1	100,0	394	n.d.
S2709	Mur	Schellgaden	A.Resentini	43	7	11	0	0	0	0	0	0	0	2	29	1	0	2	3	0	2	100,0	375	n.d.
SUBCRETED AUSTROALPINE BASEMENTS																								
S2077	Buthier	Thoules	G. Vezzoli	30	6	18	0	0	1	0	0	0	0	2	19	5	0	1	4	4	8	100,0	363	n.d.
SUBCRETED OPHIOLITES																								
S3430	Mallero della Val Ventir	Rifugio Porro	A.Resentini	0	0	0	0	0	0	0	0	0	0	0	0	0	80	0	0	17	2	100,0	n.d.	18
DEEP STRUCTURAL LEVEL																								
CONTINENTAL ECLOGITES (CRETACEOUS AXIAL BELT)																								
S2194	Arnad	Arnad	A.Resentini	39	5	14	0	0	0	0	0	0	0	4	16	1	0	10	4	1	6	100,0	399	n.d.
S2195	Rio Fer	Clapey	A.Resentini	35	1	10	0	0	0	0	0	0	0	4	19	3	1	10	3	3	10	100,0	400	n.d.
S2295	Vogna	Riva Valdobbia	A.Resentini	40	1	6	0	0	0	0	0	0	4	4	24	5	0	4	2	4	6	100,0	359	n.d.
S2290	Sermenza	Cerva	A.Resentini	42	8	10	0	0	0	0	0	0	0	3	22	2	0	5	1	1	4	100,0	381	n.d.
S2293	Gronda	Rassa	A.Resentini	37	7	14	1	0	0	0	0	0	0	3	19	1	0	6	2	3	7	100,0	419	n.d.
S2292	Sorba	Rassa	A.Resentini	54	7	7	0	0	0	0	0	0	0	3	12	1	0	7	3	2	5	100,0	385	n.d.
S2294	Artogna	Otra	A.Resentini	37	8	10	0	0	0	0	0	0	0	4	16	1	0	9	2	3	10	100,0	366	n.d.
S2299	Riale	Piode	A.Resentini	46	5	6	0	0	0	0	0	0	1	2	18	1	0	11	2	1	7	100,0	385	n.d.
S3758	Rio di Salto	Pianlargo	A.Resentini	37	2	5	0	0	0	0	0	0	0	0	9	1	0	12	11	10	13	100,0	421	n.d.
S3755	Valclava	Valcalva	A.Resentini	36	2	3	0	0	0	0	0	0	0	1	12	0	0	11	8	5	22	100,0	396	n.d.
S2694	Lausslingbach	Obdach	A.Resentini	49	2	11	0	0	0	0	0	0	0	1	11	0	0	5	6	7	8	100,0	424	n.d.
S2695	Kienbergbach	Kathal	A.Resentini	36	1	7	0	0	0	1	0	0	0	0	10	0	0	16	8	6	15	100,0	421	n.d.
S2692	Lavant	Taxwirt	A.Resentini	36	1	3	0	0	0	1	0	0	0	0	8	0	0	7	5	2	38	100,0	430	n.d.
S2689	Weissenbach	St. Margarethen	A.Resentini	40	1	5	0	0	2	6	0	0	0	0	12	0	0	8	3	2	20	100,0	409	n.d.
S2691	Twimberg	Twimberg	A.Resentini	45	2	5	0	0	0	2	0	0	0	0	6	0	0	14	4	6	16	100,0	420	n.d.
S2690	St. Gertraud	St. Gertraud	A.Resentini	45	1	4	0	0	0	4	0	0	0	0	3	0	0	9	4	2	28	100,0	429	n.d.
S1527	Lavant	Effendorf	A.Resentini	45	1	3	0	0	0	3	0	0	0	0	9	1	0	16	4	3	16	100,0	359	n.d.
S1532	Kainach	Weitendorf	A.Resentini	49	2	4	0	0	0	2	0	0	5	0	11	0	0	6	2	2	17	100,0	nd	n.d.
S1528	Sulm	Seggau	A.Resentini	48	2	4	0	0	0	3	0	0	2	0	14	0	0	6	3	1	17	100,0	nd	n.d.
S1529	Lassnitz	Kaindorf	A.Resentini	58	4	4	0	0	0	0	0	0	1	0	9	2	0	7	2	2	13	100,0	nd	n.d.
S3399	Mislinja	Mislinja	A.Resentini	31	4	6	0	0	0	2	0	0	0	0	41	2	0	5	3	2	3	100,0	370	n.d.
S3398	Dravinja	Loska Gora	A.Resentini	29	1	4	0	0	1	14	0	0	0	0	24	3	0	6	7	6	5	100,0	399	n.d.
S3393	Lobnica	Ruse	A.Resentini	32	2	3	0	0	0	0	0	0	0	1	21	3	0	9	5	13	10	100,0	403	n.d.
CONTINENTAL ECLOGITES (EOCENE AXIAL BELT)																								
S2414	Gilba	Brossasco	A.Resentini	43	10	12	0	0	0	0	0	0	0	0	11	1	0	6	2	1	12	100,0	406	n.d.
S3018	Parigi	Martiniana Po	A.Resentini	45	8	7	0	0	0	0	0	0	0	1	16	1	2	7	5	0	7	100,0	395	0
S3017	Croesio	Croesio	A.Resentini	41	2	3	0	0	0	1	0	0	1	0	26	0	1	10	5	1	9	100,0	407	n.d.
S2177	Stura di Vallegrande	Forno	G. Vezzoli	47	15	12	0	0	0	0	0	0	0	0	15	0	0	7	4	0	1	100,0	389	n.d.
S2076	Grand Eyvia	Valnontey	G. Vezzoli	52	8	9	0	0	0	0	0	0	0	1	11	0	0	9	5	0	5	100,0	391	n.d.
S3138	Valsoera	Lago La Balma	A.Resentini	35	11	7	0	0	0	0	0	0	0	3	36	1	0	2	5	0	0	100,0	381	n.d.
S2176	Orco	Casetti	G. Vezzoli	48	17	13	0	0	0	0	0	0	0	1	12	1	0	3	3	0	3	100,0	373	n.d.
S2395	Anza	Croppo	G. Vezzoli	58	5	5	0	0	0	0	0	0	0	0	7	0	0	12	6	0	6	100,0	384	n.d.

Sample	River	Site	Operator	Q	KF	P	Lvf	Lvm	Lcc	Lcd	Lp	Lch	Lms	Lmv	Lmf	Lmb	Lu	Ms	Bt	A+POS	& HM	TOTAL	MI	Luc/Lu
CONTINENTAL ECLOGITES (EOCENE AXIAL BELT - continued)																								
S1068	Toce	Domodossola	M. Russo	55	7	14	0	0	1	0	0	0	0	0	3	1	0	6	5	0	6	100,0	420	n.d.
S1876	Toce	Oira	L. Mattavelli	49	6	10	0	0	1	0	1	0	0	1	2	0	0	6	14	2	7	100,0	nd	n.d.
S1877	Isorno	Montecretese	G. Vezzoli	35	15	13	0	0	0	0	0	0	1	0	3	0	0	10	5	13	5	100,0	413	n.d.
S1900	Onsernone	Sauressio	G. Vezzoli	46	21	20	0	0	0	0	0	0	0	1	1	0	0	3	5	1	1	100,0	441	n.d.
S1888	Campo	Cevio	A.Resentini	46	4	14	0	0	0	2	0	0	0	0	8	0	0	9	7	6	5	100,0	407	n.d.
S1886	Maggia	Bignasco	L. Mattavelli	47	8	12	0	0	0	0	0	0	0	1	1	1	0	7	10	6	7	100,0	477	n.d.
S1054	Maggia	Tegna	M. Russo	67	5	13	0	0	0	0	0	0	0	0	1	2	0	4	4	3	0	100,0	405	n.d.
S1890	Verzasca	Frasco	L. Mattavelli	51	9	15	0	0	0	0	0	0	0	0	0	1	0	9	9	4	1	100,0	491	n.d.
S1053	Verzasca	Tenero	M. Russo	46	7	18	0	0	0	0	0	0	0	0	5	3	0	6	8	5	2	100,0	417	n.d.
S1893	N Cugnasco	N Cugnasco																						
S1896	W Preonzo	W Preonzo																						
S1049	Moesa	Arbedo	M. Russo	56	4	19	0	0	0	0	0	0	1	0	3	1	0	4	5	6	2	100,0	420	n.d.
S1902	Marmontana	Roveredo	A.Resentini	40	7	11	0	0	0	0	0	0	0	0	15	1	0	3	6	12	5	100,0	421	n.d.
S1898	Calanca	Grono	L. Mattavelli	43	10	14	0	0	0	0	0	0	0	0	0	0	0	11	15	4	2	100,0	479	n.d.
S1897	Moesa	Lostallo	L. Mattavelli	45	8	9	0	0	1	0	0	0	0	1	1	0	0	11	7	8	7	100,0	448	n.d.
S1884	Boggia	Grondona	M. Russo	54	3	23	0	0	0	0	0	0	0	0	1	1	0	4	9	4	0	100,0	411	n.d.
OCEANIC ECLOGITES (EOCENE AXIAL BELT)																								
S148	Arrestra	Cogoleto	M. Russo	15	3	4	1	0	1	1	0	0	1	0	13	10	42	3	3	3	4	100,0	337	0
S142	Varenna	Pegli	A.Resentini	10	0	4	0	0	5	4	2	0	1	0	14	6	49	0	0	4	1	100,0	322	1
S2829	Stura del Turchino	Ovada	A.Resentini	20	0	10	0	0	1	0	0	0	0	1	17	5	26	0	0	9	9	100,0	351	2
S3558	Orba	Olbicella	A.Resentini	3	0	9	0	0	0	0	0	0	0	3	1	4	70	2	1	5	3	100,0	358	1
S175	Orba	Capriata	M. Russo	19	4	3	0	0	2	0	1	0	0	11	13	0	45	0	0	0	3	100,0	298	nd
S3016	Po	Pian del Re	A.Resentini	6	0	20	0	0	0	0	0	0	0	0	10	15	28	1	0	11	7	100,0	342	1
S3745	Casternone	Valdellatorre	A.Resentini	6	0	6	0	0	0	0	0	0	1	0	2	0	23	0	0	58	4	100,0	358	6
S2178	Stura di Ala	Ceres	A.Resentini	8	0	18	0	0	2	0	0	0	0	1	2	8	23	3	0	24	10	100,0	389	1
S2193	Chalamy	Champdepraz	G. Vezzoli	10	1	6	0	0	2	1	1	0	1	5	3	2	29	2	0	29	10	100,0	342	1
MIXED AXIAL-BELT UNITS																								
SHALLOW STRUCTURAL LEVEL																								
S2069	Dranse	Vogny	A.Resentini	11	2	3	0	0	52	4	12	1	13	1	2	0	0	0	0	0	0	100,0	111	n.d.
S3415	La Sarine	Broc	A.Resentini	14	1	1	0	0	57	7	9	3	8	0	0	0	0	0	0	0	0	100,0	58	n.d.
S3416	La Jogne	Charmey	A.Resentini	13	2	3	0	0	53	4	7	3	14	0	1	0	0	0	0	0	0	100,0	97	n.d.
S3419	Simme	Wimmis	A.Resentini	13	0	1	0	0	39	12	9	2	23	0	1	0	0	0	0	0	0	100,0	96	n.d.
S3057	Vilters	Vilters	A.Resentini	5	0	1	0	0	11	0	45	0	34	3	1	0	0	0	0	0	0	100,0	56	n.d.
S3740	Julia	Tiefencastel	A.Resentini	17	0	2	0	0	24	18	7	0	14	0	15	0	2	0	0	0	1	100,0	204	n.d.
INTERMEDIATE STRUCTURAL LEVEL																								
S1139	B. di Pallare	Carcare	M. Russo	40	4	1	0	0	0	2	0	0	22	2	15	4	4	3	1	0	0	100,0	294	20
S2331	Ubaye	La Barge	A.Resentini	21	0	0	0	0	15	9	8	0	32	0	12	0	1	0	0	0	2	100,0	169	n.d.
S1861	Buthier	Castello	G. Vezzoli	31	2	15	0	0	6	0	1	0	3	3	15	7	1	2	3	2	10	100,0	332	n.d.
S1862	Buthier	Roisane	G. Vezzoli	33	2	10	0	0	5	0	0	0	5	4	15	6	1	1	1	4	13	100,0	323	n.d.
S1860	Artanavaz	Roisane	G. Vezzoli	39	4	4	0	0	4	2	0	0	3	4	26	2	0	9	2	0	2	100,0	349	n.d.
S1211	Mera	Chiavenna	M. Russo	54	12	14	0	0	0	0	0	0	1	0	6	1	0	5	5	2	1	100,0	415	n.d.
S2498	Aurino	Lutago	A.Resentini	42	5	12	0	0	6	1	3	0	0	1	10	3	1	4	3	4	4	100,0	365	n.d.
S3088	Pfitscherbach	S. Giacomo	A.Resentini	43	5	6	0	0	9	4	1	0	0	0	11	2	0	7	6	2	4	100,0	350	n.d.
S2448	Tux	Persal	A.Resentini	25	2	1	0	0	7	2	2	0	5	0	52	0	0	1	0	0	3	100,0	325	n.d.
S2449	Gerlos	Zell am Ziller	A.Resentini	34	6	7	0	0	4	2	1	0	2	1	37	0	0	6	0	0	1	100,0	357	n.d.
S2447	Ziller	N Hausling	A.Resentini	54	5	6	0	0	0	0	0	0	0	1	16	1	0	6	5	1	3	100,0	359	n.d.
S1574	Ziller	Ramsau	M. Russo	47	2	8	0	0	2	3	0	0	11	5	12	0	0	3	6	1	1	100,0	274	n.d.
S1572	Krimml	Wald	M. Russo	40	3	8	0	0	3	2	0	0	7	3	26	2	1	2	2	1	1	100,0	339	n.d.
S1572	Krimml	Wald	A.Resentini	40	3	7	0	0	0	4	0	0	1	1	41	0	2	0	1	0	0	100,0	322	0
S1569	Fuschbach	Bruck a.d.Gr.	M. Russo	28	0	0	0	0	26	4	5	0	4	5	21	1	1	3	1	0	0	100,0	252	n.d.
S2462	Fuscher	Ferleiten	A.Resentini	28	0	1	0	0	40	7	3	0	0	0	11	0	1	4	0	0	4	100,0	290	n.d.
S1568	Gasteiner	Lend	M. Russo	47	5	4	0	0	5	2	1	0	4	5	18	1	0	2	2	1	3	100,0	318	n.d.
S2719	Reisseck	Preisdorf	A.Resentini	45	7	10	0	0	2	1	1	0	0	1	25	1	0	2	3	2	0	100,0	383	n.d.
S2721	Tristenspitze	Obervellach	A.Resentini	32	5	12	0	0	1	0	1	0	0	1	20	7	0	5	5	9	3	100,0	375	n.d.
S2722	Malnitzbach	Malnitz	A.Resentini	34	1	3	0	0	13	1	3	0	0	0	37	1	0	2	3	0	1	100,0	349	n.d.
S2725	Fragrantbach	Innerfragrant	A.Resentini	24	4	5	0	0	6	6	1	0	0	1	29	0	0	20	5	0	0	100,0	355	n.d.
S2466	Zirknitz	Grosskirchheim	A.Resentini	25	3	4	0	0	20	6	2	0	0	0	24	0	1	8	3	1	3	100,0	332	n.d.
S2465	Zirm	Pockhorn	A.Resentini	34	4	7	0	0	7	2	1	0	0	0	31	0	0	7	4	0	3	100,0	370	n.d.
S1516	Malta	Gmund	M. Russo	46	6	11	0	0	0	0	0	0	1	0	17	6	1	1	5	4	3	100,0	382	n.d.
S2717	Radlbach	Radl	M. Russo	38	8	13	0	0	0	0	0	0	0	1	14	6	0	3	5	6	6	100,0	389	n.d.
MIXED STRUCTURAL LEVELS																								
S2080	Ayassse	Hone	G. Vezzoli	32	5	5	0	0	3	1	0	0	2	6	14	0	8	7	3	4	8	100,0	368	0
S2296	Sesia	Alagna	G. Vezzoli	41	6	8	0	0	0	0	0	0	1	1	17	1	2	8	6	2	8	100,0	442	17
S1872	Anza	Piedimulera	G. Vezzoli	45	9	10	0	0	0	0	0	0	1	3	0	0	0	12	3	8	10	100,0	411	n.d.
MIXED AXIAL BELT LEVELS																								
S482	Grana	S.Benigno	M. Russo	28	1	3	0	0	13	13	1	0	14	5	16	0	0	3	3	0	0	100,0	276	n.d.
S481	Maira	Busca	M. Russo	38	1	1	0	0	12	10	2	0	13	8	7	2	0	3	2	0	0	100,0	248	n.d.
S480	Varaita	Costigliole	M. Russo	40	1	4	0	0	1	0	0	0	13	3	16	4	6	6	3	1	2	100,0	328	0

Sample	River	Site	Operator	Q	KF	P	Lvf	Lvm	Lcc	Lcd	Lp	Lch	Lms	Lmv	Lmf	Lmb	Lu	Ms	Bt	A+POS	& HM	TOTAL	MI	Luc/Lu
MIXED AXIAL BELT LEVELS (continued)																								
S475	Maira	Casalgrasso	M. Russo	48	3	9	0	0	10	3	0	0	12	3	8	0	1	2	1	1	0	100,0	263	n.d.
S479	Po	Staffarda	G. Vezzoli	39	5	9	0	0	0	0	0	0	0	1	3	5	15	6	3	4	9	100,0	402	0
S478	Pellice	Bibiana	M. Russo	25	2	8	0	0	2	0	0	0	4	18	17	0	3	10	5	0	4	100,0	n.d.	0
S477	Chisone	Pinerolo	M. Russo	32	1	7	0	0	7	0	0	0	5	2	25	6	2	5	4	0	3	100,0	355	n.d.
S554	Dora Riparia	Avigliana	M. Russo	20	0	0	0	0	28	7	4	0	13	4	14	0	4	3	2	0	0	100,0	254	n.d.
S2179	Stura di Viù	Fucine	A.Resentini	19	0	10	0	0	9	0	1	0	1	1	11	5	16	4	0	12	13	100,0	337	4
S555	Stura di Lanzo	Lanzo	M. Russo	32	6	5	0	0	0	0	0	0	3	5	6	23	7	4	4	3	2	100,0	331	0
S556	Orco	Cuorgné	M. Russo	34	7	9	0	0	1	0	0	0	6	4	19	9	3	4	1	1	2	100,0	323	0
S2175	Soana	Pont Canavese																						
S2191	Savara	Molere	G. Vezzoli	34	5	12	0	0	4	1	0	0	1	2	17	4	0	5	1	5	8	100,0	380	n.d.
S1857	Savara	Villeneuve	G. Vezzoli	38	5	7	0	0	6	5	0	0	1	5	10	4	0	9	1	3	5	100,0	314	n.d.
S1858	Grand Eyvia	Aymaviles	G. Vezzoli	29	3	6	0	0	7	6	2	0	3	2	11	5	4	4	1	5	12	100,0	358	0
S910	Lys	Pont S.Martin	G. Vezzoli	47	3	6	0	0	0	0	0	0	0	4	21	0	3	5	3	3	7	100,0	425	0
S912	Evancon	Verres	G. Vezzoli	20	3	14	0	0	0	0	0	0	0	3	21	8	11	1	1	7	12	100,0	358	0
S2081	Clavalitè	Barche	G. Vezzoli	21	1	8	0	0	5	0	0	0	1	3	14	5	4	7	1	11	19	100,0	374	0
S2079	Emilius	Pollein	A.Resentini	27	1	14	0	0	0	0	0	0	0	1	5	4	3	12	2	15	15	100,0	394	11
S994	Marmore	Chatillon	G. Vezzoli	30	2	10	0	0	2	1	1	0	1	7	14	5	3	3	1	10	9	100,0	345	0
S2058	Borgne	Bramois	A.Resentini	32	7	10	0	0	8	2	0	0	0	1	14	6	5	2	0	2	8	100,0	352	0
S2055	Navisence	Chippis	A.Resentini	41	5	9	0	0	4	1	1	0	1	5	13	5	2	2	0	3	8	100,0	336	0
S2050	Vispa	Neubruch	A.Resentini	42	4	6	0	0	2	2	0	0	0	0	13	1	1	6	1	7	13	100,0	381	n.d.
S2048	Brig	Brig	A.Resentini	41	3	4	0	0	9	7	1	0	1	0	10	0	0	7	3	4	10	100,0	386	n.d.
S1873	Ovesca	Villadossola	L. Mattavelli	44	5	10	0	0	1	0	0	0	0	1	2	2	2	11	8	7	8	100,0	nd	n.d.
S1874	Bogna	Domodossola	L. Mattavelli	38	8	8	0	0	3	0	0	0	1	1	0	2	2	8	4	11	14	100,0	361	n.d.
S1875	Diveria	Crevoladossola	G. Vezzoli	50	11	9	0	0	3	0	1	0	0	1	7	0	0	5	5	4	5	100,0	409	n.d.
S1878	Melezzo	Masera	L. Mattavelli	54	8	16	0	0	0	0	0	0	0	1	1	1	0	11	6	0	2	100,0	nd	n.d.
S1895	Brenno	Biasca	M. Russo	46	2	9	0	0	4	5	1	0	4	1	5	0	0	8	7	2	7	100,0	434	n.d.
S2391	E Ponte	Ponte	A.Resentini	61	3	6	0	0	3	1	0	0	0	1	6	0	0	4	8	2	4	100,0	409	n.d.
S1887	Bavona	Fontana	L. Mattavelli	48	8	12	0	0	2	2	0	0	0	0	0	0	0	6	11	4	7	100,0	454	n.d.
S2477	Tauernbach	Gruben	A.Resentini	47	6	9	0	0	0	0	0	0	0	1	16	3	0	4	6	3	4	100,0	388	n.d.
S2476	Frossnitz	Gruben	A.Resentini	36	4	15	0	0	10	6	1	0	0	1	11	2	0	4	2	1	8	100,0	363	n.d.
S2474	Isel	Pragraten	A.Resentini	43	2	8	0	0	9	2	2	0	0	2	15	3	0	7	3	1	3	100,0	342	n.d.

Heavy-Mineral Assemblages of Modern Sands from the Alpine Axial Belts

Sample	River	Site	Operator	grain size (µm)	grain size (φ)	HMC (weight%)	% transparent	% opaque	% turbid	TOTAL	HCI Index	MMI Index	zircon	tourmaline	rutile	other Ti-oxides	titanite	apatite	monazite+xenotime	barite	blue-green hornblende	green hornblende	green-brown hornblende	brown hornblende	actinolite	Na-amphiboles	other amphiboles	clinopyroxene	enstatite	hypersthene	olivine	spinel	epidote group	chloritoid	carpholite	prehnite+pumpellyite	garnet	staurolite	kyanite	andalusite	sillimanite	others	TOTAL
SHALLOW STRUCTURAL LEVEL																																											
OFFSCRAPED REMNANT-OCEAN TURBIDITES																																											
S14	Argentina	Taggia	S. Monguzzi	345	1,5	0,1	56	11	34	100,0	31	n.d.	7	12	8	4	1	0	0	0	4	1	2	1	0	0	0	5	0	3	0	0	22	0	0	0	23	0	0	0	0	1	100,0
S438	Impero	Imperia	S. Andò	595	0,8	0,4	77	10	13	100,0	32	57	2	4	2	3	1	1	0	0	11	0	6	2	3	2	0	7	2	3	0	0	23	0	0	0	25	1	0	0	1	0	100,0
S639	Merula	Andora	S. Monguzzi	435	1,2	0,0	66	7	27	100,0	29	45	20	1	4	3	2	0	0	0	12	3	2	4	1	1	0	4	0	2	0	1	23	3	0	0	11	0	0	0	2	0	100,0
S15	Arroscia	Ortovero	S. Andò	1000	0,0	0,0	27	19	54	100,0	n.d.	n.d.	16	10	9	2	0	0	0	0	6	0	1	0	0	0	0	3	1	3	0	0	20	0	0	0	27	1	0	0	1	0	100,0
S2329	Parpaillon	La Condamine	P. Paparella	239	2,1	0,0	10	45	45	100,0	n.d.	n.d.	36	29	25	0	0	0	0	0	0	0	0	0	0	0	0	4	4	0	0	0	4	0	0	0	0	0	0	0	0	0	100,0
S2322	Crévoux	Crévoux	P. Paparella	203	2,3	0,0	12	58	30	100,0	n.d.	n.d.	36	20	0	0	0	0	0	0	0	0	0	4	4	0	0	8	0	0	0	0	12	0	0	0	16	0	0	0	0	0	100,0
S3417	Hundsdrügg	Garstatt	M. Padoan	265	1,9	0,2	30	13	57	100,0	69	n.d.	2	9	3	16	0	26	0	0	1	5	0	9	1	0	0	0	0	0	0	11	11	0	0	0	2	0	3	0	0	0	100,0
S3418	Affl. Sx. Färmel	Matten	M. Padoan	353	1,5	0,3	28	14	58	100,0	n.d.	n.d.	10	35	6	25	0	8	0	0	0	4	0	2	0	0	0	0	0	0	0	0	8	0	0	0	0	0	2	0	0	0	100,0
S3578	trib. Dx Hero	Riedern	M. Padoan	299	1,7	0,2	35	13	52	100,0	n.d.	n.d.	5	24	7	13	0	9	0	0	0	4	1	0	2	0	0	0	0	0	0	0	34	0	0	0	0	0	0	0	0	0	100,0
S3054	Furna	Furna	P. Paparella	274	1,9	0,0	7	67	27	100,0	n.d.	n.d.	10	58	2	0	3	0	0	2	13	2	0	0	0	0	0	5	0	0	0	0	2	0	0	0	3	0	0	0	2	0	100,0
S3053	Fideris	Fideris	P. Paparella	161	2,6	0,1	27	29	43	100,0	5	n.d.	13	16	15	0	3	1	0	0	19	2	1	0	4	0	0	6	0	0	0	1	10	0	0	3	6	1	0	0	0	0	100,0
S3052	Luzein	Luzein	M. Padoan	290	1,8	1,3	65	13	22	100,0	5	n.d.	0	0	0	0	0	0	0	0	39	6	0	0	1	0	0	0	0	0	0	0	47	0	0	0	5	0	0	0	0	0	100,0
S3059	Satteins	Satteins	P. Paparella	287	1,8	0,0	22	43	35	100,0	2	n.d.	7	8	5	0	0	0	0	0	37	2	0	0	2	0	0	0	0	0	0	0	18	0	0	0	17	2	0	0	0	0	100,0
S3060	Duns	Duns	P. Paparella	330	1,6	0,0	54	12	35	100,0	5	n.d.	8	10	14	0	1	0	0	0	25	2	1	1	5	0	0	0	0	0	0	1	26	0	0	0	9	1	0	0	0	0	100,0
S3061	Thuringerberg	Thuringerberg	P. Paparella	416	1,3	0,0	26	24	50	100,0	5	n.d.	16	28	16	0	0	1	0	7	7	0	1	0	3	0	0	1	0	0	0	0	12	0	0	0	10	0	0	1	0	0	100,0
S3072	Bolgenbach	Obermaiselstein	P. Paparella	370	1,4	0,0	48	8	44	100,0	n.d.	n.d.	4	14	13	0	0	0	0	0	0	0	0	0	0	0	0	0	0	0	0	0	0	0	0	0	68	0	0	0	0	0	100,0
S3079	Bichl	Bichl	P. Paparella	379	1,4	0,0	56	12	32	100,0	4	43	0	1	4	1	1	0	0	0	27	0	2	0	3	0	1	1	0	0	0	0	14	0	0	0	36	9	3	0	1	1	100,0
S3080	Bad Heilbrunn	Bad Heilbrunn	P. Paparella	354	1,5	0,0	60	16	24	100,0	6	35	7	8	7	0	1	3	0	0	10	1	1	0	0	0	0	0	0	0	0	0	11	0	0	0	43	10	1	0	0	0	100,0
S3365	Voeckla	Haslau	M. Padoan	410	1,3	0,4	41	14	45	100,0	n.d.	n.d.	3	11	7	4	1	4	0	0	1	2	0	0	0	0	0	0	0	0	0	0	7	0	0	0	54	2	0	0	0	0	100,0
S3367	Wessenaurach	Reindlmuehl	M. Padoan	337	1,6	0,6	46	13	41	100,0	n.d.	33	2	13	6	3	4	3	0	0	1	0	0	0	0	0	0	0	0	0	0	0	2	0	0	0	60	4	0	0	0	0	100,0
S3375	Hiesbach	Hiesbach	M. Padoan	430	1,2	1,3	65	5	30	100,0	10	100	0	1	1	0	3	1	0	0	7	3	0	0	1	1	0	1	0	0	0	0	39	0	0	0	36	0	0	0	3	0	100,0
S3369	Klausbach	Kogl	M. Padoan	328	1,6	0,3	33	10	57	100,0	n.d.	n.d.	8	14	10	7	5	5	0	0	2	1	0	0	0	0	0	0	0	0	0	0	8	0	0	0	39	2	0	1	0	0	100,0
OFFSCRAPED BRIANÇONNAIS COVERS																																											
S3575	trib. Sx Fildrich	Grimmialp	M. Padoan	294	1,8	0,3	52	5	44	100,0	n.d.	n.d.	9	15	6	13	0	12	0	0	1	1	0	1	1	0	0	0	0	0	0	0	39	1	0	0	1	0	0	0	1	0	100,0
OFFSCRAPED/OBDUCTED OPHIOLITES																																											
S4027	Gimont	Gimont	M. Padoan	812	0,3	23,6	54	15	31	100,0	35	n.d.	0	0	0	0	1	0	0	0	10	4	3	4	9	0	0	33	0	0	0	0	36	0	0	0	0	0	0	0	0	0	100,0
S3731	Totalp	Wolfgang	M. Padoan	374	1,4	79,8	48	16	36	100,0	n.d.	n.d.	0	0	0	3	0	0	0	0	0	0	0	0	5	0	0	57	0	0	0	0	33	0	0	0	0	0	0	0	0	0	100,0
INTERMEDIATE STRUCTURAL LEVEL																																											
SUBCRETED CALCSCHISTS																																											
S2318	Aigue Blanche	Ville Vieille	P. Paparella	223	2,2	1,3	28	6	66	100,0	n.d.	n.d.	0	0	0	3	5	0	0	0	5	0	0	5	17	29	2	17	0	0	0	0	14	5	0	0	0	0	0	0	0	0	100,0
S2319	Guil	Ville Vieille	P. Paparella	114	3,1	1,9	30	7	62	100,0	n.d.	0	0	5	2	4	2	0	0	0	0	0	0	0	8	2	1	1	0	0	0	0	13	63	0	0	0	0	0	0	0	0	100,0
S3021	San Michele	San Michele	M. Padoan	192	2,4	5,7	22	2	76	100,0	86	n.d.	2	2	0	0	0	4	0	0	4	4	2	47	2	0	0	0	0	0	0	0	22	7	0	0	2	0	0	0	0	0	100,0
S2192	Gressan	Gressan	S. Monguzzi	362	1,5	8,0	80	3	17	100,0	2	n.d.	1	0	2	0	2	0	0	0	10	0	0	0	38	0	0	1	0	0	0	0	43	0	0	0	3	0	0	0	0	0	100,0
S2078	St. Barthelemy	Nus	S. Monguzzi	256	2,0	11,7	73	2	25	100,0	14	0	1	0	0	0	2	0	0	0	7	1	0	1	13	3	1	2	0	1	0	0	58	3	0	1	4	0	0	0	0	0	100,0
S1853	Dora di Verney	Pre St. Didier	S. Monguzzi	194	2,4	3,8	37	12	51	100,0	29	0	2	7	2	0	0	0	0	0	5	3	3	1	3	6	0	1	1	1	0	0	47	6	0	1	16	0	0	0	0	0	100,0
S1854	Liconi	Morgex	S. Monguzzi	194	2,4	2,8	38	20	42	100,0	42	0	1	21	6	0	5	0	0	0	2	2	2	1	3	0	1	1	1	0	0	0	35	14	0	0	8	0	0	1	0	0	100,0
S3048	Rabiusa	Bonaduz	P. Paparella	233	2,1	1,8	43	18	39	100,0	2	n.d.	0	2	4	0	1	5	0	0	23	1	0	0	2	0	0	0	0	0	0	0	51	0	0	0	10	0	0	0	0	0	100,0
S3046	Tartar	Tartar	P. Paparella	561	0,8	0,0	5	17	78	100,0	n.d.	n.d.	0	38	3	0	0	0	0	3	3	0	0	0	0	0	0	3	0	0	0	0	34	7	0	0	7	0	0	0	0	0	100,0
S3047	Rothenbrunnen	Rothenbrunnen	P. Paparella	213	2,2	0,6	11	9	80	100,0	n.d.	0	12	46	21	1	0	0	0	0	4	0	0	0	0	0	0	1	0	0	0	0	6	3	0	1	3	0	0	0	0	0	100,0
S1753	Tasnan	Ardez	P. Paparella	169	2,6	4,7	69	5	26	100,0	4	n.d.	0	1	0	0	1	0	0	0	58	6	1	0	3	0	0	0	0	0	0	0	19	0	0	1	8	0	0	0	0	0	100,0
S2418	Griosch	Griosch	P. Paparella	244	2,0	1,1	32	6	62	100,0	5	n.d.	3	18	11	0	2	0	0	0	40	2	2	0	3	0	0	0	0	0	0	0	14	0	0	1	7	0	0	0	0	0	100,0
S1756	Lavranca	Ramosch	P. Paparella	208	2,3	0,5	47	19	34	100,0	12	n.d.	3	6	1	0	0	0	0	0	40	6	2	2	3	0	0	6	0	0	0	0	23	0	0	1	4	0	0	0	0	0	100,0
S2419	Arina	Serviezell	P. Paparella	140	2,8	0,6	65	13	22	100,0	6	n.d.	2	21	3	0	0	0	0	0	37	0	3	0	9	0	0	2	0	0	0	0	18	0	0	0	3	1	0	0	0	0	100,0
S2422	Mundin	Spiss	P. Paparella	157	2,7	2,5	26	2	72	100,0	n.d.	n.d.	0	2	0	0	0	0	0	0	1	0	0	0	3	0	0	16	0	0	0	0	78	0	0	0	0	0	0	0	1	0	100,0
S2420	Mutller	Tschlin	P. Paparella	294	1,8	6,6	59	8	34	100,0	7	n.d.	0	10	2	0	0	0	0	0	63	2	0	4	1	0	0	1	0	0	0	0	14	0	0	0	1	0	0	0	0	0	100,0
S2421	Tea	Martina	P. Paparella	125	3,0	0,5	29	14	58	100,0	3	n.d.	0	12	1	0	1	0	0	0	47	1	1	0	5	0	0	1	0	0	0	0	25	0	0	0	4	1	0	0	0	0	100,0
S1758	Scherbeng	Schalkl	P. Paparella	244	2,0	4,1	28	2	70	100,0	35	n.d.	0	0	1	0	0	0	0	0	7	1	3	3	1	0	1	6	0	0	0	0	76	0	0	0	2	0	0	0	1	0	100,0
S2432	Schmirnbach	St. Jodok	P. Paparella	137	2,9	2,3	77	5	18	100,0	n.d.	3	0	5	3	1	4	0	0	0	1	0	0	0	5	0	0	1	0	0	0	0	70	5	0	0	6	1	0	0	0	0	100,0
S2433	Padaster	Steinach	P. Paparella	294	1,8	0,6	20	34	46	100,0	2	n.d.	0	29	9	4	0	0	0	0	27	1	0	0	0	0	0	0	0	0	0	0	21	0	0	0	9	0	0	0	0	0	100,0
S2452	Kapruner	Kesselfall	P. Paparella	218	2,2	5,3	78	5	16	100,0	n.d.	0	0	3	2	0	7	0	0	0	2	0	0	0	5	0	0	0	0	0	0	0	53	19	0	0	7	0	0	0	0	0	100,0
S2459	Rauriser	Taxenbach	P. Paparella	205	2,3	11,5	78	12	9	100,0	0	0	0	2	1	0	1	0	0	0	7	0	0	0	4	0	0	0	0	0	0	0	66	15	0	0	3	0	0	0	0	0	100,0
S2460	Sulzbach	Fusch	P. Paparella	154	2,7	7,3	75	6	19	100,0	n.d.	0	0	0	1	0	1	0	0	0	0	0	0	0	9	0	0	0	0	0	0	0	81	6	0	0	0	0	0	0	0	0	100,0
S2461	Breitebenkopf	Bad Fusch	P. Paparella	291	1,8	5,3	20	72	8	100,0	0	0	0	2	3	2	1	0	0	0	5	0	0	0	6	0	0	0	0	0	0	0	58	23	0	0	1	0	0	0	0	0	100,0
S1567	Grossarl	Breitenebenaim	P. Paparella	70	3,8	3,9	72	10	18	100,0	n.d.	0	0	0	0	2	0	0	0	0	1	0	0	0	2	1	0	0	0	0	0	0	88	3	0	0	0	0	0	0	0	0	100,0

Sample	River	Site	Operator	grain size (µm)	grain size (φ)	HMC (weight%)	% transparent	% opaque	% turbid	TOTAL	HCI Index	MMI Index	zircon	tourmaline	rutile	other Ti-oxides	titanite	apatite	monazite+xenotime	barite	blue-green hornblende	green hornblende	green-brown hornblende	brown hornblende	actinolite	Na-amphiboles	other amphiboles	clinopyroxene	enstatite	hypersthene	olivine	spinel	epidote group	chloritoid	carpholite	prehnite+pumpellyite	garnet	staurolite	kyanite	andalusite	sillimanite	others	TOTAL
SUBCRETED CALCSCHISTS (continued)																																										
S2464	Moll	Franz Joseph Hohe	P. Paparella	177	2,5	6,5	92	4	4	100,0	0	n.d.	1	2	0	0	5	0	0	0	7	0	0	0	3	0	0	0	0	0	0	0	68	0	0	0	14	0	0	0	0	0	100,0
S2494	Val Rossa	Casere	P. Paparella	150	2,7	17,3	94	4	2	100,0	0	n.d.	0	0	0	0	5	0	0	0	14	0	0	0	19	0	0	0	0	0	0	0	58	0	0	0	3	0	0	0	0	0	100,0
SUBCRETED BRIANÇONNAIS COVERS																																										
S2343	Pesio	Chiusa di Pesio	M. Padoan	478	1,1	3,4	32	7	61	100,0	n.d.	n.d.	13	1	1	4	3	1	0	0	0	4	0	4	0	0	0	0	0	0	0	0	66	0	0	0	1	0	0	0	0	0	100,0
S2344	Ellero	Villanova Mondovì	M. Padoan	368	1,4	3,9	49	5	46	100,0	n.d.	n.d.	17	0	1	5	3	9	0	0	2	1	1	1	2	26	0	0	0	0	0	0	28	1	0	0	4	0	0	0	1	0	100,0
S17	Tanaro	Bagnasco	S. Andò	277	1,9	1,5	17	11	72	100,0	7	n.d.	16	3	2	0	4	0	0	0	18	0	0	1	3	1	0	0	1	0	0	0	44	1	1	0	3	1	0	0	0	0	100,0
S1140	B. di Millesimo	Millesimo	S.Andò	524	0,9	2,7	51	6	44	100,0	32	n.d.	1	1	0	0	1	6	0	0	5	26	0	2	4	0	1	0	0	0	0	0	47	0	0	0	3	1	0	0	0	0	100,0
S1141	B. di Mallare	Ferrania	E.Mauri	467	1,1	4,8	72	11	18	100,0	28	n.d.	1	1	0	0	0	0	0	0	3	18	0	0	0	3	0	2	0	0	0	0	56	1	0	1	9	0	0	0	0	0	100,0
S184	Neva	Cisano	S. Andò	345	1,5	1,0	17	5	78	100,0	n.d.	n.d.	0	10	0	0	0	2	0	0	0	0	0	0	3	3	0	5	0	3	0	0	71	0	0	2	0	0	0	0	0	0	100,0
S185	Varatello	Loano	S. Andò	955	0,1	1,6	16	14	70	100,0	18	48	2	1	1	0	1	0	0	0	16	3	1	2	2	0	0	6	0	0	0	0	30	0	0	1	25	2	1	0	0	0	100,0
S158	Porra	Finale	S. Monguzzi	881	0,2	0,5	41	4	55	100,0	22	25	5	3	5	0	0	0	0	0	4	3	1	0	2	0	0	2	0	1	0	0	62	4	0	0	3	0	0	0	1	0	100,0
S3020	Maira	Chiappera	M. Padoan	261	1,9	1,1	44	8	48	100,0	36	n.d.	16	3	2	2	0	3	0	0	2	19	0	2	2	2	0	0	0	0	0	0	45	0	0	0	0	0	0	0	3	0	100,0
SUBCRETED CONTINENTAL PENNINC BASEMENTS																																										
S153	Letimbro	Savona	S. Andò	699	0,5	1,5	69	9	21	100,0	10	5	5	1	1	0	5	0	0	0	30	0	2	1	9	2	0	0	0	0	0	0	35	3	0	0	3	0	0	0	0	0	100,0
S2189	Planaval	Planaval	S. Monguzzi	675	0,6	6,1	61	17	22	100,0	n.d.	0	1	1	1	0	3	0	0	0	0	0	0	0	1	3	0	0	0	0	0	0	11	33	0	0	43	0	0	0	0	0	100,0
S1856	Dora di Valgrisenche	Ravoire	S. Monguzzi	345	1,5	4,3	73	10	16	100,0	17	0	1	2	0	0	7	1	0	0	4	3	1	0	3	5	0	2	4	1	0	0	32	14	0	1	23	0	0	0	0	0	100,0
S2190	Dora di Rhemes	Rhemes	S. Monguzzi	425	1,2	6,5	66	5	28	100,0	n.d.	n.d.	2	1	2	0	7	0	0	0	5	0	0	0	18	1	0	1	0	0	0	0	38	1	0	0	26	0	0	0	0	0	100,0
S1210	Liro	Mese	E.Mauri	675	0,6	6,2	81	11	7	100,0	13	n.d.	1	2	0	0	3	0	0	0	15	5	0	1	2	0	0	1	0	0	0	0	24	0	0	0	43	1	0	1	0	0	100,0
S2441	Zemm	Ginzling	P. Paparella	253	2,0	14,9	96	3	1	100,0	0	n.d.	0	0	1	0	0	0	0	0	46	0	0	0	3	0	0	0	0	0	0	0	31	0	0	0	17	0	0	0	0	0	100,0
S2442	Floitenbach	Ginzling	P. Paparella	370	1,4	2,3	98	1	1	100,0	1	n.d.	0	0	0	0	1	0	0	0	46	2	0	0	8	0	0	0	0	0	0	0	37	0	0	0	6	0	0	0	0	0	100,0
S2443	Stillupbach	Mayrhofen	P. Paparella	165	2,6	0,4	93	3	3	100,0	2	n.d.	2	0	0	0	5	0	0	0	7	0	0	0	3	0	0	0	0	0	0	0	69	0	0	0	13	0	0	0	0	0	100,0
S2446	Sonderbach	In der Au	P. Paparella	274	1,9	4,0	99	0	0	100,0	0	n.d.	0	0	0	0	2	0	0	0	24	0	0	0	3	0	0	0	0	0	0	0	63	0	0	0	7	0	0	0	0	0	100,0
S2444	Hundskehlbach	Barenbad	P. Paparella	181	2,5	2,0	100	0	0	100,0	1	n.d.	0	0	0	0	1	0	0	0	22	0	0	0	1	0	0	0	0	0	0	0	67	0	0	0	7	0	0	0	0	0	100,0
S2445	Ziller	Barenbad	P. Paparella	724	0,5	3,6	96	1	3	100,0	3	n.d.	0	0	0	0	3	0	0	0	11	0	0	0	2	0	0	0	0	0	0	0	74	0	0	0	8	0	0	0	0	0	100,0
S2713	Melnikfall	Faller Tumpf	P. Paparella	630	0,7	9,7	99	1	0	100,0	3	n.d.	0	0	4	0	6	0	0	0	42	3	0	0	8	0	0	0	0	0	0	0	31	0	0	0	4	0	0	0	0	0	100,0
S2715	Malta	Koschach	P. Paparella	691	0,5	12,0	99	0	1	100,0	1	n.d.	0	0	0	0	1	0	0	0	48	0	0	0	4	0	0	0	0	0	0	0	39	0	0	0	7	0	0	0	0	0	100,0
S2716	Gossbach	Koschach	P. Paparella	144	2,8	3,7	99	1	0	100,0	0	n.d.	0	0	0	0	5	0	0	0	29	0	0	0	2	0	0	0	0	0	0	0	63	0	0	0	0	0	0	0	0	0	100,0
S2723	Seebach	Stappitz	P. Paparella	119	3,1	3,8	94	4	3	100,0	0	n.d.	0	0	1	0	3	0	0	0	45	0	0	0	7	0	0	0	0	0	0	0	41	0	0	0	2	0	0	0	0	0	100,0
S2495	Griesbachthal	San Pietro	P. Paparella	256	2,0	3,0	97	1	2	100,0	0	n.d.	1	0	1	0	1	0	0	0	8	0	0	0	0	0	0	0	0	0	0	0	81	0	0	0	6	0	0	0	0	0	100,0
S2496	Keilbachthal	Cadipietra	P. Paparella	228	2,1	3,9	98	2	0	100,0	0	n.d.	1	0	1	0	1	0	0	0	30	0	0	0	5	0	0	0	0	0	0	0	54	0	0	0	6	0	0	0	0	0	100,0
S2497	Trippach	San Giovanni	P. Paparella	315	1,7	6,1	98	1	1	100,0	0	n.d.	0	0	2	0	1	0	0	0	36	0	0	0	1	0	0	0	0	0	0	0	49	0	0	0	11	0	0	0	0	0	100,0
S3091	Mesole	Lago di Mesole	P. Paparella	213	2,2	5,2	96	1	2	100,0	0	n.d.	1	0	1	0	0	0	0	0	58	0	0	0	4	0	0	0	0	0	0	0	27	0	0	0	8	0	0	0	0	0	100,0
S2450	Habach	Habach	P. Paparella	326	1,6	16,9	89	4	7	100,0	0	n.d.	0	0	6	0	0	0	0	0	41	0	0	0	8	0	0	0	0	0	0	0	45	0	0	0	1	0	0	0	0	0	100,0
S2451	Hollersbach	Hollersbach	P. Paparella	241	2,1	27,3	80	2	17	100,0	1	n.d.	0	0	0	0	1	0	0	0	42	0	0	0	2	0	0	0	0	0	0	0	53	0	0	0	0	0	0	0	0	0	100,0
S1570	Stubach	Uttendorf	P. Paparella	218	2,2	14,8	86	6	8	100,0	7	n.d.	0	0	1	2	6	0	0	0	36	0	4	0	1	0	0	0	0	0	0	0	45	1	0	0	4	0	0	0	0	0	100,0
S2710	Lieser	Tendel	P. Paparella	477	1,1	16,3	88	7	4	100,0	0	n.d.	0	0	5	0	0	0	0	0	28	0	0	0	3	0	0	0	0	0	0	0	60	0	0	0	3	0	0	0	0	0	100,0
S2714	Schlejerfall	Koschach	P. Paparella	561	0,8	13,4	98	2	0	100,0	0	n.d.	0	0	1	0	2	0	0	0	55	0	0	0	1	0	0	0	0	0	0	0	39	0	0	0	2	0	0	0	0	0	100,0
S2718	Muhldorfer	Muhldorf	P. Paparella	208	2,3	11,6	91	6	4	100,0	2	n.d.	0	0	1	0	2	0	0	0	43	1	0	1	1	0	0	0	0	0	0	0	44	1	0	0	6	0	1	0	0	0	100,0
S2709	Mur	Schellgaden	P. Paparella	370	1,4	9,5	79	17	4	100,0	0	n.d.	0	0	2	0	2	0	0	0	16	0	0	0	0	0	0	0	0	0	0	0	75	0	0	0	4	0	0	0	0	0	100,0
SUBCRETED AUSTROALPINE BASEMENTS																																										
S2077	Buthier	Thoules	S. Monguzzi	271	1,9	16,0	70	1	29	100,0	57	98	0	0	1	0	1	0	0	0	4	0	2	5	1	0	0	8	2	4	0	0	23	0	0	0	41	0	0	0	7	0	100,0
SUBCRETED OPHIOLITES																																										
S3430	Mallero della Val Ventina	Rifugio Porro	M. Padoan	626	0,7	57,7	40	33	27	100,0	n.d.	n.d.	0	0	0	0	5	0	0	0	2	1	0	0	0	0	0	52	6	3	0	0	25	0	0	0	7	0	0	0	0	0	100,0
DEEP STRUCTURAL LEVEL																																										
CONTINENTAL ECLOGITES (CRETACEOUS AXIAL BELT)																																										
S2194	Arnad	Arnad	S. Monguzzi	794	0,3	7,5	89	1	10	100,0	n.d.	n.d.	0	0	0	0	4	0	0	0	2	0	0	0	2	0	0	0	0	0	0	0	80	0	0	0	10	0	0	0	0	0	100,0
S2195	Rio Fer	Clapey	S. Monguzzi	776	0,4	20,4	91	0	9	100,0	n.d.	n.d.	0	0	1	0	1	0	0	0	3	0	0	0	5	11	0	4	0	0	0	0	55	0	0	0	18	0	0	0	0	0	100,0
S2295	Vogna	Riva Valdobbia	S. Monguzzi	477	1,1	17,1	72	2	26	100,0	24	n.d.	1	0	0	0	2	0	0	0	11	1	1	2	5	3	0	2	0	0	0	0	52	0	0	0	17	0	0	0	0	0	100,0
S2290	Sermenza	Cerva	S. Monguzzi	489	1,0	11,0	62	2	36	100,0	28	n.d.	0	0	1	0	4	0	0	0	12	1	0	4	4	0	0	0	0	0	0	0	53	0	0	0	18	0	0	0	0	0	100,0
S2293	Gronda	Rassa	S. Monguzzi	758	0,4	16,4	87	0	13	100,0	10	n.d.	1	0	2	0	3	0	0	0	4	0	0	0	7	8	0	1	0	0	0	0	43	2	0	0	28	0	0	0	0	0	100,0
S2292	Sorba	Rassa	S. Monguzzi	301	1,7	13,4	93	1	6	100,0	2	n.d.	0	0	0	0	2	0	0	0	9	0	0	0	2	0	0	1	0	0	0	0	70	0	0	0	16	0	0	0	0	0	100,0
S2294	Artogna	Otra	S. Monguzzi	315	1,7	21,9	78	1	22	100,0	14	n.d.	0	0	0	0	3	0	0	0	8	0	0	1	5	2	0	1	0	0	0	0	50	1	0	0	29	0	0	0	0	0	100,0
S2299	Riale	Piode	S. Monguzzi	281	1,8	16,9	82	1	17	100,0	n.d.	n.d.	0	0	1	0	3	0	0	0	1	0	0	0	6	2	0	0	0	0	0	0	58	1	0	0	30	0	0	0	0	0	100,0
S3758	Rio di Salto	Pianlargo	M. Padoan	302	1,7	15,3	91	8	0	100,0	12	n.d.	0	2	2	0	1	0	0	0	28	14	0	0	8	0	0	2	0	0	0	0	9	0	0	0	28	2	0	0	0	0	100,0
S3755	Valclava	Valcalva	M. Padoan	616	0,7	18,6	84	12	4	100,0	13	33	1	1	1	0	5	1	0	0	17	11	0	0	5	0	0	0	0	0	0	0	13	0	0	0	38	7	0	0	0	0	100,0
S2694	Lausslingbach	Obdach	P. Paparella	536	0,9	13,6	66	10	24	100,0	3	n.d.	0	0	2	0	0	0	0	0	33	2	0	0	1	0	0	0	0	0	0	0	13	0	0	0	47	0	0	0	0	0	100,0
S2695	Kienbergbach	Kathal	P. Paparella	268	1,9	17,2	95	3	3	100,0	5	n.d.	0	0	2	0	4	1	0	0	20	0	0	1	3	0	0	0	0	0	0	0	17	0	0	0	50	0	0	0	0	0	100,0
S2692	Lavant	Taxwirt	P. Paparella	362	1,5	25,3	95	3	2	100,0	7	61	0	1	1	0	2	0	0	0	8	1	0	0	0	0	0	0	0	0	0	0	11	0	0	0	66	1	7	0	0	0	100,0
S2689	Weissenbach	St. Margarethen	P. Paparella	561	0,8	32,7	97	1	2	100,0	n.d.	69	0	1	0	0	1	0	0	0	2	1	0	0	0	0	0	2	0	0	0	0	7	0	0	0	79	0	6	0	1	0	100,0

Sample	River	Site	Operator	grain size (µm)	grain size (φ)	HMC (weight%)	% transparent	% opaque	% turbid	TOTAL	HCI Index	MMI Index	zircon	tourmaline	rutile	other Ti-oxides	titanite	apatite	monazite+xenotime	barite	blue-green hornblende	green hornblende	green-brown hornblende	brown hornblende	actinolite	Na-amphiboles	other amphiboles	clinopyroxene	enstatite	hypersthene	olivine	spinel	epidote group	chloritoid	carpholite	prehnite+pumpellyite	garnet	staurolite	kyanite	andalusite	sillimanite	others	TOTAL
CONTINENTAL ECLOGITES (continued)																																											
S2691	Twimberg	Twimberg	P. Paparella	250	2,0	30,9	90	10	0	100,0	3	n.d.	1	0	3	0	1	0	0	0	17	1	0	0	1	0	0	0	0	0	0	0	23	0	0	0	50	1	1	0	0	0	100,0
S2690	St. Gertraud	St. Gertraud	P. Paparella	345	1,5	31,1	94	4	2	100,0	14	50	0	0	4	0	1	0	0	0	7	4	0	0	0	0	0	0	0	0	0	0	17	0	0	0	63	1	1	0	0	0	100,0
S1527	Lavant	Effendorf	P. Paparella	163	2,6	28,6	88	8	4	100,0	11	67	0	2	4	0	3	0	0	0	15	5	1	0	0	0	0	1	0	0	0	0	11	0	0	0	54	0	4	0	0	0	100,0
S1532	Kainach	Weitendorf	P. Paparella	262	1,9	22,5	94	3	3	100,0	2	58	0	1	0	0	0	0	0	0	8	0	0	0	1	0	0	0	0	0	0	0	10	0	0	0	74	1	3	0	0	0	100,0
S1528	Sulm	Seggau	P. Paparella	119	3,1	25,5	91	2	7	100,0	n.d.	64	0	1	0	0	1	0	0	0	3	0	0	0	1	0	0	0	0	0	0	0	15	0	0	0	73	0	5	0	0	0	100,0
S1529	Lassnitz	Kaindorf	P. Paparella	247	2,0	18,0	97	1	2	100,0	11	58	0	2	0	0	0	0	0	0	5	1	0	0	0	0	0	0	0	0	0	0	7	0	0	0	76	1	6	0	0	0	100,0
S3399	Mislinja	Mislinja	M. Padoan	1177	-0,2	12,1	92	3	5	100,0	14	n.d.	1	0	1	0	6	1	0	0	20	9	0	1	3	0	0	0	0	0	0	0	36	0	0	0	21	0	0	0	0	0	100,0
S3398	Dravinja	Loska Gora	M. Padoan	700	0,5	16,6	88	6	6	100,0	15	n.d.	0	0	1	0	5	0	0	0	23	19	0	0	14	0	0	1	0	0	0	0	21	0	0	0	14	0	0	0	0	0	100,0
S3393	Lobnica	Ruse	M. Padoan	503	1,0	32,6	93	3	4	100,0	13	n.d.	0	0	2	0	4	1	0	0	29	19	0	0	9	0	0	0	0	0	0	0	15	0	0	0	16	0	1	0	1	0	100,0
CONTINENTAL ECLOGITES (EOCENE AXIAL BELT)																																											
S2414	Gilba	Brossasco	S. Andò	675	0,6	16,2	97	0	3	100,0	n.d.	0	1	0	3	0	2	0	0	0	4	0	0	0	1	0	0	0	0	0	0	0	60	3	0	0	25	0	0	0	0	0	100,0
S3018	Parigi	Martiniana Po	M. Padoan	1000	0,0	11,3	94	0	6	100,0	n.d.	n.d.	0	1	0	0	0	0	0	0	1	0	0	0	1	0	0	0	0	0	0	0	81	0	0	0	14	0	0	0	0	0	100,0
S3017	Croesio	Croesio	M. Padoan	1000	0,0	11,0	79	10	11	100,0	15	0	0	0	3	1	5	1	0	0	8	6	0	0	0	2	0	0	0	0	0	1	35	8	0	0	29	0	0	0	0	0	100,0
S2177	Stura di Vallegrande	Forno	S. Monguzzi	588	0,8	1,8	74	4	22	100,0	n.d.	n.d.	3	3	4	0	2	0	0	0	0	0	0	0	0	0	0	0	0	0	0	0	57	0	0	0	29	0	0	0	0	0	100,0
S2076	Grand Eyvia	Valnontey	S. Monguzzi	134	2,9	4,1	81	2	18	100,0	6	n.d.	1	0	1	0	4	0	0	0	10	2	0	0	4	1	1	2	0	0	0	0	39	1	0	0	32	0	0	1	0	0	100,0
S3138	Valsoera	Lago La Balma	E.Mauri	851	0,2	12,2	96	0	4	100,0	7	n.d.	0	0	2	0	2	0	0	0	6	2	0	0	3	7	0	2	0	0	0	0	51	0	0	0	24	0	0	0	0	0	100,0
S2176	Orco	Casetti	S. Monguzzi	281	1,8	7,3	81	4	15	100,0	3	17	0	0	0	0	1	0	0	0	10	1	0	0	3	0	0	1	0	0	0	0	44	3	0	0	35	0	1	0	0	0	100,0
S2395	Anza	Croppo	S. Monguzzi	134	2,9	7,1	77	3	20	100,0	n.d.	33	0	1	1	0	0	0	0	0	2	0	0	0	2	0	0	0	0	0	0	0	13	3	0	0	73	0	3	0	0	0	100,0
S1068	Toce	Domodossola	S. Monguzzi	268	1,9	15,2	83	7	10	100,0	11	52	1	0	1	0	1	0	0	0	27	7	1	1	4	0	1	3	0	1	0	0	10	0	0	0	38	3	0	3	1	0	100,0
S1876	Toce	Oira	S. Monguzzi	196	2,4	3,9	87	6	6	100,0	11	n.d.	3	1	1	0	2	0	0	0	17	6	1	0	7	0	0	3	0	0	1	0	46	0	0	0	11	0	0	1	0	0	100,0
S1877	Isorno	Montecretese	S. Monguzzi	268	1,9	13,6	98	0	2	100,0	10	58	0	0	2	0	0	0	0	0	47	12	3	0	4	0	0	2	0	0	1	0	10	0	0	0	10	2	2	0	1	0	100,0
S1900	Onsernone	Sauressio	S. Monguzzi	660	0,6	3,3	91	1	8	100,0	31	75	1	1	0	0	2	0	0	0	19	11	10	3	0	0	0	4	2	2	0	0	29	0	0	0	9	1	1	1	2	0	100,0
S1888	Campo	Cevio	S. Monguzzi	358	1,5	12,2	87	5	9	100,0	10	43	1	0	0	0	2	0	0	0	38	7	4	0	8	0	0	4	1	0	0	0	17	0	0	0	15	3	1	1	0	0	100,0
S1886	Maggia	Bignasco	S. Monguzzi	616	0,7	9,5	96	1	2	100,0	19	56	0	1	0	0	0	0	0	0	34	20	5	1	0	0	0	4	0	0	0	0	13	0	0	0	17	1	1	0	1	0	100,0
S1054	Maggia	Tegna	E.Mauri	358	1,5	10,2	92	4	4	100,0	12	49	0	0	2	0	0	0	0	0	28	7	0	2	1	2	1	5	0	0	0	0	27	1	0	0	21	3	4	0	1	0	100,0
S1890	Verzasca	Frasco	S. Monguzzi	456	1,1	4,2	97	0	3	100,0	24	n.d.	1	0	0	0	1	0	0	0	31	22	12	1	4	0	0	2	0	0	0	0	7	0	0	0	16	0	1	0	0	0	100,0
S1053	Verzasca	Tenero																																									
S1893	N Cugnasco	N Cugnasco	S. Monguzzi	518	1,0	11,3	93	2	5	100,0	24	71	0	0	0	0	3	0	0	0	39	4	16	3	5	1	0	4	0	0	0	0	7	0	0	0	15	0	1	0	1	0	100,0
S1896	W Preonzo	W Preonzo	S. Monguzzi	445	1,2	12,4	95	1	3	100,0	26	70	0	0	0	0	0	0	0	1	25	23	8	2	4	0	0	4	3	0	6	0	12	0	0	0	5	0	4	0	0	0	100,0
S1049	Moesa	Arbedo	E.Mauri	239	2,1	8,6	95	1	4	100,0	41	n.d.	1	0	0	0	2	0	0	0	7	31	0	9	2	0	1	3	1	0	0	0	21	0	0	0	21	0	0	0	0	0	100,0
S1902	Marmontana	Roveredo	S. Monguzzi	338	1,6	13,1	92	1	6	100,0	46	93	0	0	0	0	1	0	0	0	16	18	19	11	5	0	0	4	1	0	1	0	5	0	0	0	13	0	1	0	3	0	100,0
S1898	Calanca	Grono	S. Monguzzi	536	0,9	5,8	93	4	3	100,0	29	57	0	0	1	0	1	0	0	0	18	9	8	3	2	0	0	4	0	0	0	0	18	0	0	0	30	2	1	0	1	0	100,0
S1897	Moesa	Lostallo	S. Monguzzi	308	1,7	11,6	88	3	9	100,0	40	58	0	0	0	0	0	0	0	0	11	9	12	3	3	0	0	2	2	1	0	0	15	0	0	0	36	3	0	0	2	0	100,0
S1884	Boggia	Grondona	S. Monguzzi	406	1,3	5,4	96	1	3	100,0	42	n.d.	1	1	0	0	2	0	0	0	16	29	24	5	8	0	1	1	0	0	0	0	3	0	0	0	6	0	0	0	0	0	100,0
OCEANIC ECLOGITES (EOCENE AXIAL BELT)																																											
S148	Arrestra	Cogoleto	S. Monguzzi	430	1,2	34,4	80	1	19	100,0	10	n.d.	1	0	1	0	2	0	0	0	20	2	1	1	14	1	0	9	0	1	0	0	40	0	0	0	4	0	0	0	1	0	100,0
S142	Varenna	Pegli	S. Monguzzi	338	1,6	9,5	49	1	50	100,0	22	n.d.	0	0	0	0	0	0	0	0	3	2	1	0	19	4	1	9	1	1	0	0	47	0	1	0	8	0	0	0	1	0	100,0
S2829	Stura del Turchino	Ovada	M. Padoan	384	1,4	29,7	76	18	7	100,0	20	n.d.	0	1	1	1	4	0	0	0	7	4	1	0	18	0	0	1	0	0	0	0	59	0	0	0	1	0	0	0	1	0	100,0
S3558	Orba	Olbicella	M. Padoan	812	0,3	47,5	76	10	14	100,0	1	n.d.	0	0	2	0	0	0	0	0	15	0	0	0	27	0	0	10	0	2	0	0	38	0	0	0	5	0	0	0	0	0	100,0
S175	Orba	Capriata	S. Andò	506	1,0	16,0	78	2	20	100,0	0	n.d.	0	0	1	0	0	0	0	0	9	0	0	0	28	3	0	7	1	0	0	0	44	1	0	0	3	0	0	0	1	0	100,0
S3016	Po	Pian del Re	M. Padoan	412	1,3	40,2	95	3	2	100,0	29	33	0	0	0	0	1	0	0	0	1	9	0	0	6	1	1	1	0	0	0	0	74	1	0	0	0	0	1	0	0	0	100,0
S3745	Casternone	Valdellatorre	M. Padoan	655	0,6	60,9	76	4	19	100,0	n.d.	n.d.	0	0	0	0	0	0	0	0	1	0	0	0	0	0	0	29	51	0	4	0	14	0	0	0	0	0	0	0	0	0	100,0
S2178	Stura di Ala	Ceres	M. Padoan	1000	0,0	52,3	98	2	0	100,0	20	n.d.	0	0	0	0	0	0	0	0	9	15	0	0	13	1	0	0	0	0	0	0	59	0	0	0	1	0	0	0	0	0	100,0
S2193	Chalamy	Champdepraz	S. Monguzzi	379	1,4	32,3	92	0	7	100,0	0	n.d.	0	0	0	0	1	0	0	1	12	0	0	0	37	0	0	6	0	0	2	0	40	0	0	0	0	0	0	0	0	0	100,0
MIXED AXIAL-BELT UNITS																																											
SHALLOW STRUCTURAL LEVEL																																											
S2069	Dranse	Vogny	P. Paparella	542	0,9	0,2	55	24	21	100,0	25	0	0	0	0	0	4	0	0	0	10	1	3	1	2	12	0	1	0	0	0	0	58	3	0	0	2	0	0	0	0	0	100,0
S3415	La Sarine	Broc	M. Padoan	294	1,8	0,4	30	11	59	100,0	n.d.	n.d.	6	4	12	5	2	11	2	0	1	1	0	0	0	0	0	0	0	0	0	1	27	0	0	0	25	0	2	0	1	0	100,0
S3416	La Jogne	Charmey	M. Padoan	760	0,4	0,4	26	25	49	100,0	n.d.	89	4	5	6	2	0	8	0	0	3	1	0	3	3	0	0	0	0	0	0	0	47	0	0	0	12	0	2	2	3	0	100,0
S3419	Simme	Wimmis	M. Padoan	284	1,8	0,4	28	13	59	100,0	n.d.	n.d.	8	23	6	4	2	8	0	0	2	0	0	2	8	0	0	0	0	0	0	0	15	0	0	0	13	0	6	0	4	0	100,0
S3057	Vilters	Vilters	M. Padoan	310	1,7	0,5	16	32	52	100,0	n.d.	n.d.	8	15	5	5	21	10	0	0	15	8	0	0	0	0	0	0	0	0	0	0	13	0	0	0	0	0	0	0	0	0	100,0
S3740	Julia	Tiefencastel	M. Padoan	647	0,6	59,3	20	18	62	100,0	38	n.d.	6	8	4	2	0	2	0	0	8	14	4	4	4	0	0	0	0	0	0	0	43	0	0	0	0	0	0	0	0	0	100,0
INTERMEDIATE STRUCTURAL LEVEL																																											
S1139	B. di Pallare	Carcare	E.Mauri	1447	-0,5	2,3	65	13	22	100,0	20	n.d.	2	2	0	0	3	0	0	0	4	6	0	0	2	12	0	3	1	0	0	0	59	2	0	0	7	0	1	0	0	0	100,0
S2331	Ubaye	La Barge	P. Paparella	125	3,0	0,8	11	5	84	100,0	43	n.d.	0	0	0	0	4	0	0	1	6	1	2	4	14	1	2	8	0	0	0	0	46	1	1	6	1	0	0	0	0	0	100,0
S1861	Buthier	Castello	S. Monguzzi	338	1,6	26,1	67	5	28	100,0	53	100	0	0	0	0	0	0	0	0	2	4	4	3	2	0	1	3	1	3	0	0	27	0	0	0	45	0	0	0	4	0	100,0
S1862	Buthier	Roisane	M. Padoan	397	1,3	1,5	48	4	48	100,0	n.d.	n.d.	9	9	5	4	5	3	0	0	0	1	3	1	0	1	0	1	0	0	0	1	17	1	0	0	37	1	0	0	1	1	100,0
S1860	Artanavaz	Roisane	S. Monguzzi	262	1,9	2,6	62	3	35	100,0	4	15	1	2	1	0	2	0	0	0	6	1	0	0	1	18	0	2	0	1	0	0	40	4	0	0	14	1	1	1	0	0	100,0
S1211	Mera	Chiavenna	E.Mauri	435	1,2	16,1	84	8	9	100,0	29	n.d.	1	1	0	0	1	0	0	0	17	23	0	6	12	0	5	3	0	0	0	0	16	0	0	0	12	1	1	0	0	0	100,0

Sample	River	Site	Operator	grain size (µm)	grain size (φ)	HMC (weight%)	% transparent	% opaque	% turbid	TOTAL	HCI Index	MMI Index	zircon	tourmaline	rutile	other Ti-oxides	titanite	apatite	monazite+xenotime	barite	blue-green hornblende	green hornblende	green-brown hornblende	brown hornblende	actinolite	Na-amphiboles	other amphiboles	clinopyroxene	enstatite	hypersthene	olivine	spinel	epidote group	chloritoid	carpholite	prehnite+pumpellyite	garnet	staurolite	kyanite	andalusite	sillimanite	others	TOTAL
INTERMEDIATE STRUCTURAL LEVEL (continued)																																											
S2498	Aurino	Lutago	P. Paparella	268	1,9	8,7	84	9	8	100,0	2	n.d.	0	1	2	0	1	0	0	0	39	1	0	0	4	0	0	0	0	0	0	0	36	0	0	0	14	0	0	0	0	0	100,0
S3088	Pfitscherbach	S. Giacomo	P. Paparella	88	3,5	5,7	98	2	0	100,0	0	n.d.	0	1	3	0	0	0	0	0	29	0	0	0	1	0	0	0	0	0	0	0	63	0	0	0	3	0	0	0	0	0	100,0
S2448	Tux	Persal	P. Paparella	308	1,7	7,1	11	59	29	100,0	8	n.d.	9	11	7	2	0	0	0	0	13	1	1	0	3	0	0	0	0	0	0	0	45	0	0	0	7	0	0	0	0	0	100,0
S2449	Gerlos	Zell am Ziller	P. Paparella	122	3,0	2,1	15	53	32	100,0	0	n.d.	6	30	9	2	0	0	0	0	5	0	0	0	3	0	0	0	0	0	0	0	40	2	0	0	2	0	0	0	0	0	100,0
S2447	Ziller	N Hausling	P. Paparella	194	2,4	2,6	95	4	1	100,0	2	n.d.	0	0	0	0	1	0	0	0	32	1	0	0	2	0	0	0	0	0	0	0	57	0	0	0	6	0	0	0	0	0	100,0
S1574	Ziller	Ramsau	P. Paparella	233	2,1	5,0	82	9	9	100,0	14	n.d.	0	0	1	1	2	0	0	0	50	0	0	8	0	0	0	0	0	0	0	0	31	0	0	0	7	0	0	0	0	0	100,0
S1572	Krimml	Wald	P. Paparella	185	2,4	3,2	66	19	14	100,0	0	n.d.	1	0	1	1	0	0	0	0	35	0	0	0	0	0	0	0	0	0	0	0	44	1	0	0	16	0	0	0	0	0	100,0
S1569	Fuschbach	Bruck a.d.Gr.	P. Paparella	322	1,6	5,7	70	18	12	100,0	0	0	0	1	2	1	1	0	0	0	5	0	0	0	2	0	0	0	0	0	0	0	67	19	0	0	2	0	0	0	0	0	100,0
S2462	Fuscher	Ferleiten	P. Paparella	165	2,6	3,4	37	13	50	100,0	0	n.d.	1	15	8	3	2	0	0	0	9	0	0	0	2	0	0	1	0	0	0	0	40	0	0	0	18	0	0	0	0	0	100,0
S1568	Gasteiner	Lend	P. Paparella	330	1,6	8,4	66	12	22	100,0	0	n.d.	0	0	0	0	2	0	0	0	26	0	0	0	2	0	0	0	0	0	0	0	59	0	0	0	8	0	0	0	0	0	100,0
S2719	Reisseck	Preisdorf	P. Paparella	379	1,4	5,1	89	8	3	100,0	0	8	0	1	2	0	0	0	0	0	48	0	0	0	5	0	0	0	0	0	0	0	31	3	0	0	8	0	0	0	0	0	100,0
S2721	Tristenspitze	Obervellach	P. Paparella	203	2,3	17,1	92	8	0	100,0	0	n.d.	0	0	2	0	0	0	0	0	66	0	0	0	4	0	0	0	0	0	0	0	26	0	0	0	0	0	0	0	0	0	100,0
S2722	Malnitzbach	Malnitz	P. Paparella	330	1,6	5,1	56	17	27	100,0	0	0	0	6	3	0	3	0	0	0	5	0	0	0	16	0	0	0	0	0	0	0	63	3	0	0	1	0	0	0	0	0	100,0
S2725	Fragrantbach	Innerfragrant	P. Paparella	97	3,4	0,7	54	23	23	100,0	n.d.	0	0	5	20	2	8	0	0	0	1	0	0	0	2	0	0	0	0	0	0	0	33	25	0	0	2	0	0	0	0	0	100,0
S2466	Zirknitz	Grosskirchheim	P. Paparella	194	2,4	3,1	69	13	18	100,0	7	0	0	2	11	0	4	2	0	0	7	0	0	0	21	0	0	0	0	0	0	0	41	7	0	0	3	0	0	0	0	0	100,0
S2465	Zirm	Pockhorn	P. Paparella	362	1,5	4,0	67	17	17	100,0	3	1	0	5	5	0	2	2	0	0	5	0	0	0	1	0	0	0	0	0	0	0	25	47	0	0	4	0	1	0	0	0	100,0
S1516	Malta	Gmund	P. Paparella	315	1,7	23,3	93	2	5	100,0	1	n.d.	0	0	0	0	0	0	0	0	45	1	0	0	0	0	0	0	0	0	0	0	44	0	0	0	7	0	0	0	0	0	100,0
S2717	Radlbach	Radl	P. Paparella	301	1,7	15,6	95	3	2	100,0	1	n.d.	0	0	1	0	2	1	0	0	59	0	0	0	2	0	0	0	0	0	0	0	32	0	0	0	1	0	0	0	0	0	100,0
DEEP STRUCTURAL LEVEL																																											
S2080	Ayassse	Hone	S. Monguzzi	379	1,4	12,6	84	1	15	100,0	4	50	0	0	0	0	3	0	0	0	12	2	0	0	24	2	1	8	2	2	0	0	35	1	0	0	3	0	2	1	1	0	100,0
S2296	Sesia	Alagna	S. Monguzzi	354	1,5	11,3	85	0	15	100,0	5	n.d.	0	0	0	1	0	0	0	0	17	1	0	0	10	0	0	3	0	0	0	0	19	0	0	0	48	0	0	0	0	0	100,0
S1872	Anza	Piedimulera	S. Monguzzi	581	0,8	14,7	76	3	22	100,0	19	59	0	0	0	0	0	0	0	0	10	1	1	1	3	0	0	1	1	0	0	0	16	1	0	0	57	0	3	0	1	0	100,0
MIXED STRUCTURAL LEVELS																																											
S482	Grana	S.Benigno	E.Mauri	241	2,1	1,8	58	9	33	100,0	50	0	0	2	1	0	0	0	0	0	2	2	0	2	7	10	2	2	0	1	0	0	56	11	0	0	2	0	0	1	0	0	100,0
S481	Maira	Busca	E.Mauri	379	1,4	2,0	60	7	33	100,0	18	8	0	6	1	0	1	0	0	0	6	2	0	1	3	7	1	2	1	0	0	1	52	12	2	0	7	0	0	0	1	0	100,0
S480	Varaita	Costigliole	E.Mauri	574	0,8	15,0	74	6	20	100,0	0	6	0	1	3	0	0	0	0	0	9	0	0	0	1	7	0	3	0	0	0	0	39	5	0	0	31	0	0	0	0	0	100,0
S475	Maira	Casalgrasso	E.Mauri	291	1,8	2,5	79	14	8	100,0	44	0	2	5	0	0	0	0	0	0	2	2	0	2	0	6	0	2	1	0	0	0	50	10	2	0	14	0	0	0	0	0	100,0
S479	Po	Staffarda	E.Mauri	388	1,4	22,5	80	8	13	100,0	19	7	0	0	1	0	0	1	0	0	6	5	0	0	4	4	0	3	0	0	0	0	39	8	0	0	25	0	1	0	0	0	100,0
S478	Pellice	Bibiana	E.Mauri	392	1,4	12,0	88	3	9	100,0	5	n.d.	1	1	0	0	2	0	0	0	18	2	0	0	5	1	0	1	0	0	0	0	39	2	0	0	26	0	0	0	0	0	100,0
S477	Chisone	Pinerolo	E.Mauri	1217	-0,3	4,5	82	4	14	100,0	12	n.d.	0	0	0	0	0	0	0	0	9	1	0	1	3	5	0	0	1	0	0	0	40	1	0	0	36	0	0	0	0	0	100,0
S554	Dora Riparia	Avigliana	E.Mauri	294	1,8	1,1	67	9	24	100,0	14	13	2	1	1	0	0	0	0	0	8	6	0	0	2	7	0	2	1	0	0	0	49	5	0	0	13	0	0	0	0	0	100,0
S2179	Stura di Viù	Fucine	M. Padoan	251	2,0	36,4	81	10	9	100,0	10	n.d.	0	0	0	0	4	0	0	0	9	4	0	0	15	1	0	3	0	0	1	0	61	0	0	0	1	0	0	0	0	0	100,0
S555	Stura di Lanzo	Lanzo	E.Mauri	691	0,5	18,7	91	2	7	100,0	3	n.d.	0	0	1	0	0	0	0	0	28	3	0	0	2	7	0	2	1	0	0	0	53	0	0	0	2	0	0	0	0	0	100,0
S556	Orco	Cuorgné																																									
S2175	Soana	Pont Canavese	M. Padoan	n.d.	n.d.	n.d.	91	3	6	100,0	17	n.d.	1	0	0	1	2	1	0	0	11	11	0	0	7	2	0	0	0	0	0	0	55	1	0	0	7	0	0	0	0	0	100,0
S2191	Savara	Molere	S. Monguzzi	131	2,9	15,1	88	0	12	100,0	5	n.d.	0	0	0	0	3	0	0	0	6	0	0	0	32	0	0	0	0	0	0	0	53	0	0	0	4	0	0	0	0	0	100,0
S1857	Savara	Villeneuve	S. Monguzzi	131	2,9	6,2	83	3	14	100,0	7	n.d.	1	0	0	0	2	0	0	0	20	1	1	0	7	0	0	0	0	1	0	0	43	1	0	1	17	0	0	0	1	0	100,0
S1858	Grand Eyvia	Aymaviles	S. Monguzzi	304	1,7	5,0	79	6	15	100,0	1	13	0	0	1	0	3	0	0	0	13	0	0	0	8	3	1	2	1	1	0	0	34	3	0	0	27	0	0	1	0	0	100,0
S910	Lys	Pont S.Martin	E.Mauri	574	0,8	19,9	90	2	8	100,0	25	n.d.	1	0	0	0	1	0	0	0	1	4	0	0	3	1	1	3	2	0	0	0	33	0	0	0	49	0	0	0	0	0	100,0
S912	Evancon	Verres	E.Mauri	518	1,0	35,8	89	3	8	100,0	11	n.d.	0	1	0	0	0	0	0	0	14	7	0	0	5	0	0	2	0	0	0	0	60	0	0	0	9	0	0	0	0	0	100,0
S2081	Clavalitè	Barche	S. Monguzzi	144	2,8	44,0	88	0	12	100,0	2	n.d.	0	0	0	0	2	0	0	0	20	1	0	0	16	5	1	3	1	2	0	0	35	0	0	0	11	0	0	1	0	0	100,0
S2079	Emilius	Pollein	M. Padoan	262	1,9	39,6	98	0	2	100,0	18	n.d.	0	0	1	0	0	1	0	0	4	5	0	0	18	3	0	0	0	0	0	0	58	0	0	0	11	0	0	0	0	0	100,0
S994	Marmore	Chatillon	E.Mauri	281	1,8	26,6	83	3	14	100,0	30	n.d.	0	0	0	0	2	0	0	0	5	13	0	1	11	0	0	3	5	2	0	0	48	0	0	0	8	0	0	0	0	0	100,0
S2058	Borgne	Bramois	M. Padoan	143	2,8	17,1	64	7	29	100,0	33	n.d.	1	2	0	1	3	0	0	0	2	4	1	0	8	1	0	0	0	0	0	0	76	0	0	0	0	0	0	0	0	0	100,0
S2055	Navisence	Chippis	P. Paparella	203	2,3	18,0	59	13	28	100,0	17	n.d.	1	0	0	0	2	0	0	0	17	0	1	2	13	0	0	1	0	0	0	0	54	0	0	0	5	0	0	0	0	0	100,0
S2050	Vispa	Neubruch	M. Padoan	134	2,9	12,7	84	6	10	100,0	18	n.d.	1	0	0	3	7	1	0	0	9	8	0	0	15	0	0	0	0	0	0	0	40	0	0	0	13	0	0	0	0	0	100,0
S2048	Brig	Brig	M. Padoan	147	2,8	16,5	89	8	3	100,0	7	n.d.	1	0	1	0	0	1	0	0	25	5	0	0	8	0	0	0	0	0	0	0	39	0	0	0	19	0	0	0	0	0	100,0
S1873	Ovesca	Villadossola	S. Monguzzi	287	1,8	14,1	90	3	7	100,0	4	29	0	0	0	0	0	0	0	0	40	1	1	0	21	0	1	3	0	0	0	0	22	1	0	0	5	2	0	0	0	0	100,0
S1874	Bogna	Domodossola	S. Monguzzi	137	2,9	25,6	97	1	2	100,0	2	n.d.	1	1	1	0	2	0	0	0	49	1	1	0	14	0	0	1	1	1	0	0	24	0	0	0	0	0	0	2	0	0	100,0
S1875	Diveria	Crevoladossola	S. Monguzzi	271	1,9	10,2	89	6	4	100,0	10	42	0	0	0	0	1	0	0	0	22	2	0	2	4	0	0	3	0	1	0	0	26	2	0	0	32	0	0	2	1	0	100,0
S1878	Melezzo	Masera	S. Monguzzi	175	2,5	0,3	90	3	7	100,0	8	n.d.	7	1	2	0	12	0	0	0	24	3	2	0	4	0	0	7	0	1	1	0	23	0	0	0	11	0	1	0	0	0	100,0
S1895	Brenno	Biasca	S. Monguzzi	274	1,9	3,3	88	3	9	100,0	14	50	1	1	1	0	1	0	0	0	15	5	1	0	2	0	0	0	0	0	0	0	8	2	0	0	52	2	6	0	1	0	100,0
S2391	E Ponte	Ponte	S. Monguzzi	262	1,9	1,3	63	14	22	100,0	n.d.	n.d.	7	7	11	0	1	0	0	0	1	0	0	0	0	0	0	2	0	0	0	0	55	1	0	0	16	0	0	0	0	0	100,0
S2477	Tauernbach	Gruben	P. Paparella	268	1,9	17,1	98	2	1	100,0	0	n.d.	2	0	1	0	0	0	0	0	10	0	0	0	0	0	0	0	0	0	0	0	71	0	0	0	17	0	0	0	0	0	100,0
S2476	Frossnitz	Gruben	P. Paparella	165	2,6	12,3	88	5	7	100,0	1	0	0	0	1	0	1	0	0	0	12	0	0	0	12	0	0	0	0	0	0	0	55	7	0	0	11	0	0	0	0	0	100,0
S2474	Isel	Pragraten	P. Paparella	213	2,2	12,7	93	6	2	100,0	2	n.d.	0	0	0	0	1	0	0	0	8	0	0	0	6	0	0	0	0	0	0	0	57	0	0	0	25	0	0	0	0	0	100,0

Acknowledgments:

Eduardo Garzanti, Giovanni Vezzoli, Marco Malusà and Sergio Andò are heartily acknowledged for all their support, advices and discussions through the years.

Marta Padoan, Paolo D'Adda, Stefano Zanchetta and Marta Limoncelli are thanked for their help and friendship. Fruitful discussions with Maria Mange and Pieter Vermeesch are warmly acknowledged.

Also, I would like to thank my fellow doctoral students and all other students at the Laboratory for Provenance Studies (Paolo, Antonio, Paolo, Milena, Giorgio, Daniele, Marco, Filippo, Michele, Manuel, Mara, Laura, Marta, Paola, Michele, Alessandro, Andrea) and all my friends (Giovanna, Stefano, Davide, Alberto, Giulia, Maddalena (& Matildina), Manuela, Chiara, Laura, Manuela, Giovanni (& Giuseppe), Paolo, Valentino, Marta, Michele, Gaia, Alessia, Francesca, Stefano, Alessandro, Max, Francesco, Ilaria, Andrea and Silvia (last?!?- but certainly not least)) for making these years a very enjoyable experience and for turning into reality the quotation "Life is what happens to you while you're busy making other plans" (John Lennon).

Thanks to my parents and my brother for all their support, the stimulating discussions about science, knowledge and life and for letting me pursue my trial-and-error "ideal for living" (cit).